High-Sensitivity GNSS Doppler and Velocity Estimation for Indoor Navigation

He, Zhe

He, Z. (2013). High-Sensitivity GNSS Doppler and Velocity Estimation for Indoor Navigation (Unpublished doctoral thesis). University of Calgary, Calgary, AB. doi:10.11575/PRISM/26368
http://hdl.handle.net/11023/499
doctoral thesis

UNIVERSITY OF CALGARY

High-Sensitivity GNSS Doppler and Velocity Estimation for Indoor Navigation

by

Zhe He

A THESIS

SUBMITTED TO THE FACULTY OF GRADUATE STUDIES

IN PARTIAL FULFILMENT OF THE REQUIREMENTS FOR THE

DEGREE OF DOCTOR OF PHILOSOPHY

DEPARTMENT OF GEOMATICS ENGINEERING

CALGARY, ALBERTA

JANUARY 2013

UNIVERSITY OF CALGARY

FACULTY OF GRADUATE STUDIES

The undersigned certify that they have read, and recommend to the Faculty of Graduate Studies for acceptance, a thesis entitled "High-Sensitivity GNSS Doppler and Velocity Estimation for Indoor Navigation" submitted by Zhe He in partial fulfilment of the requirements of the degree of doctor of philosophy.

Supervisor, Professor Gérard Lachapelle, Geomatics Engineering

---

Co-supervisor, Professor Mark Petovello, Geomatics Engineering

---

Professor Kyle O'Keefe, Geomatics Engineering

Professor Xin Wang, Geomatics Engineering

Professor Geoffrey Messier, Electrical and Computer Engineering

---

Professor René Landry, ETS Montréal

Date

ABSTRACT

Doppler measurements in global navigation satellite system (GNSS) receivers are useful for various purposes since they not only convey velocity and attitude information, but also directly relate with carrier phase measurements. When it comes to poor signal conditions, conventional high sensitivity GNSS receivers usually extend integration time in order to maintain track of weak GNSS signals. However, due to low signal-to-noise ratio (SNR) and multipath effects, the navigation accuracy is still degraded in this case. Thus maintaining track of Doppler frequency with acceptable accuracy in challenged indoor environments is important and will be beneficial for both standalone and integrated solutions. This thesis investigates how to obtain more reliable and robust Doppler frequency and velocity estimates with GNSS signals for indoor navigation.

Doppler errors due to indoor multipath and user dynamics are first investigated. Experimental results show that these errors are further affected by some multipath statistics such as averaged multipath angle of arrivals (AOAs). A directional signal/multipath model is thus developed to characterize such errors.

To mitigate the adverse effects brought by multipath signals, a direct vector receiver with GLONASS capability is therefore proposed and developed. It is shown that when the user has partial visibility of line-of-sight (LOS) satellite signals, both the velocity and Doppler estimation accuracy is improved as compared to conventional high sensitivity receivers. Geometry dependent factors are defined and used to quantify such improvements.

Finally, the benefits of using such Doppler measurements for consistent navigation are evaluated in two real indoor environments. Doppler measurements from both direct

vector receiver and conventional high sensitivity receiver are tightly integrated with a PDR algorithm. Results show that in large open space indoor environments, the former integration strategy significantly improves the navigation accuracy. For office like indoor environments, improvements of the former integration strategy are not very apparent, but still outperform the conventional integration strategy. All these indicate that the quality of Doppler estimated by direct vector receiver is as good as or better than the conventional one for the indoor environments considered herein.

Acknowledgements

First, I wish to acknowledge and thank my supervisor Professor Gérard Lachapelle for his consistent guidance, support, encouragement and countless opportunities he afforded me. I will always remember that the beginning of my GNSS and navigation career is owed in large part to him. I also offer my regards to the knowledgeable Professor Mark Petovello, my co-supervisor, for his continuous support and insightful comments. His logical way of thinking has been the most valuable and important guide to this work and will continue to be beneficial to my future career.

Second, I would also like to express my gratitude to Dr. Valerie Renaudin, with whom I gained great experience about pedestrian navigation when working on the RIM project. I would like to equally express my gratitude to Dr. Cillian O'Driscoll and Dr. Daniele Borio for their patient tutorials, not to mention their GNSS receiver lecture notes from which I learnt great knowledge.

Third, thanks to all my colleagues in PLAN group for their support, answering all kinds of my naive questions and sharing good times with me. Warm thanks to Tao Li, Da Wang, Tao Lin, Martin, Peng Xie, Debo, Melania, Martin, Billy, Antonio, Tiantong, Boxiong… Special thanks to Yuhang, Yuqi, Bo Li, Anup, and Rakesh for helping me collect data even in cold winters, -20^{o}C!

Finally, I am most grateful to my parents, and my wife, Rong, whose love and devotion made everything possible.

TABLE OF CONTENTS

List of Tables

LIST OF FIGURES AND ILLUSTRATIONS

LIST OF SYMBOLS AND ABBREVIATIONS

Symbol	Definition
$\mathbf{b}_{gyro}, \mathbf{b}_{acc}$	Gyro, and accelerometer biases
C_i	Received signal power of i^{th} satellite
C_b^n	Rotation matrix from b-frame to n-frame
c	Speed of light
$d_i(\bullet)$	Transmitted navigation bits of i^{th} satellite
d_{ion}	Ionospheric delay
d_{trop}	Tropospheric delay
dt , dT_i	Receiver and i^{th} satellite clock bias
$\dot{dt}, \dot{dT}_i$	Receiver and i^{th} satellite clock drift
$d\rho$	Orbital errors
$\mathbf{f}^b$	Specific forces sensed by accelerometers
$f_{D,i}$	Doppler frequency of i^{th} satellite
$\mathbf{g}$	Gravity vector
$\mathbf{H}$	Design matrix
$\mathbf{I}$	Fisher information matrix
$I_m(\bullet)$	m^{th} Bessel function
N_0	Noise spectral density
M	Number of satellites
$r(t)$	Received signal
$\mathbf{r}_{rx}$, $\mathbf{r}_{tx,i}$	Position vector of receiver, and i^{th} satellite
t_{rx}	Receiver time

$t_{tx,i}$	Transmit time of i^{th} satellite
$\mathbf{R}_x, \mathbf{R}_y\ \mathbf{R}_z$	Rotation matrices about x, y and z axis respectively
$\mathbf{v}_{rx}, \mathbf{v}_{tx,i}$	Velocity vector of receiver, and i^{th} satellite
y_k	Correlator output of k^{th} block
ξ, η, ψ	Pitch, roll, and azimuth
$\boldsymbol{\omega}_{ib}^{b}$	Angular rate sensed by gyroscopes
Ω_{bc}^{a}	Skew-symmetric matrix which indicates the rotation rate of frame 'c' to frame 'b' expressed in frame 'a'
$\delta s, d\xi, d\eta, d\psi$	differential scale change and rotation angles from PZ90 with respect to WGS84
ϕ	Carrier phase introduced by communication channel
$\eta(t)$	Additive white Gaussian noise
τ_i	Code delay of i^{th} satellite
ρ_i	Pseudorange of i^{th} satellite
$\dot{\rho}_i$	Pseudorange rate of i^{th} satellite
$\varepsilon_{\rho,i}, \varepsilon_{f_D,i}$	Noise in pseudorange and Doppler for i^{th} satellite
λ_i	Wavelength of transmitted signal for i^{th} satellite
$\lambda_{EDOP}, \lambda_{NDOP}, \lambda_{UDOP}, \lambda_{TDOP}$	Geometry dependent factor in east, north, up and time axis

Abbreviation	Definition
AOA	Angle of arrival
AWGN	Additive white Gaussian noise
CRLB	Cramer-Rao lower bound

DCM	Direction cosine matrix
DFT	Discrete Fourier transform
DLL	Delay lock loop
DRC	Doppler removal and correlation
ENU	East, north and up
FIM	Fisher information matrix
FLL	Frequency lock loop
GLONASS	Global navigation satellite system
GNSS	Global navigation satellite system
GPS	Global positioning system
HSGNSS	High sensitivity GNSS
HSGPS	High sensitivity GPS
IF	Intermediate frequency
INS	Inertial navigation system
IMU	Inertial measurement unit
LOS	Line-of-sight
LNA	Low noise amplifier
MEMS	Micro-electro-mechanical systems
MLE	Maximum likelihood estimate
mSDFT	modulated Sliding DFT
NCO	Numerical controlled oscillator
NED	North, east, and down
NLOS	Non-line-of-sight
OCXO	Oven-controlled crystal oscillator
ODFT	Overlapping DFT

PDF	Probability density function
PDR	Pedestrian dead reckoning
PLL	Phase lock loop
PRN	Pseudo-random noise
PSD	Power spectral density
PZ90	Parametri Zemli 1990
RAIM	Receiver autonomous integrity monitoring
RFID	Radio-frequency identification
RMS	Root mean square
RTK	Real time kinematic
SDFT	Sliding DFT
SDFT-ZP	Sliding DFT with zero padding
SNR	Signal-to-noise ratio
UTC	Universal time coordinated
UTCSU	UTC Soviet Union
UTCUSNO	UTC US Naval Observatory
UWB	Ultra-wide band
WGS84	World Geodetic System 1984

Chapter One: **INTRODUCTION**

Given the increasing demand of global navigation satellite system (GNSS) receivers and other sensors for pedestrian positioning and navigation, extensive research has been done to improve the accuracy of such integrated systems in signal challenged environments, especially for indoor applications. Such integrated systems often rely on the absolute accuracy of GNSS measurements, such as pseudorange and Doppler measurements. Unfortunately, the received signals are often severely attenuated and/or faded in indoor environments. The accuracy of these measurements is also usually quite poor even with high sensitivity receivers, which is the common trade-off between availability and accuracy. The benefits of using such measurements to directly integrate with inertial sensors are often limited, due to the degraded accuracy. Various factors affect the quality of the measurements from GNSS receivers. Some factors rely on the signal processing techniques implemented in the GNSS receivers, and some factors further depend on the characteristics of the environments. This thesis focuses on characterization of high sensitivity GNSS receiver Doppler measurements indoors, explores a more reliable Doppler estimation algorithm for indoor high sensitivity receivers, and also assesses the potential benefits of integrating such Doppler measurements with a pedestrian dead reckoning (PDR) algorithm for indoor applications.

This chapter first reviews the background of the related techniques that are commonly used in GNSS receivers, inertial sensors, and integrated systems. Then, the limitations of the previous research on high sensitivity receivers integrated with PDR indoors are

discussed. After that the objectives and contributions of this thesis are illustrated. In the end, the outline for the rest of the thesis is listed and briefly described.

1.1 Background

With a view to developing a self-contained navigation system that has long term stability, a high sensitivity GNSS (HSGNSS) receiver and an inertial navigation system (INS) are two good candidates. These are two proper techniques that have complementary characteristics for indoor positioning and navigation. The accuracy of GNSS receivers is time invariant and ranges from metre level to centimetre level (Lachapelle 2009, Misra & Enge (2001)), while the errors in inertial navigation systems drift without external updates (El-Sheimy 2007, Titterton & Weston (2004)). In outdoor environments, GNSS/INS integration has proven to be effective, and promising accuracy are obtained and guaranteed by various algorithms, as reported by Kubo et al (1999), Petovello (2003), Sun et al (2008), Soloviev et al (2008) and Li et al (2010) to name a few. When it comes to indoor applications, the story is totally different as will be discussed in the following paragraphs.

1.1.1 GNSS Receivers

As signal degradation is inherent for indoor GNSS signals, harsh environments usually bring about challenges for GNSS receivers. The cause of measurement quality degradation is two-fold. First, the received signal power is usually severely attenuated according to the type of environment (see Table 1.1), and leads to degraded pseudorange and Doppler measurements. For example, the signal attenuation for common wooden

walls is typically around 2.4 dB. But for shopping mall type concrete walls, the signal attenuation can be up to 16.7 dB. Second, the presence of multipath will also directly affect the quality of the receiver measurements.

Table 1.1: Building materials and signal attenuation (from Kjaergaard et al 2010)

Building Type	Wall				Roof	dB
	External	dB	Internal	dB		
Wood	Wood	2.4	Wood	2.4	Tiles	5.19
Brick	Double Brick	10.38	Brick	5.19	Tiles	5.19
School main building	Double Brick & Concrete	10.38 14.76	Brick Concrete	5.19 9.57	Tiles Tiles	5.19 5.19
Shopping mall	Reinforced Concrete Tinted Glass Glass	16.70 24.44 2.43	Brick	5.19	Flagstone Sand Concrete	N/A 2 9.57
Tower block	Double Brick Around Concrete	19.95	Brick	5.19	Tiles	5.19

To deal with the decreased signal power, the common technique is to obtain additional processing gain using various methods. In high sensitivity GNSS receivers extended integration time is often applied. From a practical standpoint, there are many factors or details that need to be considered to implement a high sensitivity receiver, such as polarity change of data bits in the received code, presence of frequency estimation error, and receiver dynamics to name a few. A full treatment of these details can be found in van Diggelen (2009). To mitigate the adverse effects brought by non-line-of-sight (NLOS) signal components, there are several possible methods that have been proposed such as antenna diversity suggested by Counselman (1989), narrow correlator reported by van Dierendonck et al (1992), Bayesian estimation approach conducted by Giremus et al (2005 and 2007), multiple hypothesis testing based multipath mitigation methods in

urban area reported by Spangenberg et al (2010), and batch processing method reported by van Graas et al (2005) to name a few. Early commercial GPS receiver design was influenced by high precision survey and mapping applications and thus focused on multipath mitigation under the situation where both line-of-sight (LOS) and NLOS signals are present at the antenna, or using wideband receivers which can resolve the multipath and direct signals. Similar work has been done by Steingass & Lehner (2004), who measured the wideband navigation channel for high precision applications, and Larson et al (2008), who reported multipath statistics for urban environments. But for high sensitivity receivers, the situation is more complicated. It is common to receive both LOS and NLOS signals at the same time, while it is also not uncommon to receive only NLOS signals in seriously degraded environments (van Diggelen 2009).

Although various enhanced signal processing algorithms have been applied to obtain additional processing gain, generally speaking, the quality of measurements is usually degraded. Many researchers have investigated the performance of such HSGNSS receivers in various indoor environments. For example, Kjærgaard et al (2010) has reported that in shopping malls or tower block buildings pseudoranges are largely biased and can result in 20 to 60 m two dimensional root-mean-square (RMS) errors even with commercial high sensitivity receivers. In signal degraded environments, the systematic error (Petovello et al 2003) due to multipath in a pseudorange measurement will further deteriorate the navigation solution if integrated with PDR sensors.

Therefore, researchers have proposed to use advanced receiver architectures or to integrate with external sensors such as an inertial measurement unit (IMU) to achieve

better performance. Soloviev et al (2004) used a HSGPS integrated with INS, and reported GPS signal can be tracked as low as 15 dB-Hz.

In general, HSGNSS receiver measurements are beneficial to positioning only when the LOS signal is above a certain threshold. If integration time is not long enough to get adequate processing gain, or the LOS signal power is much lower than that of NLOS signals, the measurement quality of both the pseudorange and Doppler will dramatically deteriorate, and will gradually cause loss of lock on the signal. With this in mind, the indoor GNSS receiver may lack short term stability. This means that it is quite possible for the received signal power at certain epochs to be extremely low, in which case the output measurement might be of little use or even bias the final navigation solution. But on average, the high sensitivity receiver maintains tracking of the LOS signal, thus long term accuracy can be assumed.

On the other hand, as is well known, Russia has begun an accelerated revitalization of its GLONASS. Adding GLONASS to GPS will also improve the geometry of navigation. O'Driscoll et al (2010) reported that the combined use of GPS and GLONASS in a high sensitivity receiver will provide a near two-thirds increase in the number of available satellites. In harsher environments (C/N_0 on the order of 10 dB-Hz), improvements in accuracy and availability will be more apparent. GLONASS is therefore also considered and used in this research as an augmentation to GPS.

1.1.2 Inertial Sensors and Integration

With an increasing demand for a low-cost, reliable pedestrian navigation system, attention has been drawn to the use of many sensors or devices, such as Wi-Fi, inertial sensors, radio-frequency identification (RFID), ultra-wide band (UWB), and ZigBee radios, to integrate with GPS receivers. In particular, inertial sensors can provide dead-reckoning information for personal positioning, which is proven to be of great potential (Mezentsev et al 2003, Petovello et al 2003, Babu& Wang 2006, Pany et al 2009).

The distinct advantages of inertial sensors over GNSS receivers and other devices are their autonomy (i.e., they are self-contained). They can sense tri-axis acceleration and angular rate with respect to the inertial reference frame, and output such measurements at relatively higher rates than most GPS receivers (50 Hz or more is common for IMU, while GPS output rate is often set between 1 Hz to 20 Hz).

The inherent limitation of using such inertial systems is the accumulation of position errors over time and distance traveled. Unless external measurements are available (such as the high sensitivity receiver discussed in the last section) to update the system, the errors may continue to accumulate to the point where the system positioning accuracy is too poor and no longer useful.

In personal positioning, the user most likely moves around on foot. Thus, many researchers take advantage of this user induced 'platform dynamic' to identify the step length, and finally to perform PDR algorithm with inertial sensors. Much research has thus been done on PDR methods such as Foxlin (2005), Randell et al (2003), Ladetto et al (2001), Goyal et al (2011), and Shin et al (2010). However, most reported PDR

positioning accuracy largely depends on heading and step length estimation. Positioning error is a function of distance traveled. Recent work has been attempting to fuse high sensitivity GPS receivers with PDR sensors to get improved system performance.

It is known that GNSS receivers may suffer short-term unavailability indoors or urban canyons, while inertial sensors lack long-term reliability. The idea to compensate each sensor's drawbacks by integrating these complementary systems is not new (Kim et al 2003, Jovancevic et al 2004, Gebre-Egziabher et al 2005, Bullock et al 2006, Kiesel et al 2007). In order to take advantage of both systems, the inertial sensor can predict the user's dynamic according to system dynamic equations, and then use this information to aid GPS if it is experiencing the outage. When GPS is working normally, the inertial sensor errors can be estimated by using GPS updates. Commonly, a Kalman filter is used for integrating the two systems (El-Sheimy 2007). A lot of research has also been done using different integration methods between GNSS receiver with INS for various applications (Tazartes & Mark, 1988, Sennott & Senffner 1997, Petovello 2003).

Although various applications of GPS/INS integration have proven to be quite successful, focus in this thesis is on the benefits in the context of indoor positioning and navigation using high sensitivity GNSS receivers and inertial sensors. In order to fully utilize the pedestrian dynamic equation to further suppress accumulating errors, a PDR algorithm is usually implemented instead of traditional strap-down inertial mechanization equations. The major challenge for PDR algorithms is the heading estimation, since the step length estimation has reached a level of usual accuracy (Shin & Park 2001, Renaudin et al 2012). With this in mind, researchers have proposed and assessed the possibility of using

high sensitivity GNSS receivers to integrate with PDR algorithms in urban canyons, and in some mild indoor environments. For example, Lachapelle (2007) reported performance of using pedestrian dead-reckoning with micro-electro-mechanical systems (MEMS) IMU to aid high sensitivity GPS in some harsh environments; as an extension, Afzal et al (2011) proposed a method to mitigate the perturbation in orientations for indoor navigation by use of multiple magnetometers. Salychev et al (2000) assessed the feasibility and performance of using a low-cost motion sensor integrated with GPS and differential GPS.

To deal with the difficulties faced by the integration of a high sensitivity receiver and inertial sensors in mild and harsh environments, the following possible solutions are possible: (1) by using more satellites, there are more chances to receive LOS signals. Satellite navigation systems other than GPS can be used, such as GLONASS, (2) alternatively, a multi-frequency software receiver structure is a possibility (O'Driscoll et al 2009), (3) receiver autonomous integrity monitoring (RAIM) techniques can help receivers to reject measurements that are generated from pure reflected signals. Moreover, increasing the number of satellites will also improve geometry, thus making RAIM more effective (Brown & Sturza 1990), (4) multiple hypotheses testing might be useful, such as selecting amongst multiple hypotheses to estimate and eliminate the mean jump in the measurements caused by NLOS signals as reported by Spangenberg et al (2010). Other researchers have focused on modeling and estimating NLOS signal components from the pseudorange measurement aspects, such as Giremus et al (2005,

2007), Spangenberg et al (2010). Unfortunately, the above works only showed results conducted in simulation mode or at most conducted in urban canyon environments.

Although the aforementioned research was shown to be effective, each technique still suffers limitations indoors. To this end, additional work needs to be done to refine, merge, and improve these techniques, as described below.

1.2 Limitations of Previous Research

When it comes to severe signal degradation, Doppler estimation with a high sensitivity GPS receiver will also experience the threshold effect. Due to the fact that maximum likelihood estimation of sinusoid frequency is nonlinear, it inherently suffers threshold effects, i.e., below a certain threshold there will be large error estimates (outliers) that will exhibit large estimation bias and variance (Kay 1993a). Without external aiding information (such as bit aiding and/or inertial solution feedback), this effect will eventually lead to undesirable positioning results. Aside from various algorithms to increase the processing gain discussed in the above paragraphs, the integration of high sensitivity receivers with IMUs has proven to be effective such as using MEMS inertial sensors integrated with HSGPS. For example, Pany et al (2009) reported an ultra-tight integration architecture using a high sensitivity GNSS receiver with a MEMS IMU. The receiver's integration time was further extended up to 2 seconds, and thus was able to track signals as weak as 1.5dB-Hz. However, this type of approach generally relies on the high sensitivity GNSS receivers' pseudorange measurements. In such a case, once multipath dominates the received signals, the benefit of using GNSS to update the PDR algorithm will be limited. It may even deteriorate the performance of the integrated

system. The question arises therefore as to whether and how much sensitivity receivers can improve PDR performance in indoors.

Some researchers have noticed the importance of the Doppler measurements, which exhibit a certain level of immunity over the communication channel induced impairments as compared with pseudorange measurements (Borio et al 2010). The frequency estimation or tracking has been thoroughly investigated in the field of communications (Natali 1984). In GNSS receivers, conventional Doppler frequency estimation is based on frequency lock loop (FLL) or phase lock loop (PLL). Frequency discriminators usually count on the carrier phase increment, such as the cross-product frequency discriminator, etc. as discussed by Ward et al (2006). A loop filter is used to further suppress the loop noise. However, if the carrier phase has cycle slips or the signal power is too weak, the frequency tracking error will increase. The block processing technique discussed by van Graas et al (2005) can provide maximum likelihood estimates of the Doppler frequency in weak signal environments. In addition, the Cramer-Rao lower bound (CRLB) of Doppler frequency estimation in weak signal environment by using block processing is illustrated by Borio et al (2010). In general, these contributions showed the effectiveness and the bounds of using block processing to estimate the Doppler frequency especially in weak signal environments.

However, in order to achieve better frequency estimation, non-coherent frequency discriminators are often used. Pany (2010) has introduced and discussed a new type of non-coherent frequency discriminator, which is implemented by using the so called ‘F-Correlator’ divided by ‘P-Correlator’. Brenner (2011) has claimed a kind of discrete

Fourier transform (DFT) based linear frequency discriminator in a patent, but lacks the performance analysis. As a result, an investigation into some improved non-coherent Doppler frequency estimators and the corresponding performance analysis is needed.

If reliable Doppler frequency tracking is possible, several potential advantages can be realized even in difficult indoor environments. In terms of measurement availability, one obvious advantage of maintaining Doppler frequency tracking is that carrier phase can still be predicted. Soloviev & Dickman (2011) reported results of using advanced receiver structure (open loop tracking and deep integration) to maintain carrier phase measurements in deep indoors. Petovello et al (2008) investigated the effects of using extended coherent integration times on weak signal for real time kinematic (RTK) positioning in an ultra-tight receiver. Pany et al (2012) reported a differencing correlator scheme which can still provide the carrier phase measurements indoors, but it is based on a static indoor scenario with glass window on one side, and extremely long coherent integration time is used in order to get an accurate enough Doppler frequency. It should be known that the instability of the oscillators will also affect the long integration as discussed in Gaggero (2008). Although the above algorithms can mitigate a certain level of multipath induced positioning error in real indoor environments, the static assumption is generally not applicable for pedestrian navigation. Rather, the more common situation includes some level of user dynamics. The effects of such indoor multipath and user dynamics on Doppler frequency tracking have not been considered and assessed in previous research. As a result, a more thorough analysis of Doppler frequency estimation in indoor multipath environments is needed.

Finally, with regards to high sensitivity GNSS integrated with PDR, little research has been done to assess the potential benefits of using Doppler measurements to help the heading estimation in PDR algorithm. Renaudin et al (2012) showed some results of using conventional HSGPS Doppler measurements to integrate with PDR algorithm. Such Doppler measurements are based on the maximum likelihood estimate (MLE). It presents the benefits of such integration in various indoor environments, and indicates that the performance is sometimes limited and may rely on specific indoor environments. As an extension to this research, the potential benefits of using the proposed Doppler estimates over conventional ones to tightly integrate with PDR need to be explored, especially for indoor pedestrian applications.

1.3 Objective and Contributions

Due to the limitation of the research mentioned in the previous section, this thesis expands upon the work described above with the aim of improving the Doppler and velocity estimation in weak signal environments and to enhance indoor positioning and navigation performance.

With regard to the limitations listed in the previous section, the objectives of this thesis are to investigate the following aspects of a high sensitivity GNSS receiver and GNSS/PDR integrated system:

1) *Doppler error characterization indoors:* As stated in the previous sections, it is well known that relatively accurate Doppler estimation is quite beneficial to both the velocity and attitude estimation of the integrated system since they exhibit some degree of immunity over channel induced impairments, as compared to

pseudorange measurements. The major challenges for indoor Doppler frequency estimation are two-fold. The first one is signal power attenuation, which is due to various obstacles along the propagation path, such as concrete walls, glasses, windows, etc. The second one is the combined effects of user motion and multipath, which can cause the so-called fading phenomenon. Both factors can degrade the quality of the measurements and navigation accuracy. Furthermore, in order to get a more reliable Doppler frequency estimate in indoor environments, the factors that affect the precision and accuracy of Doppler measurement will all be investigated. Real indoor experimental data will be used to assess the model proposed herein.

2) *Improved Doppler/Velocity Estimation in indoors:* Once the Doppler errors in indoor environments are known, the next questions are how to get a more reliable estimation of Doppler in some indoor environments, and does this estimate outperform the conventional methods which use block processing technique?

3) *High sensitivity GNSS/PDR tight integration for consistent navigation in indoor:* Since Doppler measurements convey information about the user's attitude, the long term PDR heading drift can be significantly mitigated if moderate quality Doppler frequency updates are available. Once reliable indoor Doppler measurements are available, the heading errors from PDR-only algorithm, PDR integrated with Doppler from conventional high sensitivity receiver and PDR integrated with Doppler with the proposed algorithm can be compared. And real

experimental data will be used to evaluate the effectiveness of the proposed method.

The major contributions of this thesis to the field of navigation and positioning can be summarized as follows

1) Characterization of Doppler frequency estimation errors in indoor environments. Much research has already been done to deal with SNR effects on Doppler estimation accuracy. However, the indoor multipath influence on the quality of high sensitivity receiver's Doppler measurements has not been thoroughly analyzed and thus is one focus of this thesis. A multipath/signal model has been developed which tries to relate Doppler errors with statistics of the multipath and user dynamic. Real experimental data is used in order to verify the models proposed.
2) Development of a reliable Doppler/velocity estimation method indoors. Conventional high sensitivity GNSS receivers use block processing techniques to estimate Doppler and code phase in bad signal conditions. Each satellite is being tracked independently. Once multipath dominates some satellite signals, it will lead to biased measurements, and may further result in non-convergent solutions. Given this, a direct vector receiver structure with GLONASS capability, is proposed, developed and investigated. The proposed algorithm fully uses mutual information among all satellites, and assumes no a priori information about the indoor multipath statistics. It is shown that this direct vector receiver will outperform a conventional one when it has partial visibility for some LOS satellite

signals. Even in the NLOS dominated scenarios, this direct vector receiver performs no worse than the conventional high sensitivity receiver.

3) Evaluation of the benefits of integrating high sensitivity Doppler measurements with PDR algorithm for indoor navigation. The integrated solutions with Doppler measurements from conventional high sensitivity receivers and direct vector receivers are tested and assessed with real experimental data.
4) Analysis of the GNSS dilution of precision (DOP) metrics with a geometric approach. Some useful terms such as *geometry dependent factor*, *DOP correlation coefficients* are defined and derived in the Appendix A. They are convenient to better characterize the user-satellite geometry and have been used to evaluate the performance of the proposed direct vector receiver.

1.4 Thesis Outline

The thesis contains seven chapters and one appendix. The remaining six chapters are organized as described below.

Chapter 2 summarizes the fundamental techniques and methodologies that are used in GNSS, INS and GNSS/INS integrated systems. It forms the basis for the development of all succeeding chapters.

Chapter 3 focuses on Doppler frequency estimation with additive white Gaussian noise (AWGN). The CRLB for signal amplitude, code phase, as well as Doppler frequency are shown. Then some coherent and non-coherent frequency estimation algorithms are reviewed. In particular, a novel sliding DFT (SDFT) based non-coherent frequency

estimation algorithm is presented and its advantages over DFT based frequency estimation in high sensitivity receivers are discussed.

Chapter 4 focuses on characterization of Doppler errors based on real indoor observations from HSGNSS receivers. An indoor signal/multipath model is developed. Experimental data is processed and analyzed to show the consistency with the proposed model.

Chapter 5 discusses a reliable Doppler and velocity estimation algorithm for indoor narrowband multipath environments. A direct vector receiver is thus proposed, and investigated. The Doppler and velocity estimation performance with direct vector receiver is compared with that of conventional high sensitivity receivers. Two real indoor data sets are also processed and analyzed in order to verify the effectiveness of the proposed method.

Chapter 6 presents HSGNSS/PDR tight integration results, in order to assess the potential benefits of Doppler measurements for enhanced indoor navigation.

Chapter 7 presents conclusions and recommendations.

Appendix A introduces a geometric approach to characterize the GNSS DOP metric. Closed form expressions for the geometry dependent factor, joint DOP, and DOP correlation coefficients are derived. Real experimental data is analyzed to illustrate the usefulness of such terms. These terms are used to further evaluate the performance of the proposed algorithm in previous chapters.

The flow chart depicting the inter-relationship of the thesis chapters is shown in Figure 1.1.

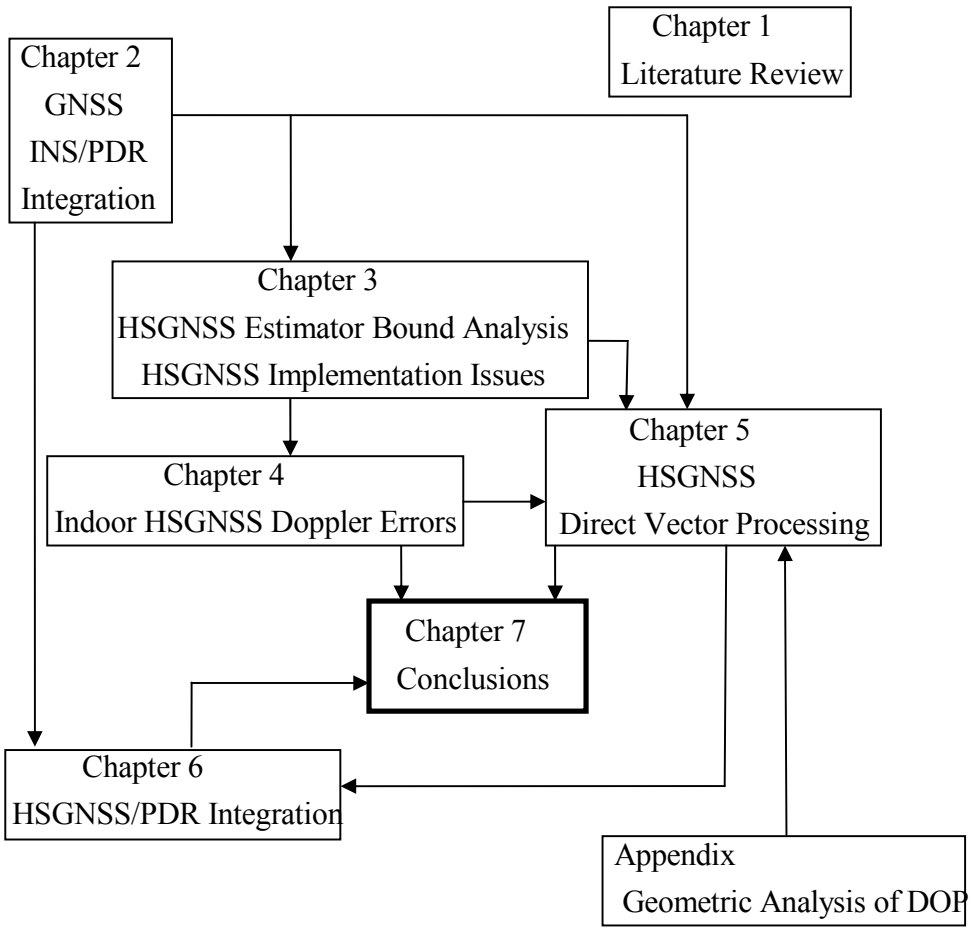

Figure 1.1 Flow chart of the thesis structure

Chapter Two: **OVERVIEW OF GNSS, INS, AND INTEGRATION**

This chapter reviews some fundamental techniques in GNSS receivers, INS, and GNSS/INS integration. First, GLONASS and GPS systems are compared, and the basic components of a GNSS receiver are introduced. After that, two commonly used inertial mechanization methods are revisited, namely the strap-down mechanization and dead-reckoning algorithms. Various GNSS/INS integration mechanisms are then reviewed.

2.1 Overview of Global Navigation Satellite System (GNSS)

Positioning and navigation using electronic systems have a long history. They are usually divided into two categories: active ranging systems and passive ranging systems (O'Driscoll & Borio 2009). For an active ranging system, a device is often operated by first transmitting a signal, and then detects the reflection/return signal to compute the absolute distance between the device and the targets, such as radar or sonar. The distance is directly estimated by measuring the round trip delay. For the second category, it is called passive ranging systems. These devices do not transmit any signals to the 'targets'. Instead, they rely on receiving the signals from the 'targets'. This also indicates that in order to measure the distance, the timing information should be encoded in the transmitted signals. The GNSS system belongs to this latter category, and the measuring device is commonly known as a receiver. The 'targets' that transmit signals are the satellites in various known orbits and frequency bands. And as inherent for a passive ranging system, the primary function of the GNSS receiver would be to keep track of the timing information contained in the transmitted signal. Additionally, the GNSS receiver

would also be capable of extracting some extra navigation information contained in the transmitted signal, such as satellite position, velocity, clock errors, etc, which will be used to compute the navigation solution. Because of their full availability, only GPS and GLONASS are chosen and used in this thesis.

2.1.1 GPS & GLONASS Signal, Time, and Coordinate

Aside from the well known GPS, GLONASS is an alternative satellite navigation system operated and maintained by the Russian government. Each GLONASS satellite transmits its standard precision signal using a frequency division multiple access (FDMA) technique located around 1602.0 MHz (L1 band for GLONASS). Each centre frequency can be computed given the satellite's frequency channel number shown in Table 2.2.

With the GLONASS modernization, there is a growing trend to process GPS signals along with GLONASS. Combing GPS with GLONASS will provide an increased number of satellite observations, will markedly increase spatial distribution of the satellite geometry, and will also reduce the DOP factors. In some cases, joint processing GPS and GLONASS signals will speed up RTK positioning. In Table 2.1, Table 2.2, and Table 2.3, some key differences between GPS and GLONASS system are listed. Detailed information can be found in ICD-GPS (2004), ICD-GLONASS (2008).

Table 2.1: Satellite orbits comparison between GLONASS and GPS

	GLONASS	GPS
Orbital Planes	3, spaced by 120^o	6, spaced by 60^o
Satellites per orbital plane	8, evenly spaced	4, unevenly spaced
Orbital plane inclination	64.8^o	55^o
Altitude	19,100 km	20,200 km
Orbital period	11 hour 15 min[1]	11 hour 58 min
Orbital Parameter	satellite position, velocity and accelerations	modified Keplerian

[1] Polischuk et al (2002)

Table 2.2: Signal characteristics comparison between GLONASS and GPS

	GLONASS	GPS
Frequency band	L1: (1602 + k*9/16) MHz L2: (1246 + k*7/16) MHz	L1: 1575.42 MHz L2: 1227.6 MHz
PRN codes	C/A, P(Y)	C/A, P(Y)
Code frequency	C/A:0.511MHz;P: 5.11MHz	C/A: 1.023MHz;P: 10.23MHz

Table 2.3: Navigation message comparison between GLONASS and GPS

	GLONASS	GPS
Super-frame duration (min)	2.5	12.5
Super-frame capacity (bit)	7500	37500
Frame duration (s)	30	6
Word duration (s)	2	0.6
Word capacity (bit)	200	30
Number of words in frame	15	10
Time Reference	UTC_{SU}	UTC_{USNO}
Coordinate Reference	PZ90	WGS84

When jointly processing GLONASS and GPS signals, one has to first account for the differences in their time scale and coordinates. For example, GLONASS and GPS both have their own time scales, which are different realizations of universal time coordinated (UTC). GLONASS satellite clocks are corrected with respect to the UTC_{SU} (UTC Soviet Union), while GPS satellite clocks are corrected referenced to the UTC_{USNO} (UTC US Naval Observatory). UTC_{SU} and UTC_{USNO} are only two of the local UTC. On the other side, GPS time is maintained by the GPS master control station, which usually keeps the GPS time within 100 ns with respect to UTC_{USNO}. It has also reported that UTC_{SU} differs from the UTC by some microseconds, while UTC_{USNO} only differs from UTC by a few nanoseconds (Roßbach 2000). Whenever the time differences between UTC_{SU} and

UTC_{USNO} are not known a priori to the receiver, the time in GPS scale and GLONASS scale is thus also unknown. Then the clock offset between these two times in different references should be estimated as an additional state.

The geodetic datum for the GLONASS is Parametri Zemli 1990 (PZ90), some reference uses Parameters of Earth 1990, i.e., PE90. GPS system uses the World Geodetic System 1984 (WGS84). The detailed description of PZ90 can be found in ICD-GLONASS (2008).

Due to the fact that WGS84 is more widely accepted than PZ90, it is quite common to transform the GLONASS PZ90 coordinates to WGS84. The following 7-parameter coordinate transformation can be used, as reported by Soler & Hothem (1988).

$$\begin{bmatrix} x \\ y \\ z \end{bmatrix}_{WGS84} = \begin{bmatrix} \Delta x \\ \Delta y \\ \Delta z \end{bmatrix} + (1+\delta s) \begin{bmatrix} 1 & d\xi & -d\psi \\ -d\xi & 1 & d\eta \\ d\psi & -d\eta & 1 \end{bmatrix} \begin{bmatrix} x \\ y \\ z \end{bmatrix}_{PZ90} \tag{2.1}$$

In equation(2.1), $\Delta x, \Delta y, \Delta z$ represent the translation offsets, δs denotes the differential scale change, $d\xi$, $d\eta$, $d\psi$ denote the differential rotation from PZ90 with respect to the WGS84. Once the 7 parameter transformations are known, any point in PZ90 can be converted into WGS84 coordinates. Table 2.4 lists some parameters to transform one point from PZ90 coordinate to WGS84 coordinate.

Table 2.4: Some transformation parameters from PZ90 to WGS84

Parameter	Δx	Δy	Δz	$d\eta$	$d\xi$	$d\psi$	δs
Value[1]	-0.47m	-0.51m	-2.00m	-0.002''	-0.001''	-0.356''	$22*10^{-9}$
Value[2]	0m	2.5m	0m	0	0	-0.4''	0
Value[3]	0.40m	0.36m	-0.48m	0.024''	-0.012''	-0.343''	0
Value[4]	-0.36m	0.08m	0.18m	0	0	0	0

[1]Mitrikas et al (1998); [2]Misra et al (1996); [3] Roßbach (2001); [4]the empirical values used in this thesis are as the ones reported in Revenivykh (2012)

2.1.2 Signal Tracking and Measurements

The primary functionality of a GNSS receiver is to determine its position and velocity by processing the incoming signals from the satellites. Processing is usually divided into two cascaded stages, i.e., signal tracking and navigation solution computation. The signal tracking is to estimate the incoming signal's synchronization parameters, such as code phase (or time delay), Doppler frequency, and carrier phase. These parameters are then used to generate the measurements for all available satellites. The navigation solution computation is to estimate the user's position and velocity based on the above measurements, along with decoded navigational information from all the available satellites.

The role of signal tracking is to keep track of the synchronization parameters from the incoming signal as accurately as possible and then to generate the measurements. With the satellites in orbit transmitting the signals, the receiver first generates a local replica, and correlates the incoming signal with the local replica in order to obtain a rough or coarse estimation of the signal parameters.

For example, the received complex envelope signal in additive Gaussian noise can be expressed as

$$r(t) = \sum_{i=1}^{M} \sqrt{2C_i}\, d_i(t-\tau_i)\, p_i(t-\tau_i) e^{j(2\pi f_{D,i} t + \phi_i)} + \eta(t), \quad t \in [0, T_{obs}] \tag{2.2}$$

In equation (2.2), the subscript i stands for the i^{th} satellite, M being the number of available satellites in view, C_i the received signal power, $d_i(\bullet)$ the transmitted navigation bits, $p_i(\bullet)$ the spreading code, or pseudo-random noise code (PRN code), τ_i the code delay, $f_{D,i}$ the Doppler frequency, ϕ_i the carrier phase introduced by the communication channels. $\eta(t)$ is the additive white complex Gaussian noise, with the spectral density of N_0 watt/Hz over the pre-correlation bandwidth (single side bandwidth).

With the received signal model shown in equation(2.2), the correlation process is illustrated in Figure 2.1, and is expressed in the forthcoming equation. In Figure 2.1, the correlation process in GNSS receivers is also called Doppler removal and correlation (DRC). The incoming signal first removes the Doppler effects and then dispreads it with the corresponding PRN code. After the integration and dump, $y_k(\hat{\tau}_i, \hat{f}_{D,i}, \hat{\phi}_i)$ is the correlator output for the i^{th} satellite in epoch k with estimated time delay $\hat{\tau}_i$,Doppler frequency $\hat{f}_{D,i}$ and carrier phase $\hat{\phi}_i$ .The statistics of the correlator outputs will be further discussed in later chapters. The correlation process is carried out as

$$y_k(\hat{\tau}_i, \hat{f}_{D,i}, \hat{\phi}_i) = \frac{1}{T_{coh}} \int_{(k-1)T_{coh}}^{kT_{coh}} r(t)\, p_i(t-\hat{\tau}_i) \exp(-j(2\pi \hat{f}_{D,i} t + \hat{\phi}_i))dt \qquad (2.3)$$

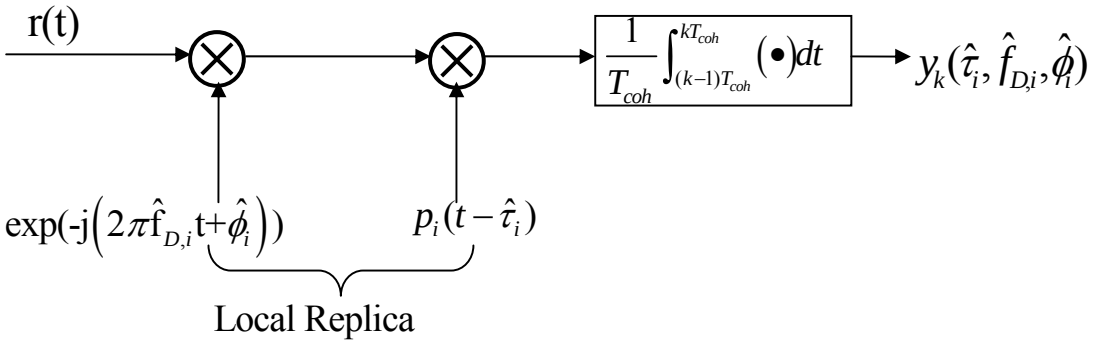

Figure 2.1: Doppler Removal & Correlation (DRC)

However, the Doppler frequency and code delay estimated by this coarse estimation is usually too rough for high precision positioning and navigation purposes. Fine signal estimation with feedback control such as delay lock loop (DLL), FLL and PLL is often applied right after the correlation process in order to maintain precise tracking of the code phase and Doppler. This fine signal tracking is a coupled process with code and carrier tracking blocks, such as using PLL and DLL individually to accurately lock the incoming signals' Doppler, carrier phase, and code phase. This coupled tracking diagram is shown in Figure 2.2, where PLL provides the carrier Doppler and carrier phase to update the carrier numerically controlled oscillator (NCO), while DLL updates the code phase or time delay for code NCO. The NCOs will then generate the local replica with desired signal parameters. In this way, the receiver continuously tracks the incoming signal.

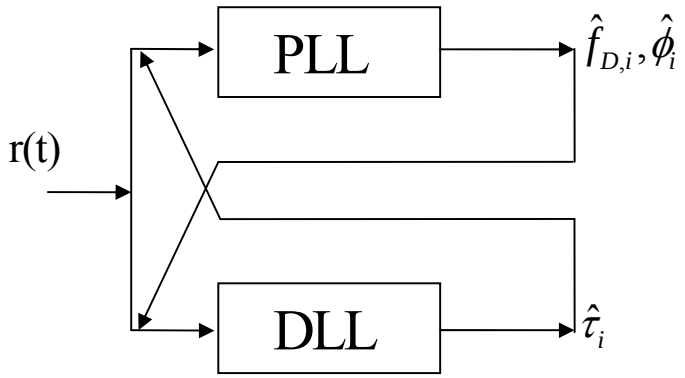

Figure 2.2: Conventional receiver tracking loops

The mechanism for either PLL or DLL is similar, and uses linear feedback control loops. A generic single tracking loop diagram is shown in Figure 2.3. Assume that the received signal $r(t)$ first correlates with the local replica, which is controlled by the local code and carrier NCOs, after the DRC module, the correlation output is fed to the discriminator. The discriminator is by design, an approximate linear function of the error to be estimated, and it will be sensitive to this tracking error. For example, in a FLL, there are various types of frequency discriminators, such as those in Table 5.4 of (Ward et al 2006). The outputs of the discriminator are related to the parameter estimation errors that are of interest. By using the loop filter, the loop noise is further suppressed, and finally the smoothed correction term is used to update the local NCO.

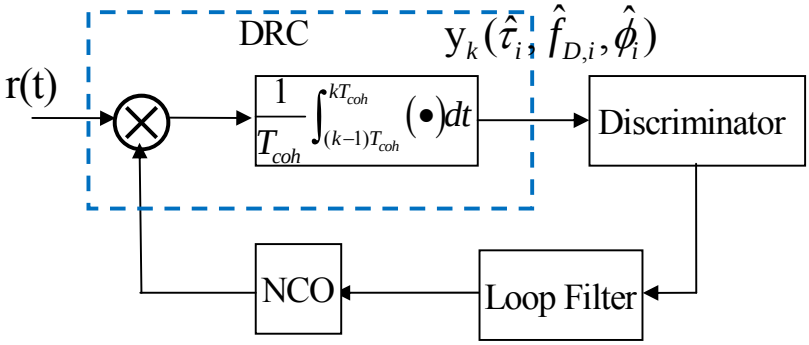

Figure 2.3: Generic tracking loop

Detailed discussion of designing classical PLL, FLL, and DLL for GNSS receivers can be found in classic textbooks such as Spilker (1996), van Dierendonck (1996), Ward et al (2006), Misra & Enge (2001), to name a few. Various advanced techniques are also available to enhance the performance of the receiver. For example, in order to improve the code phase tracking performance and to mitigate the multipath effects, narrow correlator techniques have been proposed and proven effective (van Dierendonck et al 1992).

With the code phase, Doppler frequency, and carrier phase being accurately tracked, the receiver is still not capable to immediately generate measurements. The timing contained in the incoming signals and the informational data bits should be further extracted. In order to get the data bit timing, a bit synchronization process is required. There are a number of techniques to achieve data bit synchronization, the most commonly used being histogram methods, as discussed in Spilker (1977). After the bit synchronization, and navigation message decoding, the receiver is then able to generate the measurements, such as pseudorange, carrier phase and Doppler frequency. The quality of the

pseudoranges is directly related to the code phase tracking jitter, and similar arguments also apply for the Doppler frequency and carrier phase.

For a C/A code receiver, in order to keep track of the transmit time, each tracking channel will count the number of the C/A periods (1 ms), the numbers of navigation data bits (20 ms), the number of the words (0.6 s), and the Z-counter (1.5 s). In the mean time, code NCO maintains track of the code phase which is below 1 chip. The transmit time can be simply expressed as

$$t_{tx,i} = 1.5 * \mathrm{Z}_{\mathrm{counter}} + 0.6 * \mathrm{Word}_{\mathrm{counter}} + 0.02 * \mathrm{Bit}_{\mathrm{counter}} + 0.001 * \mathrm{CA}_{\mathrm{counter}} + \mathrm{codePhase/codeRate} \quad (2.4)$$

As shown in this equation, the transmit time of each satellite can be precisely tracked by DLL. Once it is at a measurement epoch, the receiver simply picks the transmit time out from each channel. Along with the internally maintained receiver time, the pseudorange measurements are generated as

$$\rho_i = c(t_{rx} - t_{tx,i}) \quad [m] \quad (2.5)$$

In equation(2.5), c is the speed of light, i.e., 299,792,459 m/s, t_{rx} is the receiver time for this epoch and $t_{tx,i}$ is the transmit time of the i^{th} satellite according to equation(2.4). As can be seen from equation(2.5), the pseudorange is obtained by differencing the receiver time with the satellite transmit time.

The major errors in the pseudorange measurement come from two parts. Firstly, an error might arise from the clocks biases in both receiver and satellite side. And secondly, the DLL tracking loop will be affected by tracking jitters. In views of clock biases, if these

errors are expressed as the difference between receiver clock error dt , and satellite clock error dT_i , then the pseudorange measurement model will be as follows

$$\begin{aligned}\rho_i &= \rho_{i,ideal} + \varepsilon_{\rho,i} \\ &= r_i + c(dt - dT_i) + \varepsilon_{\rho,i} \quad [m]\end{aligned} \tag{2.6}$$

In equation(2.6), subscript i represents i^{th} satellite, ρ_i is the receiver's pseudorange measurements, r_i is the geometric range $\left\|\mathbf{r}_{rx} - \mathbf{r}_{tx,i}\right\|$, $\varepsilon_{p,i}$ is the noise term either from the code tracking loop or multipath.

For high precision applications, modeling of the measurements is usually of great importance. The actual pseudorange observation contains many other error terms besides the receiver induced noise, and can be written as (Lachapelle 2009).

$$\rho_i = r_i + d\rho_i + c(dt - dT_i) + d_{ion,i} + d_{trop,i} + \varepsilon_{\rho,i} \tag{2.7}$$

where ρ_i is the receiver's pseudorange measurements, r_i is the geometric range, $d\rho_i$ consists of the orbital errors, dt and dT_i denotes receiver and satellite clock errors, respectively, $d_{ion,i}$ is the ionospheric delay, $d_{trop,i}$ is the tropospheric delay and $\varepsilon_{p,i}$ is the noise term either from the code tracking loop or multipath.

The second important measurement for positioning and navigation is the derivative of the pseudorange, i.e., pseudorange rate. It is directly related to velocity and can be written as

$$\begin{aligned}\dot{\rho}_{i,diff} &= \frac{d\rho_{i,obs}}{dt} = \dot{\rho}_i + \dot{\varepsilon}_{\rho,i} \\ &= (\mathbf{v}_{rx} - \mathbf{v}_{tx,i})\mathbf{u}_{rx}^{tx,i} + c(\dot{dt} - \dot{dT}_i) + \dot{\varepsilon}_{\rho,i} \\ &= \dot{r}_i + c(\dot{dt} - \dot{dT}_i) + \dot{\varepsilon}_{\rho,i} \qquad [m/s]\end{aligned} \tag{2.8}$$

where $\dot{r}_i$ is the geometric range rate ($d\left\|\mathbf{r}_{rx} - \mathbf{r}_{tx,i}\right\| / dt$), $\dot{dt}$ and $\dot{dT}_i$ are the corresponding receiver and satellite clock drift terms. $\dot{\rho}_{i,diff}$ denotes the pseudorange rate obtained by differencing pseudorange measurements, $\dot{\rho}_i$ is the pseudorange rate without noise. The upper dot represents the time derivative. By definition, this pseudorange rate can be computed by directly differencing the pseudorange measurements between epochs, but this is not a practical procedure because it will result in very noisy measurements. For example, $\dot{\varepsilon}_{\rho,i}$ will be quite large and makes measurements not useful. As it is shown in the next equation, there is an apparent relationship between pseudorange rate and Doppler measurement, which can be extracted from the carrier tracking loop, either the PLL or FLL. In either case, the corresponding Doppler measurement will be at least 100 times less noisy than that from differencing pseudorange measurements (Ward et al 2006).

The Doppler is a frequency shift measured by the receiver whenever there is relative motion between the satellite and the receiver. A signal is first transmitted with the frequency f_{tx} by a satellite moving at velocity $\mathbf{v}_{tx}$. If a user moving at velocity $\mathbf{v}_{rx}$, it will then receive such a signal with a frequency of f_{rx} as shown

$$f_{rx} \approx f_{tx,i}(1-\frac{(\mathbf{v}_{rx}-\mathbf{v}_{tx,i})\mathbf{u}_{rx}^{tx,i}}{c}) = f_{tx,i}(1-\frac{\dot{r}_i}{c}) = f_{tx,i}-\frac{\dot{r}_i}{\lambda_i} \tag{2.9}$$

where $f_{tx,i}$ is the i^{th} satellite transmitted signal frequency, f_{rx} is the received signal frequency, $\mathbf{v}_{tx,i}$ is velocity vector of the i^{th} satellite, $\mathbf{v}_{rx}$ is the velocity vector of the receiver, $\mathbf{u}_{rx}^{tx.i} = \frac{(\mathbf{r}_{rx}-\mathbf{r}_{tx,i})}{\left\|\mathbf{r}_{rx}-\mathbf{r}_{tx,i}\right\|}$ is the unit direction vector along the line-of-sight from receiver to the i^{th} satellite, c is the speed of light, $\dot{r}_i$ is the geometric range rate ($d\left\|\mathbf{r}_{rx}-\mathbf{r}_{tx,i}\right\|/dt$), λ_i is the wavelength of the transmitted signal, and the upper dot is the time derivative.

Before differencing the received carrier frequency with the transmitted carrier frequency in order to get the Doppler, it is noted that there are inherent errors in both frequencies. Some error terms have nothing to do with the signal processing, nor the communication channels, because they are due to hardware limitations, such as the local oscillators' instability. As it has already been shown in equation(2.8), the clock drift term is related to pseudorange rate measurements and this term significantly affects local reference frequency. The clock drift term is commonly defined as the time increment over one second, but it is also related to the frequency deviation of the clock. Hence, the clock drift term can also be defined as the deviation of the frequency of the clock with respect to the reference frequency. For example, assuming a clock is supposed to operate at reference frequency of f_0 with a drift term $\dot{dt}$, (or equivalently stating that the expected reference period is T_0). But due to the clock drift terms, its reference period is extended by a factor

$(1+\dot{dt})$, and accordingly, its reference frequency is shorted by Δf Hz, as it is shown in the equation below. This frequency deviation is $-\dot{dt}$ multiplied by the reference frequency. The relationship between the clock drift and the frequency deviation can be written as follows if the second order smaller terms are neglected:

$$(1+\dot{dt})T_0 = \frac{1}{f_0 - \Delta f} \Leftrightarrow \Delta f = -f_0 \dot{dt} \tag{2.10}$$

With the clock drift induced frequency deviations, the Doppler measurements can then be obtained by differencing the local carrier frequency with the transmitted carrier frequency, shown as

$$f_{D,i} = f_{rx}(1-\dot{dt}) - f_{tx,i}(1-\dot{dT}_i) + \varepsilon_{f_D,i} = -\frac{\dot{r}_i}{\lambda_i} - \frac{c}{\lambda_i}(\dot{dt} - \dot{dT}_i) + \varepsilon_{f_D,i} = -\frac{1}{\lambda_i}\dot{\rho}_i + \varepsilon_{f_D,i} \tag{2.11}$$

where $\dot{\rho}_i$ is the pseudorange rate for the i^{th} satellite, which is shown in equation(2.8) and $f_{D,i}$ is the Doppler frequency that can be estimated from the receiver. As shown, the Doppler measurement differs from the differenced pseudorange rate measurement by only a scale, i.e., $-\frac{1}{\lambda_i}$, but the noise term $\varepsilon_{f_D,i}$ is significantly reduced as compared to $\dot{\varepsilon}_{\rho,i}$ shown in equation(2.8). Throughout the thesis, the term Doppler measurements will be used interchangeably with pseudorange rate measurements, since they are essentially representing the same piece of information.

Given the observation equations(2.7), (2.8) and (2.11), the navigation solution can be computed by using either least squares or Kalman filter. If an additional base receiver is available, then the differential processing can be applied. This will further eliminate some

of the common error terms, and may improve the positioning accuracy. Standard navigation solution algorithms can be found in Lachapelle (2009), Misra & Enge (2001), to name a few.

2.1.3 Receiver Architecture

The architecture of a standard GNSS receiver is shown in Figure 2.4. It is usually called scalar receiver due to the fact that it processes each satellite per channel in parallel. For each channel, DLL and PLL are used together to keep track of the code phase, Doppler, and/or carrier phase, as discussed in the last section. Then the measurements are generated according to equation(2.5) and equation(2.11). These measurements are finally fed forward to the navigation filter, which computes the final navigation solution. It should be noted that each channel's DRC module is only controlled by its individual NCO. The NCO is only updated by its own tracking loops internally.

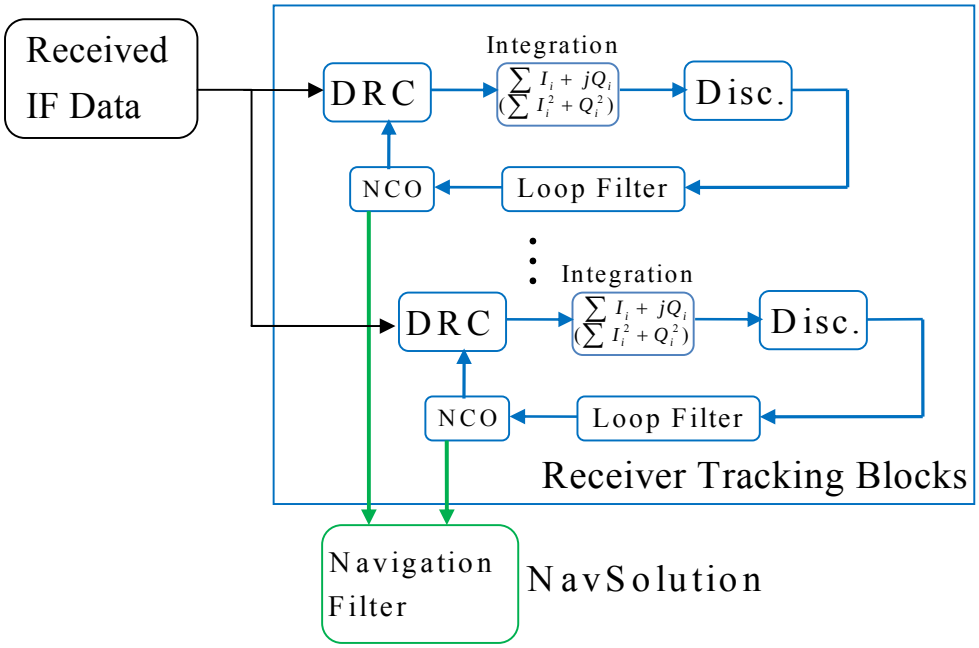

Figure 2.4: Standard scalar GNSS receiver architecture

The natural advantage of the scalar receiver is its ease of implementation. All channels are processed in parallel, without corruption from each other. Detailed analysis on scalar receiver tracking can be found in Ward et al (2006), Misra & Enge (2001), van Dierendonck (1996) and Spilker (1996).

A vector receiver is commonly introduced and known as a variant of the standard scalar GNSS receiver. In such receivers, vector tracking estimates the position and velocity of the receiver directly. There are no individual tracking loops and all are replaced by one single navigation filter. The local signal generator is only controlled by the navigational feedback, i.e., from the computed range and range rate to each satellite. For implementation efficiency, a cascaded vector GNSS receiver is often used as shown in

Figure 2.5. This cascaded approach associates each channel with a local channel filter, which estimates the tracking errors. Then the outputs from these local channel filters are fed to the final navigation filter at a low rate. In this way, both the state numbers of the navigation filter and the computation loads are reduced, thus improving the efficiency. Once the navigation filter computes a solution, the NCO of each satellite will also be adjusted by the navigation feedback. Thus, in such a vector tracking mode, the NCO will be controlled by navigation feedback and the local channel filter jointly.

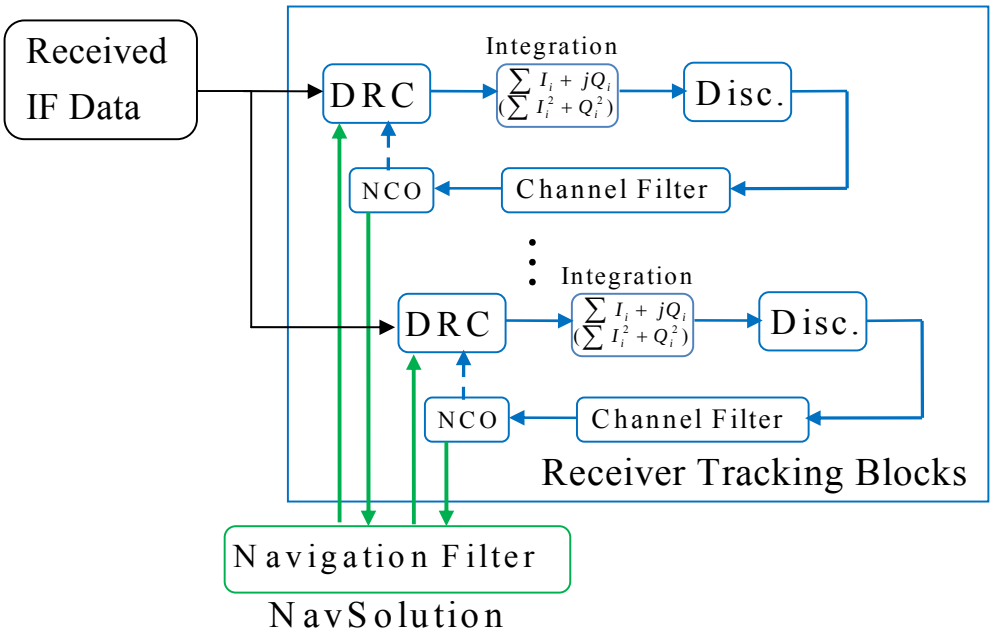

Figure 2.5: Cascaded vector GNSS receiver architecture

Various researchers have discussed the advantages of this vector tracking receiver, Spilker (1996) mentioned that the process noise is reduced in all channels, and thus the receiver is far less likely to fall in the non-linear tracking regions. Others reported the

potential benefits of vector tracking in weak signal environments, such as Petovello & Lachapelle (2006), Ohlmeyer (2006), Pany&Eissfeller (2006), Gustafson et al (2000), to name a few.

The above two GNSS receiver architectures are commonly termed "standard GNSS receivers" and only work well under mild environments. When the user comes to more challenged environments, such receivers usually lose lock of the incoming signal. In the following, high sensitivity GNSS receivers are reviewed. They are termed "high sensitivity" because extended integration is used, which provides the additional processing gain needed for weak signal conditions. In this thesis, HSGNSS receivers also use assisted information, so they can also be called *assisted GNSS* (AGNSS). For consistency of terminology, AGNSS and HSGNSS are used interchangeably throughout the thesis. Two types of high sensitivity GNSS receivers are used whose architectures are further shown in the following.

The first one is called *conventional high sensitivity receiver*, as shown in Figure 2.6. This type of high sensitivity receiver uses block processing techniques as discussed in van Graas et al (2005). By using block processing techniques, this conventional high sensitivity receiver actually generates measurements using MLE, namely Doppler and code phase MLE. As shown in the figure, the received IF signal samples pass through the DRC module. Navigation data bits are wiped off with external bit aiding when available. Extended coherent and/or non-coherent integrations are then applied in order to get a "correlation map" with the desirable pre-detection SNR. For each channel, measurements are then constructed by choosing the maximum peak that appears in the correlation map

over the uncertainty range. With measurements from all channels, the navigation filter begins to estimate the user position and velocity. Once the navigation solution is computed and the navigation feedback is enabled, the centres of the correlators can be controlled by the navigation solution in a vector-tracking mode.

In addition, the HSGNSS receivers used in this work may also accept "external aiding" consisting of receiver position and velocity information. This can be used to specify the location of the correlator grid for each satellite and, since the external information is accurate, it can reduce the size of the correlator grid (i.e., search space). The motivation for this is to reduce the processing complexity in order to better evaluate the proposed algorithms in different environments. That said, a comparison of results obtained with and without external aiding is also performed to confirm that results are nearly the same in both cases (but with different computational requirements). Details of the software used for processing will be provided later in the thesis prior to data analysis. The bottom line, however, is that receivers used can be considered as conventional HSGNSS receivers with minor modifications to reduce the computational burden without significantly affecting navigation performance.

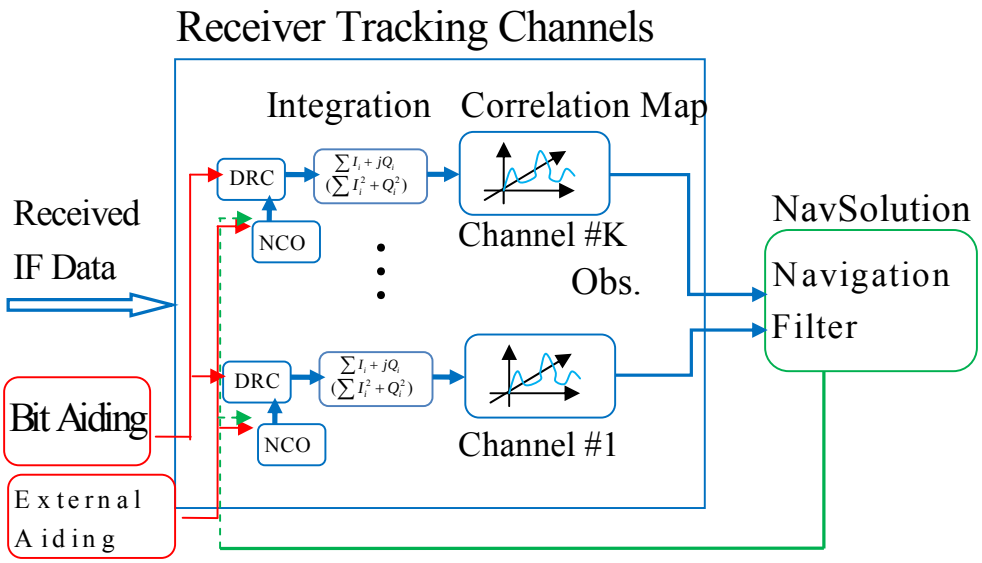

Figure 2.6: Conventional HSGNSS receiver architecture

Generally speaking, a conventional HSGNSS receiver suffices to maintain acceptable performance over weak signal conditions. In order to further improve the measurement accuracy, a *direct vector HSNGSS receiver*, shown in Figure 2.7, is proposed and developed. Due to the fact that this thesis focuses on Doppler and velocity estimations for indoor navigation, only the velocity domain projections are shown. The basic difference between a direct vector HSGNSS receiver and a conventional HSGNSS receiver is that the former utilizes navigation solution MLE while the latter only utilizes measurement MLE. A detailed discussion on this receiver is included in Section 5.1. A performance comparison between the two types will be conducted under various environments in Chapter 5 and 6.

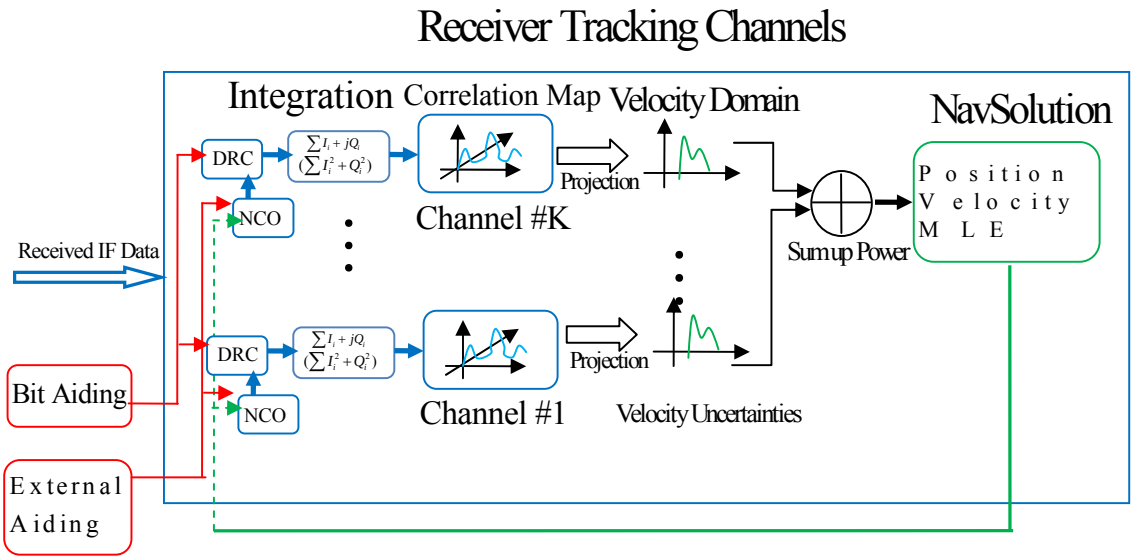

Figure 2.7: Direct vector HSGNSS receiver architecture

In this section, the basic structures of various GNSS receivers were reviewed and discussed. The diagrams shown aimed at providing a clear understanding of state-of-the-art receivers and depict how those algorithms/modules are implemented in the software used in this thesis. Furthermore, the diagrams of the conventional and direct vector HSGNSS receiver that are used/developed in this thesis were briefly shown here in order to better understand later chapters.

2.1.4 Software Receiver

The primary software used in this thesis is GSNRx™ (GNSS Software Navigation Receiver) developed at the University of Calgary by the PLAN Group (Petovello et al 2008). Two existing versions that can be categorized as conventional HSGNSS receivers are used to estimate Doppler measurements and 'conventional' HSGNSS velocity. In order to implement the proposed direct vector HSGNSS as discussed in Figure 2.7,

modifications are done on existing GSNRx^{TM} as will be discussed in Chapter 5. The velocity estimation based on this algorithm is called 'direct' method in later chapters.

2.2 Overview of Inertial Navigation Systems

INS is a self-contained system that can provide position, velocity and attitude information. This autonomy makes it a good compliment to GNSS. Typically, sensors having a triad of accelerometers and gyroscopes orthogonally mounted are called IMU. INS is the system that includes IMU and is capable of computing the navigation states, such as position, velocity, and attitude. Computation of these navigational states depends on the mechanization equations. In this section, a review of inertial techniques is briefly presented. The basic coordinate frames are defined. The initial alignment and mechanizations are then discussed. Two common mechanization methods are reviewed, namely strap-down mechanization and PDR mechanization.

2.2.1 Coordinate Frames

In an inertial navigation system, there are several important frames in order to perform the inertial mechanizations. In this thesis, only the following four essential frames are encountered, and thus are presented.

Inertial Frame (i-frame) has its origin at the centre of the earth and axes are non-rotating with respect to the fixed stars.

Earth Frame (e-frame) has its origin at the centre of the Earth and axes fixed with respect to Earth, Oz_e is along with Earth's polar axis. Ox_e lies along the intersection of the plane of the Greenwich meridian with the Earth's equatorial plane (Titterton & Weston 2004).

Navigation Frame (n-frame) refers to a local geodetic frame, which centers its origin in the navigation system, while aligning its axes to geodetic east, north, and vertical. Some textbooks refer the n-frame to the north-east-down (NED), but throughout this thesis, the navigation frame is defined as geodetic east-north-vertical up (ENU).

Body Frame (b-frame) is the frame in which the accelerometers and gyroscopes output measurements. The axes in b-frame are the same as the IMU's body axes.

Once all the reference frames are defined, the mechanization equation can be derived in a certain frame. For our application, the local level frame (l-frame) is chosen as the navigation frame, which uses ENU as shown in Figure 2.8.

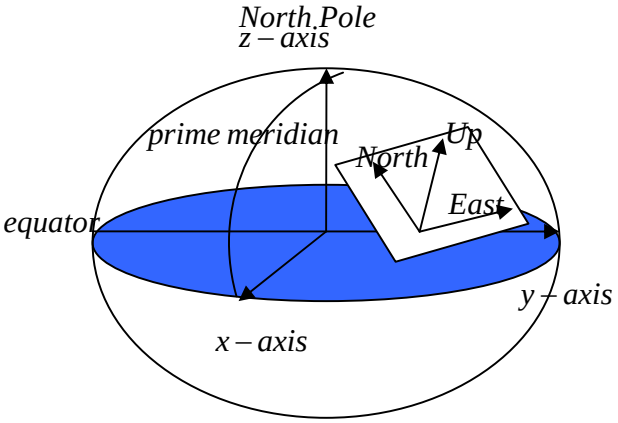

Figure 2.8: Coordinate frames

2.2.2 Initial Alignment

Initial alignment is the process whereby the orientation of the axes of an inertial navigation system is determined with respect to the reference frame (Titterton & Weston 2004). The presumption of the mechanization equations is that all initial conditions are already known, such as initial position, velocities, and attitudes. The former two can be

easily input by the user, but the attitudes are commonly obtained from the INS by this initial alignment process.

There are several methods for the coarse alignment. For example, in analytical coarse alignment, the initial position (ϕ, λ, h), gyro and accelerometer measurements ($\mathbf{f}^b, \boldsymbol{\omega}_{ib}^b$), and bias ($\mathbf{b}_{gyro}, \mathbf{b}_{acc}$) are given, then C_b^n can be computed (adding $\mathbf{V} = \mathbf{f}^b \times \boldsymbol{\omega}_{ib}^b$). C_b^n denotes the rotation matrix from the b-frame to the n-frame. Then the corresponding roll, pitch, azimuth can be calculated. Another way for coarse alignment is accelerometer leveling and gyro compassing, as is shown in Figure 2.9.

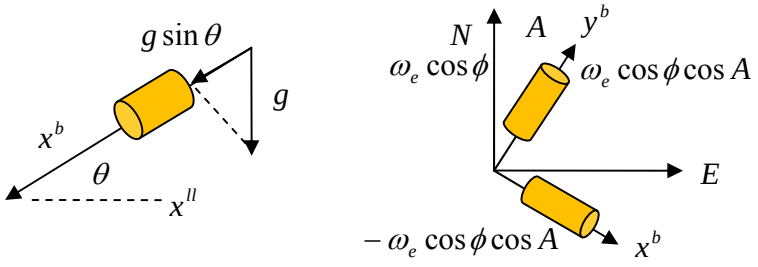

Figure 2.9: Accelerometer leveling and gyro compassing coarse alignment

Initial pitch, roll and heading angles can be estimated by using the following equations

$$\xi = -sign(f_z)\sin^{-1}\left(\frac{f_x}{g}\right)$$
$$\eta = sign(f_z)\sin^{-1}\left(\frac{f_y}{g}\right) \qquad (2.12)$$
$$\psi = \tan^{-1}\left(-\frac{\omega_x^b}{\omega_y^b}\right)$$

In equation(2.12), f_x, f_y are the accelerometer measurements in the x, y axes, while ω_x, ω_y are the corresponding gyroscope measurements. ξ, η, ψ are the initial pitch, roll and heading angles. The sign of the gravity $-sign(f_z)$ is added, which denotes the sign of the rotation. The heading angle indicates the angle with respect to the north. With the initial attitude angle estimated, the initial direction cosine matrix (DCM) is (El-Sheimy 2007)

$$C_b^n = \mathbf{R}_{z^b}(\psi)\mathbf{R}_{x^b}(-\eta)\mathbf{R}_{y^b}(-\xi) \tag{2.13}$$

In equation(2.13), $\mathbf{R}$ is the rotation matrix, and the subscripts x^b, y^b, z^b denote the axes of the rotation.

2.2.3 Mechanization Equations

After the initial coarse alignment, along with known initial position, and velocity information, the navigational states can be computed by using the mechanization equations.

Strap-down Mechanization

The output of the alignment is the initial rotation matrix from body frame to the local level frame. Given the initial position, the local gravity g^l can be calculated. The rotation vector from the e-frame to i-frame with respect to l-frame (ω_{ie}^l) can also be computed given the above initial conditions. The equations that govern the dynamics of the user motion in the local level frame are as follows (El-Sheimy 2007).

$$\begin{bmatrix} \dot{\mathbf{r}}^l \\ \dot{\mathbf{v}}^l \\ \dot{C}_b^l \end{bmatrix} = \begin{bmatrix} D^{-1}\mathbf{v}^l \\ C_b^l\mathbf{f}^b - (2\Omega_{ie}^l + \Omega_{el}^l)\mathbf{v}^l + \mathbf{g}^l \\ C_b^l(\Omega_{ib}^b - \Omega_{il}^b) \end{bmatrix} \tag{2.14}$$

where $\mathbf{r}^l$, $\mathbf{v}^l$, and $\mathbf{g}^l$ are the position vector, velocity vector, and gravity vector in the local level frame. $\mathbf{f}^b$ is the specific force vector in the body frame, C_b^l is the rotation matrix from the body frame to the local level frame. Ω_{ib}^b is the skew-symmetric matrix of the gyro sensed measurements, while Ω_{il}^b accounts for the combined effects of earth rotation and the local level frame motion. Ω_{ie}^l is the skew-symmetric matrix form of the angular velocity vector describing the Earth rotation at the local level frame. Ω_{el}^l is the skew-symmetric matrix form of the angular velocity vector describing the rotation of the local level frame with respect to the e-frame, and represented in the l-frame. The matrix D^{-1} represents the relationship between the derivatives of the position vector and the velocity vector in the local level frame and is

$$D^{-1} = \begin{bmatrix} 0 & \frac{1}{R+h} & 0 \\ \frac{1}{(R+h)\cos\phi} & 0 & 0 \\ 0 & 0 & 1 \end{bmatrix} \tag{2.15}$$

The angular velocity vectors describing the effects of the earth rotation and local level motion are expressed as

$$\omega_{ie}^{l} = \begin{bmatrix} 0 \\ \omega_e \cos\varphi \\ \omega_e \sin\varphi \end{bmatrix}, \omega_{el}^{l} = \begin{bmatrix} \dfrac{-V^n}{M+h} \\ \dfrac{V^e}{N+h} \\ \dfrac{V^e \tan\varphi}{N+h} \end{bmatrix} \tag{2.16}$$

$$\omega_{il}^{b} = C_l^b (\omega_{ie}^{l} + \omega_{el}^{l})$$

The raw measurements from the inertial sensors are the angular and velocity increments. Generally speaking, they are associated with various error terms, such as biases, scale factor, axis non-orthogonalities, etc (Titterton & Weston 2004). The modeling of these errors can be done in the calibration process in either the laboratory or in the field. They can also be estimated in navigation process. The following equation expresses the angular and velocity increments with gyro and accelerometer biases in the body frame.

$$\begin{aligned} \Delta\boldsymbol{\theta}_{ib}^{b} &= \Delta\hat{\boldsymbol{\theta}}_{ib}^{b} - \mathbf{b}_{gyro}\Delta t \\ \Delta\mathbf{v}_{f}^{b} &= \Delta\hat{\mathbf{v}}_{f}^{b} - \mathbf{b}_{acc}\Delta t \end{aligned} \tag{2.17}$$

Standard local level frame mechanization is shown in Figure 2.10. First, the attitude is updated by using quaternion differential equations. Once the rotation matrix from the b-frame to the l-frame is calculated in the attitude update step, it is then possible to calculate the Coriolis correction and gravity and to transform the specific force from the b-frame to l-frame. Velocity and position can then be updated by using the modified Euler formula. Detailed implementation can be found in Schwarz & Wei (1999), Titterton & Weston (2004) and El-Sheimy (2007).

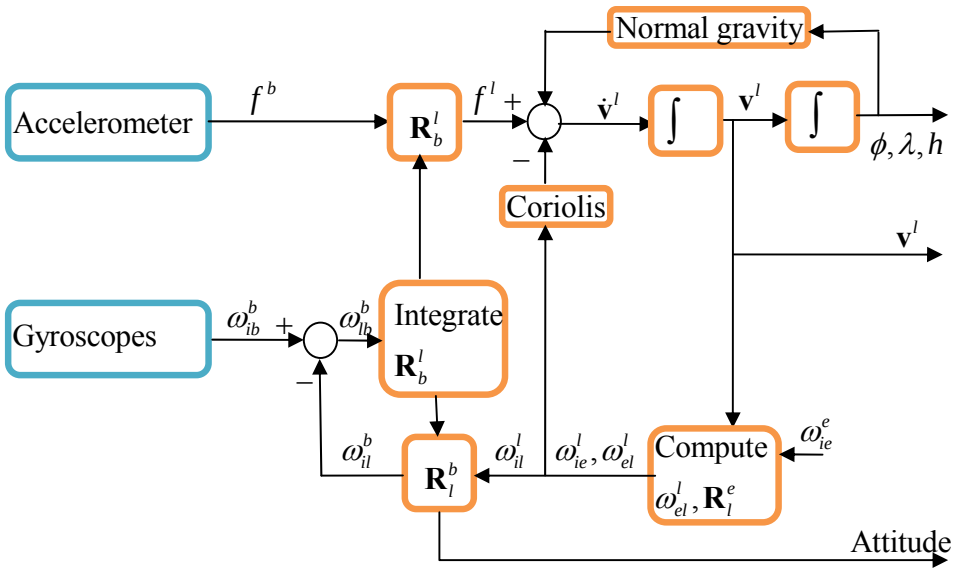

Figure 2.10: Local level frame mechanization (Schwarz & Wei 1999)

In practical implementations, the performance of a strap-down inertial navigation system is often limited by various errors. The source of these errors may be categorized as initial alignment errors, inertial sensor errors, and computational errors. A good error dynamic model will thus benefit the system performance. The error models or error dynamic equations can be obtained by simply perturbing the mechanization equation(2.14). For a complete treatment of the INS error equations, the reader is referred to Schwarz & Wei (1999), Titterton & Weston (2004) and El-Sheimy (2007).

PDR Mechanization

With low grade IMUs, the strap-down mechanization accumulates errors very fast if no external updates are available. However, the PDR is a good alternative that fully exploits the kinematics of the human walking, and accumulates error more slowly. The underlying

idea of the PDR is to propagate the user position by using step length and heading instead of integrating acceleration and angular velocities. In order to implement a PDR algorithm, the step length and user heading have to be estimated. The step length can be estimated by using low cost accelerometers or odometers, the accuracy of which has reached a level of practical use (e.g. Renaudin et al 2012). The user heading can be estimated either from a vertical gyroscope, or a magnetometer. The diagram of a basic PDR algorithm is shown in Figure 2.11.

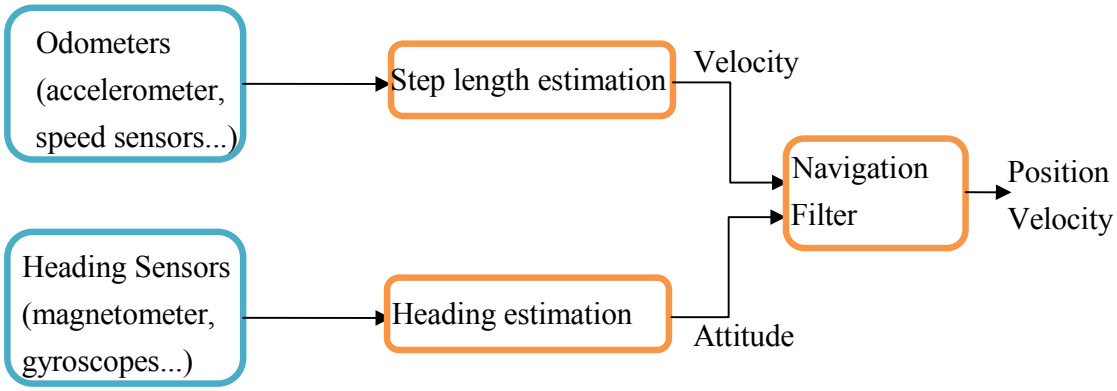

Figure 2.11: PDR mechanization

Scrutinizing Figure 2.10 and Figure 2.11, one easily discovers the following facts. First, in strap-down mechanization, the gyro bias term will cause the misalignment of the INS, and therefore results in a projection of the acceleration vector in a wrong direction. This indicates that a gyro bias will introduce a quadratic error in the velocity, and a cubic error in position in strap-down mechanization (El-Sheimy 2007). However, as shown in Figure 2.11, the PDR mechanization only integrates the heading once to obtain the position. The position error is proportional to the step length errors and heading errors. Second, there are several feedback loops in the strap-down mechanization, while there are only feed

forward paths in the PDR mechanization. This shows there is no coupling between the velocity estimation and the attitudes in the PDR mechanization, which is major difference from the strap-down mechanization.

In Figure 2.12, the horizontal errors of the strap-down mechanization and PDR mechanization are illustrated. For a gyro with 1deg/hr bias running for 200 s, the standard strap-down mechanization results in more than 350 m horizontal positioning error. If PDR mechanization is used with a step length scale factor of 1.2, then the final horizontal positioning error is less than 50 m. This figure is generated by simply integrating the errors over time.

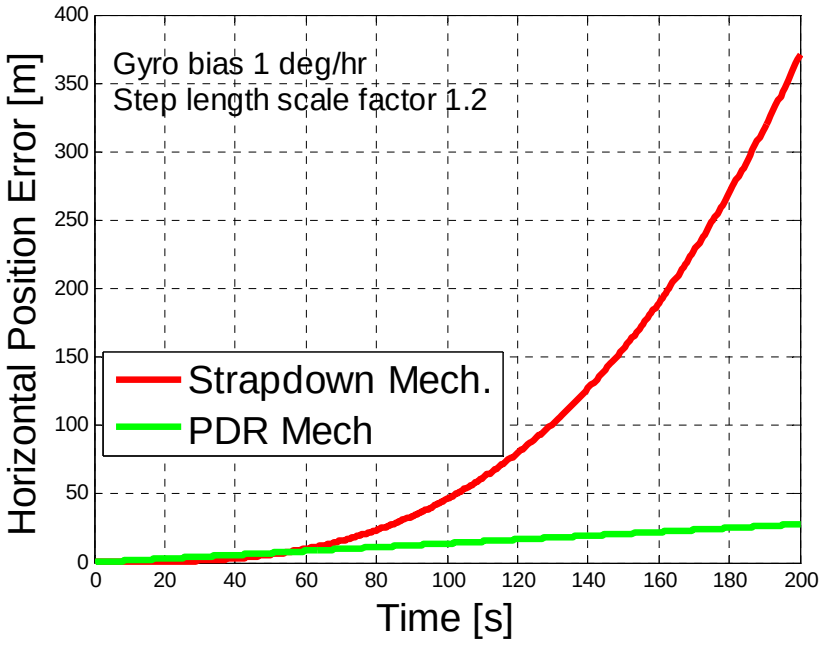

Figure 2.12: INS PDR horizontal positioning error

The equations that govern the pedestrian user motion dynamics are relatively simple and can be written as

$$\dot{E} = v_h \sin(\phi)$$
$$\dot{N} = v_h \cos(\phi) \quad (2.18)$$
$$\dot{U} = v_u$$

where E, N, U denotes the east, north and up displacement. Upper dots denote the time derivative. v_h and v_u indicates the horizontal and vertical velocities and ϕ is the user heading angle. The step length can be estimated from accelerometers, while user heading angle can be estimated by gyroscopes, magnetometers, and other heading sensors. The step detection algorithm used in the thesis is shown in Figure 2.13. A step event is declared once a step valid flag is true when the acceleration variance exceeds some pre-defined threshold.

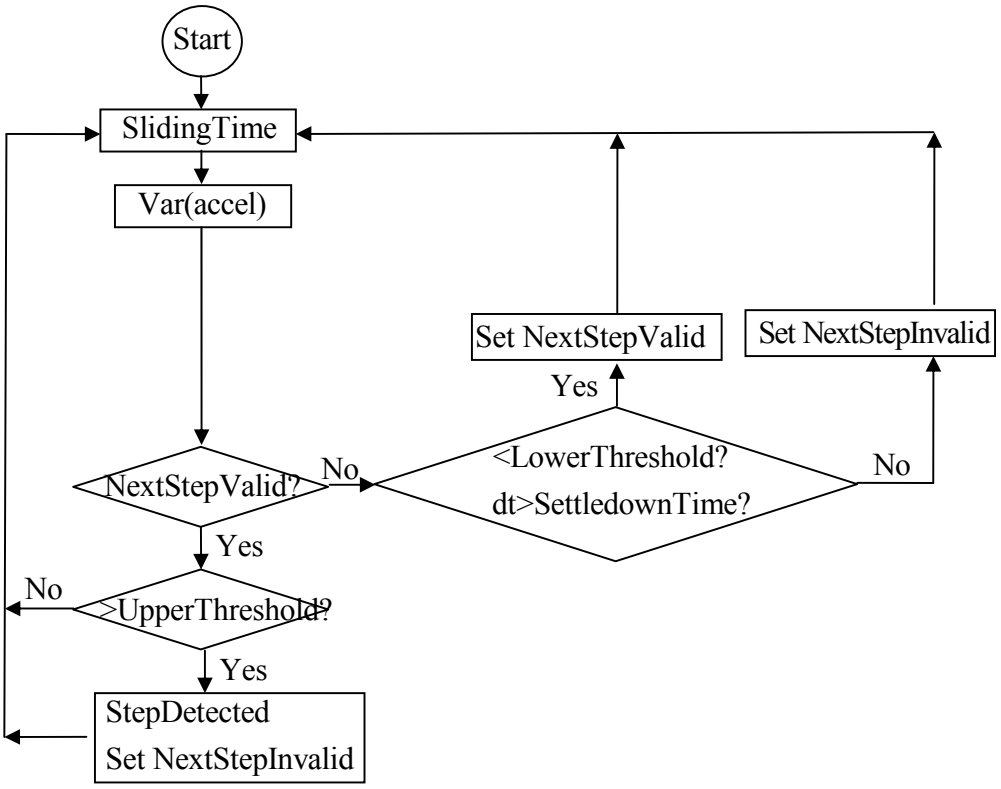

Figure 2.13 Flow chart of a simple step detection algorithm

In order to propagate the user position according to equations(2.18), the step length information between steps/epochs is needed. Generally speaking, there are two different situations that are encountered in pedestrian navigation. The first case is that inertial sensors are rigidly attached to the some part of the user's body, a common assumption for the PDR. For examples, the accelerometers can be attached rigidly to the belt, the foot, or even in a backpack. In these cases, the gait cycle is directly related to the sensor inertial forces at those locations. The second case assumes that the inertial sensors to detect the step length are non-body fixed, which means that during the movement of the pedestrian

user, the inertial sensor might experience some additional dynamics, such as arbitrary hand swing.

For the former scenarios, there are many robust and reliable algorithms for step detection and estimation. Common techniques use the time domain patterns in the accelerometer outputs which are related to the gait cycle. If the user is walking, the even step can be detected once the acceleration is over some threshold. Detailed treatment of this issue can be found in Ladetto (2000), Mezentsev et al (2005), Beauregard & Haas (2006) to name a few. For the latter scenarios, an effective method is developed and can be found in Renaudin et al (2012). It utilizes the frequency domain pattern of the accelerometer measurements, such as using short time Fourier transform to get the character frequency information from the measurements. As for complicated pedestrian activities, pattern recognition algorithms can be used in order to classify the user mode (Andersson 2012), and various parameters can be associated with these modes. Error analysis of the step length estimation has also been done in previous work, and can be found in Leppäkoski et al (2002) and Mezentsev et al (2005).

The key issue in PDR is the heading determination, since inaccurate heading can rapidly deteriorate the navigation solution. Whenever the inertial sensors are rigidly attached in some part of the user body, the heading estimation is relatively simple, either magnetometers or IMU can be used. For example, Ladetto & Merminod (2002) analyzed the performance and benefits of using magnetometer and gyroscope to determine the heading. And multi-magnetometers are proven useful for more reliable orientation estimation (Afzal et al 2011).

2.3 Overview of GNSS/INS Integration

Integration GNSS receiver with INS is not a new technology. There are three kinds of GNSS/INS integration schemes: loose, tight, and ultra-tight integration.

2.3.1 GNSS/INS Loose Integration

In GNSS/INS loose integration, the position and velocity solutions from GNSS receivers are used to integrate the INS. INS errors are periodically estimated by using GNSS position and velocity updates. The diagram of the GNSS/INS loose integration is shown in Figure 2.14. $\Delta\boldsymbol{\theta}, \Delta\mathbf{v}$ are the angular, and velocity increments from IMUs, and as described in equation(2.17), $\delta\mathbf{X}$ is the INS error state, for example, a fifteen state INS error model, $\delta\mathbf{X} = \left[\delta\mathbf{r}^T, \delta\mathbf{v}^T, \delta\boldsymbol{\varepsilon}^T, \dot{\mathbf{d}}^T, \dot{\mathbf{b}}^T\right]^T$ which denotes position errors, velocity errors, attitude errors, gyro drift error, and accelerometer bias errors accordingly.

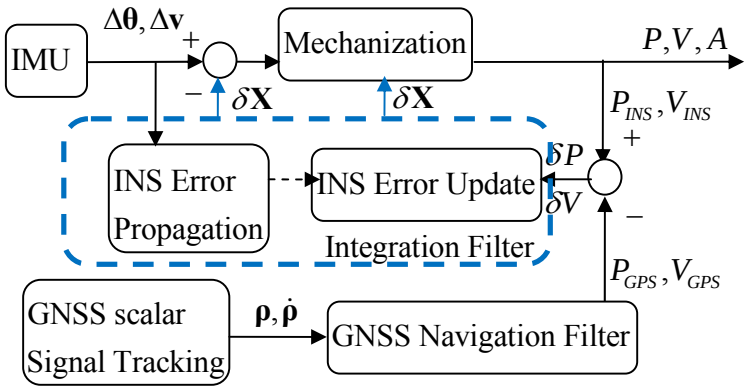

Figure 2.14: GNSS/INS loose integration

As it is shown in Figure 2.14, the blue dash block is the integration filter. Whenever the position and velocity information from the GNSS receiver is available, then the INS

errors will be updated by using this new information. If the positions and velocities from GNSS receivers are not available, the integration filter simply propagates the INS error by using its error model, and outputs the INS alone solution. For fifteen state INS error models, the design matrix can be simply expressed as.

$$\mathbf{H} = \begin{bmatrix} \mathbf{I}_{3\times3} & \mathbf{0}_{3\times3} & \mathbf{0}_{3\times9} \\ \mathbf{0}_{3\times3} & \mathbf{I}_{3\times3} & \mathbf{0}_{3\times9} \end{bmatrix} \tag{2.19}$$

In GNSS/INS loose integration, the GNSS possesses its own navigation filter, while the INS also uses a Kalman filter to predict its navigational errors. The separated Kalman filter structure simplifies the implementation, provides robustness of the final solution, but extra process noises that are induced may impact the performance of the integrated system (Petovello 2003).

2.3.2 GNSS/INS Tight Integration

In a GNSS/INS tight integration, the GNSS receiver uses its pseudorange and Doppler measurements to integrate with the INS as shown in Figure 2.15.

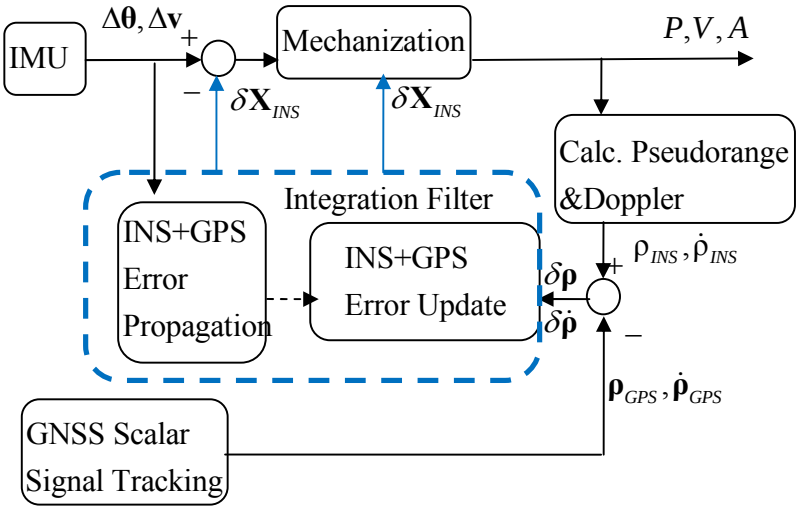

Figure 2.15: GNSS/INS tight integration

The GNSS receiver does not have a navigation filter. The integration filter states not only include the INS error states described earlier, but also include additional GNSS states, such as clock bias and clock drift terms. The GNSS receiver uses its pseudorange and Doppler measurements to update the integration filter. Given the satellite ephemeris, INS predicted position and velocity information, the INS predicted pseudorange and Doppler measurements can be estimated. The tight integration has several benefits over the loose integration. The most apparent one is that only one navigation filter is used, which means that less process noise is added in the final solution and the filtering of GNSS measurements is improved (Petovello 2003). Some researchers also found that tight integration is more sensitive to the fault detection and isolation, which can monitor the quality of pseudorange and Doppler measurements (Mats 1996).

2.3.3 GNSS/INS Ultra-tight Integration

An ultra-tight integration diagram is shown in Figure 2.16. There are several major differences between the tight and ultra-tight integration. First, the GNSS tracking loops in ultra-tight mode are in vector tracking mode. For cascaded implementation, such tracking loops have their own channel filter as discussed in Section 2.1.3. However, the receiver in tight integration uses scalar tracking loops. The second difference is that, with an ultra-tight receiver, the navigation solution is used to compute code phase and Doppler corrections, and these correction terms are then applied to control the NCO of each channel.

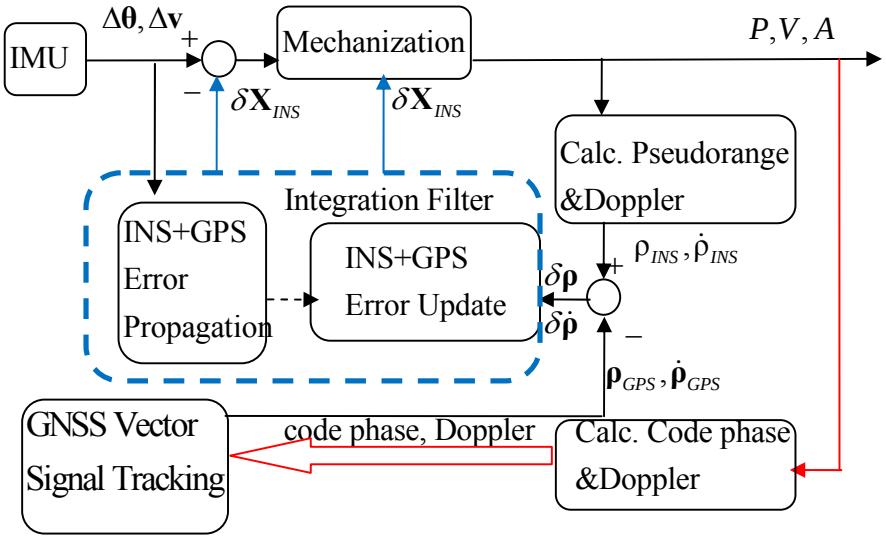

Figure 2.16: GNSS/INS ultra-tight integration

In terms of system performance, the ultra-tight integration offers the most benefits in navigation accuracy and system robustness, especially when a highly accurate INS is used. However, if the quality of the INS is low, the noise in the navigation feedback

might exceed the normal tracking jitters, and this will limit the additional benefits brought by the ultra-tight receiver architecture.

2.3.4 HSGNSS/PDR Integration

The diagram of the HSGNSS/PDR integration is very similar to GNSS/INS integration diagrams shown above, and thus will not be show here. However, there are still a few differences. The first difference comes from the inertial systems themselves with the PDR filter being much simpler as compared to the INS filter. As it is shown in Equation (2.18), the PDR mechanization is purely driven by step length and heading, while INS strap-down mechanization is driven by acceleration and angular rate measurements. The second difference comes from the GNSS part. HSGNSS usually uses open loop processing strategies and usually has a large search spacing over the code phase and Doppler domains. When the quality of the integrated navigation solution is relatively poor, the benefits of ultra-tight architecture are usually limited. This is because the search space is not reduced, nor are the user dynamics well compensated. In this thesis, only the HSGNSS/PDR tight integration will be discussed and evaluated.

Chapter Three: **DOPPLER ESTIMATION IN ADDITIVE WHITE GAUSSIAN NOISE**

This chapter focuses on the discussion of Doppler frequency estimation techniques encountered in AWGN. The CRLB of the Doppler frequency, signal amplitude and code phase in GNSS receivers are first reviewed. The performance of a non-coherent frequency discriminator is shown and compared to the Doppler CRLB. It is noted that MLE will asymptotically approach the CRLB and is relatively easy to implement. Thus, the MLE of Doppler frequency in a weak signal environment is discussed with focus on implementation. Finally, a method that uses SDFT to increase the NCO feedback rate with bearable computation load is also introduced.

3.1 CRLB of GNSS code phase and Doppler

The Doppler frequency in GNSS receivers plays an important role as discussed in Section 2.1.2. The CRLB of the Doppler frequency with high sensitivity receivers in white Gaussian noise is now reviewed. The consequences of the multipath will be further discussed in the next chapter.

The received complex envelope expression of a generic GNSS signal can be expressed in the following form:

$$r(t) = ax(t-\tau_0)e^{j(2\pi f_D(t-\frac{T_{obs}}{2})+\phi_0)} + w(t), \quad t \in [0, T_{obs}] \tag{3.1}$$

where a is the signal amplitude, $x(t)$ is the multiplication of the PRN code with navigation data bits, f_D is the Doppler frequency shift due to the satellite and/or local user motion, ϕ_0 is the initial carrier phase, $w(t)$ is the additive Gaussian noise with the spectral density of N_0 watt/Hz over the pre-correlation bandwidth (single side bandwidth).

To simplify the analysis, assume that the initial carrier phase is zero. In the discrete form, such a received signal is sampled at a frequency of $f_s = 1/T_s$, and the entire observation period contains $N = T_{obs}/T_s$ samples. When the front-end filtering bandwidth is close to the Nyquist sampling frequency, i.e., $f_s/2$, the sampled noise term $w(nT_s)$ is generally a white sequence. The variance of any given sample is $\frac{N_0}{2T_s}$. The start of the epoch is assumed to be zero and there are N samples in the integration interval. Each of the samples has the following expression:

$$\begin{aligned} r[n] &= r(nT_s) = s[n] + w[n] \\ &= a_n x(nT_s - \tau_0) e^{j2\pi f_D (nT_s - \frac{N-1}{2}T_s)} + w(nT_s), \quad n \in [0, N-1] \end{aligned} \tag{3.2}$$

In equation(3.2), the received signal has N samples. Since the complex signal ($s[n]$) is embedded in the complex Gaussian noise ($w[n]$), the received signals will have a Gaussian distribution for complex random variables. With the stationary assumption of the Gaussian noise and orthogonality of the in-phase (real) and quadratic phase (complex) channel, the noise terms in such channels are uncorrelated (Proakis 2001).

Before describing the complex Gaussian PDF (probability density function), the complex correlation has to be clearly defined as there are generally two ways to relate the low pass equivalent signal with the band pass signal, which differs by a scale of $\sqrt{2}$. In terms of complex correlation, some textbooks do not introduce an additional $1/2$, because there is already a scaling of $1/\sqrt{2}$ in the low pass equivalent signal, such as Papoulis (1965). In other textbooks such as Stein & Jones (1967) and Proakis (2001), there is no scaling in the low pass equivalent signal. However, the complex correlation is defined with an additional $1/2$. This thesis chooses the latter representation and this will be consistent throughout the thesis. For example, the auto-correlation between received complex samples is

$$\phi_{rr}(m) = \frac{1}{2} E\left(r^*[n] r[n+m]\right) \tag{3.3}$$

where $(\bullet)^*$ represents the complex conjugate and it indicates that the variance of the complex samples will equal either the real or the imaginary parts of the samples. With the above definition, the covariance matrix is also different by $1/2$ compared to that in Kay (1993a). The PDF of the received complex samples are shown as

$$p(\mathbf{r};\boldsymbol{\theta}) = \frac{1}{(2\pi \bullet \frac{N_0}{2T_s})^{N/2}} \exp\left\{ -\frac{1}{2} \bullet \frac{2T_s}{N_0} \sum_{n=0}^{N-1} (r[n] - s_\theta[n])^H \left(r[n] - s_\theta[n]\right) \right\} \tag{3.4}$$

In equation (3.4), $\boldsymbol{\theta} = [a, \tau_0, f_d]$ represents the parameters that need be estimated. It includes signal amplitude, code delay and Doppler frequency. The signal $s_\theta[n]$ represents the complex signal sample at n and it is a function of the estimated parameters.

With the probability distribution expressed, one can easily obtain the CRLB of the parameter θ_i. It is the i^{th} diagonal element in the inverse of the Fisher information matrix (FIM), denoted as

$$\mathrm{var}\left(\hat{\theta}_i\right) \geq \left[\mathbf{I}^{-1}\right]_{i,i} \tag{3.5}$$

The circumflex accent denotes the estimated value. More details of the FIM can be found in Kay (1993a). As in this case, the derivatives can be easily obtained; the diagonal elements in the FIM can be derived as

$$\begin{aligned}
I_{a,a} &= \frac{2T_s}{N_0}\sum_{n=0}^{N-1}\frac{1}{2}\left(\frac{\partial s_\theta[n]}{\partial a}\right)^* \frac{\partial s_\theta[n]}{\partial a} = \frac{T_s}{N_0}\sum_{n=0}^{N-1}\left|x(nT_s-\tau_0)\right|^2 = \frac{T_{coh}}{N_0} \\
I_{\tau,\tau} &= \frac{2T_s}{N_0}\sum_{n=0}^{N-1}\frac{1}{2}\left(\frac{\partial s_\theta[n]}{\partial \tau}\right)^* \frac{\partial s_\theta[n]}{\partial \tau} = \frac{T_s a^2}{N_0}\sum_{n=0}^{N-1}x'^*(nT_s-\tau_0)x'(nT_s-\tau_0) = \frac{T_s a^2}{N_0}R_{x'x'}(0) \\
I_{f_D,f_D} &= \frac{2T_s}{N_0}\sum_{n=0}^{N-1}\frac{1}{2}\left(\frac{\partial s_\theta[n]}{\partial f_D}\right)^* \frac{\partial s_\theta[n]}{\partial f_D} = \frac{(2\pi a)^2 T_s}{N_0}\sum_{n=0}^{N-1}\left(nT_s-\frac{N-1}{2}T_s\right)^2\left|x(nT_s-\tau_0)\right|^2 = \frac{(2\pi)^2 a^2 T_s^3}{N_0}\bullet\frac{N(N^2-1)}{12}
\end{aligned} \tag{3.6}$$

In equation (3.6), $1/2$ is due to the complex correlation defined above. $T_{coh} = NT_s$ is the coherent integration time. $R_{x'x'}(\bullet)$ is the auto-correlation function of derivatives of x. This term is also known as power of the differentiated signaland it has been shown that $R_{x'x'}(0) = -R''_{xx}(0) = E\left[x'(t)\right]^2$, which is directly related to the loop of the DLL (Spilker 1996).

The off-diagonal elements in the FIM are expressed as

$$\begin{aligned}
I_{a,\tau} &= \frac{2T_s}{N_0}\sum_{n=0}^{N-1}\frac{1}{2}\left(\frac{\partial s_\theta[n]}{\partial a}\right)^* \frac{\partial s_\theta[n]}{\partial \tau} = -\frac{aT_s}{N_0}R_{xx'}(0) = 0 \\
I_{a,f_D} &= \frac{2T_s}{N_0}\sum_{n=0}^{N-1}\frac{1}{2}\left(\frac{\partial s_\theta[n]}{\partial a}\right)^* \frac{\partial s_\theta[n]}{\partial f_D} = j\frac{2\pi T_s^2}{N_0}\sum_{n=0}^{N-1}\left(n-\frac{N-1}{2}\right)\left|x(nT_s-\tau_0)\right|^2 = 0 \\
I_{\tau,f_D} &= \frac{2T_s}{N_0}\sum_{n=0}^{N-1}\frac{1}{2}\left(\frac{\partial s_\theta[n]}{\partial \tau}\right)^* \frac{\partial s_\theta[n]}{\partial f_D} = -j\frac{2\pi a T_s^2}{N_0}\sum_{n=0}^{N-1}\left(n-\frac{N-1}{2}\right)x'^*(nT_s-\tau_0)x(nT_s-\tau_0) = 0
\end{aligned} \tag{3.7}$$

The off-diagonal elements in the FIM denote the correlation between the desired parameters. If these elements are zero, then each desired parameter can be estimated separately without degradation of accuracy.

Using equations (3.6) and (3.7), the inverse FIM can be expressed as

$$\mathbf{I}^{-1} = \begin{bmatrix} \frac{N_0}{T_{coh}} & 0 & 0 \\ 0 & \frac{N_0}{T_s a^2 R_{x'x'}(0)} & 0 \\ 0 & 0 & \frac{12N_0}{(2\pi T_s)^2 a^2 T_s N(N^2-1)} \end{bmatrix} \tag{3.8}$$

The diagonal elements in the inverse of FIM ($\mathbf{I}^{-1}$) represents the CRLBs of the signal amplitude, code phase, and Doppler frequency and are further discussed below.

3.1.1 Code phase CRLB

For the code phase CRLB, it is shown that

$$CRLB(\hat{\tau}_0) = [\mathbf{I}]^{-1}_{\tau\tau} = \frac{N_0}{T_s a^2 R_{x'x'}(0)} \tag{3.9}$$

This result can also be interpreted in the frequency domain. If the baseband signal normalized power spectral density (PSD) over the infinite bandwidth is defined as $G_x(f)$, then the auto-correlation function of the derivatives of x can also be interpreted as

$$\begin{aligned} R_{x'x'}(0) &= \sum_{n=0}^{N-1} x'^*(nT_s-\tau_0)x'(nT_s-\tau_0) \approx \frac{1}{T_s}\sum_{n=0}^{N-1}\int_{nT_s}^{(n+1)T_s} x'^* x' dt \\ &= \frac{1}{T_s}\sum_{n=0}^{N-1}\int_{nT_s}^{(n+1)T_s}\left(\int_{-\infty}^{\infty} X(f_1) j2\pi f_1 e^{i2\pi f_1 t} df_1\right)^*\left(\int_{-\infty}^{\infty} X(f_2) j2\pi f_2 e^{i2\pi f_2 t} df_2\right) dt \\ &= \frac{1}{T_s}(2\pi)^2 T_{coh}\int_{-\infty}^{\infty} G_x(f) f^2 df \end{aligned} \tag{3.10}$$

Since the noise is white over the spectrum, the noise power spectral density N_0 can be replaced by G_w and a deterministic signal amplitude is assumed, i.e., $a = \sqrt{2C_s}$, where C_s is the signal carrier power. Then the corresponding CRLB of the code phase has the following form:

$$CRLB(\hat{\tau}_0) = [\mathbf{I}]^{-1}_{\tau\tau} = \frac{N_0}{T_s a^2 R_{x'x'}(0)} = \frac{G_w}{T_s 2C_s \frac{1}{T_s}(2\pi)^2 T_{coh}\int_{-\infty}^{\infty} G_x(f) f^2 df}$$
$$= \frac{1}{2(2\pi)^2 T_{coh}\int_{-\infty}^{\infty} \frac{C_s G_x(f)}{G_w} f^2 df} \tag{3.11}$$

Equation (3.11) is exactly the same as developed by Bertz (2009), equation (39). This equation states that the tracking accuracy of the code phase depends on the spectral shape of the signal and noise and a frequency weighting effect takes place. If more signal powers are located at higher frequency, it will improve the code phase estimation accuracy.

3.1.2 Doppler frequency CRLB

For simplicity, assuming that the signal has deterministic amplitude $\sqrt{2C}$, then the Doppler frequency CRLB can be expressed as

$$CRLB(\hat{f}_D) = [\mathbf{I}]^{-1}_{f_D f_D} = \frac{12N_0}{(2\pi T_s)^2 a^2 T_s N(N^2-1)}$$
$$= \frac{12}{(2\pi T_s)^2 (2C/N_0 T_s) N(N^2-1)} \tag{3.12}$$

Equation (3.12) matches the well-known results shown in Rife & Boorstyn (1974) and in this case, the term $2\frac{C}{N_0}T_s$ indicates SNR. This equation also represents the block

processing Doppler frequency estimation bounds (Borio et al 2010). As the coherent integration time increases, the frequency tracking bound is lowered.

3.1.3 Signal amplitude CRLB and squaring loss

The CRLB of the signal amplitude is

$$CRLB(\hat{a}) = [\mathbf{I}]^{-1}_{aa} = \frac{N_0}{T_{coh}} \tag{3.13}$$

As it is also shown in equation (3.8), the CRLB of the code phase and Doppler frequency both depends on signal amplitude, while signal amplitude accuracy depends only on the integration interval and noise variance.

Whenever a GNSS receiver is used in severe signal degraded environments, signal amplitude estimation is usually poor, which will inevitably deteriorate the code phase and Doppler estimation accuracy. If the signal amplitude could be treated as deterministic or perfectly known a priori, then one could simply use $a = \sqrt{2C}$ instead of a for code phase and Doppler frequency CRLB. However, in real scenarios, the signal amplitude is usually not deterministic or known a priori. Rather it is usually a random variable that needs to be estimated. Then the disturbances present in the signal amplitude estimation will in turn deteriorate the code phase and frequency accuracy. This is often called the squaring loss (Pany 2010) and is given by

$$\gamma_{\text{square loss}} = 1 + \frac{1}{2C / N_0 T_{coh}} \tag{3.14}$$

3.2 Doppler estimation with non-coherent discriminator

In conventional GNSS receivers, carrier tracking loops can use either the frequency discriminators and/or carrier phase discriminators to obtain the tracking errors. These errors are fed to the loop filers and NCOs. Generally speaking, coherent frequency discriminators, such as the cross product frequency discriminators (Natali 1984), rely on the signal coherency to estimate the frequency errors between epochs. However, when operating in weak signal conditions, the coherency of the carrier phase is not guaranteed. Thus commonly used coherent frequency discriminators are not effective. Instead, the non-coherent frequency discriminators which only use the absolute signal power to obtain the tracking errors are more robust under these circumstances.

Some researchers have discussed various non-coherent discriminator based frequency estimator such as Natali (1984), Juang & Chen (2009) and Pany (2010) to name a few. This section reviews one open loop Doppler frequency estimator that is based on non-coherent frequency discriminator. The statistics of such a power based non-coherent frequency discriminator are first derived. Following that, the Doppler tracking jitter of this frequency estimator is compared with the block processing CRLBs.

For each coherent integration block, the total coherent integration time is $T_{Coh} = NT_s$, and N is the number of samples during the total coherent integration. Then, the k^{th} block of the received samples could be expressed as

$$\mathbf{r_k} = \begin{bmatrix} r_k[0] \\ r_k[1] \\ \vdots \\ r_k[N-1] \end{bmatrix}, \quad k \in [0, K-1]$$

$$\begin{aligned} r_k[n] &= r(kT_{coh} + nT_s) \\ &= a_k x(kT_{coh} + nT_s - \tau_0) e^{j(2\pi f_k nT_s + \phi_k)} + w(kT_{coh} + nT_s), \quad n \in [0, N-1] \end{aligned} \tag{3.15}$$

Accordingly, the k^{th} block local code and local carrier are

$$\mathbf{x_k} = \begin{bmatrix} x_k[0] \\ x_k[1] \\ \vdots \\ x_k[N-1] \end{bmatrix} = \begin{bmatrix} x[kT_{coh} - \hat{\tau}_k] \\ x[kT_{coh} + T_s - \hat{\tau}_k] \\ \vdots \\ x[kT_{coh} + (N-1)T_s - \hat{\tau}_k] \end{bmatrix},$$

$$\mathbf{lo}_{k,\hat{f}_{D,i}} = \begin{bmatrix} lo_{k,\hat{f}_{D,i}}[0] \\ lo_{k,\hat{f}_{D,i}}[1] \\ \vdots \\ lo_{k,\hat{f}_{D,i}}[N-1] \end{bmatrix} = \begin{bmatrix} 1 \\ \exp(j2\pi \hat{f}_{D,i} T_s) \\ \vdots \\ \exp(j2\pi \hat{f}_{D,i} (N-1)T_s) \end{bmatrix} \tag{3.16}$$

In equation(3.16), $\mathbf{lo}_{k,f_{D,i}}$ represents the local carrier vector of the k^{th} block with Doppler frequency $f_{D,i}$ and element of $lo_{k,\hat{f}_{D,i}}[n]$, and $\mathbf{x_k}$ denotes the local PRN code vector with elements of $x_k[n]$. The indices of such elements are in the range $[0, N-1]$. Then the correlator output at k^{th} block will be

$$y_{k,\hat{f}_{D,i}} = \frac{1}{N} \sum_{n=0}^{N-1} r_k[n] (x_k[n] lo_{k,\hat{f}_{D,i}}[n])^*, \quad k \in [0, K-1] \tag{3.17}$$

In equation (3.17), k represents the k^{th} processing block, N is the total number of l samples for the whole coherent integration and $\hat{f}_{D,i}$ is the candidate Doppler frequency

for the local carrier. The term $y_{k,\hat{f}_{D,i}}$ denotes the correlator output for the k^{th} processing block with the candidate Doppler frequency $\hat{f}_{D,i}$ and code phase $\hat{\tau}_k$.

In terms of the in-phase and quadratic-phase components, the correlator outputs for the k^{th} processing block can be further expressed as

$$\begin{aligned} y_k &= aR_{xx}(\tau_k)\frac{\sin \pi \Delta f_k N T_s}{N \sin \pi \Delta f_k T_s}\exp(j\varphi_k)+\eta_k \\ &= s_k + \eta_k, \quad k \in [0, K-1] \\ s_k &= I_k + jQ_k \\ \eta_k &= \eta_{k,I} + j\eta_{k,Q}, \quad k \in [0, K-1] \end{aligned} \tag{3.18}$$

In equation (3.18), the subscript $f_{D,i}$ of the correlator output is omitted for convenience. Δf_k is defined as the difference between true Doppler and the candidate Doppler, i.e. $f_{D,k,true} - \hat{f}_{D,i}$. The phase term φ_k is defined as $\phi_k + 2\pi f_{D,k,true} k T_{Coh} + \pi \Delta f_k T_{Coh}$. The terms $\eta_{k,I}$ and $\eta_{k,Q}$ denote the in-phase and quadratic-phase correlator output noise terms, whose means are zeros, $E\left[\eta_{k,I}^2\right] = E\left[\eta_{k,Q}^2\right] = \frac{N_0}{2T_{coh}}$, and $E\left[\eta_{k,I}\eta_{k,Q}\right] = 0$.

The correlator outputs with Doppler frequencies of $\Delta f_k \pm df$ could be used for non-coherent frequency discriminators. *df* is the frequency deviation from the candidate frequency. These two outputs are called slow and fast correlator outputs, as shown in Figure 3.1.

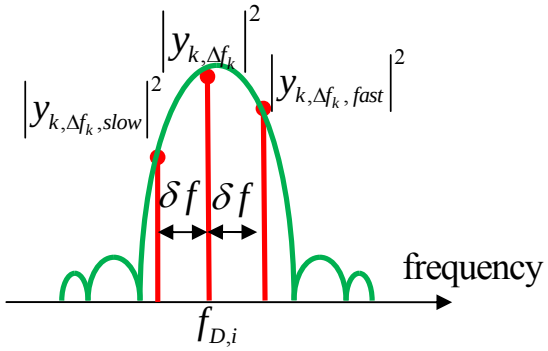

Figure 3.1: Correlator outputs with slow, fast and candidate Doppler frequency

The slow-fast correlator based non-coherent frequency discriminator is defined as

$$\begin{aligned} D(\Delta f_k) &= \left\| y_{k,slow} \right\|^2 - \left\| y_{k,fast} \right\|^2 \\ &= I_{k,slow}^2 + Q_{k,slow}^2 - (I_{k,fast}^2 + Q_{k,fast}^2) + \varepsilon_{k,\delta f} \end{aligned} \tag{3.19}$$

where $k \in [0, K-1]$ is the index of the processing block. Fast correlator output means the incoming signal mixes with a relatively fast local carrier ($\Delta f_k + \delta f$), while slow correlator outputs indicates mixing with a relatively slow local carrier ($\Delta f_k - \delta f$). The maximum value is considered as the 'frequency prompt'. With the non-coherent frequency discriminator, the tracking error will be estimated more accurately. The discriminator gain is then computed as

$$\begin{aligned} K_D &= \frac{\partial E\left[D(\Delta f_k)\right]}{\partial \Delta f_k}\Big|_{\Delta f_k = 0} \\ &= 2\pi a^2 T_{Coh} \operatorname{sinc}\left(\pi \delta f T_{Coh}\right) \left(\frac{2\sin(\pi \delta f T_{Coh}) - 2\pi \delta f T_{Coh} \cos(\pi \delta f T_{Coh})}{\left(\pi \delta f T_{Coh}\right)^2} \right) \end{aligned} \tag{3.20}$$

The discriminator S-curve is plotted in Figure 3.2.

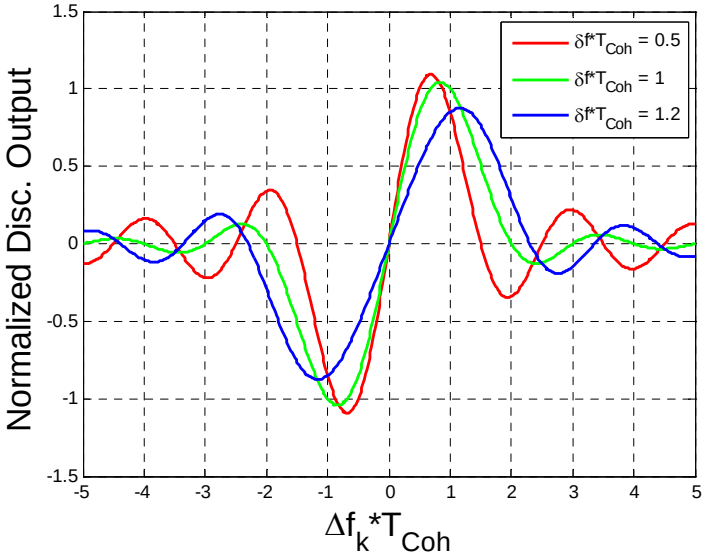

Figure 3.2: S-curve of non-coherent frequency discriminator

The noise in the discriminator outputs can be shown as

$$\begin{aligned}\mathrm{var}[D(\Delta f_k)] &= 8a^2 \frac{N_0}{2T_{Coh}} \mathrm{sinc}^2(\pi\delta f T_{Coh})(1-\mathrm{sinc}(2\pi\delta f T_{coh})) \\ &+ 8\left(\frac{N_0}{2T_{Coh}}\right)^2 \left(1-\mathrm{sinc}^2(2\pi\delta f T_{coh})\right)\end{aligned} \tag{3.21}$$

Equation (3.21) shows the variance of the non-coherent frequency discriminator. The noise variance of a similar non-coherent frequency discriminator has also been reported in Juang & Chen (2009), but the results (equation (19)) shown there missed a square for the noise variance. With the discriminator gain and noise variances derived, the open loop tracking jitter or Doppler frequency estimation accuracy can then be shown as

$$\sigma^2_{\tilde{f},open} = \frac{\mathrm{var}[D_k(\tilde{f}_k)]}{K_D^2}$$
$$= \frac{8a^2 \frac{N_0}{2T_{Coh}} \mathrm{sinc}^2(\pi\delta f T_{Coh})(1-\mathrm{sinc}(2\pi\delta f T_{coh})) + 8\left(\frac{N_0}{2T_{Coh}}\right)^2 \left(1-\mathrm{sinc}^2(2\pi\delta f T_{coh})\right)}{4\pi^2 a^4 \mathrm{sinc}^2(\pi\delta f T_{coh}) \left\{\frac{2\sin(\pi\delta f T_{Coh}) - 2\pi\delta f T_{Coh}\cos(\pi\delta f T_{Coh})}{(\pi\delta f T_{Coh})^2}\right\}^2} \quad (3.22)$$

This also represents the accuracy of the open loop fine frequency estimator. In Figure 3.3, the performance of such a non-coherent discriminator based frequency estimator with various frequency step sizes is compared with that of the block processing Doppler CRLB. In this figure, it is shown that when the pre-detection SNR is above 10 dB, the accuracy of the non-coherent discriminator based frequency estimator approaches the CRLB. The non-coherent frequency discriminators with larger frequency offset spacing ($\delta f T_{coh}$) have larger linear region but perform worse than the one with smaller frequency offset spacing.

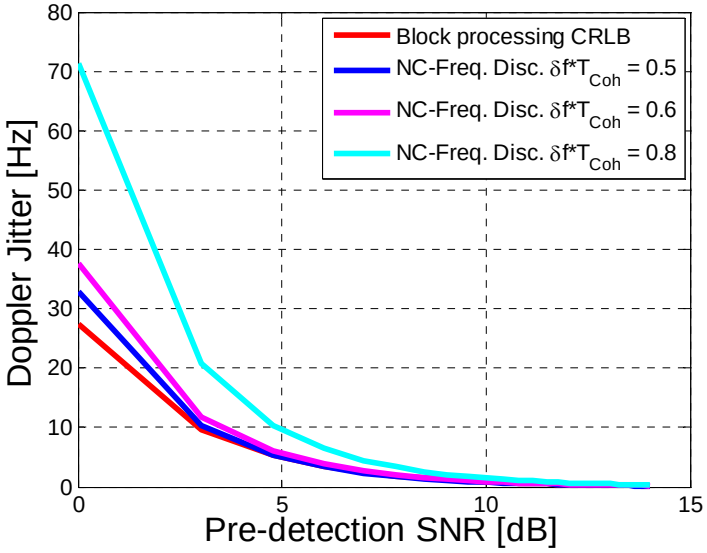

Figure 3.3: Performance of open loop non-coherent discriminator based frequency estimator

Whenever the computation load is a serious consideration of the system, the above non-coherent discriminator based frequency estimation can be applied in HSGNSS receivers, since it only costs a few correlations. However, the MLE will asymptotically approach CRLB as the number of observations increases (Kay 1993a) and is very practical for implementation. MLE is thus the ultimate solution when computation load is not a concern. In the next section, the Doppler MLE with focus on implementation will be further discussed.

3.3 Doppler MLE – serial search, DFT, and SDFT

The Doppler MLE can be derived by maximizing the probability density functions $p(\mathbf{r};\boldsymbol{\theta})$ with respect to f_D. For example, Rife & Boorstyn (1974) have shown such an estimator as follows:

$$\hat{f}_{d,ML} = \arg\max_{f_D} \left| \sum_{n=0}^{N-1} r[n] \exp(-j2\pi f_D n T_s) \right|^2 \tag{3.23}$$

For implementation of ML Doppler frequency estimator, two fundamental approaches can be found in the conventional high sensitivity receivers: serial frequency search and parallel frequency search as shown in Figure 3.4. The first approach will go through all the hypotheses and is time consuming but easy to implement. The latter approach is commonly implemented using a DFT algorithm. The total coherent integration time is T_{Coh} and can be expressed as $NT_s = LN_pT_s = LT_p$, where N is the length of the samples, T_s is the sampling time, N_p is the sample length of the partial coherent integration samples and T_p is the partial coherent integration time. The received samples within one coherent integration interval are considered as one block. For example, $\mathbf{r}_k$ denotes the k^{th} coherent integration block, which is composed of samples $r[kN]$, $r[kN+1]$, $\cdots$, $r[(k+1)N-1]$ with length N. These N samples can be broken into L partial coherent integration. The correlator output for each such partial coherent integration is termed $y_{k,l}$, where $l = 1:L$. A block of the correlator outputs can also be represented in vector form $\mathbf{y}_k = [y_{k,1}, y_{k,2}, ..., y_{k,L}]^T$.

As the length of the coherent integration time increases, the parallel search method will be much faster than that of the serial search method. This is because the serial Doppler search forces the receiver to go through every Doppler hypothesis sequentially. However, the parallel Doppler search is based on post-correlation spectral analysis, which tests

multiple hypotheses in parallel. For the parallel search, one can also optimize the performance of the searching engine based on some trade-offs (Ma et al 2011).

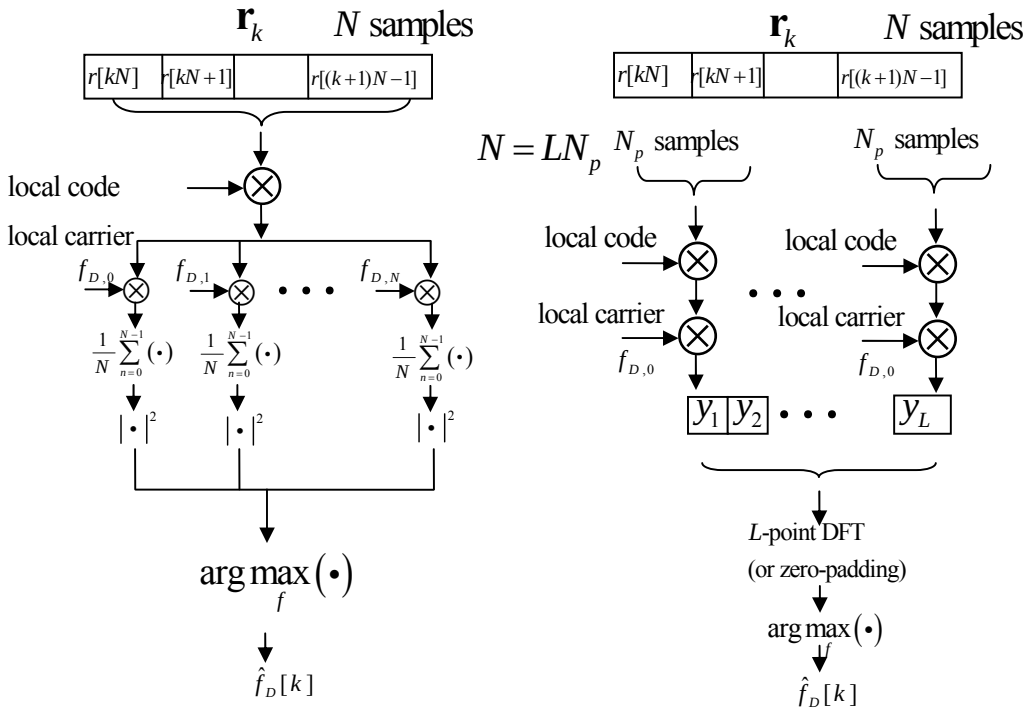

Figure 3.4: Serial (left) and parallel/DFT (right) Doppler frequency MLE

In Figure 3.4 either the serial or parallel method needs to process all N samples, and then output a Doppler frequency estimate at the rate of $1/(NT_s)$. The DFT based parallel Doppler estimator is generally more efficient as compared to the serial method shown on the left. In addition, zero padding could be applied in order to improve the frequency estimation resolution. However, the major disadvantages of the DFT approach are that it can only give one averaged Doppler estimate over the whole integration interval, and the transient information between adjacent integration intervals is lost. Most importantly, the channel NCO feedback rate from the navigation solution is usually limited to the reciprocal of

coherent integration time. To increase the NCO feedback rate, overlapping DFT (ODFT) with zero padding is shown in Figure 3.5.

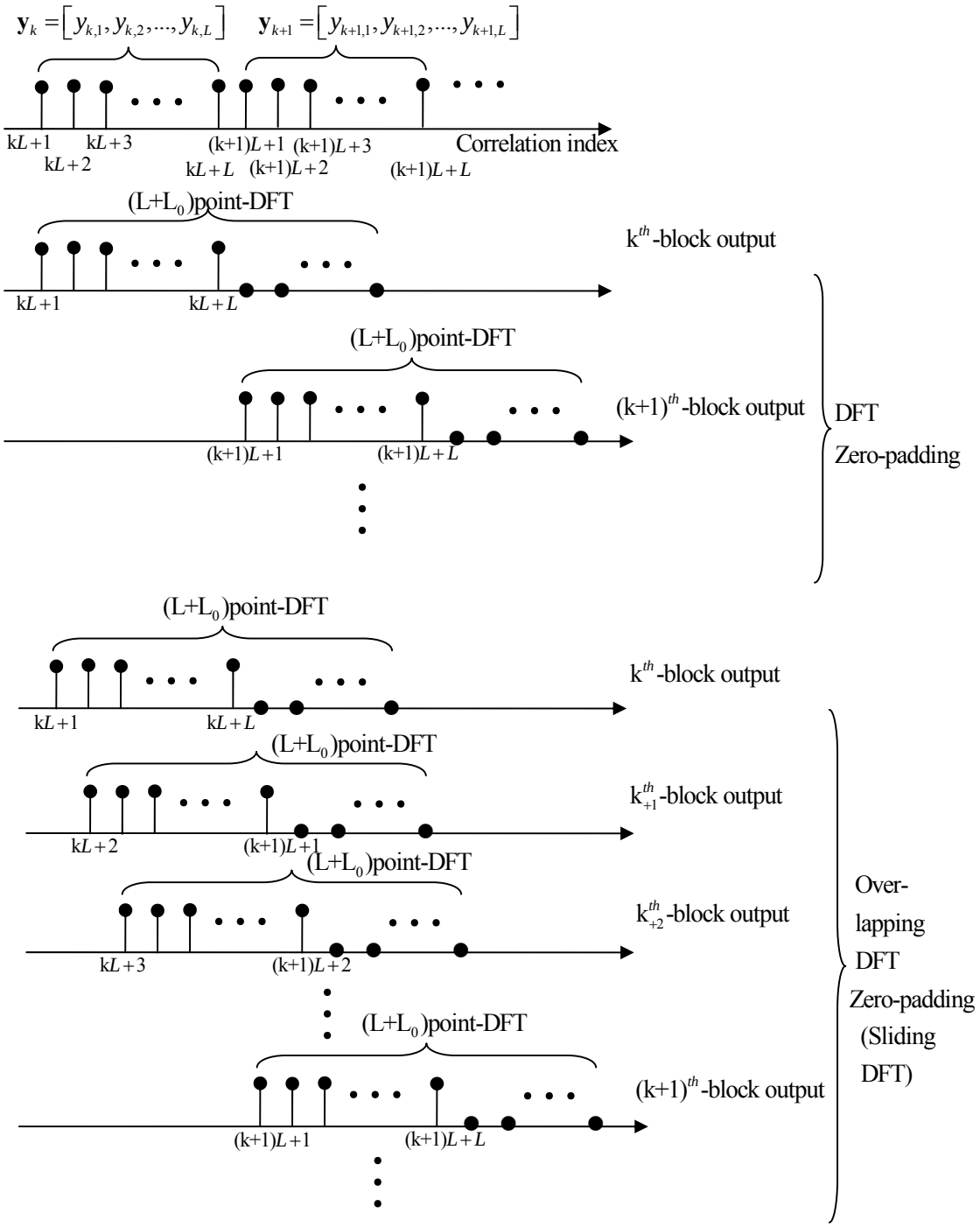

Figure 3.5: DFT, overlapping DFT and sliding DFT based Doppler frequency estimation

In Figure 3.5, one can see that the ODFT can not only provide the Doppler frequency estimate for each block of correlator outputs ($\mathbf{y_k}, \mathbf{y_{k+1}}, \ldots$), but also can give the estimates when sliding between adjacent blocks. In this way, the transient information between the blocks can still be estimated and used. The major challenge for directly using ODFT is that the computation load is significantly increased. However, SDFT has been proven to be computationally effective to be used as ODFT. Another important advantage is that the SDFT can focus on the frequency bands that are of interest, which further decreases the computation load.

As for our application, the SDFT can also be zero padded in order to get a desirable resolution. The SDFT with zero padding (SDFT-ZP) are proposed as follows. Assume that the total size of the DFT is $N_{DFT} = L + L_0 = M_{DFT} L$. It means that zeros added in the end are $(M_{DFT} - 1)$ times the correlator outputs in one block. The DFT of the zero padded sequence ending at $y[n]$ and evaluated at frequency bin m can be expressed as

$$\begin{aligned} Y_n[m] &= y[n - \frac{N_{DFT}}{M_{DFT}} + 1] + y[n - \frac{N_{DFT}}{M_{DFT}} + 2] e^{-j\frac{2\pi}{N_{DFT}}m} + \cdots + y[n] e^{-j\frac{2\pi}{N_{DFT}}m(\frac{N_{DFT}}{M_{DFT}} - 1)} \\ &= \sum_{l=0}^{\frac{N_{DFT}}{M_{DFT}} - 1} y[n - \frac{N_{DFT}}{M_{DFT}} + 1 + l] e^{-j\frac{2\pi}{N_{DFT}}ml} \end{aligned} \tag{3.24}$$

Similarly, the DFT ending at $y[n-1]$, evaluated at frequency bin m, can be expressed as

$$
\begin{aligned}
Y_{n-1}[m] &= \sum_{l=0}^{\frac{N_{DFT}}{M_{DFT}}-1} y[n-\frac{N_{DFT}}{M_{DFT}}+l]e^{-j\frac{2\pi}{N_{DFT}}ml} \\
&= y[n-\frac{N_{DFT}}{M_{DFT}}]+y[n-\frac{N_{DFT}}{M_{DFT}}+1]e^{-j\frac{2\pi}{N_{DFT}}m}+\cdots+y[n-1]e^{-j\frac{2\pi}{N_{DFT}}m(\frac{N_{DFT}}{M_{DFT}}-1)}
\end{aligned}
\tag{3.25}
$$

Then the iterative update equation for SDFT-ZP is

$$
Y_n[m] = e^{j\frac{2\pi}{N_{DFT}}m}\left(Y_{n-1}[m]-y[n-\frac{N_{DFT}}{M_{DFT}}]+y[n]e^{j\frac{2\pi}{M_{DFT}}m}\right) \tag{3.26}
$$

The structure of the SDFT-ZP is illustrated in Figure 3.6.It shows that each branch of DFT values within the frequency band of interest is composed of two parts, the comb filter and the resonator.

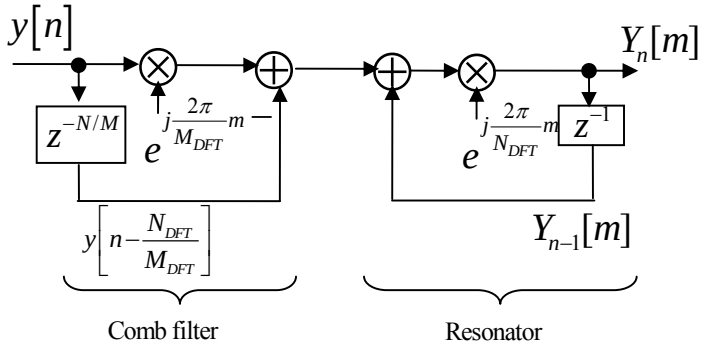

Figure 3.6: Structure of SDFT-ZP

Furthermore, the frequency transfer function of the SDFT-ZP can be expressed as

$$
\begin{aligned}
Y_{n,m}(z) &= e^{j\frac{2\pi}{N_{DFT}}m}(Y_{n,m}(z)z^{-1}+e^{j\frac{2\pi}{M_{DFT}}m}Y(z)-Y(z)z^{-\frac{N_{DFT}}{M_{DFT}}}) \\
H_{SDFT-ZP}(z) &= \frac{Y_{n,m}(z)}{Y(z)} = \frac{e^{j\frac{2\pi}{N_{DFT}}m}(e^{j\frac{2\pi}{M_{DFT}}m}-z^{-\frac{N_{DFT}}{M_{DFT}}})}{1-e^{j\frac{2\pi}{N_{DFT}}m}z^{-1}}
\end{aligned}
\tag{3.27}
$$

It can be seen in equation (3.27) that the poles of the transfer function for SDFT are located on the unit circle. Due to the numerical precision, this standard SDFT can occasionally result in numerical stability problems. However, there are many variations of SDFT that possess numerical stability, such as the modulated SDFT (mSDFT) discussed in Duda (2010), although this will not be further discussed herein.

Both serial and parallel Doppler search methods discussed here are known as ML frequency estimators. Heavy computational load is required in both approaches, but they asymptotically approach the Doppler frequency CRLB.

3.4 Summary

This chapter reviewed the Doppler estimation methods in AWGN. A non-coherent discriminator based Doppler estimator has been analyzed and is compared with block processing Doppler MLE, which are the two basic methods used in the thesis. Regarding implementation, a SDFT method with zero padding is also proposed to increase the channel NCO feedback rate with a bearable computation load.

Chapter Four: **HSGNSS DOPPLER ERROR CHARACTERIZATION INDOORS**

It has been shown in the previous chapter how Doppler frequency could be estimated with high sensitivity GNSS receivers in AWGN. However when it comes to indoor multipath environments, noise is not the only source that influences the parameter estimation accuracy. This chapter investigates the indoor multipath effects on Doppler estimation in high sensitivity receivers.

4.1 Multipath characteristics and signal model

In the following, the received signal is only analyzed for a single channel or satellite without loss of generality. This is reasonable since PRN codes between satellites are quasi-orthogonal, the receiver can always process one satellite per channel without much consideration for the other satellite signals received, so long as the received signal strengths are approximately equal across all channels (to avoid cross-correlation effects associated with the near-far problem).

The radio frequency (RF) signal received at the static antenna can be expressed as (Ward et al 2006)

$$s_{LOS,RF}(t) = \mathrm{Re}\{\alpha_{0,i}(t)x_i(t-\tau_{0,i})e^{-j\phi_{0,i}}e^{j2\pi f_c(t-\tau_{0,i})}\}. \quad (4.1)$$

In equation (4.1), α_0, τ_0 and ϕ_0 are the LOS amplitude, time delay, and carrier phase for this satellite and $x(t) = d(t)p(t)$ is the product of the spreading code or pseudo random noise (PRN) code, *p(t)*, and the navigation data bits, *d(t)*. f_c is the transmitted carrier frequency.

Similarly, in a multipath environment, the NLOS signal for this satellite received at the antenna can also be expressed as

$$s_{NLOS,RF}(t) = \mathrm{Re}\left\{\left(\sum_{m=1}^{M_{MP}} \alpha_m(t)x(t-\tau_m)e^{-j\phi_m}e^{j2\pi f_c(t-\tau_m)}\right)\right\}, \quad M_{MP} \geq 1. \tag{4.2}$$

In equation(4.2), M_{MP} is the number of multipath (reflected) signals for this satellite's transmitted signal. α_m, τ_m and ϕ_m are the amplitude, time delay and carrier phase of the mth multipath for this satellite. If the LOS and NLOS are both received, the composite RF signal is given by the summation of equations (4.1) and (4.2).

Upon receipt of the signal, the receiver first down-converts it to near baseband. The complex envelope or low pass equivalent signal can then be expressed as

$$\begin{aligned} r_l(t) &= \alpha_{0,i}(t)x_i(t-\tau_{0,i})e^{-j\phi_{0,i}}e^{j2\pi f_c(t-\tau_{0,i})} \\ &\quad + \sum_{m=1}^{M_{MP}} \alpha_m(t)x(t-\tau_m)e^{-j\phi_m}e^{j2\pi f_c(t-\tau_m)} + w(t), \qquad M_{MP} \geq 1. \end{aligned} \tag{4.3}$$

In equation(4.3), $w(t)$ is the input additive noise, here assumed to be independent of the signal with a flat power spectrum over the pre-correlation bandwidth.

In order to incorporate the effects of user-induced Doppler shifts, it is necessary to expand the communication channel induced delay with additional user motion. A common assumption for this delay is that each individual channel path (including LOS transmit path) changes at a constant rate with respect to the short integration interval. Then each received signal is assumed to have a constant frequency over the integration interval. The delay rate (i.e., frequency) depends on the angle of arrival (AOA) of the

signals and direction of user motion (Fontan & Espineira 2008). The LOS delay can be expressed as

$$\tau_0 = d_0 / c - v_{\max} t / c \cos\alpha_0 \cos\varepsilon_0 \tag{4.4}$$

In equation(4.4), d_0 is the initial LOS length of the propagation path, c is the speed of light, $v_{\max}$ is the maximum local velocity or speed of the user, and α_0 and ε_0 are the LOS azimuth and elevation angle, respectively. Here the satellite velocity induced propagation distance changes are included in d_0. When it comes to indoor multipath environments, the individual NLOS delay can be expressed in a similar way as

$$\tau_m = d_m / c - v_{\max} t / c \cos\alpha_m \cos\varepsilon_m, \quad 1 \le m \le M_{MP}. \tag{4.5}$$

In equation (4.5), the subscript m represents the m^{th} multipath signal for this satellite, and d_m , α_m and ε_m are the propagation distance, azimuth and elevation angle for this individual multipath component. It is further assumed that the speed of light in free space propagation is a constant for GNSS positioning.

For a narrowband receiver, the front-end filtering will round off the correlation function, which leads to undistinguishable time delays between very close multipath and the direct signal. This thesis does not focus on resolving multipath in the time delay dimension. In typical indoor environments, by using a narrowband receiver, a narrowband fading model (Goldsmith 2005) can be assumed (as is done herein). This means that the time delay between multipath and direct signal is non-resolvable, implying $x(t-\tau_m) \approx x(t-\tau_0)$, and $d_0 \approx d_m$.

Then the complex envelope of the received satellite signal can be expressed as

$$
\begin{aligned}
r_l(t) &= \alpha_0(t)x(t-\tau_0)e^{j2\pi v_{\max}t/\lambda\cos\alpha_0\cos\varepsilon_0 - j\phi_0 - j2\pi d_0/\lambda} \\
&\quad + \sum_{m=1}^{M_{MP}} \alpha_j(t)x(t-\tau_m)e^{j2\pi v_{\max}t/\lambda\cos\alpha_m\cos\varepsilon_m - j\phi_m - j2\pi d_m/\lambda} + w(t) \\
&= \sqrt{2C}x(t-\tau_0)h(t) + w(t)
\end{aligned}
\tag{4.6}
$$

In equation (4.6), $\sqrt{2C}$ represents the signal amplitude and C is the signal carrier power. By doing this, the component $h(t)$ is normalized with unit amplitude. $\phi_0^{'}$ and $\phi_m^{'}$ are the new LOS and NLOS phases and $\lambda = c/f_c$ is the signal wavelength. Upon closer inspection, the received complex envelope GNSS signal can be considered as a code sequence, $x(t)$, multiplied with the component $h(t)$. This latter component is termed the channel gain series, which is related to the multipath statistics and has the form

$$
\begin{aligned}
h(t) &= \alpha_0(t)e^{j2\pi v_{\max}t/\lambda\cos\alpha_0\cos\varepsilon_0 + j\phi_0^{'}} + \sum_{m=1}^{M_{MP}} \alpha_m(t)e^{j2\pi v_{\max}t/\lambda\cos\alpha_m\cos\varepsilon_m + j\phi_m^{'}} \\
&= \sqrt{\frac{K}{K+1}}e^{j(2\pi f_{Dmax}t\cos\alpha_0\cos\varepsilon_0 + \phi_0^{'})} + \frac{1}{\sqrt{K+1}}\frac{1}{\sqrt{M_{MP}}}\sum_{m=1}^{M_{MP}} a_m e^{j(2\pi f_{Dmax}t\cos\alpha_m\cos\varepsilon_m + \phi_m^{'})} \\
&= h_{LOS}(t) + h_{NLOS}(t) \qquad M_{MP} \geq 1.
\end{aligned}
\tag{4.7}
$$

In equation (4.7), K represents the Ricean factor, which is the ratio between the LOS and NLOS signal powers (Tepedelenlioglu et al 2001). Whenever the Ricean factor is near zero, the NLOS signal(s) tends to dominate the LOS signal. If the Ricean factor is large enough, then all the multipath components can be ignored and this leads to a LOS dominated scenario. f_{Dmax} is the maximum local Doppler caused by the user motion ($f_{Dmax} = v_{max}/\lambda$). a_m is the newly defined amplitude of the mth multipath signal such that

$\lim_{M\to\infty} 1/M \sum_{m=1}^{M} a_m^2 = 1$. A similar approach for modeling the multipath and LOS signal in 2D case can be found in Tepedelenlioglu et al (2001).

In dense indoor multipath environments, it will be more convenient to treat all the multipath signals as an average during short time intervals. In this way, not only the essential multipath statistics are kept, but also all the nuisance parameters are neglected. Along this line of reasoning, the NLOS channel gain series is further simplified as

$$h_{NLOS}(t) = \frac{1}{\sqrt{K+1}} e^{j(2\pi f_{Dmax} t \cos\alpha_M \cos\varepsilon_M + \phi'_{M,0})} \tag{4.8}$$

In equation (4.8), $\phi'_{M,0}$ is the averaged initial carrier phase for all multipath signals and α_M, ε_M denotes the averaged azimuth and elevation angles of all the multipath components, which are random variables. All the multipath statistics are fully preserved by using different angular distribution functions. The corresponding distribution not only can represent one single "average" AOA for the NLOS signal, but also can handle the case where signals are coming from multiple "average" directions. For simplicity, only one "averaged" AOA for the NLOS signal is considered, such as von Mises distribution and discrete distribution discussed in the following.

The von Mises distribution is a common angular distribution function, whose PDF has the following form:

$$f(\theta) = \frac{1}{2\pi I_0(\kappa_\theta)} e^{\kappa_\theta \cos(\theta - \theta_{avg})} \quad , \theta \in (-\pi, \pi] \tag{4.9}$$

In equation (4.9), θ is the angular random variable, $I_0(\bullet)$ is the 0^{th} Bessel function of the first kind, κ_θ is a measure that indicates the concentration of the angle and θ_{avg} is the averaged scattering direction of multipath angle. Heuristically, the concentration parameter will determine the beamwidth of the received multipath signal. In the extreme case, when this parameter goes to zero, the beamwidth becomes infinite and one will obtain isotropic scattering, i.e., NLOS signals are received from all azimuths. However, if this parameter is infinite, the beamwidth is zero and an extremely strong directional scattering will be present.

To illustrate this, consider the following properties (Simon et al 1995):

$$\lim_{\kappa_\theta \to 0} f(\theta) = \lim_{\kappa_\theta \to 0} \frac{1}{2\pi I_0(\kappa_\theta)} e^{\kappa_\theta \cos(\theta - \theta_{avg})} = \frac{1}{2\pi} \tag{4.10}$$

$$\lim_{\kappa_\theta \to \infty} f(\theta) = \lim_{\kappa_\theta \to \infty} \frac{1}{2\pi I_0(\kappa_\theta)} e^{\kappa_\theta \cos(\theta - \theta_{avg})} = \delta(\theta - \theta_{avg}) \tag{4.11}$$

From above equations, it is useful to explicitly define the multipath beamwidth parameter. It has been reported that for large but not infinite κ_θ, the PDF resembles a Gaussian PDF (Abdi et al 2002, Mardia 1975), with mean value θ_{avg} and standard deviation $1/\sqrt{\kappa_\theta}$. So in this thesis, it is assumed that the beamwidth, β, of the multipath AOA is $1/\sqrt{\kappa_\theta}$, as follows:

$$\beta = 1/\sqrt{\kappa} \tag{4.12}$$

Due to the fact that the multipath azimuth and elevation angles can be treated as independent, both angles could be characterized by using von Mises' distribution.

However, this will complicate the theoretical analysis. One convenient way to deal with the elevation angle is to approximate the angular distributions as a summation of discrete pulses. For example,

$$f(\theta) = \sum \Pr_{\theta_i} \delta(\theta - \theta_i), \theta_i \in \{\text{pre-defined range of } \theta\} \tag{4.13}$$

In equation (4.13), $\Pr_{\theta_i}$ is the probability weight of the multipath angle θ_i, $\delta(\theta - \theta_i)$ is the impulse located at θ_i, and $\{\theta_i\}$ is the set of all admissible angles.

On the other hand, the averaged multipath azimuth angle is modeled by von Mises' distribution and the averaged multipath elevation angle is modeled by a discrete distribution. By taking the Fourier transform of the correlation function of channel gain series, the channel distorted carrier PSD is of the following form (He et al 2012a):

$$P_{hh}(f) = \left(\frac{1}{K+1} \frac{\exp(\kappa_\alpha \cos(\alpha_{avg}) \frac{f}{f_{Dmax} \cos\varepsilon}) \cosh[\kappa_\alpha \sin(\alpha_{avg}) \sqrt{1-(\frac{f}{f_{Dmax}\cos\varepsilon})^2}]}{\pi I_0(\kappa_\alpha) \sqrt{1-(\frac{f}{f_{Dmax}\cos\varepsilon})^2}} \right) * \sum \Pr_{\varepsilon_i} \delta(\varepsilon - \varepsilon_i) + \frac{K}{K+1} \delta(f - f_{Dmax} \cos\alpha_0 \cos\varepsilon_0) \tag{4.14}$$

Equation (4.14) shows how the received signal carrier power is distributed over the Doppler domain. It is apparent that the shape of the PSD is not only related with the LOS azimuth and elevation angle (α_0, ε_0), but also is a function of multipath statistics, such as averaged multipath AOAs and Ricean factor.

Having discussed how transmitted signals are distorted by the propagation channels, it is natural to see how these will affect the Doppler estimates in the GNSS receivers. With the analytical expression of the received complex envelope signal shown in equation

(4.6), the MLE of Doppler can be assessed and examined. For receivers that implement block processing techniques (Borio et al 2010), the following product is the correlation which is evaluated over all code phase (τ_m) and Doppler ($f_{D,l}$) dimensions, the subscript m and l denotes the index of the candidate searching values.

$$y[n]_{(\tau_m, f_{D,l})} = r[n]x(nT_s - \tau_m)e^{-j2\pi f_{D,l} nT_s} \tag{4.15}$$

The expression $r[n] = r_l(nT_s)$ is used to denote a digital sequence of the complex envelope signal, which is sampled at the frequency $f_s = 1/T_s$ and where n is the discrete time index. From this, the Doppler MLE can be written as

$$\begin{aligned}
\hat{f}_D &= \arg\max_{l=1:L} \frac{1}{N}\left|\sum_{n=0}^{N-1} y[n]_{(\tau_m, f_{D,l})}\right|^2_{\tau_m=\tau_0} \\
&= \arg\max_{l=1:L} \frac{1}{N}\left|\sum_{n=0}^{N-1} r[n]x(nT_s - \tau_m)e^{-j2\pi f_{D,l} nT_s}\right|^2_{\tau_m=\tau_0} \\
&\approx \arg\max_{l=1:L} 2C \bullet \frac{1}{N}\left|\sum_{n=0}^{N-1} h[n]e^{-j2\pi f_{D,l} nT_s}\right|^2 = \arg\max_{l=1:L} 2C \bullet I_{hh}(f_{D,l})
\end{aligned} \tag{4.16}$$

In equation (4.16), the Doppler MLE is obtained by searching all the candidate Doppler values within a pre-defined searching range, such as $\{f_{D,1}, f_{D,2}, ..., f_{D,L}\}$, and then selecting the Doppler value that yields the largest value of the test statistics, $2CI_{hh}(f_{D,l})$. As it is also shown in equation (4.16), the test statistic $2CI_{hh}(f_{D,l})$ depends on the parameters defined in the channel gain series in equation (4.7) and is also the periodogram of the channel gain series, which gives an estimate of the PSD of $h[n]$. The term $h[n]$ is the discrete version of $h(t)$, as shown in equation (4.7). The periodogram

($I_{hh}(f)$) could be considered the true signal power spectrum ($P_{hh}(f)$) convolved with a window spectrum and thus will have some sort of distortion. This window power spectrum is affected by the integration time. However, it is also known that the averaged periodogram is asymptotically an unbiased estimator of the true power spectrum (Oppenheim et al 1998). Therefore, the correlator outputs over Doppler searching range are related with the PSD of the channel gain series. Whenever the multipath effects are severe, the Doppler measurements estimated by block process techniques will be significantly influenced. So the major bias contained in the Doppler measurement comes from the channel distortion.

From the actual PSD of channel gain series, it is apparent that if Ricean factor (K) is large (i.e., the LOS signal is dominant), the multipath induced distortion becomes small. In other words, the peaks in the carrier power spectrum will be dominated by the LOS signal path, which is ideally an impulse. This will eventually lead to an unbiased estimation of the Doppler frequency. The communication channel distortion can be ignored under this circumstance. However, as the Ricean factor decreases, the peak of the power spectrum could be dominated by multipath components. In this way, the essential channel parameters affecting the Doppler MLE are

$$\Omega = \{K, \alpha_{avg}, \beta_{\alpha}, \varepsilon_{avg}, \beta_{\varepsilon}, \alpha_0, \varepsilon_0\} \tag{4.17}$$

Specifically, these essential channel parameters are the Ricean factor (K), the averaged multipath azimuth angle (α_{avg}), the beamwidth of multipath azimuth (β_{α}), the averaged

multipath elevation angle (ε_{avg}), the beamwidth of multipath elevation (β_{ε}), and the LOS azimuth (α_0) and elevation angles (ε_0).

4.2 Theoretical simulation

In this section, some simulations are presented using the model introduced in the previous section.

With equations (4.14) and (4.17), the effects of channel parameters on carrier PSD can be evaluated under different scenarios. In turn, the Doppler error statistics in different multipath environments can be determined. To do this, each individual parameter from the channel parameter set is modified and the effects on the carrier power spectrum are assessed. The parameters considered here are summarized in Table 4.1.

Table 4.1: Channel parameters used for simulations

Parameter	Case A	Case B	Case C	Case D
K	0.3	0.3	0.3	0.3
α_0 [deg]	36	36	36	36
ε_0 [deg]	70	70	70	70
α_{avg} [deg]	60, 100 & 240	60	60	60
β_{α} [deg]	13	13	6, 9, 19 & 31.5	∞
ε_{avg} [deg]	45	45 & 65	15	15
β_{ε} [deg]	15	15	0	0
v [m/s]	1.5	1.5	1.5	1.5
λ [m]	0.19	0.19	0.19	0.19

It is assumed that the LOS Doppler is only due to the user motion. Satellite motion induced Doppler shifts are predictable and accurately compensated for. The distribution

of elevation angles used here is in accordance with equation (4.13) and assumes there are three impulses, one centred at an averaged elevation angle with a probability of 0.5 and the other two offset by the beamwidth, each having a probability of 0.25. The user is assumed to be moving with constant velocity in the horizontal plane (i.e., no vertical velocity) and travelling due north.

Four different cases are considered here. The focus is given to evaluate the effects of averaged multipath azimuth angle α_{avg} , averaged multipath elevation angle ε_{avg} and beamwidth of multipath azimuth β_{α} (including the infinite beamwidth case) on Doppler estimation. Figure 4.1 shows the effect of an averaged multipath azimuth (i.e., Case A). The three different curves represent the spectra from three different average multipath azimuths. Since the received Doppler is a function of the velocity projected onto the LOS, the magnitude of the Doppler shift is largest when the multipath azimuth is 60° and 240° (i.e., cos(60°) = cos(240°)). Similarly, for a multipath azimuth of 100°, the Doppler shift is smaller. In addition the amplitude is reduced compared to the other two cases since the multipath "beam" is less concentrated along the direction of motion. The y axis is the normalized power.

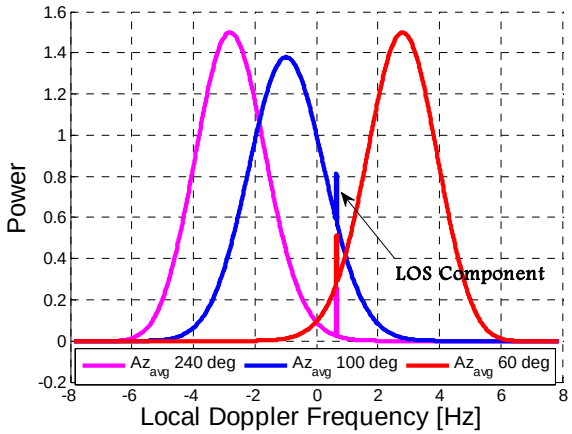

Figure 4.1: Case A: Averaged multipath azimuth angle effects on carrier PSD

Similarly, Figure 4.2 shows the effect of the average multipath elevation angle. Given that the user is assumed to move horizontally, the lower elevation multipath angle induces a more pronounced effect, both in terms of Doppler offset and power magnitude.

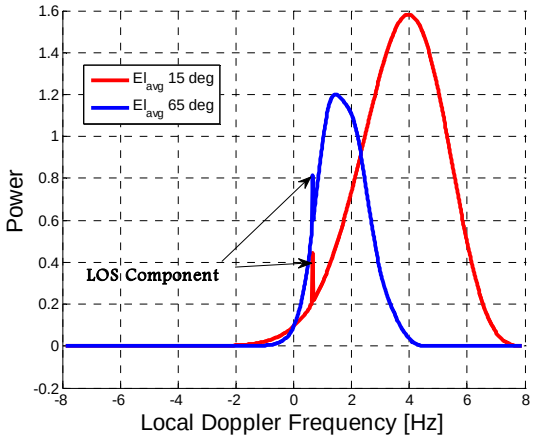

Figure 4.2: Case B: Averaged multipath elevation angle effects on carrier PSD

The effect of multipath azimuth beamwidth is shown in Figure 4.3. It is assumed that strong directionality is considered as a multipath having a beamwidth smaller than 10°.

Medium directionality of multipath indicates a beamwidth ranging from 10° to 30°. Weak directionality indicates a beamwidth larger than 30°. The beamwidth values chosen include strong, medium and weak directionality cases. The obvious point is that narrower beamwidths produce sharper carrier power spectrums. Under weak directionality, the peaks in the carrier power spectrum tend to the singular value given by the maximum Doppler shift induced by user motion (i.e., in Figure 4.3: 1.5 m/s / 0.19 m/cyc = 7.9 Hz).

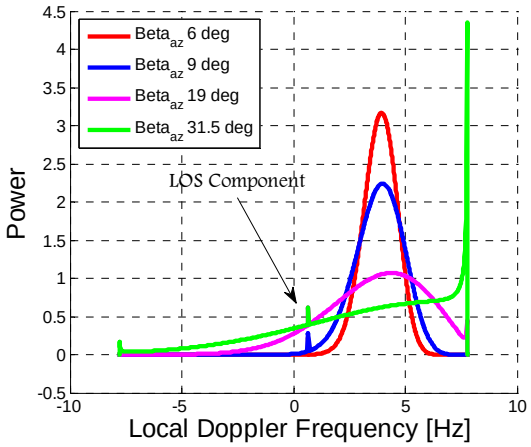

Figure 4.3: Case C: multipath beamwidth effects on carrier PSD

The final scenario extends the analysis of the effect of multipath beamwidth to the omnidirectional case. Figure 4.4 shows the carrier power spectrum for this case, which is of great importance to verify the proposed model. As shown, whenever the beamwidth of the multipath signal is infinite, the AOA uncertainty of the received multipath becomes infinite. This is based on the assumption of a spherical distribution of scatterers. With the proposed model, the carrier power spectrum also coincides with the classical U-shape

spectrum (Fontan & Espineira 2008). Due to non-zero Ricean factor, in this plot, there still exists a weak LOS signal.

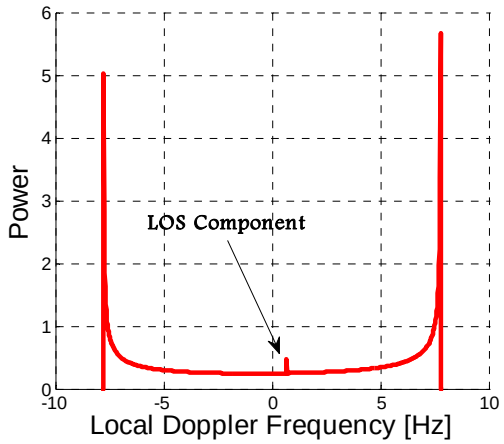

Figure 4.4: Case D: omnidirectional multipath with LOS carrier PSD

4.3 Field test and analysis

In this section real experimental data is processed and analyzed in order to validate the model proposed above. It should be noted that the objective is not to exactly replicate the indoor multipath environments, but rather to show some level of consistency for the proposed model with real data.

Test Descriptions

The following test is done to identify the Doppler errors of a high sensitivity receiver which uses block processing in indoor environments.

As it has been discussed in certain indoor environments, NLOS signal might dominate the signal if LOS component is too weak. In such cases, along with the user dynamic, Doppler biases will arise. Here, an indoor environment (kinesiology complex on the

University of Calgary campus) which has nearly no window beside the planned trajectory is shown in Figure 4.5. However, there are some windows very close to the kinesiology complex as shown in the simplified scenario. From Table 1.1, the signal attenuation of glass is much smaller than that of concrete walls; it is expected that the NLOS signal from these windows may be stronger than from elsewhere.

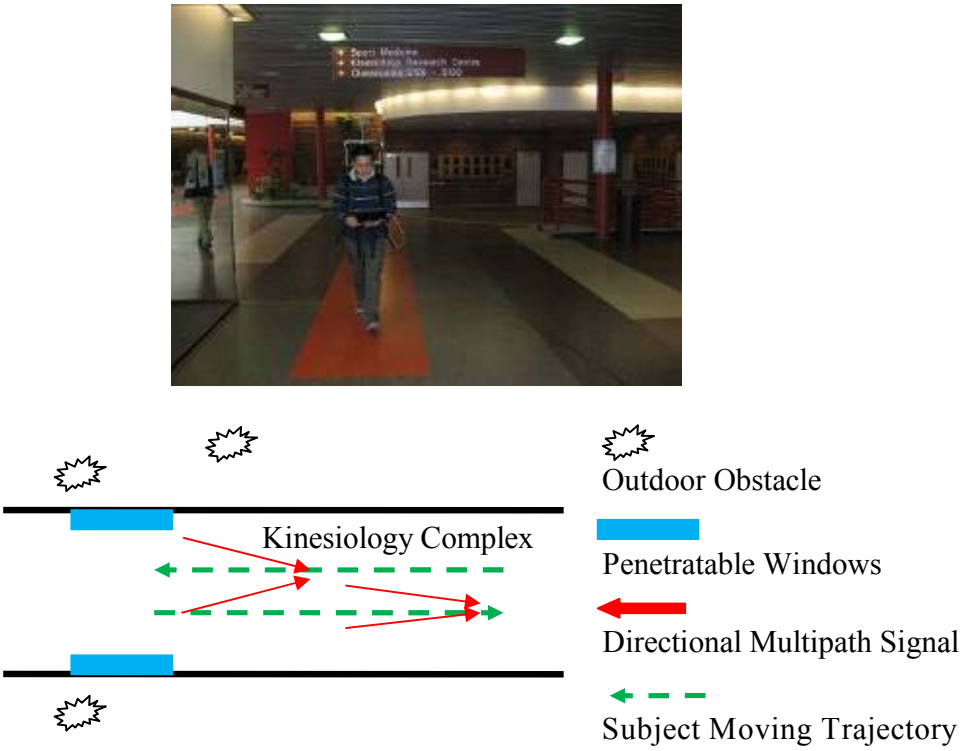

Figure 4.5: Indoor scenarios (kinesiology complex)-real and simplified

For the test, intermediate frequency (IF) samples were logged using an NI front-end (PXI-5661). In order to compute the Doppler errors in this scenario, a version of GSNRx™ was used that implements an assisted HSGNSS receiver architecture with bit aiding and external aiding (Aminian et al 2010) . Novatel SPAN CPT, SPAN SE receiver and LCI (Novatel 2010) are used for generating the reference trajectory. The results of

Doppler error characterization are based on this software with a coherent integration of 400 ms (frequency is kept constant during the integration). This is an AGPS software receiver that has a diagram similar to that shown in Figure 2.6. The external aiding here includes bit aiding, accurate satellite motion compensation and clock drift updating. User motion is uncompensated. All this is done by using an additional (static) aiding antenna outside the building and whose front-end is synchronized with that of the test receiver. As such, the effect of receiver clock drift is removed, although this does not impact results but only computational requirements, as will be shown later in Section 5.4.2.1.

The reference trajectory and sky plot are shown in Figure 4.6. The data was collected on the campus of University of Calgary. Two places including Mac Hall corridor and Kinesiology complex are marked in Figure 4.6. At the initial stage, the subject carrying the moving antenna is standing still near external aiding antenna outside. Then the user begins walking circularly to facilitate in-motion alignment of the inertial system. After that, the subject enters the indoor environment, walks back and forth several times along the direction of the corridor between the Kinesiology complex and Mac Hall before returning outside. Each indoor loop started near the middle of the length of the corridor and the user first walked towards Mac Hall, then towards Kinesiology and then returned back to the starting point.

The reference trajectory was generated by the combination of both forward and backward navigation solution generated by Inertial Explorer ^{TM} software using SPAN SE rover and LCI IMU data.

When processing the data five GPS satellites are chosen, namely PRN 7, 8, 10, 13 and 16, as shown in Figure 4.6. Each satellite has a different elevation angle and signal C/N_0. When the subject enters the kinesiology complex, the estimated C/N_0 of all satellites is in the range of 15 dB-Hz to 26 dB-Hz.

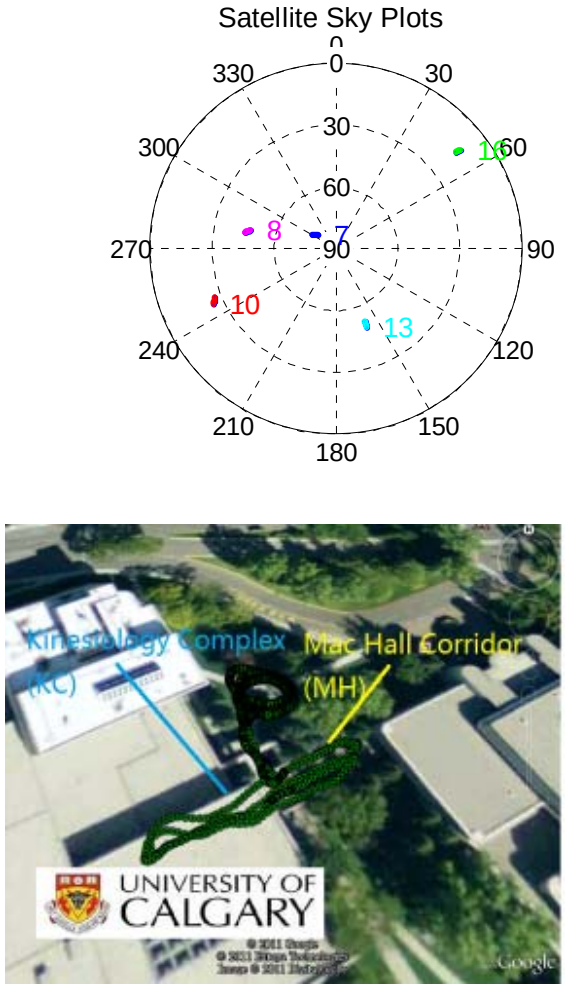

Figure 4.6: Sky plot and reference trajectory

Doppler error plots

The MLE Doppler measurement is obtained as the Doppler value associated with the maximum value of the correlator outputs. By comparing this against the true Doppler value computed from the reference solution, the Doppler errors can be computed. With this in mind, Figure 4.7 shows the Doppler errors for PRN 13. It is noted that the Doppler errors of all satellites have very similar results, thus only PRN 13 is analyzed herein without loss of generality.

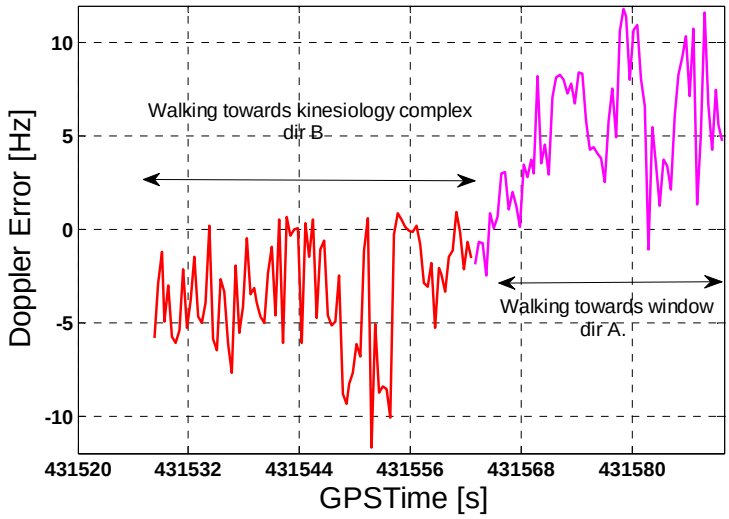

Figure 4.7: PRN 13 Doppler error plots in indoors

Figure 4.7 clearly shows that when the subject is walking towards the window (i.e., away from the Kinesiology building), this will result in a positive Doppler bias, and vice versa. This result is in accordance with Figure 4.1, which indicates that as the user walks towards the multipath source (herein assumed to be coming from the window), there will be a positive Doppler bias.

In order to validate the signal models discussed in Section 4.1, the following procedures were adopted. First, it assumed that the multipath statistics are very similar during short time intervals. In this way, the Doppler statistics over time are related with averaged multipath AOA statistics. Second, due to the fact that there is no way to jointly determine the multipath averaged azimuth, elevation angles and beamwidths, some angles have to be assumed. In the following plots, it is assumed that the averaged multipath elevation angle is 70 degrees. This assumption is based on the fact that an active antenna is used and will significantly attenuate lower elevation angle signals. With this in mind, the simulated Doppler spectral density can be calculated using equation (4.14). The measured Doppler spectral density can be also obtained by averaging the normalized carrier PSDs. These results are plotted for PRN 13 in Figure 4.8

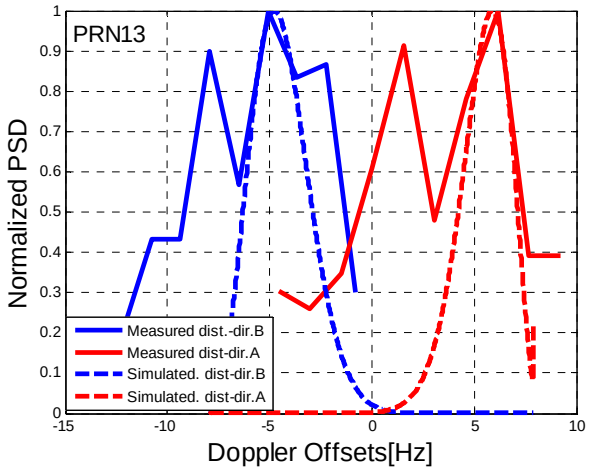

Figure 4.8: Averaged carrier PSDs (measured and simulated assuming 70°elevation angle)

In Figure 4.8, ‘dir A’ and ‘dir B’ denotes directions towards the window and kinesiology. It is observed that the Doppler measurement biases are very likely due to the existence of strong directional multipath signals. From the measured density, it can be seen that there is more than one dominant peak. This means it is highly possible that the dominant multipath signals come from more than one direction on average. This might be true since there are several windows on either side of the corridor. With the simulated density, only one dominant multipath AOA is assumed since the objective is not to exactly fit the multipath environment but to show the consistency of the models proposed with real data. In this sense, the model appears to be reasonable and will be used for assessing the receiver performance in the presence of multipath as will be shown in the next chapter.

Chapter Five: **DOPPLER AND VELOCITY ESTIMATION IN NARROWBAND MULTIPATH CHANNELS**

In this chapter, a more reliable Doppler estimation method than that discussed previously based on a direct vector-based high sensitivity receiver will be discussed and analyzed. With an indoor multipath signal model developed in the previous chapter, the performance of this receiver will be analyzed. Doppler CRLB comparisons will be made between a conventional high sensitivity receiver and a direct vector receiver. Two field test results will be shown to further validate the effectiveness of the proposed receiver architecture. In one data set, the benefits of adding GLONASS signals will be fully explored in both outdoor and indoor environments.

5.1 Direct vector high sensitivity receiver architecture

Recently, some researchers have proposed and implemented the maximum likelihood position estimate, such as Closas et al (2007), Weill (2010) and Lin et al (2011). These authors use the code phase domain correlator outputs projected into the position domain in order to obtain a position estimate. They also tend to use short coherent integration intervals. Furthermore, a large amount of non-coherent integrations are applied over data bits and between satellites in order to achieve the desirable processing gain. However, deep indoor environments such as in concrete buildings with pedestrian motion will inevitably deteriorate the code phase domain correlation shape due to strong multipath, which may lead to unacceptable results.

This thesis focuses on the Doppler dimension of the correlator outputs. The direct vector high sensitivity GNSS receiver architecture is shown in Figure 2.7.

As shown in Figure 2.6, the conventional velocity estimation method uses Doppler measurements from each tracking channel that are usually obtained by selecting the maximum peak appearing in the correlator outputs. Whenever the LOS signal strength is high, this method loses no useful information. However when a NLOS signal is present or is relatively strong, the shape of the correlator domain outputs will be distorted. The use of the conventional method can lead to a loss of useful information and give erroneous results. In contrast, as shown in Figure 2.7, it can be seen that the proposed method first projects the correlator domain output into the velocity domain, which represents how the received signal power is distributed over a specified velocity searching range. The power distribution of each channel in the velocity domain is considered as the "measurement" for that channel. The "measurements" for all channels/satellites are then summed to generate a final velocity domain power distribution. The velocity associated with the maximum power is assumed as the final estimate, which is basically the MLE of velocity.

The conventional method is a two-step estimation method, which first estimates the code delay and carrier Doppler frequency independently. These parameters are used to get the position and velocity estimates respectively. However, the MLE of velocity is a direct estimation method, which uses information from all satellites in view to jointly estimate the velocity in a single step. The joint estimate of receiver clock drift and Doppler can be expressed as (Closas et al 2007)

$$\begin{aligned}\hat{\tau}_{i,ML}, \hat{f}_{D_i,ML} &= \arg\min_{\tau_i, f_{d_i}} J_i(\tau_i, f_{D_i}), \quad i = 1,2...,M \\ &= \arg\min_{\tau_i, f_{D_i}} \{\mathbf{R}_{rr} - \mathbf{R}_{rx_i}(\tau_i, f_{D_i})\mathbf{R}^{-1}_{x_i x_i}(\tau_i, f_{D_i})\mathbf{R}^{H}_{rx_i}(\tau_i, f_{D_i})\} \\ &= \arg\max_{\tau_i, f_{D_i}} \{\mathbf{R}_{rx_i}(\tau_i, f_{D_i})\mathbf{R}^{-1}_{x_i x_i}(\tau_i, f_{D_i})\mathbf{R}^{H}_{rx_i}(\tau_i, f_{D_i})\}.\end{aligned} \tag{5.1}$$

In equation (5.1), $\hat{\tau}_{i,ML}$ is the MLE of code phase and $\hat{f}_{d_i,ML}$ is the MLE of the Doppler for the i^{th} satellite. J_i is the cost function for i^{th} satellite. R_{rx_i} denotes a matrix of complex correlation values between the received signal r and i^{th} satellite replica signal x_i. $R_{x_i x_i}$ is a correlation matrix of size $N \times N$ between the replica signal themselves. Throughout the thesis, emphasis is given to the Doppler estimate only. Code phase estimates are therefore ignored.

The Doppler of each satellite has the following linear relationship with the receiver's velocity components:

$$f_{D_i}(\mathbf{v}) = \frac{1}{\lambda}(\mathbf{v} - \mathbf{v}_{sat\_i}) \cdot \mathbf{u}_i - \frac{1}{\lambda} c\dot{dt}, \quad i = 1,2...,M \tag{5.2}$$

In equation (5.2) $\mathbf{v}$ is the user velocity, $\mathbf{v}_{sat\_i}$ is the ith satellite velocity, $\mathbf{u}_i$ is the unit vector from the ith satellite to the user, and $c\dot{dt}$ is the clock drift term. Due to the invariance principle of MLE (Kay 1993a), the MLE of velocity can thus be expressed as

$$\hat{\mathbf{v}}_{ML} = \arg\max_{\mathbf{v}} \sum_{i=1}^{M} \{\mathbf{R}_{rx_i}(\mathbf{v})\mathbf{R}^{-1}_{x_i x_i}(\mathbf{v})\mathbf{R}^{H}_{rx_i}(\mathbf{v})\}. \tag{5.3}$$

Equation (5.3) mathematically describes how the velocity power distribution is formed. It is equivalent with the position domain projection introduced by Weill (2010). The summation represents the non-coherent integration between different satellites. This summation will result in additional processing gain in a non-coherent sense. On the other

hand, this summation also implies a weighting between satellites, which is based on the received signal power distribution over the velocity search range, as will be shown in the following sections.

5.2 Analysis on probability of outliers

In the previous section, implementation of the direct vector receiver was introduced and the potential benefits in terms of reliable estimation are now discussed.

As discussed in Chapter 4, the Doppler can be estimated using the DFT of the post correlation outputs. For example, consider the single channel Doppler estimation by using post correlation DFTs. If the partial coherent integration length is N_p and L such correlation outputs are processed by DFT in order to get the frequency estimation errors, the post correlation samples have the following form:

$$\begin{aligned} y[l] &= s[l] + \eta[l] \\ &= b\exp(j\pi\Delta f_D l T_p + j\theta_0) + \eta(lT_p), \quad l = 0,1,...,L-1 \end{aligned} \tag{5.4}$$

In equation (5.4), $\eta[l]$ is the complex additive white Gaussian noise with variance $\frac{N_0}{2T_p}$.

Assuming that the frequency error is in the bin with the index l_0, then it indicates that $\frac{\Delta f_D}{2} \approx \frac{l_0}{LT_p}$. The term b includes the frequency error induced sinc function loss, and can be strictly expressed as $\sqrt{2C}R_{xx}(\Delta\tau)\sin c(\pi\Delta f_k T_{Coh})$.

Computing the DFT of both sides of equation (5.4) gives

$$
\begin{aligned}
Y_k &= \frac{1}{L}\sum_{l=0}^{L-1} y[l]e^{-j2\pi lk/L}, \quad k = 0,1,...,L-1 \\
S_k &= \frac{1}{L}\sum_{l=0}^{L-1} s[l]e^{-j2\pi lk/L}, N_k = \frac{1}{L}\sum_{l=0}^{L-1} \eta[l]e^{-j2\pi lk/L}
\end{aligned}
\tag{5.5}
$$

The DFT of the signal component could be further expressed as

$$
\begin{aligned}
S_k &= \frac{1}{L}\sum_{l=0}^{L-1} b\exp(j2\pi\frac{ll_0}{L} + j\theta_0)\exp(-j2\pi\frac{lk}{L}) \\
&= \frac{b\exp(j\theta_0)}{L}\sum_{l=0}^{L-1}\exp(j2\pi\frac{l(l_0-k)}{L}) \\
&= \frac{b\exp(j\theta_0)}{L}\delta_{kl_0}
\end{aligned}
\tag{5.6}
$$

And the DFT of the noise components can be proven to be independent zero mean complex Gaussian random variables with variance $\frac{N_0}{2T_pL}$.

Recalling that the power of the DFT outputs are used for the Doppler estimation we can write

$$
Z_k = |Y_k|^2, \quad k = 0,1,...,L-1 \tag{5.7}
$$

Then Z_k are random variables with different distributions for different indices. If $k = l_0$, it will be noncentral chi-square distributed with $\lambda = b$, otherwise it will be exponentially distributed as shown in (5.8) (Kay 1993b):

$$
\begin{aligned}
&k \neq l_0, Z_k \sim \exp(\frac{T_pL}{N_0}), f_{Z_k|H_0}(z_k \mid H_0) = \frac{T_pL}{N_0}e^{-\frac{T_pL}{N_0}z_k} \\
&k = l_0, Z_k \sim \chi^2_{nc}(b, \frac{N_0}{2T_pL}), f_{Z_k|H_1}(z_k \mid H_1) = \frac{1}{2\frac{N_0}{2T_pL}}e^{-(b^2+x)/(\frac{N_0}{T_pL})} I_0(\frac{\sqrt{x}b}{\frac{N_0}{2T_pL}})
\end{aligned}
\tag{5.8}
$$

In equation (5.8), H_0 implies that no signal present or $k \neq l_0$, while H_1 denotes $k = l_0$. In this way, the probability of a correct estimation will be

$$\begin{aligned} \Pr_{correct} &= \Pr(\text{all } z_{k|H_0} \leq z_{k|H_1}) \\ &= \int \Pr(\text{all } z_{k|H_0} \leq z_{k|H_1} \mid z_{k|H_1} = x) \Pr(z_{k|H_1} = x) dx \\ &= \int_0^{\infty} \left[\int_0^{x} f_{Z_{k|H_0}}(y) dy \right]^{L-1} f_{Z_{k|H_1}}(x) dx \end{aligned} \tag{5.9}$$

The probability of Doppler outliers can be defined as

$$\Pr_{outliner} = 1 - \Pr_{correct} \tag{5.10}$$

When it comes to the direct vector receiver, there is additional non-coherent integration among all the satellites. All the correlation power is projected onto the velocity domain. By extension, the Doppler can be calculated by using the assumed velocities. This indicates that the probability of Doppler outliers equals the probability of velocity outliers in direct vector receivers. In such cases, the DFT outputs used for Doppler or velocity estimation are

$$Z_k = \sum_{i=1}^{M} \left| Y_{k,i} \right|^2, \quad k = 0, 1, ..., L-1 \tag{5.11}$$

Accordingly, with M satellite signals processed jointly, the test statistics Z_k has the following distribution (Proakis 2001):

$$\begin{aligned} &k \neq l_0, Z_k \sim \chi_c^2\left(\frac{N_0}{2T_pL}, 2M\right), f_{Z_{k|H_0}}(z_{k|H_0}) = \frac{1}{\left(\frac{N_0}{T_pL}\right)^{\frac{M}{2}} \Gamma(M)} z_{k|H_0}^{M-1} e^{-z_{k|H_0}/\left(\frac{N_0}{T_pL}\right)} \\ &k = l_0, Z_k \sim \chi_{nc}^2\left(b, \frac{N_0}{2T_pL}, 2M\right), f_{Z_{k|H_1}}(z_{k|H_1}) = \frac{1}{2\frac{N_0}{2T_pL}} \left(\frac{z_{k|H_1}}{b}\right)^{(M-1)/2} e^{-(b^2+x)/\left(\frac{N_0}{T_pL}\right)} I_{M-1}\left(\frac{\sqrt{x}b}{\frac{N_0}{2T_pL}}\right) \end{aligned} \tag{5.12}$$

By using equations (5.8), (5.9), (5.10) and (5.12), one can then evaluate the probability of Doppler outliers for conventional and direct vector receivers.

For simplicity, signals from all satellites are assumed equally attenuated and the probabilities of outliers are shown in Figure 5.1.

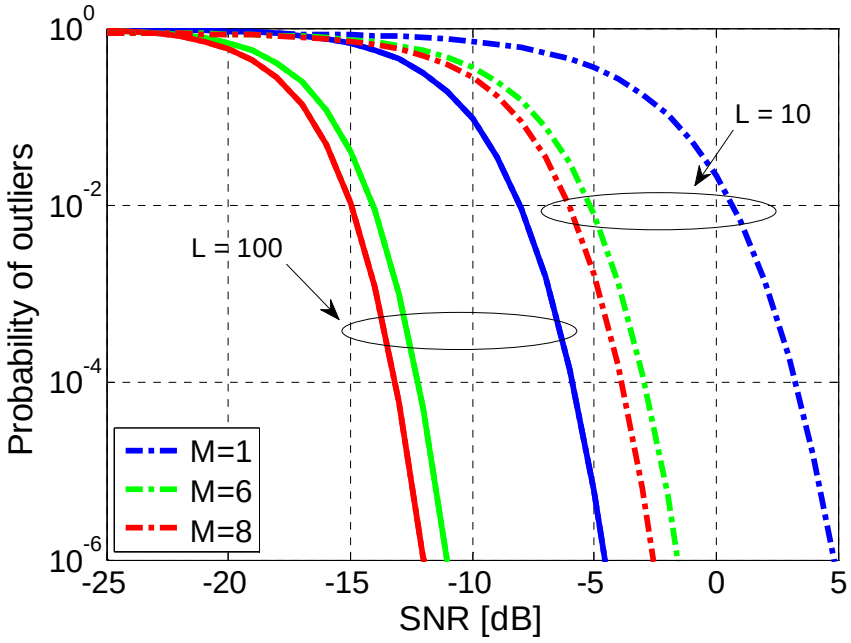

Figure 5.1: Probability of outliers (direct vector receiver vs. conventional high sensitivity receiver)

In Figure 5.1, M denotes the number of the satellites used for a direct vector receiver. When $M = 1$, it represents a conventional high sensitivity receiver. Since L denotes the number of partial coherent integrations, the larger L is, the longer the total coherent integration it is. As it is shown, either increasing coherent integration time or using more non-coherent integrations by having more satellites will lead to a more reliable estimate. The direct vector receiver can take advantage of both methods. For example, given an

outlier probability of 10^{-4}, a direct vector receiver with six satellites will introduce about 6-8 dB gain relative to a conventional high sensitivity receiver. This improvement will be much more apparent when some satellite signals are more severely attenuated than others, which is the case when a receiver has partial LOS signal visibility.

In this section, the benefits of direct vector receiver for reliable estimation were discussed; the next section, how the satellite geometry contributes to a direct vector receiver estimation accuracy will further be investigated.

5.3 Analysis on CRLB of Doppler and velocity estimation

As discussed in Chapter 4, the CRLB of the Doppler frequency in AWGN with conventional receiver has the form

$$CRLB(\hat{f}_D)_{AWGN} = \frac{12}{(2\pi T_s)^2 (2C/N_0 T_s) N(N^2-1)} \tag{5.13}$$

where $a = \sqrt{2C}$, and C is the total signal carrier power. As discussed in the previous section, in indoor environments the received signal power is usually composed of two parts, i.e., the LOS component, and the NLOS component. Thus, the received signal is

$$s_\theta[n] = s_{LOS}[n] + s_{NLOS}[n] \tag{5.14}$$

where $s_{LOS}[n]$ is the LOS component which equals $a\sqrt{\frac{K}{K+1}}x(nT_s-\tau)e^{j2\pi f_D nT_s}$, and $s_{NLOS}[n]$ is the NLOS component that equals $a\sqrt{\frac{1}{K+1}}x(nT_s-\tau)e^{j2\pi f_D \frac{\cos\alpha_m \cos\varepsilon_m}{\cos\alpha\cos\varepsilon} nT_s}$. α_m and ε_m represent the multipath averaged azimuth and elevation angles. They are random

variables, which have distributions of f_{α_m}, f_{ε_m} and with valid range of $[\alpha_{\min}, \alpha_{\max}]$, and $[\varepsilon_{\min}, \varepsilon_{\max}]$ respectively. The Fisher information matrix is then computed and averaged over the multipath AOAs:

$$I_{f_d, f_d} = \frac{1}{2} E_{\alpha_m, \varepsilon_m} \left[\frac{2T_s}{N_0} \sum_{n=0}^{N-1} \left(\frac{\partial s_\theta[n]}{\partial f_D} \right)^* \frac{\partial s_\theta[n]}{\partial f_D} \right] \tag{5.15}$$

In equation (5.15), the cross terms are relatively smaller when the integration time is long and thus are neglected. The scale $1/2$ is due to the low pass equivalent representation and complex correlation used in this thesis, as discussed in Section 3.1. The CRLB of the Doppler estimated in multipath environments can be easily expressed as follows:

$$\begin{aligned} CRLB(\hat{f}_D)_{MP} &= \frac{12}{(2\pi T_s)^2 (2C/N_0 T_s) N(N^2-1)} \gamma_{MP} \\ \gamma_{MP} &= \left\{ \frac{K}{K+1} + \frac{1}{K+1} \frac{\int \cos\alpha_m^2 f_{\alpha_m} d\alpha_m \int \cos\varepsilon_m^2 f_{\varepsilon_m} d\varepsilon_m}{\cos^2\alpha \cos^2\varepsilon} \right\}^{-1} \end{aligned} \tag{5.16}$$

In equation (5.16), it is seen that the CRLB of Doppler in indoor multipath environments is further related with a factor γ_{MP}, which represents multipath degradation. It is shown that this term indicates multipath degradation and is determined by the multipath statistics, and called the "multipath degradation factor". The CRLB of the Doppler in indoor multipath environments is thus affected not only by the SNR, but is also related to the multipath statistics, as should be intuitively expected.

In the scalar receiver, the velocity computed by using the Doppler measurements, and there is a linear relationship between a Doppler measurement and the user velocity, which has been described in Chapter 2. In order to get the CRLB of the velocity in multipath

environments, this linear relationship between velocity and Doppler could be used. This is actually the conventional navigation solution process. Assuming there are M satellites in view, the following relationship holds:

$$f_{D,i} = h_{E,i}v_E + h_{N,i}v_N + h_{U,i}v_U + h_{clkDrift,i}c\dot{dt} = \mathbf{h}_i^T\mathbf{v}$$

$$\mathbf{f}_D = [\mathbf{h}_E, \mathbf{h}_N, \mathbf{h}_U, \mathbf{h}_{clkDrift}]\begin{bmatrix} v_E \\ v_N \\ v_U \\ c\dot{dt} \end{bmatrix} = \mathbf{H}\mathbf{v}, \quad or\ \hat{\mathbf{v}} = (\mathbf{H}^T\mathbf{H})^{-1}\mathbf{H}^T\mathbf{f}_D \tag{5.17}$$

where the term $\mathbf{h}_E$ is the vector $\left[h_{E,1}, h_{E,2}, ..., h_{E,M}\right]^T$ which is the first column of the design matrix $\mathbf{H}$. From this relationship, the CRLB of the velocity in multipath environments with a scalar receiver structure can be shown as follows:

$$CRLB(\hat{\mathbf{v}})_{conv} = (\mathbf{H}^T\mathbf{H})^{-1}\mathbf{H}^T CRLB(\hat{\mathbf{f}}_D)_{MP}\mathbf{H}(\mathbf{H}^T\mathbf{H})^{-1} \tag{5.18}$$

The expression $CRLB(\hat{\mathbf{f}}_D)_{MP}$ denotes a diagonal matrix with the i^{th} element of $CRLB(\hat{f}_{d,i})_{MP}$, and similar expression applies for $CRLB(\hat{\mathbf{v}})_{conv}$.

In order to gain some insight into the velocity CRLB, only the east velocity is analyzed in detail. The analysis procedure can be easily applied to other axes. Equation (5.16) shows that the CRLB of Doppler measurements for each satellite is related to the C/N_0 and multipath statistics. By using the geometry dependent factor derived in Chapter 3, a simpler form of east velocity could be shown as

$$CRLB(\hat{v}_E)_{Conv} = CRLB(\hat{f}_{D,i})_{MP,avg}\frac{\lambda_E^2}{\sum_{i=1}^{M} h_{E,i}^2} \tag{5.19}$$

where $CRLB(\hat{f}_{d,i})_{MP,avg}$ is the Doppler CRLB averaged across all satellites, which is only an approximation. Also, λ_E is the geometry dependent factor in the east direction without any weighting, which is proportional to the east dilution of precision (EDOP), as shown in equation(A.40). Detailed treatment of the subject can be found in Appendix A. When it comes to the vector receiver, it processes all satellites jointly, and the signal model is then modified as

$$s_\theta[n] = \sum_{i=1}^{M} s_{LOS,i}[n] + s_{NLOS,i}[n] \tag{5.20}$$

where $s_{LOS,i}[n]$ and $s_{NLOS,i}[n]$ represent the LOS and NLOS components for i^{th} satellite accordingly. The FIM elements of all velocities can be expressed as

$$\begin{aligned}
I_{v_E,v_E} &= \frac{1}{2} E_{\alpha_m,\varepsilon_m}\left[\frac{2T_s}{N_0}\sum_{n=0}^{N-1}\left(\frac{\partial s_\theta[n]}{\partial f_D}\frac{\partial f_D}{\partial v_E}\right)^* \frac{\partial s_\theta[n]}{\partial f_D}\frac{\partial f_D}{\partial v_E}\right] \\
&= \sum_{i=1}^{M} E_{\alpha_m,\varepsilon_m}\left[\frac{2T_s}{N_0}\sum_{n=0}^{N-1}\left(\frac{\partial s_\theta[n]}{\partial f_D}\right)^* \frac{\partial s_\theta[n]}{\partial f_D}\right] h_{E,i}^2 \\
&= \sum_{i=1}^{M} \frac{1}{CRLB(\hat{f}_{D,i})_{MP}} h_{E,i}^2 \\
I_{v_N,v_N} &= \sum_{i=1}^{M} \frac{1}{CRLB(\hat{f}_{D,i})_{MP}} h_{N,i}^2 \\
I_{v_U,v_U} &= \sum_{i=1}^{M} \frac{1}{CRLB(\hat{f}_{D,i})_{MP}} h_{U,i}^2 \\
I_{c\dot{d}t,c\dot{d}t} &= \sum_{i=1}^{M} \frac{1}{CRLB(\hat{f}_{D,i})_{MP}} h_{clkDrift,i}^2
\end{aligned} \tag{5.21}$$

Then the vector receiver's east velocity CRLB can be expressed as

$$CRLB(\hat{v}_E)_{Dir} = (\mathbf{I})^{-1}_{v_E v_E} = \frac{\lambda^2_{E,weighted}}{\sum_{i=1}^{M} \frac{1}{CRLB(\hat{f}_{d,i})_{MP}} h^2_{E,i}} = \left\{ (\mathbf{H}^T CRLB(\hat{\mathbf{f}}_D)^{-1}_{MP} \mathbf{H})^{-1} \right\}_{v_E v_E} \tag{5.22}$$

In equation (5.22), $\lambda_{E,weighted}$ is the geometry dependent factor with a weighted design matrix (He et al 2012b).

In order to compare the CRLB of the scalar and vector receiver velocity solutions, the ratio between them can be computed as

$$\frac{CRLB(\hat{v}_E)_{Dir}}{CRLB(\hat{v}_E)_{Conv}} = \frac{\frac{\lambda^2_{E,weighted}}{\sum_{i=1}^{M} \frac{1}{CRLB(\hat{f}_{D,i})_{MP}} h^2_{E,i}}}{CRLB(\hat{f}_{D,i})_{MP,avg} \frac{\lambda^2_E}{\sum_{i=1}^{M} h^2_{E,i}}} = \frac{\lambda^2_{E,weighted}}{\lambda^2_E} \bullet \frac{\sum_{i=1}^{M} h^2_{E,i}}{\sum_{i=1}^{M} \frac{1}{CRLB(\hat{f}_{D,i})_{MP}} h^2_{E,i}}}{CRLB(\hat{f}_{D,i})_{MP,avg}} \tag{5.23}$$

In equation (5.23), it can be seen that the ratio between vector and scalar solution can be decomposed into two parts. The first part is the ratio between geometry dependent factors ($\left(\frac{\lambda_{E,weighted}}{\lambda_E} \right)^2$), which relies on the satellite geometry and weights. Generally, this ratio would be smaller than one, but occasionally it will exceed one. The second component is the ratio between CRLB values. The numerator can be considered as the weighted harmonic mean of the Doppler CRLB, while the denominator is the averaged Doppler CRLB for the conventional method. Since it is known that the harmonic mean is no larger than the arithmetic mean, the second term is smaller than one. If the Doppler CRLBs for

all satellites are exactly the same, then both components will be one, which means that the performances of the conventional and direct vector methods are the same.

It is also noted that the direct vector receiver architecture automatically weighs the Doppler according to its CRLB. Whenever one has a perfect knowledge of the multipath channel statistics and signal C/N_0, the weighted scalar receiver will have exactly the same performance as the direct vector receiver. However, it is generally very hard to get accurate information of multipath statistics and signal C/N_0 in weak signal conditions. At this point, the direct vector receiver would outperform the conventional high sensitivity receivers. It should be noted that whenever all the received satellite signals are entirely dominated by multipath or noise, then neither direct vector HSGNSS nor conventional HSGNSS will give better results. In addition, it is not possible to quantify a percentage value of improvement for all indoor scenarios and/or operational scenarios. In the following, it can be seen that such improvements is environment dependent and rely on satellite geometry. Both factors are case-specific and no general assumptions can be made.

Having discussed the velocity accuracies, it is natural to move to compare the Doppler estimation accuracy of a direct vector receiver with a conventional scalar receiver. Before analyzing the Doppler CRLBs, it is noted that the conventional scalar receiver estimates the pseudoranges and Doppler independently for all satellites, while the vector receiver first jointly processes the incoming signal to a direct position or velocity solution, and then uses this position and velocity solution to calculate the corresponding pseudorange and Doppler measurements for each satellite.

As shown in equation (5.16), the conventional Doppler MLE has a bound that is further related with SNR, the integration time, Ricean factor, and multipath AOAs. In equation (5.24), the Doppler CRLBs of the direct vector receiver are also given in order to justify the improvement by using this method.

If there are M satellites in view that are jointly processed in direct vector receiver, the Doppler frequency for the j^{th} satellite can be obtained by using the relationship showed in equation (5.17). After some manipulations, one can show that the Doppler CRLBs of a direct vector receiver for the j^{th} satellite are

$$CRLB(f_{D,j})_{vector,MP} = \frac{\lambda_{E,weighted}^2 h_{E,j}^2}{\sum_{i=1}^{M} \frac{1}{CRLB(\hat{f}_{D,i})_{scalar,MP}} h_{E,i}^2} + \frac{\lambda_{N,weighted}^2 h_{N,j}^2}{\sum_{i=1}^{M} \frac{1}{CRLB(\hat{f}_{D,i})_{scalar,MP}} h_{N,i}^2} + \frac{\lambda_{U,weighted}^2 h_{U,j}^2}{\sum_{i=1}^{M} \frac{1}{CRLB(\hat{f}_{D,i})_{scalar,MP}} h_{U,i}^2} + \frac{\lambda_{Clk,weighted}^2 h_{clkDrift,j}^2}{\sum_{i=1}^{M} \frac{1}{CRLB(\hat{f}_{D,i})_{scalar,MP}} h_{clkDrif,i}^2}$$

$$\begin{aligned} CRLB(f_{D,j})_{vector,MP} = {} & h_{E,j}^2 CRLB(\hat{\mathbf{f}}_{\mathbf{D}})_{scalar,MP,E-harmonic\,mean} \frac{\lambda_{E,weighted}^2}{\sum_{i=1}^{M} h_{E,i}^2} \\ & + h_{N,j}^2 CRLB(\hat{\mathbf{f}}_{\mathbf{D}})_{scalar,MP,N-harmonic\,mean} \frac{\lambda_{N,weighted}^2}{\sum_{i=1}^{M} h_{N,i}^2} \\ & + h_{U,j}^2 CRLB(\hat{\mathbf{f}}_{\mathbf{D}})_{scalar,MP,U-harmonic\,mean} \frac{\lambda_{U,weighted}^2}{\sum_{i=1}^{M} h_{U,i}^2} \\ & + h_{ClkDrift,j}^2 CRLB(\hat{\mathbf{f}}_{\mathbf{D}})_{scalar,MP,ClkDrift-harmonic\,mean} \frac{\lambda_{Clk,weighted}^2}{\sum_{i=1}^{M} h_{ClkDrift,i}^2} \end{aligned} \tag{5.24}$$

$$
\begin{aligned}
CRLB(f_{D,j})_{vector,MP} = & CRLB(\hat{\mathbf{f}}_{\mathbf{D}})_{scalar,MP,E-harmonic\,mean}\,\chi_{E,j} \\
& + CRLB(\hat{\mathbf{f}}_{\mathbf{D}})_{scalar,MP,N-harmonic\,mean}\,\chi_{N,j} \\
& + CRLB(\hat{\mathbf{f}}_{\mathbf{D}})_{scalar,MP,U-harmonic\,mean}\,\chi_{U,j} \\
& + CRLB(\hat{\mathbf{f}}_{\mathbf{D}})_{scalar,MP,ClkDrift-harmonic\,mean}\,\chi_{T,j}
\end{aligned}
$$

where $CRLB(\hat{\mathbf{f}}_{\mathbf{D}})_{scalar,MP,E-harmonic\,mean}$ denotes weighted harmonic mean over the east velocity direction based on the satellite geometry. The subscripts $N, U, ClkDrift$ represent the north, vertical, and clock drift direction. $\chi_{E,j}$, $\chi_{N,j}$, $\chi_{U,j}$ and $\chi_{T,j}$ represent the j^{th} satellite contribution of the geometry dependent factors on east, north, up and clock drift directions. They are expressed as follows, where terms decrease as the number of available satellites increases:

$$
\begin{aligned}
\chi_{E,j} &= h_{E,j}^2 \frac{\lambda_{E,weighted}^2}{\lambda_E^2} EDOP^2 = \lambda_{E,weighted}^2 \frac{h_{E,j}^2}{\sum_{i=1}^{M} h_{E,i}^2} \\
\chi_{N,j} &= h_{N,j}^2 \frac{\lambda_{N,weighted}^2}{\lambda_N^2} NDOP^2 = \lambda_{N,weighted}^2 \frac{h_{N,j}^2}{\sum_{i=1}^{M} h_{N,i}^2} \\
\chi_{U,j} &= h_{U,j}^2 \frac{\lambda_{U,weighted}^2}{\lambda_U^2} UDOP^2 = \lambda_{U,weighted}^2 \frac{h_{U,j}^2}{\sum_{i=1}^{M} h_{U,i}^2} \\
\chi_{T,j} &= h_{ClkDrift,j}^2 \frac{\lambda_{Clk,weighted}^2}{\lambda_{Clk}^2} TDOP^2 = \lambda_{Clk,weighted}^2 \frac{h_{ClkDrift,j}^2}{\sum_{i=1}^{M} h_{ClkDrift,i}^2}
\end{aligned}
\tag{5.25}
$$

Then the ratio between the Doppler CRLB of a conventional scalar receiver and a direct vector receiver can be expressed as

$$
\begin{aligned}
\frac{CRLB(\hat{f}_{D,j})_{vector,MP}}{CRLB(\hat{f}_{D,j})_{scalar,MP}} = & \frac{CRLB(\hat{\mathbf{f}}_{\mathbf{D}})_{scalar,MP,E-harmonic\,mean}}{CRLB(\hat{f}_{D,j})_{scalar,MP}}\chi_{E,j} + \frac{CRLB(\hat{\mathbf{f}}_{\mathbf{D}})_{scalar,MP,N-harmonic\,mean}}{CRLB(\hat{f}_{D,j})_{scalar,MP}}\chi_{N,j} + \\
& \frac{CRLB(\hat{\mathbf{f}}_{\mathbf{D}})_{scalar,MP,U-harmonic\,mean}}{CRLB(\hat{f}_{D,j})_{scalar,MP}}\chi_{U,j} + \frac{CRLB(\hat{\mathbf{f}}_{\mathbf{D}})_{scalar,MP,ClkDrift-harmonic\,mean}}{CRLB(\hat{f}_{D,j})_{scalar,MP}}\chi_{T,j}
\end{aligned}
\tag{5.26}
$$

Equation (5.26) shows the benefits brought by the direction vector receiver for Doppler frequency estimation. If the multipath effects of the j^{th} satellite are more significant than all those of other satellites, the harmonic mean of the Doppler CRLB of all satellites in east, north, vertical and clock drift directions will all be much smaller than $CRLB(\hat{f}_{D,j})_{scalar,MP}$, thus the ratios between them will be much smaller than one. These ratios will then be scaled by their contributions to the geometry dependent factors. It can be seen that the whole geometry has been used to give a Doppler estimate and the mutual information between satellites has been fully utilized.

From equation (5.26), it is simple get a loose bound for the ratio between the Doppler CRLB of the direct vector and conventional scalar receivers, as follows:

$$\frac{CRLB(\hat{f}_{D,j})_{vector,MP}}{CRLB(\hat{f}_{D,j})_{scalar,MP}} \leq \frac{CRLB(\hat{\mathbf{f}}_{\mathbf{D}})_{scalar,MP,arithmetic\ mean}}{CRLB(\hat{f}_{D,j})_{scalar,MP}}(\chi_{E,j}+\chi_{N,j}+\chi_{U,j}+\chi_{T,j}) \qquad (5.27)$$

where $CRLB(\hat{\mathbf{f}}_{\mathbf{D}})_{scalar,MP,arithmetic\ mean}$ is the arithmetic mean of the Doppler CRLB for all satellites in the multipath environment. The term $\frac{CRLB(\hat{f}_{D,j})_{scalar,MP}}{CRLB(\hat{\mathbf{f}}_{\mathbf{D}})_{scalar,MP,arithmetic\ mean}}$ denotes the j^{th} *satellite's CRLB weight*, while the term $(\chi_{E,j}+\chi_{N,j}+\chi_{U,j}+\chi_{T,j})$ denotes the j^{th} satellite's geometry dependent factor weight. Then if the j^{th} satellite's CRLB weight is much larger than its geometry dependent factor weight, there will be a significant improvement in the Doppler estimation with the proposed direct vector receiver. Otherwise, there will be some degradation in term of estimation accuracy.

In indoor environments, it is quite common that some satellites are experiencing much more multipath effects than other satellites. However, with more GNSS satellite signals processed such as GLONASS and other systems, it will no doubt decrease the satellite's geometry dependent factor weight. In this sense, the proposed method will further benefit the Doppler estimation for satellites under severe signal distortion.

5.4 Field test results and analysis

To assess the algorithm developed in the previous sections, three data sets were collected in various concrete buildings on the campus of the University of Calgary. The first data set was collected on the first floor of the engineering block. Both GPS and GLONASS L1 signals were collected in order to assess the performance of direct velocity estimation, and the benefits brought by the GLONASS. The second data set was collected inside the MacEwan Student Centre.

The primary pieces of equipment used for the data collection were an NI front-end, and a NovAtel SPAN receiver with a LCI IMU (NovAtel 2010) to provide reference measurements and trajectory. Only one moving antenna is used as shown in Figure 5.2, and a splitter is used to connect it and the NI front-end and to a Novatel SPAN receiver. The raw IF data was collected with the NI front-end at sampling frequencies of 10 MHz/12.5MHz/5MHz as complex samples. Figure 5.2 shows the GPS/GLONASS antenna, and inertial sensors used in the test. It should be noted that this picture was taken outdoors, but the data collection includes outdoor and indoor periods. Figure 5.3 shows the NI front-end used for IF data logging. Both an on-board low-noise amplifier (LNA)

and external LNA were used simultaneously in order to compensate part of the cable power loss.

Figure 5.2: Data collection equipment in the backpack

Figure 5.3: IF data and NI configuration

The term ‘conventional’ in the following denotes the standard HSGNSS processing methodology, which uses a block processing strategy to get the Doppler measurements and then least squares to compute the receiver velocity. The term ‘direct’ represents the algorithm discussed in this chapter wherein the velocity is estimated directly from the signals themselves. Once the velocity solutions of the conventional and direct methods are obtained, the errors can be computed through comparison with the reference solutions from the Novatel SPAN^{TM} system, which uses a high precision GNSS receiver that is not designed to operate in weak signal conditions and thus independent from the HSGNSS discussed herein. During weak signal periods, such a reference solution is purely based on the tactical grade IMU prediction. In order to maintain acceptable accuracy, the subject carrying the equipment walked outside of the building every few minutes in order to obtain GNSS measurements to update the IMU.

The objective of the field test was to investigate the effectiveness of direct velocity estimation algorithm. For the first data set, both GPS and GLONASS L1 signals were collected, and analyzed. For the second test, only GPS L1 signals were logged.

5.4.1 Engineering block

The reference trajectory of this data set is shown in Figure 5.4 and details on how this was obtained are included below. The pedestrian carried a backpack that included an antenna, the NovAtel SPAN system and a cable connected to the NI front-end (as shown in Figure 5.2). First, the pedestrian walked several circles outside the building for alignment of the INS. Then, the subject repeated a mostly north-south path inside the

building three times and then walked outside again. Finally, the subject repeated the circular motion under open sky in order to facilitate backward processing of the data. The reference trajectory was generated using the NovAtel Inertial Explorer™ software. The estimated 1-sigma standard deviation of position was better than 0.5 m and those for east, north and up velocity were better than 0.009 m/s, 0.008 m/s and 0.007 m/s, respectively; these values are generated by combining forward and reverse smoothed results. Figure 5.4 also shows the sky-plot during the data collection. Five GPS satellites and three GLONASS satellites were in view during the period. The total time data length is about 15 min and the indoor period lasted about 2-3 min.

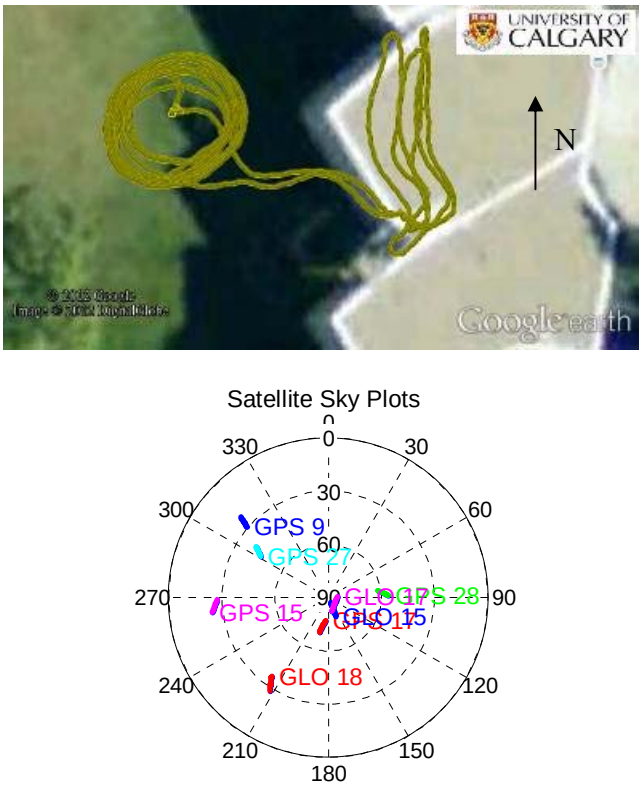

Figure 5.4: Reference trajectory and sky plot for engineering block test

Figure 5.5 shows the C/N_0 profiles for each satellite signal for the entire data set. It can be seen that for the first 900 epochs (one epoch is 0.5 s), the C/N_0 values are all within 40 to 50 dB-Hz, which is typical of open sky scenarios. Between epoch 900 and 1200 epochs, all C/N_0 values drop to 10 or 20 dB-Hz and begin to fluctuate significantly. This is the period when the pedestrian is walking inside the concrete building. Finally, from epoch 1200 to the end, the C/N_0 values return to the nominal open sky values, and do not fluctuate because the pedestrian has returned outdoor. The indoor scenario for this data set is illustrated in Figure 5.6. As shown in the figure, it is nearly entirely obscured from the sky except for some windows on one side of the building.

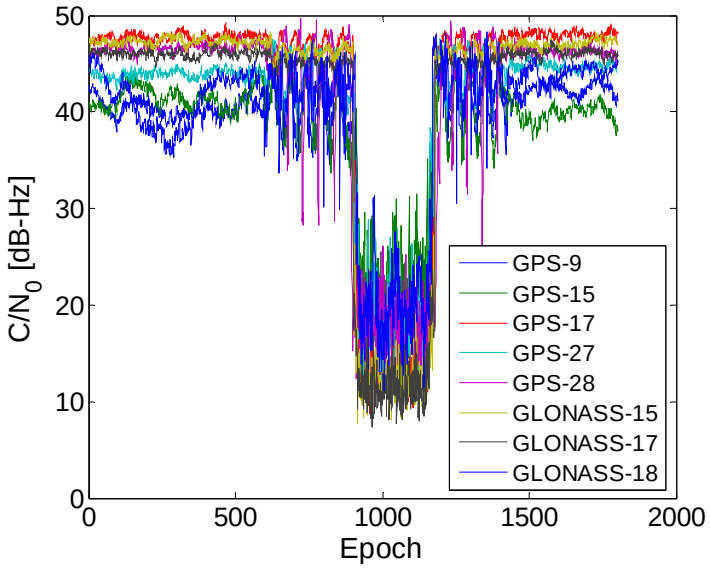

Figure 5.5: C/N_0 profiles-engineering block (one epoch is 0.5 s)

Figure 5.6: Pictures of engineering scenario facing north-west

The raw IF data was processed using a version of GSNRx™ that implements an assisted HSGNSS receiver architecture with bit aiding and external aiding was used (O'Driscoll et al 2011) to obtain the raw correlator outputs and conventional HSGNSS Doppler measurements. This version of GSNRx™ is slightly different from that used in Chapter 4 in that the aiding information does not compensate for the effect of the receiver clock error. HSGNSS receiver differences are discussed in Section 2.1.3 and 2.1.4. Results obtained without any external aiding but still operating in direct vector mode (i.e., as would be the case for a standalone HSGNSS receiver) will be further analyzed using the next data set (Section 5.4.2.1), which validates that the external aiding information does not affect the results discussed herein.

At each measurement epoch, nominal pseudorange and Doppler values for each satellite in view are computed and passed to the signal processing channels. Each channel then

computes grids of correlators around the nominal code phase and Doppler values. Finally, the maximum peaks are used to generate pseudorange and Doppler measurements.

In this thesis, a coherent integration of 500 ms is used in order to obtain raw correlator outputs. With this coherent integration time, it is expected that a desirable pre-detection SNR can be obtained. The velocity domain powers are computed using equations (5.1) and(5.3).

First, how the single epoch signal power is distributed in the velocity domains are shown with outdoor environments. In such a case, the channel distortions brought by the multipath signals can almost be neglected. After that, how the power is distributed over velocity domains in the indoor multipath environments will also be given, in order to illustrate the distortion brought by multipath signals.

Figure 5.7 is one example of how the total power is distributed over the velocity domain under open sky conditions (epoch 30). At this epoch, there were 17 bins considered for the velocity offset, each separated by 0.15 m/s. The centre of the bins is the 0 m/s point, which aligns with the reference velocity computed from the reference trajectory. The offset that is associated with the largest power is assumed as the estimator output errors (since zero offset is aligned with the reference velocity).

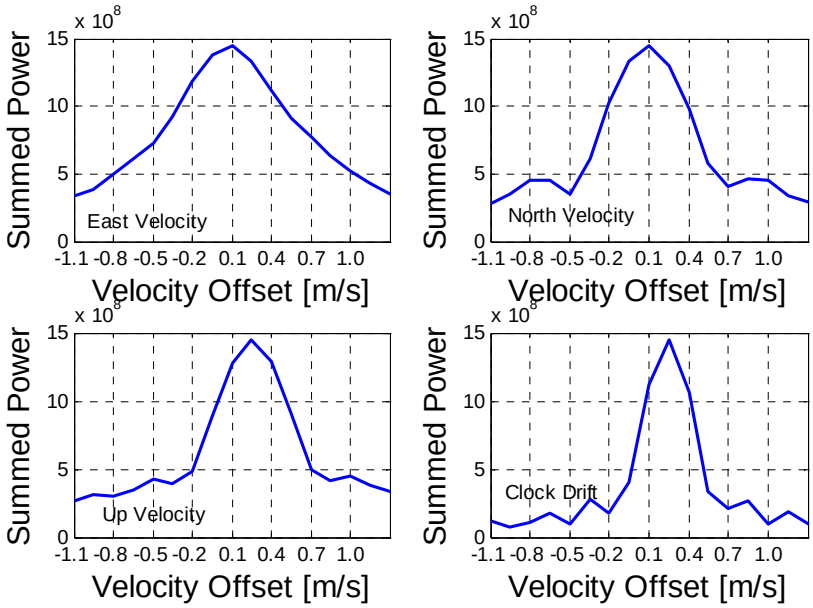

Figure 5.7: Open-sky received power distribution in velocity domain at epoch 30 (5 GPS + 3 GLONASS satellites)

From Figure 5.7, it is apparent that the received power in all components is almost entirely centered at the reference values for this open sky scenario, as intuitively expected. Specifically, in this case, the signal strength for each satellite is high enough to make an accurate Doppler estimation, and the direct MLE of velocity would also be very accurate. In this case, the peak values are only one or two bins away from the center, i.e., 0.15 m/s or 0.3 m/s offset from the reference velocity. More accurate estimates may also be possible if the searching step is reduced and some form of curve fitting is used, although this was not done here.

In contrast to the open sky case, Figure 5.8 shows the total power distribution in the velocity domain for a common indoor environment (epoch 1025). At this epoch, it is

expected that signal attenuation, along with fading, severely degrades the received signal and indeed this is reflected in the velocity domain.

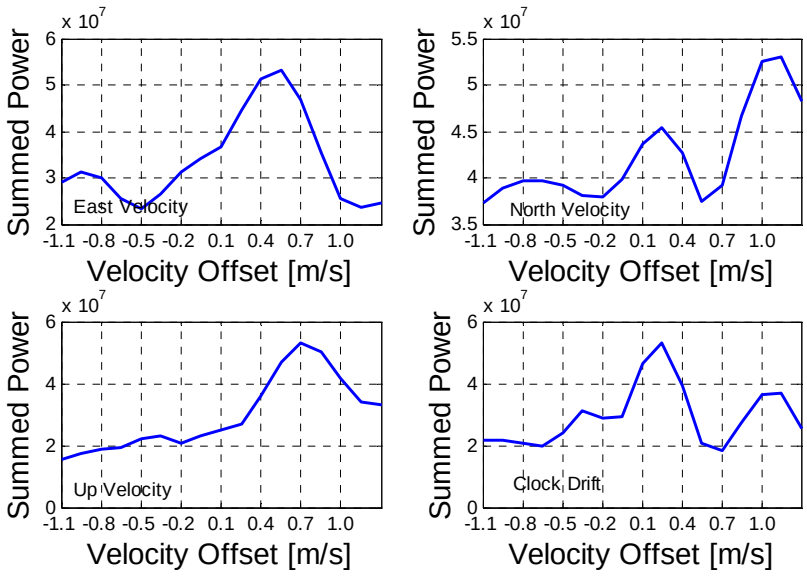

Figure 5.8: Indoor received power distribution in velocity domain at Epoch 1025 (5 GPS + 3 GLONASS satellites)

In Figure 5.8, the greatest power in east velocity dimension is still located near the centre, which indicates that the overall effects on the east velocity estimation on this epoch are not severe. As for the north velocity, there are clearly two major peaks. The greatest power is biased from the centre (about 1.0 m/s), however, there is still a 'peak' power located near the centre (0.3 m/s). Finally, the power distributions in the up velocity are also biased, but clock drift domains are very accurate. In particular, it is quite obvious that multipath significantly affects the clock drift estimation since there are three large side-lobes. But in this epoch, the multipath effects on clock drift term is not very significant. For comparison, the velocity distribution at another indoor epoch (1037) has

been chosen randomly. It is observed that, at this epoch, there are multipath induced biases in the east, north, and up axes. And the LOS signal power around the centre is relatively smaller, as seen in the east and vertical velocity domains.

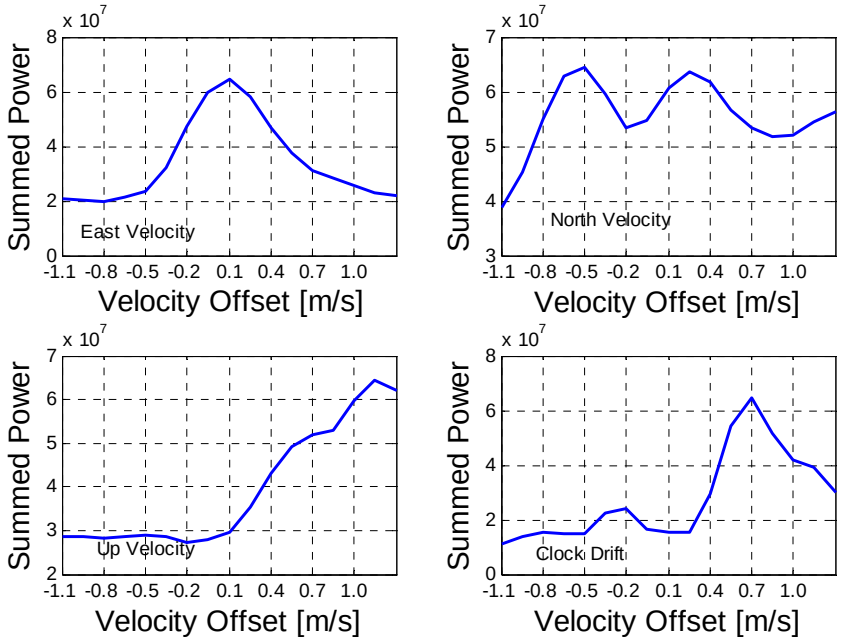

Figure 5.9: Indoor received power distribution in velocity domain at Epoch 1037 (5 GPS + 3 GLONASS)

Having examined how the total signal power is distributed in the velocity domain for single epoch, it is now beneficial to get an idea of how the trends of the received signal powers are distributed in the velocity domain over time. Figure 5.10, Figure 5.11 and Figure 5.12 are plots for the east, north, and vertical velocities under open-sky as a function of over time. These plots are from epochs 600 to 880. During this time interval, the subject has normal pedestrian dynamics. In all these figures, the left plots show the results using GPS and GLONASS data, while the right plots show GPS-only results. The

colour in each figure indicates the absolute received signal power projected on the individual velocity axis. The maximum magnitude scales of all these plots are identical and the white circles represent the maximum value detected at each epoch, that is, the MLE velocity estimate.

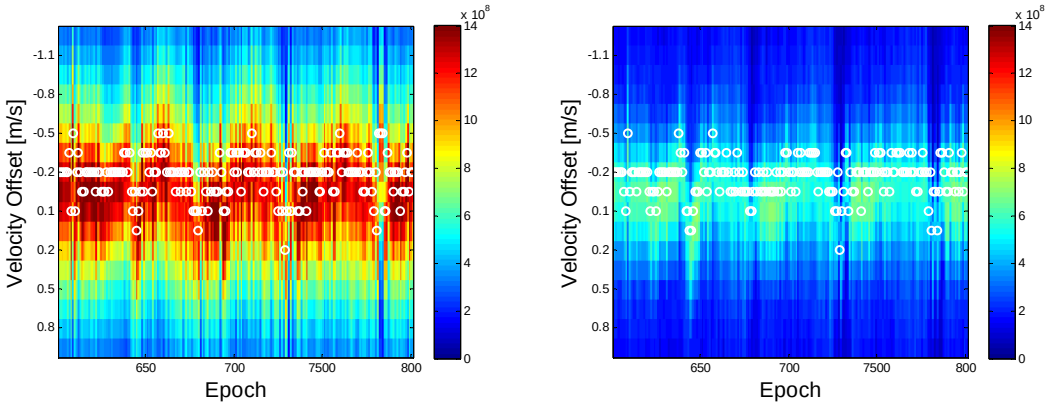

Figure 5.10: East velocity estimation errors using direct vector HSNSS 5 GPS + 3 GLONASS (left), 5 GPS (right) – engineering block outdoors (one epoch is 0.5 s)

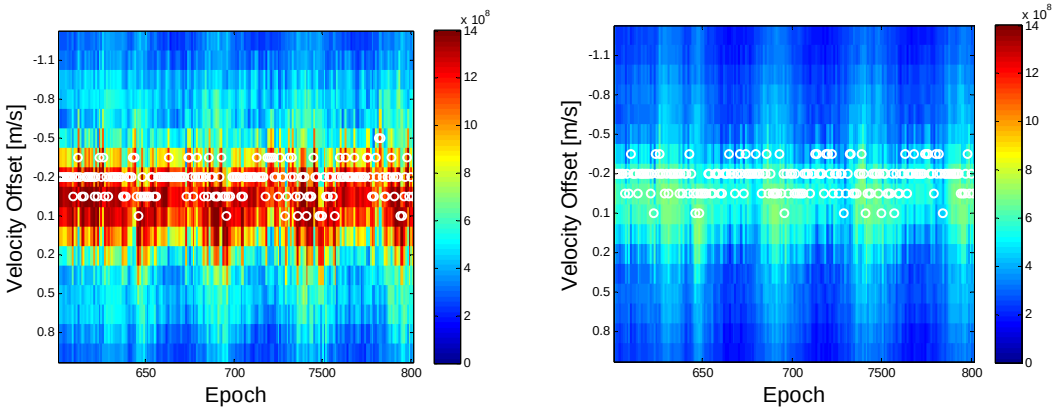

Figure 5.11: North velocity estimation error using direct vector HSGNSS 5 GPS + 3 GLONASS (left), 5 GPS (right) – engineering block outdoors (one epoch is 0.5 s)

In these figures, it is apparent that some "oscillatory" trends are present, which are systematic variations. This is due to the fact that pedestrian dynamic will periodically change the acceleration, which will result in some systematic errors. It can be observed in these figures that the largest signal power in the GPS plus GLONASS case is nearly twice that of the GPS-only case. In these figures, the GPS-only case scarcely has red points. This indicates that by processing GPS and GLONASS, more signal power is effectively used for velocity estimation. The increase in power is due to the non-coherent integration between satellites arising from the projection of each satellite's correlation map into the velocity domain. As the number of satellites increases, the cumulated power will continue to grow, which will inevitably help velocity estimation. For the up velocity, this benefit is more apparent, as shown in Figure 5.12. It is interesting to note that the power is more dispersed during some epochs for the GPS-only case, but for the GPS plus GLONASS case, the power is more centralized around the reference velocity. This phenomenon indicates that adding GLONASS satellites allocates more power around the true value, a major benefit brought by GLONASS.

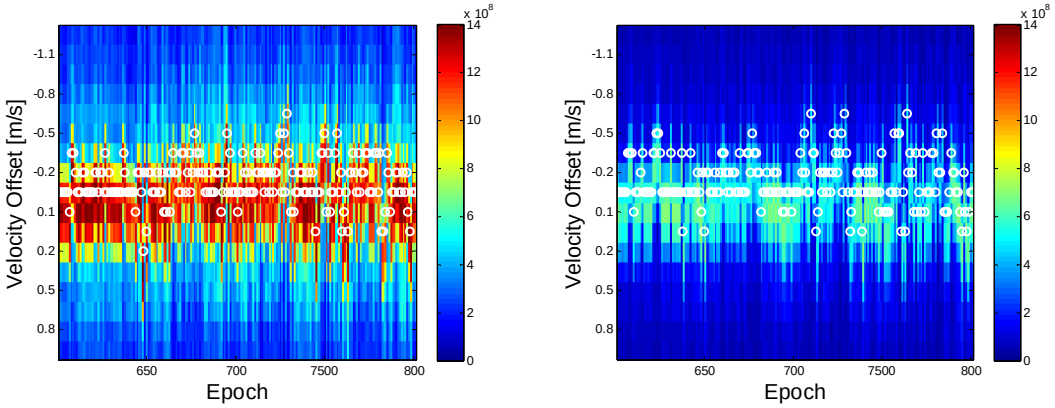

Figure 5.12: Vertical velocity estimation error using direct vector HSNGSS: 5GPS+3GLONASS (left), 5GPS (right) – engineering block outdoors (one epoch is 0.5 s)

Table 5.1 compares the RMS velocity errors (relative to the reference solution) using the different methods, such as GPS plus GLONASS with a direct vector high-sensitivity receiver, GPS-only with a direct vector high-sensitivity receiver, and GPS plus GLONASS with conventional scalar high-sensitivity receiver. The estimation accuracies are very similar, with the GPS plus GLONASS case slightly outperforming the GPS-only case in the vertical velocity axis. The 1σ uncertainty of the reference velocity is at worst 0.009 m/s (during the indoor period). However in the outdoors, this value is about only 0.001 m/s, which is small enough to quantify the improvement brought by the direct method over conventional HSGNSS.

Table 5.1: Velocity RMS errors outdoors- engineering block

Velocity RMS Error	GPS+GLONASS (Direct)	GPS-only (Direct)	GPS+GLONASS (Conventional)
East (m/s)	0.02	0.02	0.04
North (m/s)	0.01	0.01	0.05
Up (m/s)	0.03	0.04	0.07

The above figures and tables illustrate the direct velocity estimation results in outdoor environments. In the following, Figure 5.13, Figure 5.14, and Figure 5.15 represent the received power distributions over time for the indoor portion of the test. It can be seen that the power distributions are totally different from those of the outdoor case. There is also no apparent "oscillatory" trend in any direction and the velocity containing the largest amount of power is not as consistent as that shown for the outdoor case, as expected. Regarding the white circles in the outdoor cases, they are gathered near zero but indoors, they are more scattered. It is not surprising since signal conditions are expected to be worse. These figures are still illustrative, as they show the indoor signal power distributed in each velocity dimension and also account for signal attenuation, multipath, fading effects, etc. A closer scrutiny shows that even though the absolute received signal power is relatively low at certain epochs, the largest power still appears near zero, meaning that it is very near the reference velocity. Nevertheless, at some epochs multipath effects are so strong that they produce a considerable bias.

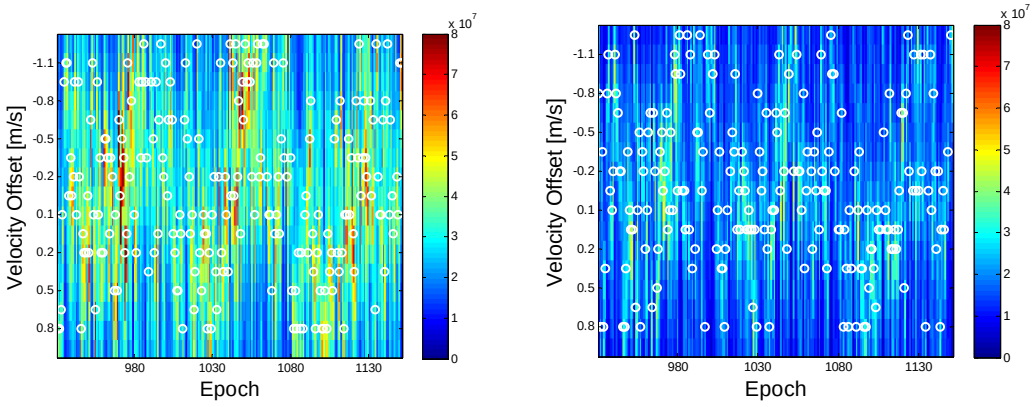

Figure 5.13: East velocity estimation error using direct vector HSGNSS 5 GPS + 3 GLONASS (left), 5 GPS (right) – engineering block indoors (one epoch is 0.5 s)

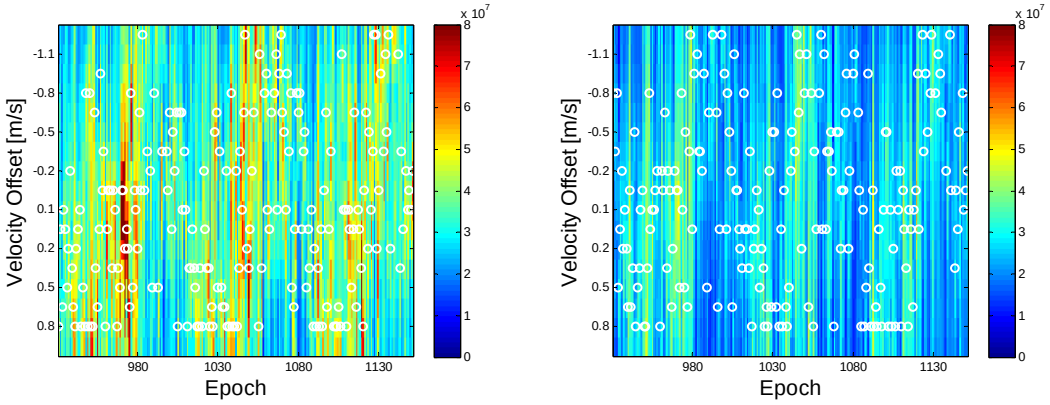

Figure 5.14: North velocity estimation error using direct vector HSGNSS 5 GPS + 3 GLONASS (left), 5 GPS (right) – engineering block indoors (one epoch is 0.5 s)

Regarding the difference between the GPS plus GLONASS and GPS-only cases, it can be observed that the absolute power of the GPS-only case is relatively smaller than that of the GPS plus GLONASS case. Also, the GPS-only vertical velocity does not contain any obvious "structure". This is because the power is spread over a wide range of velocity values. In other words, observability in this dimension is very poor. However for the GPS plus GLONASS case, it seems that the power is more concentrated. From the vertical velocity plots, it illustrates that even in the indoor cases, adding GLONASS actually increases the ability to estimate the vertical velocities.

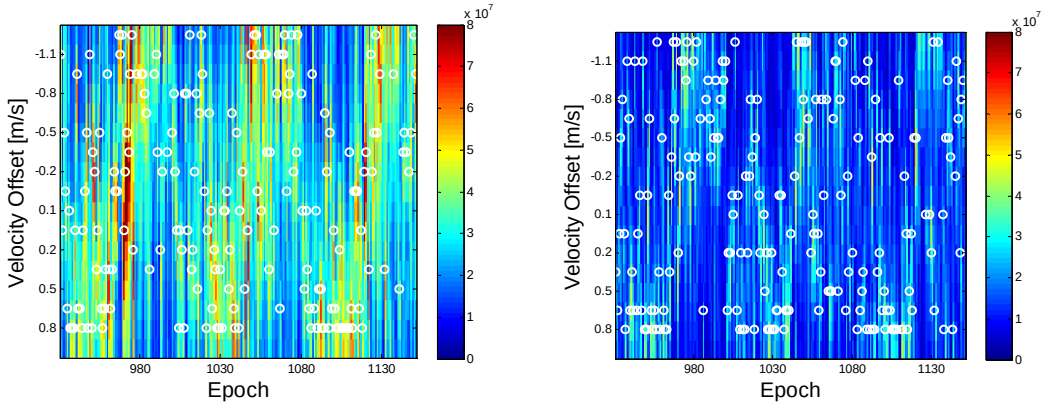

Figure 5.15: Vertical velocity estimation error using direct vector HSGNSS 5 GPS + 3 GLONASS (left), 5 GPS (right) – engineering block indoors (one epoch is 0.5 s)

The RMS velocity errors of the indoor case are listed in Table 5.2. In this case, the RMS errors of the conventional approach are very large. It is noted that given the test setup, the design matrix for the conventional method was determined by using the reference position since the solution would diverge at nearly every epoch if it iteratively used least squares. As for the direct vector receiver, the unit direction vector is also based on such reference position in order to make a fair comparison. However, it should be noted that the unit direction vector is only affected by the current position, which could be updated from previous velocity updates. And given a 1 km positioning error, the projected Doppler only has a 1 Hz systematic error at maximum (van Diggelen 2009). This indicates that for the direct vector receiver, it makes little difference whether the reference or internally updated positions are used to calculate the unit direction vector.

Table 5.2: Velocity RMS error in indoors- engineering block

Velocity RMS Error	GPS+GLONASS (Direct)	GPS-only (Direct)	GPS+GLONASS (Conventional)
East (m/s)	0.47	0.47	1.19
North (m/s)	0.57	0.59	1.03
Up (m/s)	0.73	0.76	2.15

From Table 5.2 the direct method of both the GPS-plus-GLONASS case and the GPS-only case outperform the conventional approach by approximately 50%. However, adding GLONASS did not provide any apparent benefit in the horizontal plane. This is likely because the multipath environment is the limiting factor as opposed to the open-sky case where multipath is not much of a concern. Again, for this scenario, the worst case one sigma uncertainty of reference velocity is only about 0.009 m/s, which is still small enough to quantify the improvement of the direct method over conventional HSGNSS.

5.4.2 MacEwan Student Centre

The second data set was collected inside the MacEwan Student Centre. The focus for this scenario is to evaluate the performance of direct velocity estimation inside a large building. Only GPS signals were collected and processed. Correspondingly, the raw GPS IF samples were logged using the NI front-end. A high quality oscillator, i.e. OCXO is also used in order to minimize its negative effect on long coherent integration. The software used for the previous data set was also used here to obtain the raw correlator

outputs. This software receiver also provides conventional HSGPS observations for comparison with the proposed algorithm. The coherent integration time is set 500 ms.

The reference trajectory and sky plots are shown in Figure 5.16. The estimated standard deviation of the reference position is better than 1.8 m. The estimated standard deviations of the east, north and vertical reference velocity components are better than 0.02 m/s, 0.018 m/s and 0.015 m/s, as shown in Figure 5.18. There are seven GPS satellites in view during the data collection process. Figure 5.17 shows the indoor scenarios inside the building. It can be seen that there are large spaces inside and there are no windows on either side of trajectory. However, large parts of the rooftop are made of glass.

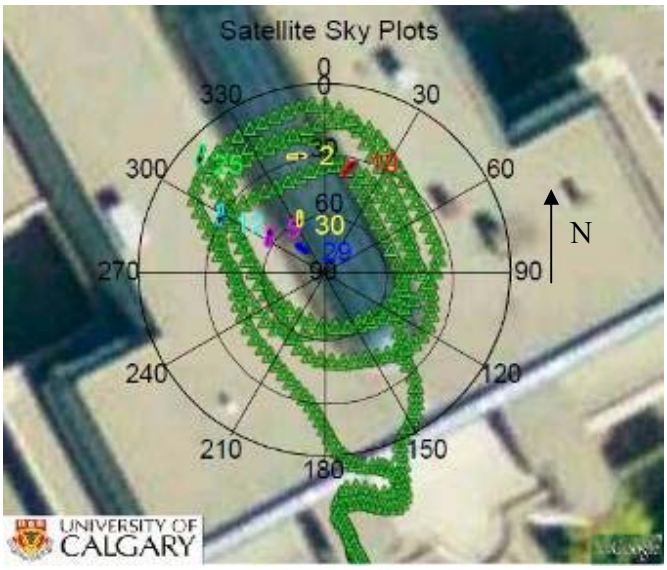

Figure 5.16: Reference trajectory and sky plots -MacEwan Indoor Test

Figure 5.17: Picture of MacEwan indoor test facing north

The C/N_0 profiles are shown in Figure 5.18. It can be seen that during open-sky scenarios, the C/N_0 values ranged from 40 to 50 dB-Hz. These represent nominal values for open sky scenarios. However, when the subject is in the building between epoch 900 and epoch 1600, the C/N_0 values drop significantly to 10 to 20 dB-Hz. After that the subject walks outside the building again and the C/N_0 increases to the nominal open sky values. The total time data length is approximately 30 min and the indoor period is approximately 5~6 min.

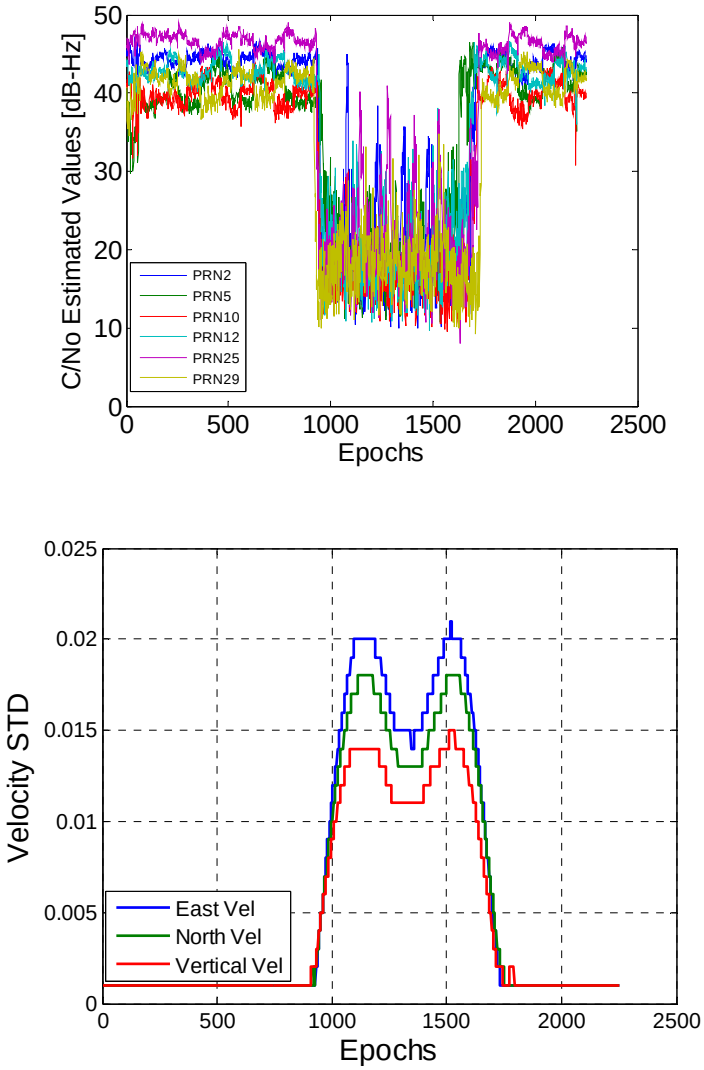

Figure 5.18: C/N_0 profile, reference velocity standard deviation – MacEwan Indoor Test

Figure 5.19 shows the power distribution trends on east, north and vertical velocities. It could be seen that the major received signal power is concentrated very near the reference velocities. Furthermore, systematic errors are also apparent, which is quite similar to the plots shown in Figure 5.10, Figure 5.11 and Figure 5.12.

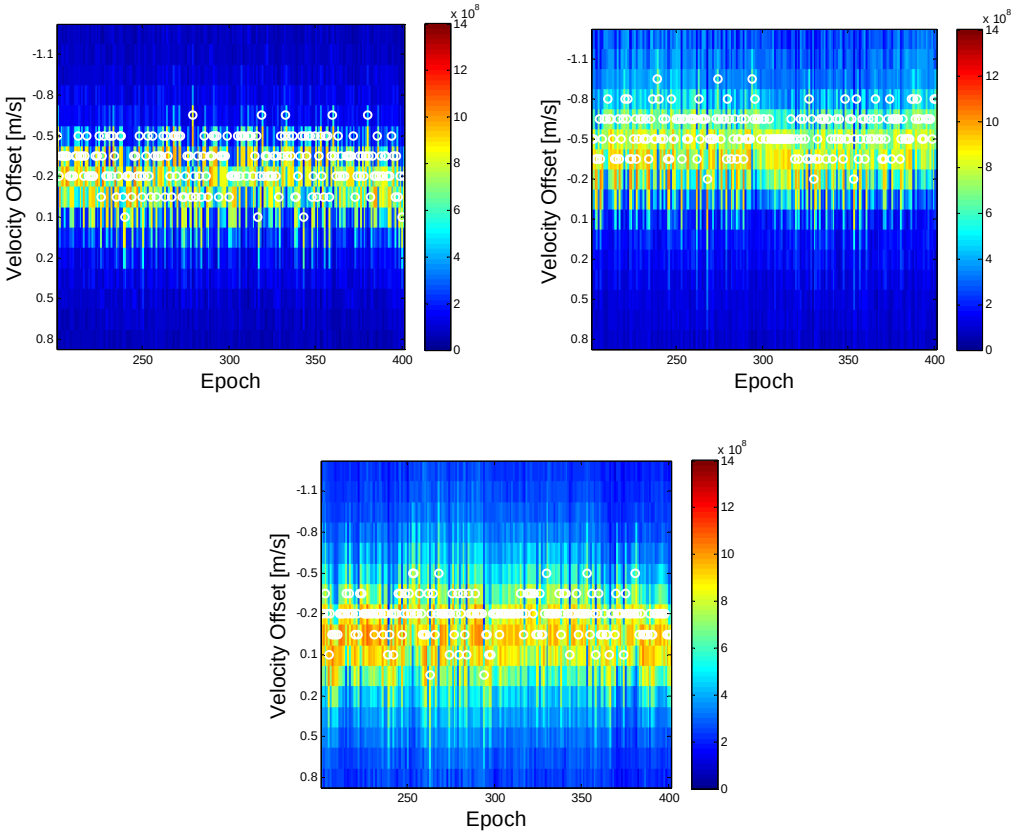

Figure 5.19: east velocity (top left), north velocity (top right) and up velocity (bottom) estimation errors using direct vector HSGPS - MacEwan outdoors (one epoch is 0.5 s)

The RMS error statistics are summarized in Table 5.3. It can be seen that both the conventional and direct velocity receiver show very similar performance. There is a slight improvement in the vertical velocity and a slight degradation in east velocity dimension when using the direct vector receiver. From Figure 5.18, one can observe that during the outdoor periods, the one-sigma standard deviation is about 0.001 to 0.002 m/s, which is small enough to quantify the differences between the direct and conventional methods.

Table 5.3: Velocity RMS errors outdoors-MacEwan

Velocity RMS Error	Direct	Conventional
East (m/s)	0.03	0.02
North (m/s)	0.02	0.03
Up (m/s)	0.02	0.04

Figure 5.20 shows the power distribution trends on the east, north, and vertical velocities in the MacEwan indoor environments. The largest power is more scattered across velocity domains as compared to the outdoor counterparts. In these figures, the maximum scale of the total received is the same as in Figure 5.13, Figure 5.14 and Figure 5.15. It can be seen that in the MacEwan case, there are epochs where more signal power is used for the velocity estimation even with 7 satellites. For example, in the engineering building, there are scarcely any red spots in all three figures even with GPS plus GLONASS (8 satellites). But there are more red spots for all three dimensions inside the MacEwan Student Centre. These results represent real scenarios. For the engineering block case, the environment is nearly entirely obscured by concrete walls. However, in the MacEwan Student Centre, there is a large glass window on the very top of the roof, which is slightly more favourable than the engineering block indoor environment.

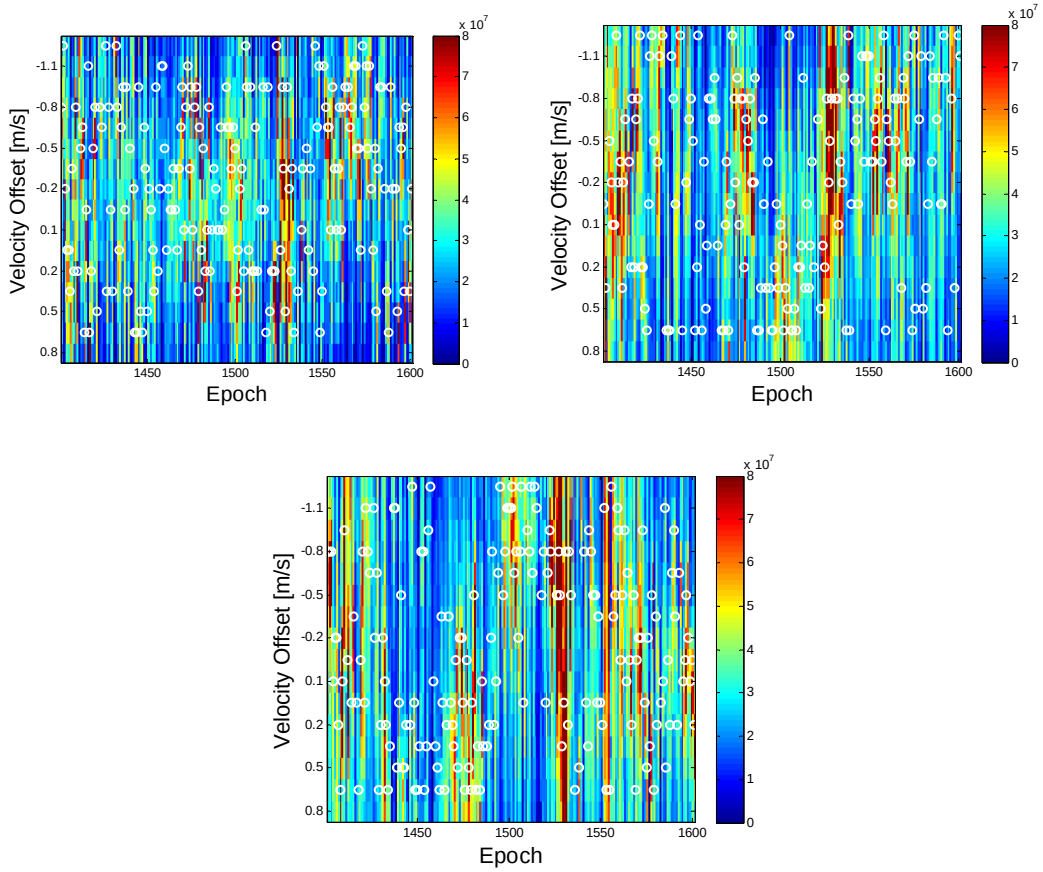

Figure 5.20: East velocity (top left), north velocity (top right) and up velocity (bottom) estimation errors using direct vector HSGPS -MacEwan indoor test (one epoch is 0.5 s)

The RMS error statistics of the MacEwan indoor scenarios are summarized in Table 5.4. The direct velocity estimation method outperforms the conventional method in all three dimensions, which is quite similar to the engineering block indoor results. Compared with Table 5.2, one could see that the velocity RMS error estimated in the MacEwan is slightly smaller than inside the engineering block. This is due to the fact that the MacEwan indoor environment is milder than that of the engineering block, and more signal power will be effectively used for the velocity estimation. Nevertheless, the

proposed algorithm does offer improvements of 11%, 44%, and 67% in east, north, and vertical axis respectively, as compared to the conventional approach. The differences between the conventional and direct method RMS errors are much larger than the one-sigma uncertainty of the reference solution (0.02 m/s in the worst case).

Table 5.4: Velocity RMS errors indoors - MacEwan

Velocity RMS Errors	Direct	Conventional
East (m/s)	0.63	0.74
North (m/s)	0.64	1.17
Up (m/s)	0.53	1.74

5.4.2.1 Discussion on stand-alone HSGNSS

The above results were obtained using an assisted HSGNSS architecture in order to reduce the computational burden (see Section 2.1.3). In this section, the data is processed using only data bit aiding and without information about the receiver's position and velocity, which is more indicative of a standalone receiver. In other words, the receiver operates in vector-tracking mode using only data bit aiding. Results will show that external aiding has little or no effect on the results presented above.

For this processing, the search space for the Doppler is ±13 Hz about the Doppler shift predicted by the navigation solution. Both the conventional and direct algorithm presented above were then used to process the data. In outdoor environments, the velocity RMS errors are exactly the same as the results shown in Table 5.3. For the indoors, the velocity RMS errors of east, north, and up axes using direct methods are 0.64, 0.65, 0.49 m/s, respectively. The slight difference only appeared in the vertical velocity axis. This is

very likely coming from interpolating the true maximum around adjacent bins. As the search step is decreased, the interpolation effects will also be reduced. So throughout the thesis, 1 Hz external coordinate aiding for shrinking the searching space is considered to have no effects on the velocity and Doppler estimation process.

5.4.3 CCIT-ICT

The third data set was collected in corridors from the CCIT building to the ICT building on the campus of the University of Calgary in December 2012. The C/N_0 profiles are shown in Figure 5.21. The equipments for the data collection are the same as that of the previous two data sets. The coherent integration time for the high sensitivity processing is set to 500 ms. Novatel SPAN^{TM} system (SPAN SE receiver and LCI IMU) and Novatel IE^{TM} are used for generating the reference trajectory. The one-sigma uncertainty of the reference velocity is better than 0.01 m/s for all epochs. This value is small enough to quantify the velocity RMS error improvements as will be shown in the following paragraphs. In order to maintain the reference trajectory accuracy, the subject walked outside every few minutes. In order to facilitate the inertial alignment and forward backward smoothing, the subject kept walking circularly outdoors at the beginning and end of a run. These are the reasons why, in Figure 5.21, the C/N_0 values sometimes go above 40 dB-Hz (outdoors) and sometimes go below 25 dB-Hz (indoors).

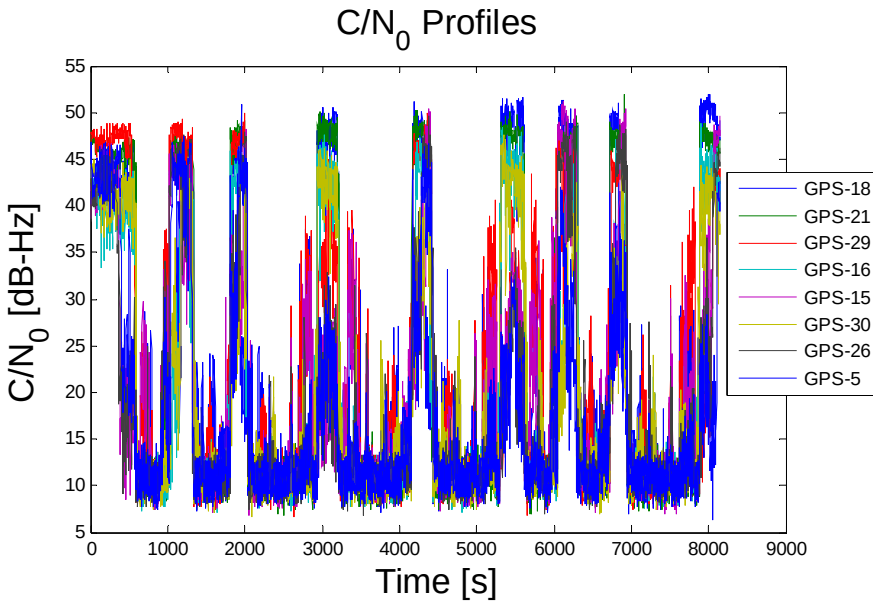

Figure 5.21: C/N_0 profile of CCIT-ICT data set

Several different indoor environments were encountered in this data set. To better assess the proposed algorithm of the direct vector processing in such environments, five spots were chosen and marked in Figure 5.22, named 'A', 'B', 'C', 'D' and 'E' (and denoted CCIT-A, CCIT-B, etc.). The scenario 'A' is an outdoor environment that is near the CCIT building starting at GPS time 327240. Scenario 'C' represents the period going from totally indoor to outdoor, with half of the sky blocked by the Earth Science Building to the east, starting at GPS time 328139. Periods 'B', 'D' and 'E' are three indoor scenarios starting at GPS times 327689, 328619, and 329434, respectively, and will be discussed in more detail in the following subsections.

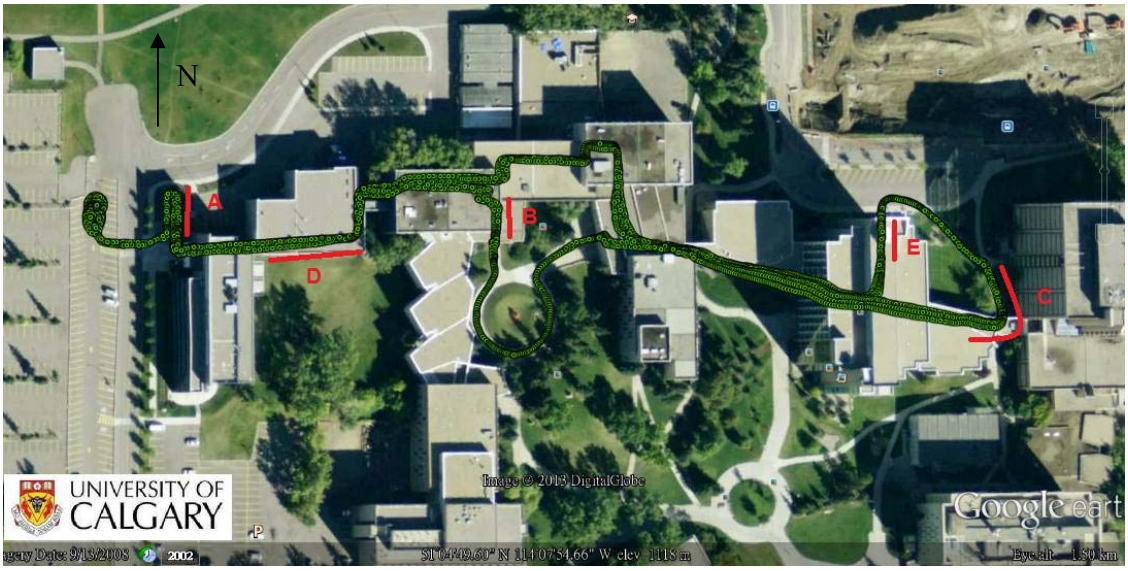

Figure 5.22 Reference trajectory of CCIT-ICT data set

The sky plot of satellites observed during this data collection is shown in Figure 5.23. The corresponding discussion will be included in the following subsections.

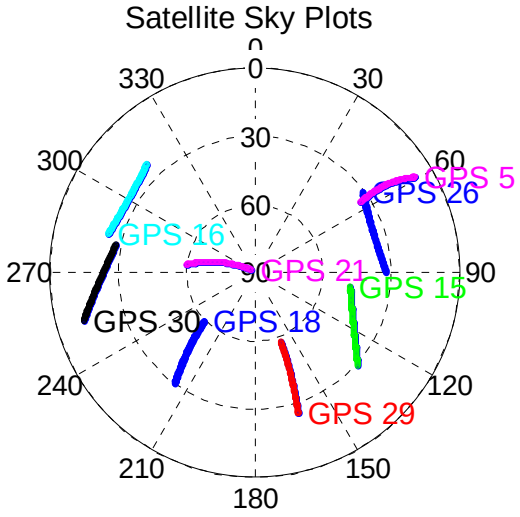

Figure 5.23 Sky plot of CCIT-ICT data set

The entire data set lasted about 4300 s (1 hr 10 min) and included about 20 min outdoors and 50 min indoors. To evaluate the general performance of the proposed direct vector HSGPS and conventional HSGPS (block processing) velocity estimation under this complex environment for such a long time period, the overall RMS errors are first summarized in Table 5.5. In this table, it is observed that the proposed algorithm outperforms the conventional HSGPS by 41%, 73%, and 89% in the east, north and up velocity axis, respectively. These statistics are based on the entire data set, which includes various complex indoor environments as well as an open sky scenario. It has already been shown in Table 5.1 and Table 5.3 that the performance of the proposed algorithm and conventional HSGPS are quite similar in open sky scenarios, hence the improvements mentioned above largely occurs in weak signal conditions. In order to further assess the performance under such environments, the five data segments are analyzed separately below.

Table 5.5 Velocity RMS errors - CCIT overall

Velocity RMS Error	Direct	Conventional
East (m/s)	0.34	0.58
North (m/s)	0.36	1.35
Up (m/s)	0.41	3.72

5.4.3.1 Results from Data Section A test

In Figure 5.24, Figure 5.25 and Figure 5.26, the velocity estimation errors of direct vector processing and conventional LSQs based on block processing in the scenario ‘A’ are

plotted. There are 580 epochs in these figures, and one epoch represents 0.5 s (the coherent integration period). From epoch 100 to epoch 580, the subject is walking from a near open sky scenario to the CCIT building. At epoch 400, the subject is quite near the CCIT building and some satellite signals are blocked. The velocity estimation errors with the direct vector processing ('direct' as mentioned in Chapter 2) and LSQ solution based on block processing techniques ('conventional' as mentioned in Chapter 2) are both shown. One can observe that as the subject approaches the building, direct vector processing gives much more smoothed results as compared to those of the conventional method. Given that some signals are obstructed by the building, the conventional solution produces several spikes during this period.

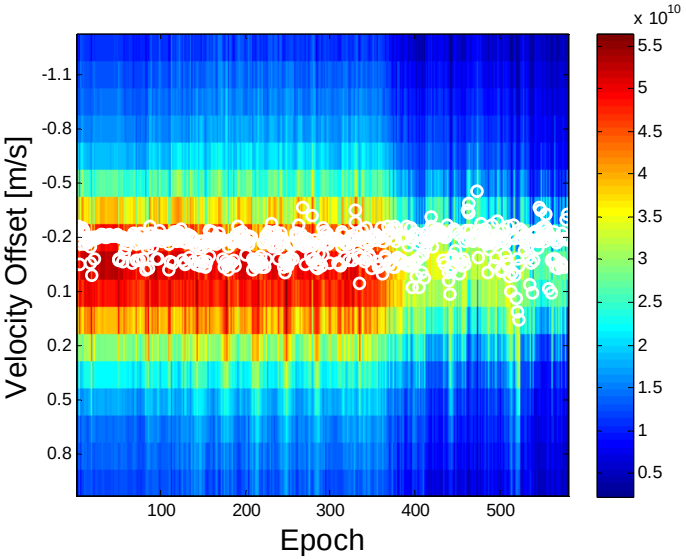

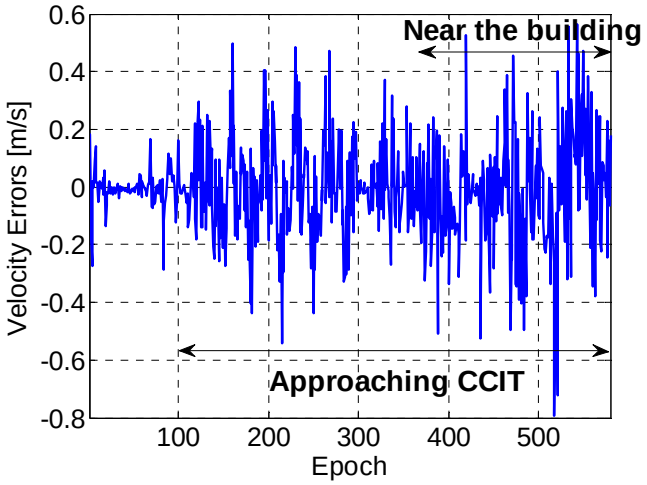

Figure 5.24: East velocity errors versus time for direct (top) and conventional (bottom) HSGNSS receivers for CCIT-A data set (one epoch is 0.5 s)

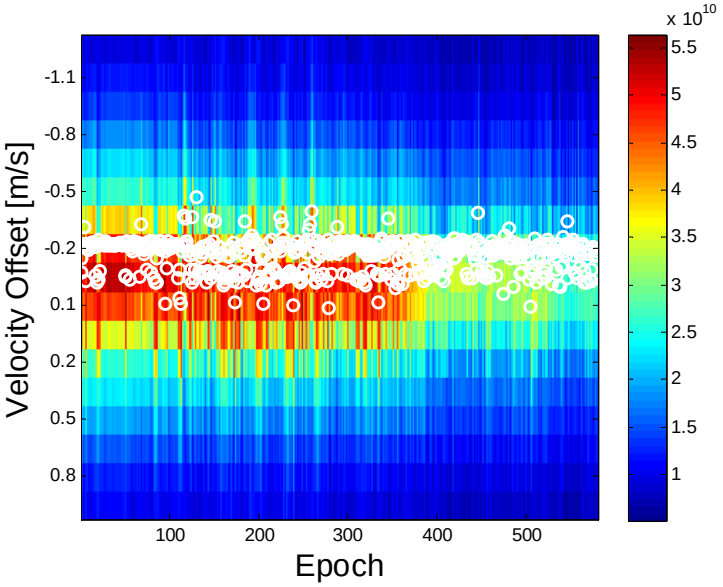

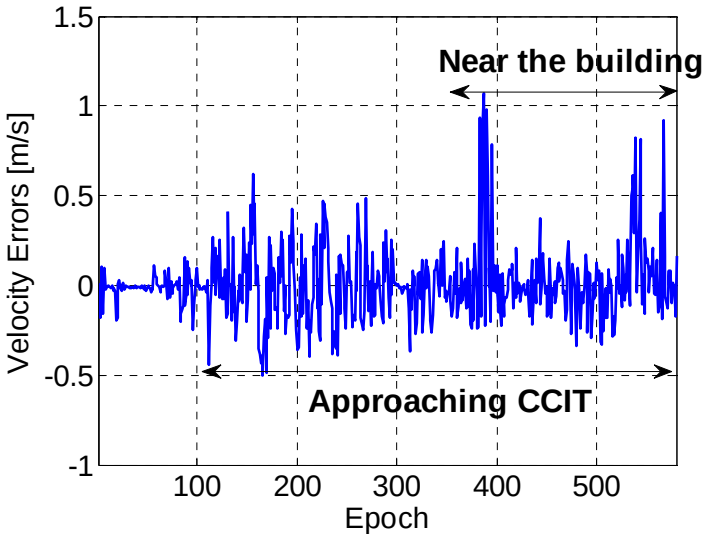

Figure 5.25: North velocity errors versus time for direct (top) and conventional (bottom) HSGNSS receivers for CCIT-A data set (one epoch is 0.5 s)

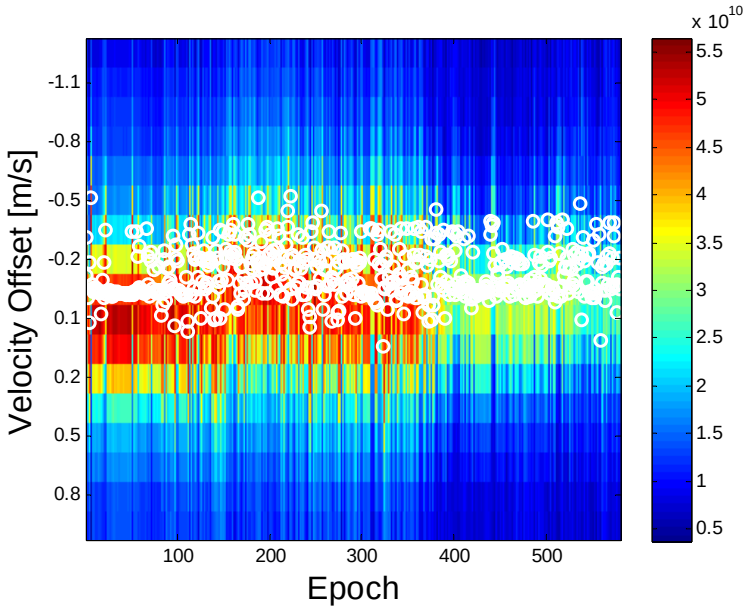

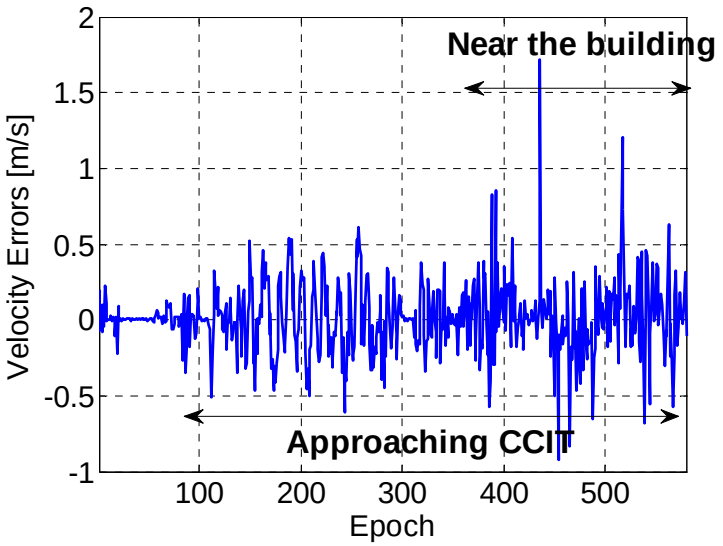

Figure 5.26: Up velocity errors versus time for direct (top) and conventional (bottom) HSGNSS receivers for CCIT-A data set (one epoch is 0.5 s)

The C/N_0 profile in this scenario is further plotted in Figure 5.27. It can be seen that three satellite signals are severely obstructed by the building from epoch 400 to epoch 580. Through scrutiny of Figure 5.22 and Figure 5.23, one can see that during this period, the west half of the sky is without any obstruction, which means that PRN 16, PRN 18, PRN 21 and PRN 30 should have better C/N_0 values as compared to those of the other satellites. And this indeed matches what one can observe in Figure 5.27. In order to better understand the real scenario, a picture where the test started just outside the building is shown in Figure 5.28.

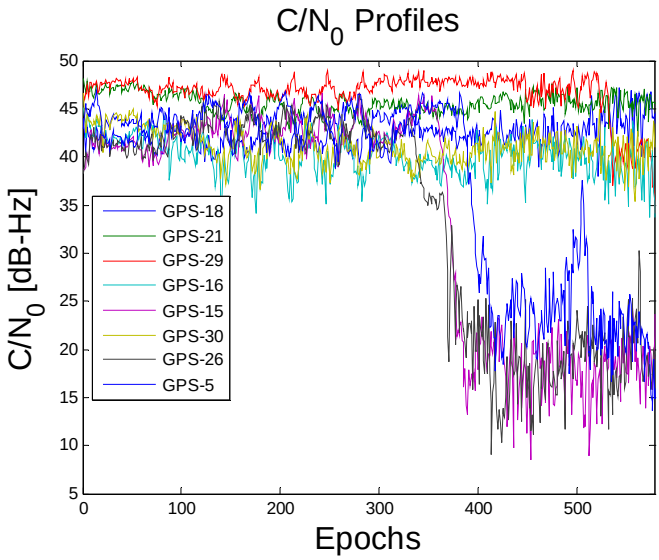

Figure 5.27: C/N_0 profile - CCIT – A (one epoch is 0.5 s)

Figure 5.28: Picture of CCIT-A test environment facing south

The velocity RMS errors are further summarized in Table 5.6. One can see that the proposed direct HSGPS outperforms the conventional HSGPS (based on block processing algorithm) in all three axes, by about 66%, 75%, and 66%, respectively.

Table 5.6: Velocity RMS errors - CCIT-A test

Velocity RMS Errors	Direct	Conventional
East (m/s)	0.01	0.03
North (m/s)	0.01	0.04
Up (m/s)	0.02	0.06

5.4.3.2 Results from Section B test

The velocity estimation errors from scenario 'B' are plotted in Figure 5.29. The starting time of these figures is 327689 s. It can be observed that from epoch 40 to epoch 100, the received signal power in the velocity domain is more concentrated around certain regions.

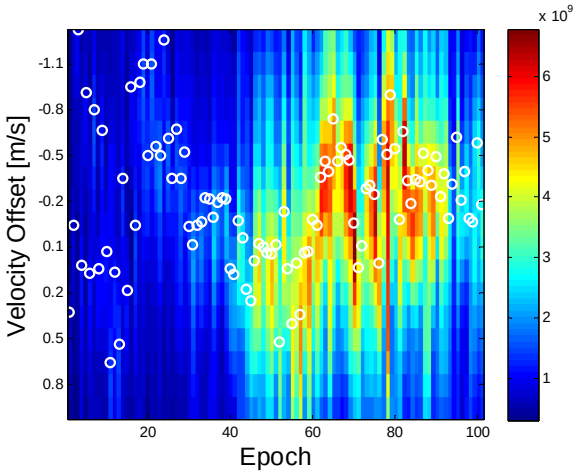

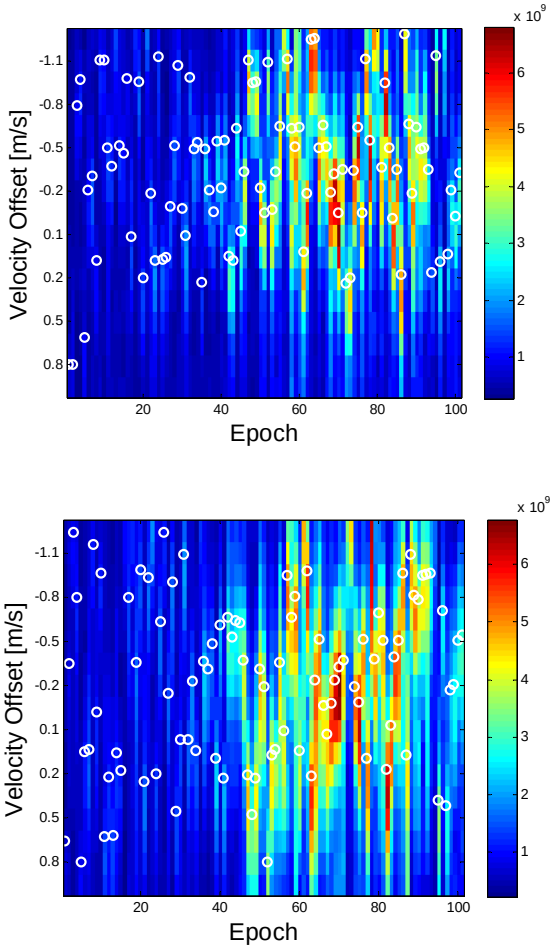

Figure 5.29: East (top), north (middle) and up (bottom) velocity estimation errors of direct vector HSGPS - CCIT-B (one epoch is 0.5 s)

The corresponding C/N_0 profile is shown in Figure 5.30. One can see that C/N_0 values of six satellites increase to between 15 dB-Hz to 35 dB-Hz during epoch 40 to 100. This is the reason why the received power over velocity domains shown in Figure 5.29 is more concentrated during this period. An example of the indoor scenario of the CCIT-B section is shown in Figure 5.31. Along with the sky plot shown in Figure 5.23, it seems that the

signals transmitted by the satellites from the south and east portions of the sky penetrate the windows more easily, such as PRN 29, PRN 15. This is confirmed in Figure 5.30.

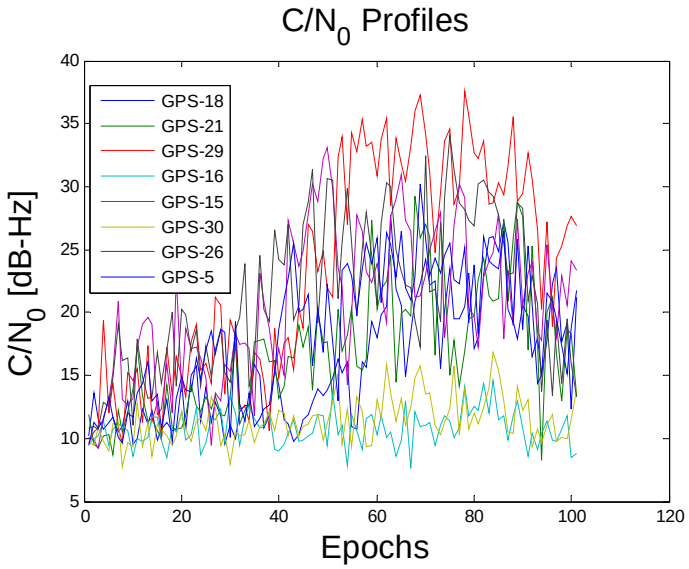

Figure 5.30: C/N_0 profile -CCIT-B (one epoch is 0.5 s)

Figure 5.31: Picture of CCIT-B test environment facing south

The velocity estimation RMS errors of the proposed direct vector HSGPS and conventional HSGPS under the CCIT-B scenario are summarized in Table 5.7. One can see the proposed algorithm outperforms the conventional one by 24%, 72%, and 83% in the east, north and up velocity axis, respectively.

Table 5.7: Velocity RMS errors - CCIT-B test

Velocity RMS Errors	Direct	Conventional
East (m/s)	0.19	0.25
North (m/s)	0.32	1.16
Up (m/s)	0.41	2.43

5.4.3.3 Results from Section C test

The velocity estimation errors of direct HSGPS in the CCIT-C scenario are plotted in Figure 5.32. Under this scenario, the subject walks from inside the ICT building to the outdoors. One can observe that, as the received signal powers increases, the velocity estimation accuracy improves. In the beginning of the indoor period, the vertical velocity appears to be more erroneous than the estimated east and north velocities. However, as the received signal power increases, all these errors decrease.

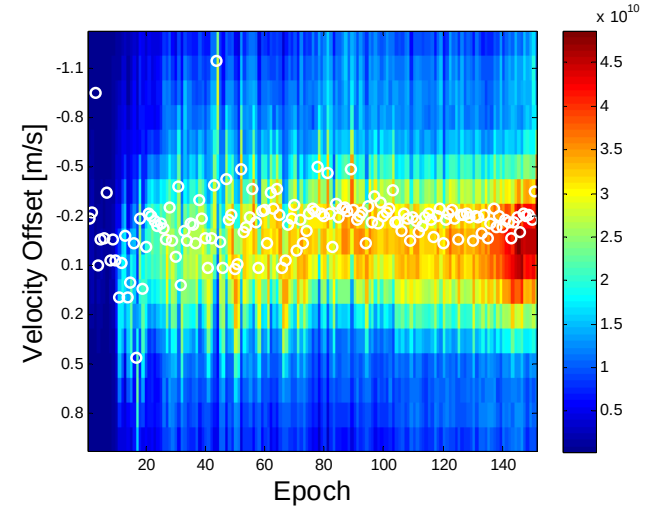
x 10^10
4.5
4
3.5
3
2.5
2
1.5
1
0.5
-1.1
-0.8
-0.5
-0.2
0.1
0.2
0.5
0.8
Velocity Offset [m/s]
20
40
60
80
100
120
140
Epoch

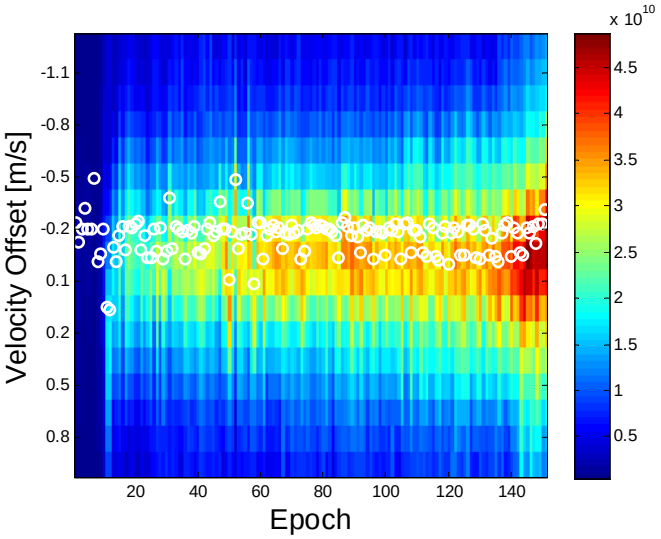
x 10^10
4.5
4
3.5
3
2.5
2
1.5
1
0.5
-1.1
-0.8
-0.5
-0.2
0.1
0.2
0.5
0.8
Velocity Offset [m/s]
20
40
60
80
100
120
140
Epoch

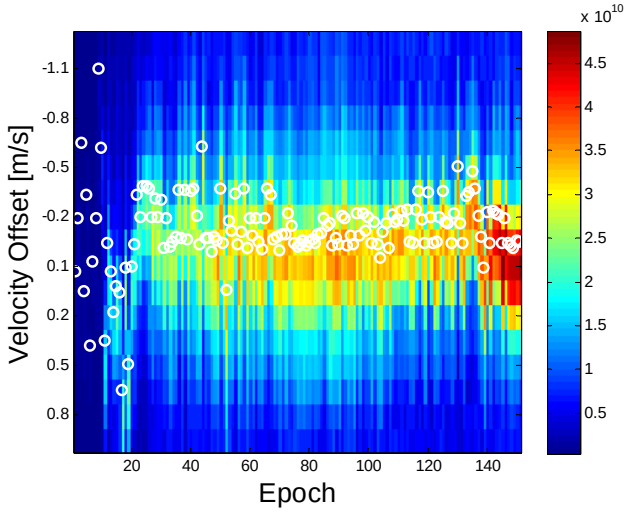

Figure 5.32: East (top), north (middle) and up (bottom) velocity estimation errors of direct vector HSGPS -CCIT-C test (one epoch is 0.5 s)

The C/N_0 profile in this scenario is shown in Figure 5.33. As one can see, in the beginning, the C/N_0 for all satellites ranges from 10 dB-Hz to 25 dB-Hz. During the outdoor periods, only three to four satellites are not severely blocked by the Earth Science Building. The test environment of CCIT-C is illustrated in Figure 5.34.

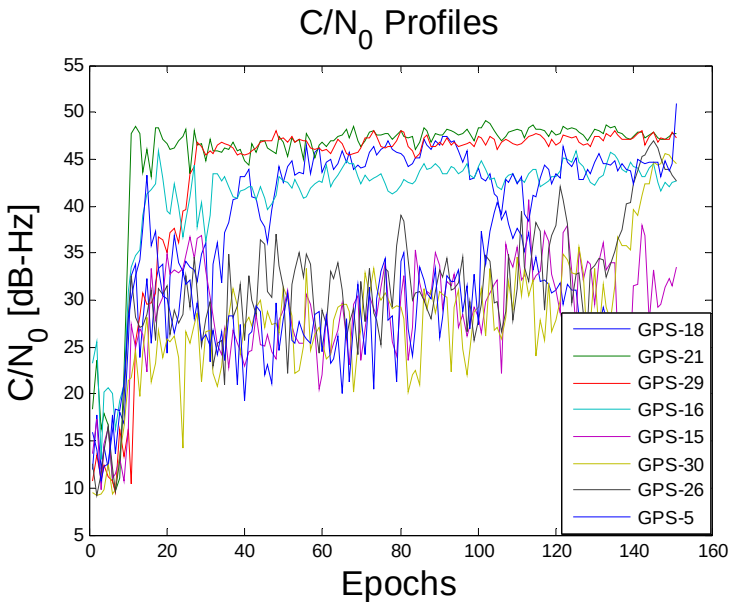

Figure 5.33: C/N_0 profile and scenario -CCIT-C test (one epoch is 0.5 s)

Figure 5.34: Picture of CCIT-C test environment facing east

The velocity RMS errors of the proposed direct vector HSGPS and conventional HSGPS in this scenario are summarized in Table 5.8. One can see the proposed algorithm

outperforms the conventional one by 75%, 92%, and 87% in the east, north and up velocity axis, respectively.

Table 5.8: Velocity RMS error -CCIT-C test

Velocity RMS Errors	Direct	Conventional
East (m/s)	0.03	0.12
North (m/s)	0.01	0.12
Up (m/s)	0.05	0.40

5.4.3.4 Results from Section D test

The velocity estimation errors of the direct vector processing of the CCIT-D test scenario are shown in Figure 5.35. It can be seen that during these epochs, east velocity estimation errors are smaller than those of the north and vertical axes. Since there are several windows on the south side of the hallway, the received signal power may still be relatively large during some epochs as shown in Figure 5.35.

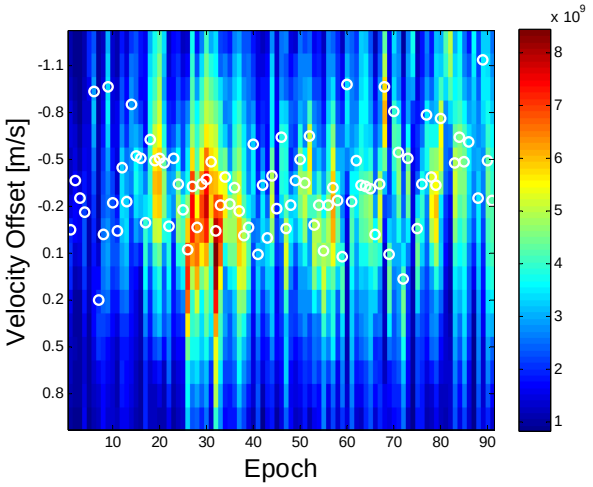

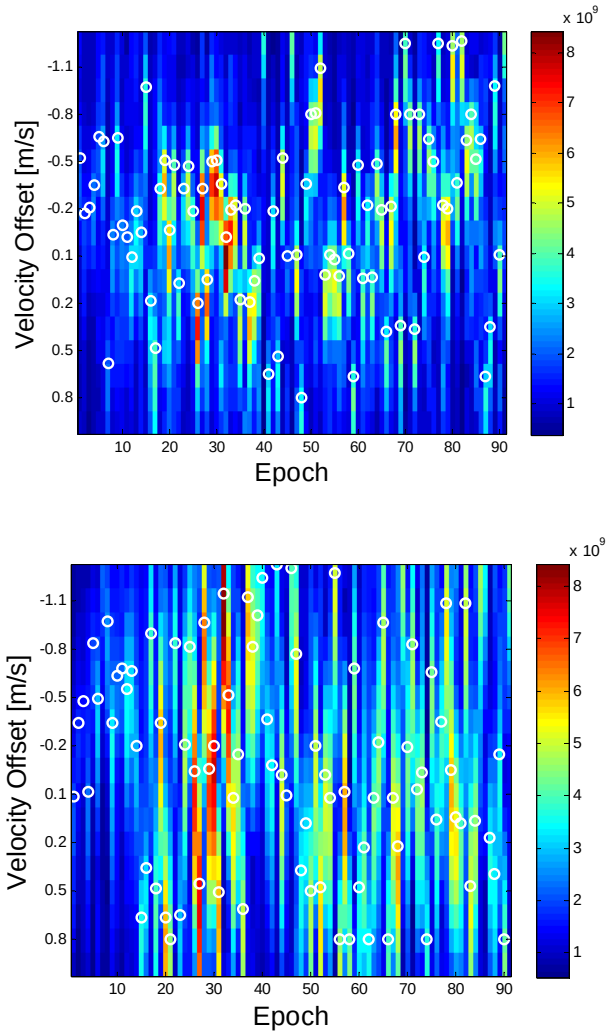

Figure 5.35: East (top), north (middle) and up (bottom) velocity estimation errors of direct vector processing -CCIT-D test (one epoch is 0.5 s)

The C/N_0 profile is shown in Figure 5.36. From this plot, one can see that the power of only three satellites is relatively stronger, being in the range of 20 to 37 dB-Hz. The other five satellites have rather weak signals in the range of 10 to 15 dB-Hz. The test environment is shown in Figure 5.37. Along with the sky plot shown in Figure 5.23, one can assume that the satellite in the south part of the sky can penetrate the windows more

easily, given the larger C/N_0 values of PRN 15, PRN 29 and PRN 18. This is the case as confirmed in Figure 5.36.

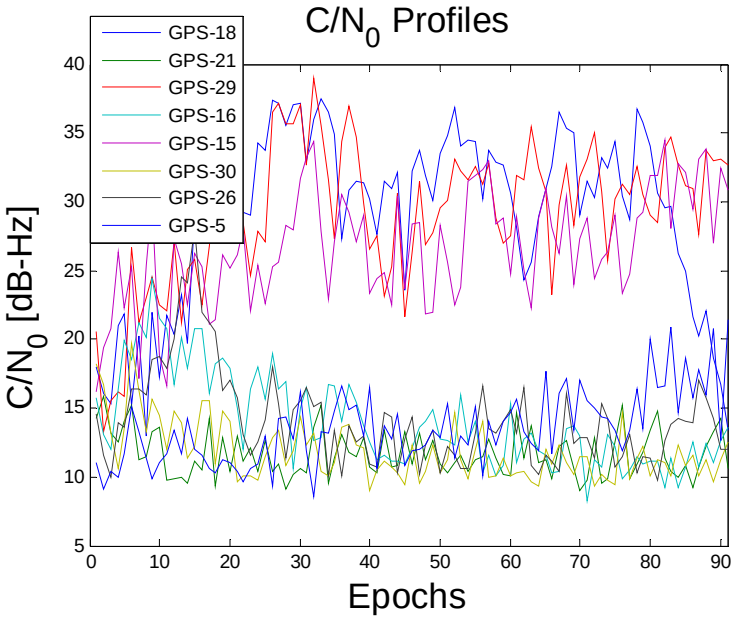

Figure 5.36: C/N_0 profile -CCIT-D (one epoch is 0.5 s)

Figure 5.37: Picture of CCIT-D test environment facing east

The velocity RMS errors of the proposed direct vector HSGPS and conventional HSGPS in this scenario are summarized in Table 5.9. One can see that the proposed algorithm outperforms the conventional one by 75%, 75%, and 89% in the east, north and up velocity axis, respectively.

Table 5.9: Velocity RMS errors -CCIT-D test

Velocity RMS Errors	Direct	Conventional
East (m/s)	0.14	0.56
North (m/s)	0.32	1.29
Up (m/s)	0.52	4.96

5.4.3.5 Results from Section E test

The last scenario to be evaluated is chosen as that from the ICT building outside to the ICT indoor food court. The velocity estimation errors of the direct vector processing in this scenario are shown in Figure 5.38. From these figures, one can observe that the received total signal power decreases with time, however the velocity estimation accuracy of the direct vector processing is about the same, which is further compared to the conventional LSQ solution in Table 5.10.

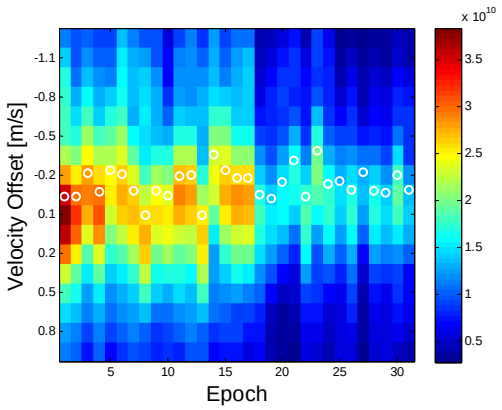

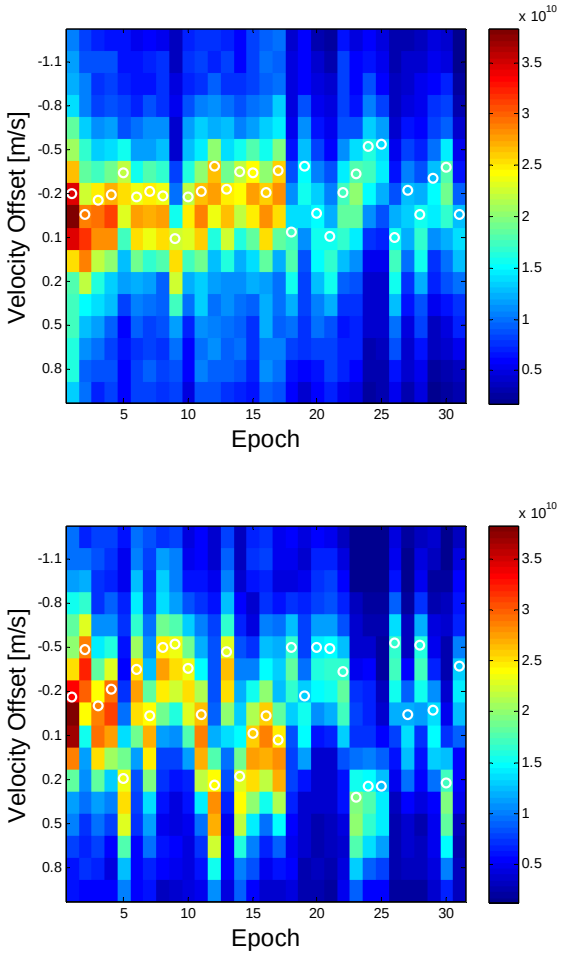

Figure 5.38: East (top), north (middle) and up (bottom) velocity estimation errors of direct vector processing -CCIT-E test (one epoch is 0.5 s)

The C/N_0 profile depicted in Figure 5.39 shows that three satellite signals are relatively strong, with range of 40 to 46 dB-Hz. All the other five satellites have weaker signals ranging from 15 to 30 dB-Hz. The test indoor environment is shown in Figure 5.40, and along with the sky plot in Figure 5.23, one can deduct that the satellites in the north-east are easier to penetrate windows, e.g. PRN 5, PRN 26, and PRN 15. This assumption is confirmed in the C/N_0 plots.

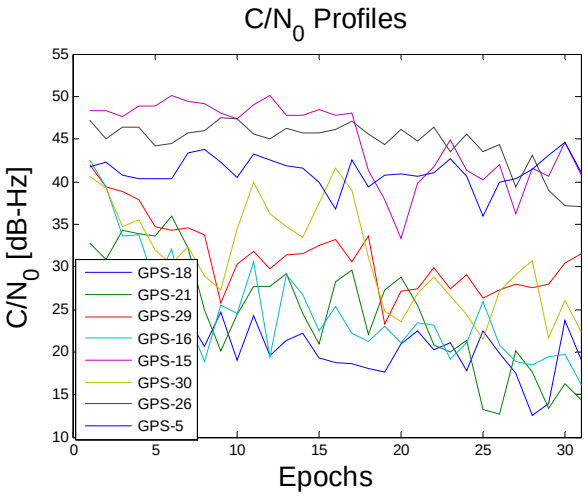

Figure 5.39: C/N_0 profile and scenario -CCIT-E test (one epoch is 0.5 s)

Figure 5.40: Picture of CCIT-E test environment facing south-east

The velocity RMS errors of the proposed direct vector HSGPS and conventional HSGPS (that using block processing techniques) in this scenario are summarized in Table 5.10. One can see that the proposed algorithm outperforms the conventional one by 21%, 50%, and 13% in the east, north and up velocity axis, respectively.

Table 5.10: Velocity RMS error -CCIT-E test

Velocity RMS Errors	Direct	Conventional
East (m/s)	0.17	0.24
North (m/s)	0.02	0.04
Up (m/s)	0.13	0.15

5.5 Summary

In this section, three field tests were processed and analyzed in order to assess the direct velocity estimation algorithm for high-sensitivity receivers. The performance of the proposed direct velocity estimation method was compared to the conventional two-stage velocity estimation algorithm and the effectiveness of the proposed algorithm was shown and validated.

The improvement of the Doppler estimated by using this direct vector receiver will be further assessed in the next chapter, which focuses on the benefits of integrating such Doppler measurements with PDR as compared to the MLE of Doppler.

Chapter Six: **HIGH SENSITIVITY GNSS/PDR INTEGRATION**

This chapter investigates the benefits of Doppler measurements estimated by using direct vector receivers. The HSGNSS/PDR integration algorithm used in this thesis is first presented. Field test results are then shown and analyzed.

6.1 HSGNSS/PDR integration algorithms

The focus of this chapter is to investigate the benefits of Doppler measurements estimated by using the direct vector receivers on PDR integration. It is also well known that Doppler measurements convey user velocity and heading information. Thus it is expected that by tightly integrating HSGPS Doppler measurements with PDR, there would be some improvement over the velocity estimation and heading estimation. If both pseudorange and Doppler measurements are used, the benefits of Doppler will be obscured. Moreover, pseudorange measurements in harsh environments would be erroneous and degrade benefits brought by the Doppler. Regarding the HSGPS Doppler/PDR integration, Renaudin et al (2012) has analyzed performance and showed the benefits are slight and strongly depend on the type of indoor environments. This chapter extends such work and only the Doppler measurements from both conventional and direct vector high sensitivity receivers are used for integration.

6.1.1 System model

The state vector for the PDR filter is given in equation (6.1) and includes the user's east, north and up coordinates in the l- frame, i.e. E, N, U , the user's horizontal and vertical velocities, heading and receiver's clock drift term in units of m/s.

$$\mathbf{x} = \left[E, \;\; N, \;\; U, \;\; v_h, \;\; \theta, \;\; v_v, \; c\dot{d}t \right] \tag{6.1}$$

It can be seen that the clock bias term does not appear, which is due to the fact that only Doppler measurements are used and no pseudorange measurements have been used to update the integration filter.

The dynamic equations of east, north, and up positions obey the classic PDR mechanization, which is

$$\begin{aligned} \dot{E} &= v_h \sin(\theta) \\ \dot{N} &= v_h \cos(\theta) \\ \dot{U} &= v_v \end{aligned} \tag{6.2}$$

The horizontal velocity, vertical velocity, user heading and receiver clock drift terms are all modeled as random walk and are driven by the following process noise shown:

$$\begin{aligned} \dot{v}_h &= \eta_{v_h} \\ \dot{v}_v &= \eta_{v_v} \\ \dot{\theta} &= \eta_\theta \\ c\ddot{d}t &= \eta_{cdt} \end{aligned} \tag{6.3}$$

In equation (6.3), η_{v_h} , η_{v_v} , η_θ , η_{cdt} are the white Gaussian process noise for the corresponding state elements. The spectral density of the clock drift error noise is computed using the clock model given in Brown & Hwang (1997). For computing random walk frequency noise, the PSD coefficients of h_{-2} timing standard is set as 10^{-20}; detailed treatment of this subject can be found in Brown & Hwang (1997).

With the system dynamic model described in equations (6.1), (6.2) and (6.3), there are some systematic errors that should be noted. The PDR derived velocities are distinct from GNSS Doppler derived velocities. By taking advantages of the repetitive pattern of

human gait cycles, the PDR algorithm can detect step events. On the other hand, GNSS Doppler derived velocities represents the averaged Doppler within the integration interval. These Doppler derived velocities may exhibit a systematic error which is in accord with the cycle of the human gait. In general, there are some errors (oscillatory discrepancies) between PDR and GNSS Doppler derived velocities and these errors are systematic for the dynamic model given above.

6.1.2 Measurement model

For the tight integration of HSGPS Doppler values with PDR algorithms, three measurements are used to update the system, namely Doppler measurements from receivers, heading estimated from such sensors and step length updates from step detection algorithms.

6.1.2.1 Doppler updates

The Doppler measurements used for update can be obtained either from conventional block processing receiver or from the direct vector receiver. The observation equation for Doppler is

$$\delta \mathbf{f}_D = \begin{bmatrix} \hat{f}_{D,1} \\ \hat{f}_{D,2} \\ \vdots \\ \hat{f}_{D,M} \end{bmatrix}_{Filter} - \begin{bmatrix} f_{D,1} \\ f_{D,2} \\ \vdots \\ f_{D,M} \end{bmatrix}_{Rx} = \frac{1}{\lambda}\mathbf{H}_{\dot{\rho},M\times 3}\begin{bmatrix} \delta v_e \\ \delta v_n \\ \delta v_u \end{bmatrix} + \frac{1}{\lambda}\mathbf{1}_{M\times 1}\delta cdt + \begin{bmatrix} \eta_{f_D,1} \\ \eta_{f_D,2} \\ \vdots \\ \eta_{f_D,M} \end{bmatrix}$$
$$= \begin{bmatrix} \frac{1}{\lambda}\mathbf{H}_{\dot{\rho},M\times 3}T_{3\times 3} & \frac{1}{\lambda}\mathbf{1}_{M\times 1} \end{bmatrix}\begin{bmatrix} \delta v_h \\ \delta\theta \\ \delta v_v \\ \delta cdt \end{bmatrix} + \boldsymbol{\eta}_{\mathbf{f}_D} \tag{6.4}$$

In equation (6.4), $\begin{bmatrix} \hat{f}_{D,1} & \hat{f}_{D,2} & \cdots & \hat{f}_{D,M} \end{bmatrix}^T_{Filter}$ are the filter predictions and $\begin{bmatrix} f_{D,1} & f_{D,2} & \cdots & f_{D,M} \end{bmatrix}^T_{Rx}$ are the measurements from the receiver. The subscript M is the number of available satellites, η_f is the noise induced by the receiver, $H_{\dot{\rho},1\times 3} = \begin{bmatrix} -\cos(\varepsilon)\sin(\alpha), & -\cos(\varepsilon)\cos(\alpha), & -\sin(\varepsilon) \end{bmatrix}$ is the design matrix from velocities to pseudorange rates, ε and α are the elevation angles and azimuth angles for each satellites, λ is the wavelength of the transmitted GNSS signal, and the $T_{3\times 3}$ matrix transforms horizontal, heading and vertical axes into ENU axes and is defined as

$$T_{3\times 3} = \begin{bmatrix} \sin(\theta) & v_h\cos(\theta) & 0 \\ \cos(\theta) & -v_h\sin(\theta) & 0 \\ 0 & 0 & 1 \end{bmatrix} \tag{6.5}$$

6.1.2.2 Step length updates

Accelerometers or other pedometers are often used to detect and estimate step lengths and to update the integrated solution. For the test conducted in this thesis, the inertial sensors are fixed on the backpack, so that the detection of steps is not a major concern in this thesis. Since there are many reliable and robust algorithms for step length detection,

and methods of step length estimation have reached a level of accuracy that can be used in practice as discussed in Section 2.2.3, it is not an issue in this thesis. For the step length measurement used herein, a step event is first detected by using accelerometers (Godha et al 2006) and the step length is calculated using an averaged reference velocity. In this way, the step length estimation error will be very small, namely

$$SL = v_h \Delta t_{step} + \eta_{SL} \tag{6.6}$$

where SL is the user's step length, Δt_{step} is the step duration and η_{SL} is the measurement noise for the step lengths.

6.1.2.3 Heading updates

In terms of heading update, there are many alternative sensors that can be used, such as magnetometers, gyroscopes, etc. If the heading information from these sensors is very reliable and accurate in the long term, it will then be very hard to assess the benefits of using GNSS Doppler measurement to constrain the long term heading drift. In order to fully assess whether Doppler measurements are beneficial for the long term heading accuracy, the heading integrated from the LCI vertical gyroscope is used for this update. As no gyro error model is used, the heading will be drifting during the period of data collection. The heading update equation is simply

$$\theta_{obs} = \theta + \eta_\theta \tag{6.7}$$

In equation (6.7), θ_{obs} is the heading observation obtained by integrating vertical gyroscopes and η_θ is the measurement noise for the heading observation.

6.2 Field Tests and Performance Analysis

In this section, three data sets will be tested. The indoor scenarios, sky plots and C/N_0 profiles for these scenarios have been already shown in Chapter 5, and will not be listed again. Only the integration results will be presented and analyzed herein.

The objective is to investigate the benefits of Doppler estimated by using direct vector receiver over the one using the conventional block processing method. It is convenient to assess the performance of the HSGNSS/PDR tight integration using both types of observations. In the following paragraphs, the performance of the PDR-only solution, HSGNSS/PDR tight integration with Doppler from the above conventional method and the proposed method will be assessed.

6.2.1 Engineering Block

The indoor scenario has been already shown, and the environments are nearly entirely obscured by the concrete walls. On one side of the building, there are some glass windows, as it is shown in Figure 5.6. Due to the fact that when the user is static, Doppler measurements will have little ability to constrain heading drift, hence only the period when the subject is moving is analyzed. Four navigation solutions are computed, namely PDR-only solution, PDR integrated with conventional GPS plus GLONASS Doppler (PDR+HSGNSS conv.), PDR integrated with proposed Doppler for GPS plus GLONASS (PDR+HSGNSS dir.), and PDR integrated with proposed Doppler for GPS-only

(PDR+HSGPS dir.). In this way, both the benefits from direct vector receiver and GLONASS capability can be assessed.

Figure 6.1 shows the position error of the above four navigation solutions. It is apparent that as time evolves, the east and north positioning errors by integrating Doppler measurements from direct vector receiver are much better than all the other solutions. By integrating PDR with conventional GNSS Doppler measurements, the positioning accuracy actually experiences some degradation. Moreover, it could also be observed that even with the proposed direct receiver, the GPS plus GLONASS solution slightly improves the solution in the vertical direction, while GPS-only solution performs a little better in the north and east direction.

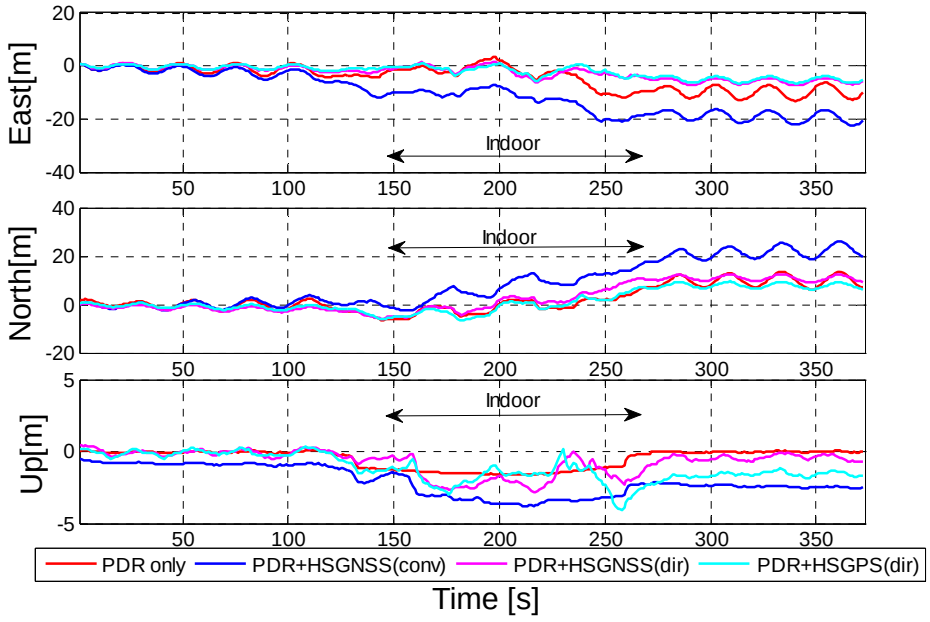

Figure 6.1: Position error plot – engineering block

Figure 6.2 shows the velocity error of these four navigation solutions. Most of the time, the curves are too close to each other, and no obvious conclusions could be made. All the

RMS error statistics for position and velocity are summarized in Table 6.1. In the position domain, PDR integrated with either GPS only or GPS plus GLONASS Doppler by using proposed algorithm outperform the other two in both east and north direction. The benefits of adding GLONASS are not obvious, since the GLONASS satellite signals in this indoor scenario may be more affected by the multipath in certain directions. As shown in north direction, the RMS north position error of GPS-only solution is only 4.80 m, while the solution with GPS plus GLONASS is 6.80 m. However, there are some improvements in the vertical velocity domain by using GPS plus GLONASS over GPS-only case.

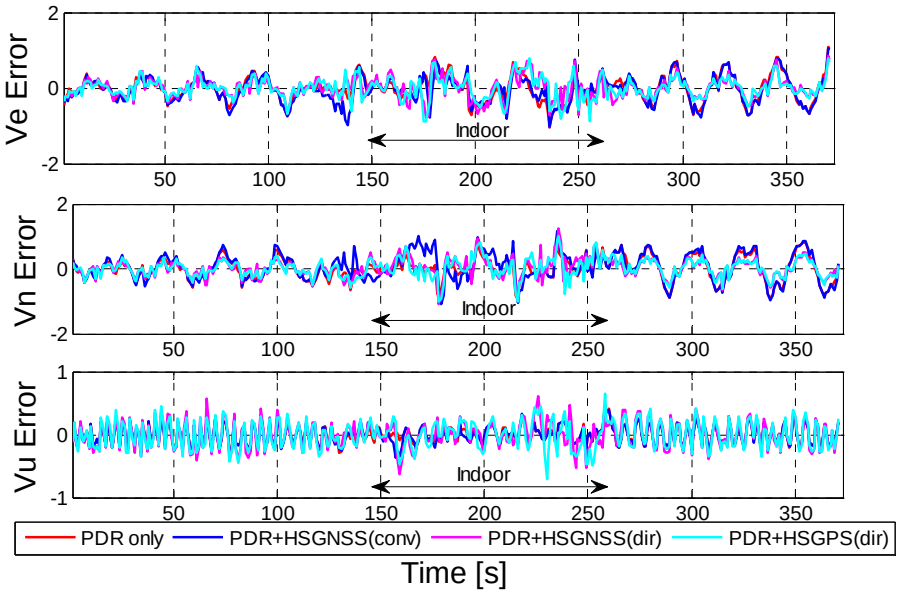

Figure 6.2: Velocity error plot - engineering block

In Table 6.1, the RMS velocity errors for the integrated solutions are very similar. And such results may obscure the position domain improvements. The reason for this is two-fold. First, these RMS statistics are based on whole trajectory, so the averaged statistics

are not enough to quantify the improvements. Second, RMS errors only reflect the relative variations, whose propagation in time is much slower than the bias.

Table 6.1: Position and velocity RMS errors – engineering block

	Position RMS Error [m]			Velocity RMS Error [m/s]		
	East	**North**	**Up**	**East**	**North**	**Up**
PDR-only	6.32	5.77	0.82	0.34	0.35	0.15
PDR+HSGNSS (conventional)	13.00	12.51	2.30	0.28	0.42	0.15
PDR+HSGPS (direct)	3.07	4.80	1.80	0.32	0.28	0.21
PDR+HSGNSS (direct)	3.52	6.80	1.11	0.28	0.29	0.20

In Table 6.2, the velocity mean errors are summarized for outdoor and indoor scenarios separately. It shows that indoors, the mean north velocity errors using the direct vector receiver are significantly improved as compared to the conventional HSGNSS solution results. For the east and up directions, they are about at the same level. Even indoors, GLONASS helps improve the east and up velocity estimation accuracy. Recall that the one sigma uncertainty of the reference east, north and vertical velocity in the worst case is only about 0.009 m/s, 0.008 m/s and 0.007 m/s, hence the RMS velocity improvements and mean velocity error improvements discussed here are still much greater than the one sigma uncertainty.

Table 6.2: Mean velocity errors – engineering block

	Outdoor Mean Error [m/s]			Indoor Mean Error [m/s]		
	East	**North**	**Up**	**East**	**North**	**Up**
PDR-only	0.01	0.04	-0.02	-0.03	0.06	0.01
PDR+HSGNSS (conventional)	-0.01	-0.01	-0.02	-0.03	0.12	0.01
PDR+HSGPS (direct)	-0.01	-0.03	-0.02	-0.03	0.06	0.04
PDR+HSGNSS (direct)	-0.01	0.03	-0.01	-0.02	0.09	0.01

Figure 6.3 shows the heading estimated from the PDR-only solution, conventional HSGPS/PDR integrated solution, and direct HSGPS/PDR integrated solution. The heading angles for the PDR updates are obtained by integrating vertical gyro. As the heading errors from the vertical gyro accumulate, a long term heading drift appears. If the Doppler measurements are beneficial, integrating these measurements will no doubt constrain the long term heading drift. If Doppler measurements are themselves erroneous (noisy and biased), it will be difficult to estimate velocities, let alone to provide heading information.

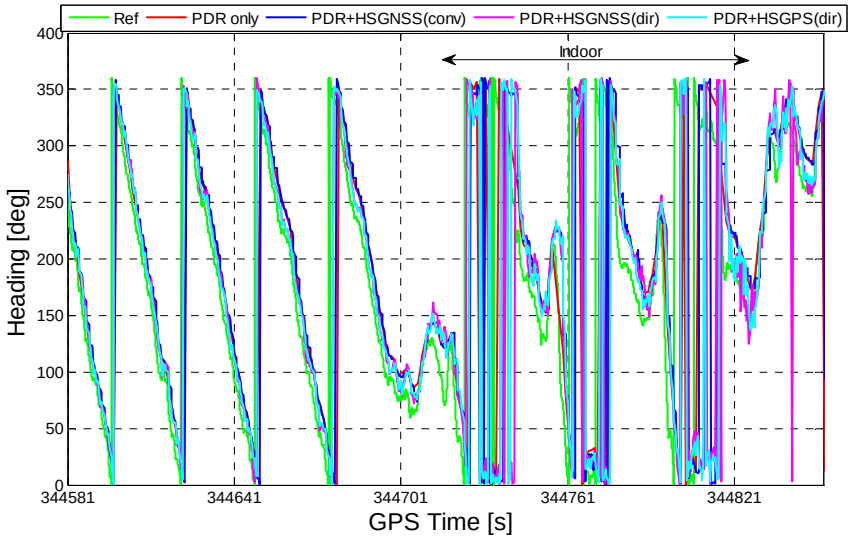

Figure 6.3: Heading of various navigation solutions - engineering block

The corresponding heading errors are plotted in Figure 6.4. It is obvious that there are large 'spikes' for all navigation solutions, which are due to changes of direction along with a decrease of velocity. For example, considering that a pedestrian is trying to change direction, he will probably first slow down and then make a turn. If this is the case, then the heading error will grow during this period. This scenario is also validated by the correlation between heading errors and the vertical gyro angular rates in all solutions.

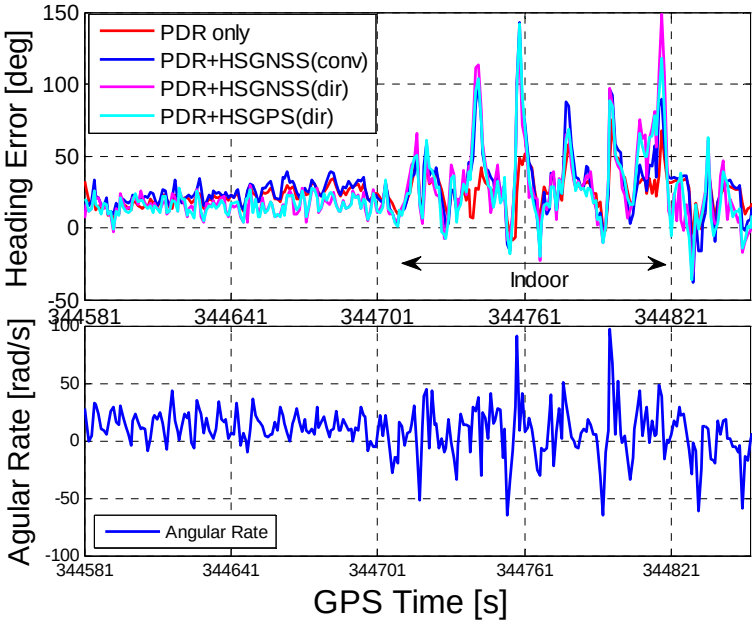

Figure 6.4: Heading errors and angular rates – engineering block

All trajectories for these navigation solutions are plotted in Figure 6.5. In order to facilitate the in-motion alignment of inertial sensors, the pedestrian performed a circular motion at the beginning and the end, and these circular motions look like loops outside the building. From the reference trajectory, these loops overlap each other. However, from the figure, the PDR-only solution suffers long term heading drifts, thus the final loops are biased. By integrating PDR with conventional GNSS Doppler measurements, the final solutions are even more biased than the PDR-only solution. For the PDR integrated with Doppler measurements from the direct vector receiver, these biases are much smaller as compared to those of the above two. Regarding the addition of GLONASS, there is no apparent conclusion that can be made from this figure. It can be

observed that the solution using GPS-only performs similarly to that using GPS plus GLONASS. This might be due to the fact that multipath effects in these types of environments dominate the signals and obscure the benefits of additional satellites.

Figure 6.5: Trajectories of various navigation solutions – engineering block

6.2.2 MacEwan Student Centre

In this section, the second indoor scenario is tested. The indoor scenario is shown in Figure 5.17, which has large open spaces, such as shopping malls. The objective is to assess the benefits of Doppler estimated from the direct vector receiver. Only GPS will be considered for convenience. Analogously, only the navigation solutions will be presented and analyzed herein.

Figure 6.6 shows the position errors of the PDR-only solution, conventional HSGPS Doppler integrated with PDR solution (PDR+HSGPS conv.), and direct vector receiver's Doppler integrated with PDR solution (PDR+HSGPS dir.). The indoor period is from 300 s to about 600 s. It can be seen that before entering the building, the three solutions are very similar. When entering the MacEwan Student Centre, position errors in the PDR-only solution and the conventional HSGPS/PDR integrated solution begin to accumulate, up to a maximum of 15 to 20 m in the east and north direction. When it comes to direct HSGPS/PDR integrated results, the errors accumulate at a lower rate and are much smaller than those of the other two cases.

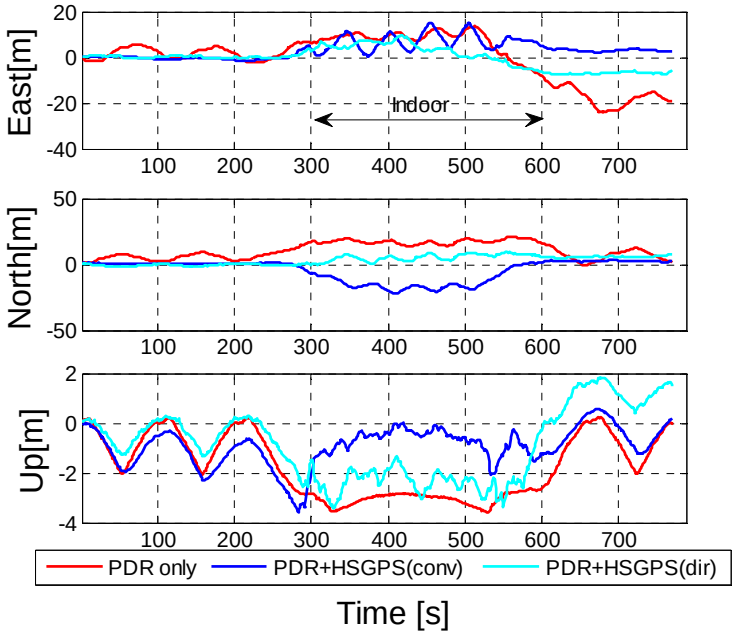

Figure 6.6: Position errors of PDR-only, PDR plus conventional HSGPS, and PDR plus direct HSGPS

Figure 6.7 shows the velocity errors of the three navigation solutions. The direct HSGPS/PDR integrated results seem slightly better than the other two, as least in the horizontal plane. However, no definitive conclusions could be made from these results.

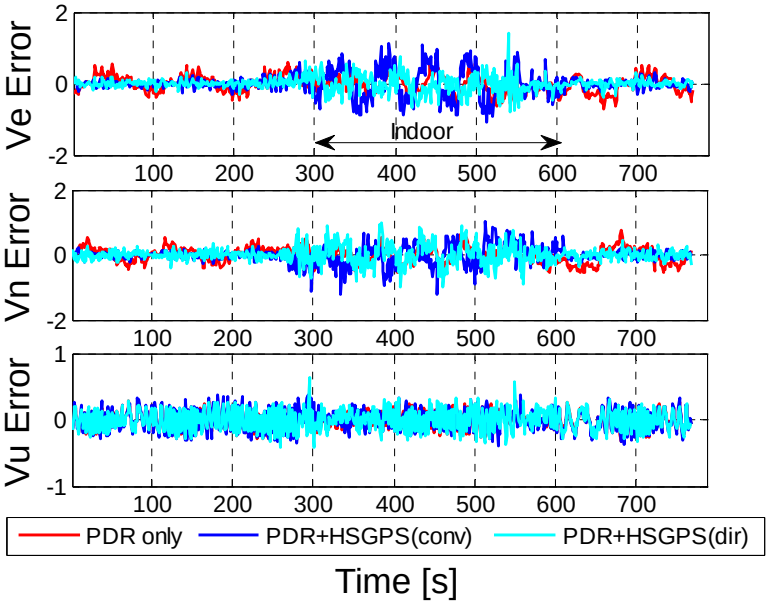

Figure 6.7: Velocity errors of various navigation solutions

In order to compare the performance of these navigation solutions, the RMS error statistics of the position and velocity are summarized in Table 6.3. It can be seen that the RMS position errors for the PDR-only solution are slightly larger than the conventional HSGPS /PDR integrated results. The overall RMS position errors have been decreased by integrating with Doppler measurements. However, by integrating PDR with conventional HSGPS Doppler measurements, the overall velocity RMS errors get worse as compared to PDR only solution. This is due to the fact that indoor multipath significantly affects conventional HSGPS Doppler measurements that use block processing technique. But, the direct HSGPS /PDR integration results clearly have the best performance among all

three solutions. Again, it should be noted that the maximum one sigma uncertainty of the reference east, north and vertical velocity is about 0.02, 0.018 and 0.015 m/s, as shown in Figure 5.18. Moreover, the RMS error differences in Table 6.3 are still relatively larger than these 'worst case' one sigma uncertainty. As a result, the improvements can be quantified and do reflect the benefits of integrating PDR with direct vector HSGPS.

Table 6.3: Position and velocity RMS errors - MacEwan

	Position RMS Error [m]			Velocity RMS error [m/s]		
	East	**North**	**Up**	**East**	**North**	**Up**
PDR-only	10.20	12.48	2.15	0.25	0.24	0.14
PDR+HSGPS (conventional)	5.18	9.14	1.20	0.31	0.26	0.16
PDR+HSGPS (direct)	4.48	4.67	1.66	0.20	0.15	0.16

Figure 6.8 shows the heading estimated from the PDR-only solution, the conventional HSGPS/PDR integrated solution and the direct HSGPS/PDR integrated solution. It can be seen that at the very beginning, the headings estimated from all three solutions are very similar to the ground truth. However, as the subject enters the building and then walks outside in several circles, the accumulated heading errors are different. The heading estimated in the PDR-only and conventional HSGPS/PDR solution are very similar from the beginning to the end, while the heading estimated from the direct HSGPS/PDR integrated system outperforms the above two.

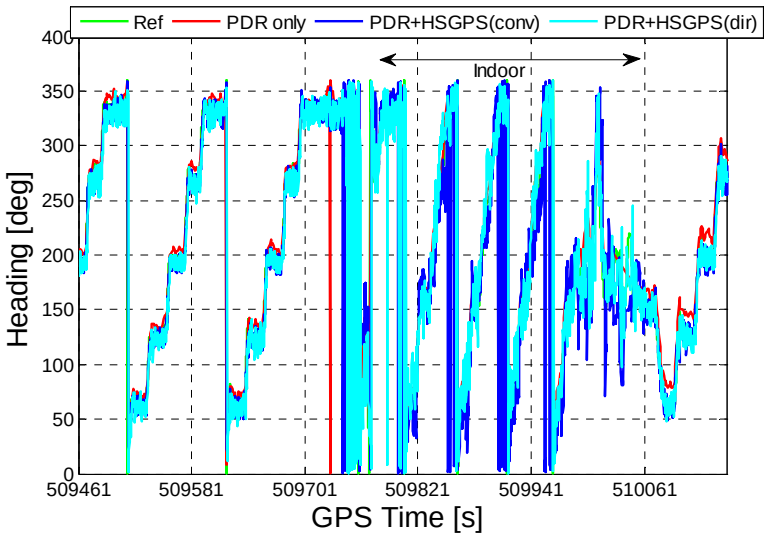

Figure 6.8: Headings of various navigation solutions

The heading errors are plotted in Figure 6.9. There are apparent oscillatory patterns in all three solutions. The main reason for this is due to user direction changes. The angular rate of the vertical gyroscope is plotted at the bottom of the figure. An obvious correlation between the heading errors and vertical angular rates is present. The other reason for this oscillatory behaviour is due to the fact that horizontal velocities are relatively small and are changing periodically. The heading observability directly depends on such Doppler or velocity estimates, hence heading errors will also change periodically.

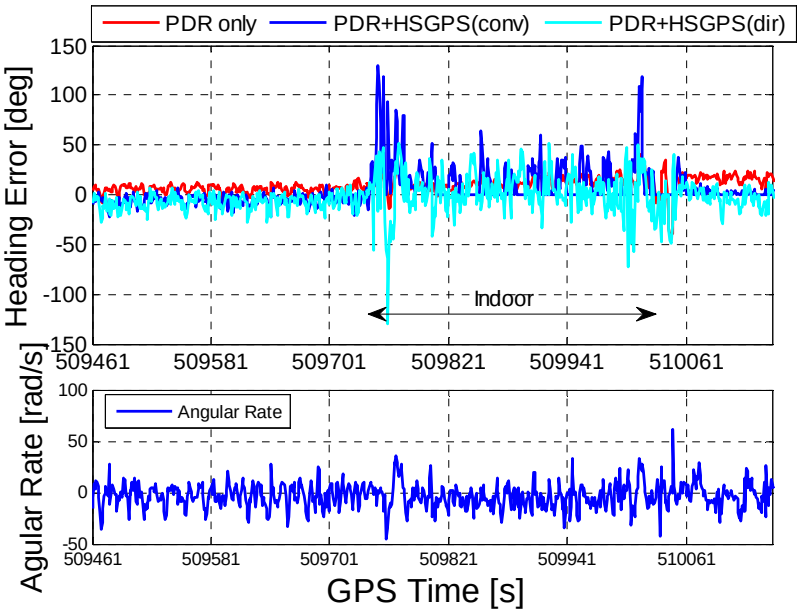

Figure 6.9: Heading errors and angular rates

Finally, the trajectories of various navigation solutions are plotted in Figure 6.10. It can be seen that the direct HSGPS/PDR integrated results outperform the other two. Integrating conventional HSGPS with PDR actually biases the final solution.

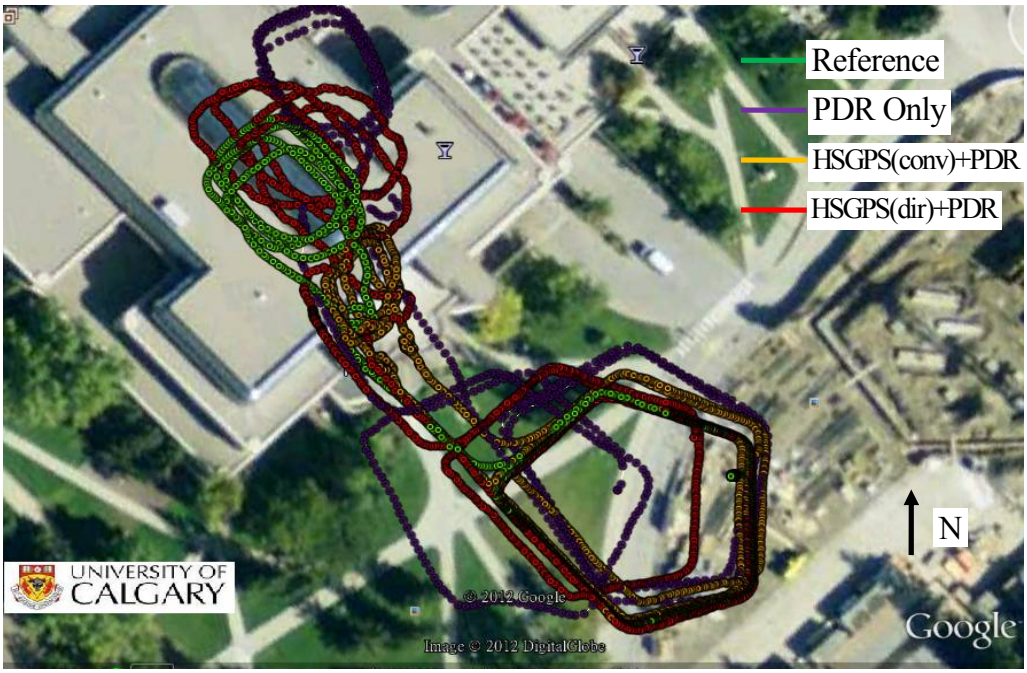

Figure 6.10: Trajectories of various navigation solutions -MacEwan

It is observed that the Doppler measurements estimated by using direct HSGNSS is superior to the Doppler estimated by using conventional block processing methods. Furthermore, integrating Doppler measurements with PDR algorithms is beneficial to dealing with the long term heading drift.

6.2.3 CCIT-ICT

In this section, the entire data set is used in order to evaluate the long term effectiveness of integration results in complex indoor environments. The indoor scenarios and satellite C/N_0 were discussed in Section 5.4.3. There are eight GPS satellites in view used for direct vector processing in order to obtain the Doppler measurements. Coherent

integration for high sensitivity processing was set to 500 ms. The time length of the data is 4300 second (1 hr 12 min).

The position errors of PDR-only, PDR integrated with conventional HSGPS, and PDR integrated with direct vector HSGPS solutions are plotted in Figure 6.11. One can see that east and north position errors in the PDR-only solution are drifting by up to 100 - 200 m during this time period. These errors mainly come from heading drift. When integrating PDR with conventional HSGPS, due to the limitations and large noise of Doppler measurements, the benefits of heading drift constraint are limited. However, when integrating PDR with direct vector HSGPS, the errors in all axes are reduced.

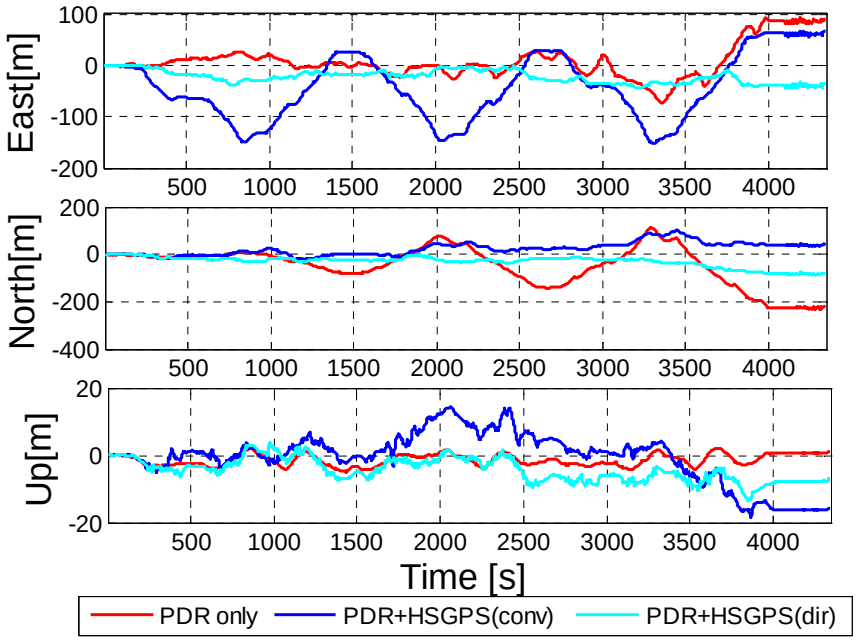

Figure 6.11: Position errors of various navigation solutions – CCIT-ICT Test

The velocity errors of these three navigation solutions are plotted in Figure 6.12. No apparent conclusions can be made based on this figure. However, it should be noted that

a small error in the velocity domain will keep accumulating and results in large positioning errors as shown in Figure 6.11. Thus the mean velocity errors will affect the navigation solution accuracy in this sense. Discussion of mean velocity errors will occur based on Table 6.5. The test statistics of RMS errors are summarized in Table 6.4.

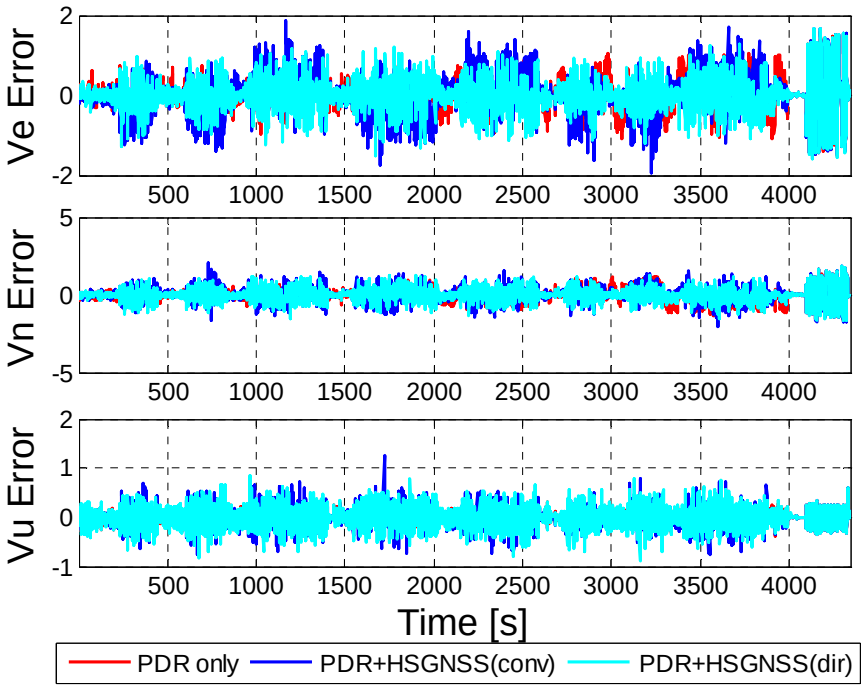

Figure 6.12: Velocity errors of various navigation solutions

Referring to Table 6.4, when integrating PDR with conventional HSGPS, the east positioning error nearly doubles. However, when integrating PDR with the proposed direct vector HSGPS, the resulting east positioning error is only about 76% of the PDR only solution. The effectiveness can also be observed in the north component. Velocity RMS error improvements can also be seen when comparing PDR integrated with the proposed direct vector HSGPS with the PDR integrated with conventional HSGPS,

yielding improvements of 16% and 9% for the east and north velocity, respectively. When comparing the PDR integrated with proposed direct vector HSGPS to the PDR-only solution, the east velocity RMS error actually increases about 0.04 m/s.

Table 6.4: Position and velocity RMS errors – CCIT test

	Position RMS Error [m]			Velocity RMS error [m/s]		
	East	North	Up	East	North	Up
PDR-only	33.65	93.18	2.23	0.38	0.47	0.16
PDR+HSGPS (conventional)	75.71	35.41	7.55	0.49	0.45	0.20
PDR+HSGPS (direct)	25.52	37.45	5.53	0.41	0.41	0.20

The velocity mean errors of all three navigation solutions are summarized in Table 6.5. It can be observed that when integrating PDR with the proposed direct vector HSGPS, the east and north velocity biases are significantly smaller than the other two. In turn, this limits the position error growth over time, as shown above.

Table 6.5: Mean velocity errors - CCIT test

	Velocity Mean error [m/s]		
	East	North	Up
PDR-only	0.02	-0.06	0.00
PDR+HSGPS (conventional)	0.02	0.01	0.00
PDR+HSGPS (direct)	-0.01	-0.01	0.00

The heading errors of the various navigation solutions are shown on the upper part of Figure 6.13. It can be seen that the errors of both integrated solutions are fluctuating when the subject is walking. There are several reasons for this. First, it is because the indoor environment encountered herein is much more complex than the scenarios

discussed in the previous two sections (Section 6.2.1 and Section 6.2.2). Second, the subject is changing direction frequently in this data set due to the building structure. Third, during some epochs, the GPS signal is too weak to generate any better Doppler measurements (like totally blocked case). However, in general, it can be seen that PDR integrated with the proposed direct vector HSGPS performs better than PDR integrated with conventional HSGPS. Regarding the heading errors of the PDR-only solution, it is drifting away slowly and finally has a bias of about -60 deg. When integrating PDR with Doppler measurements (either conventional or direct vector HSGPS), this long term drifting is significantly reduced. The middle part Figure 6.13 shows the reference heading obtained with the Novatel SPAN^{TM} system. The estimated one sigma uncertainty in heading is below 0.05 deg from the beginning to the end. The bottom plot in Figure 6.13 is the angular rate of the vertical gyro. It can be seen that there is a correlation between the angular rate and heading errors. When the user changes his/her direction rapidly, the estimated Doppler heading errors grow.

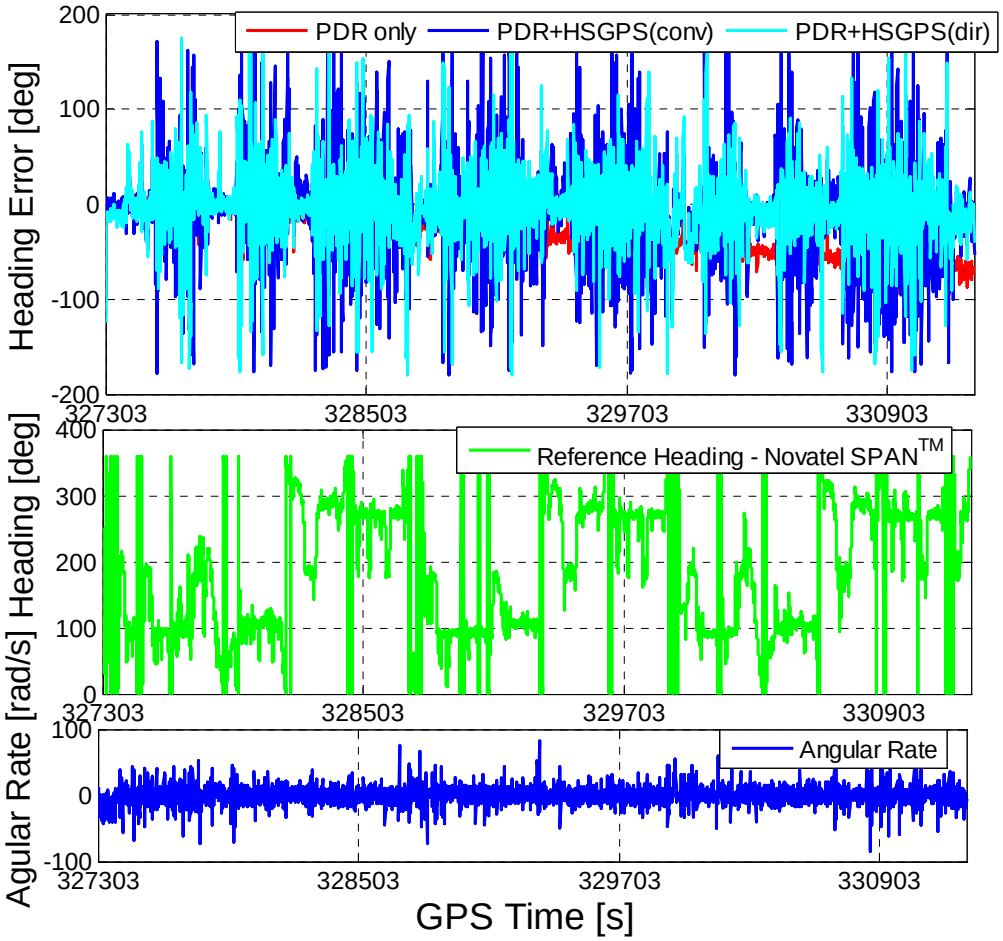

Figure 6.13: Heading errors of various navigation solutions, reference heading (middle) and angular rate (bottom) – CCIT-ICT test

Finally, the trajectories of various navigation solutions are plotted in Figure 6.14. It can be observed that for this time interval (4300 s), the PDR-only solution is drifting far away from the reference, but the general shape of the trajectory is reasonable. When integrating the PDR with conventional HSGPS, not only is the trajectory biased, but the general shape also deteriorates. However, when integrating PDR with the proposed direct vector

HSGPS, one can observe a bias reduction and the general shape of the trajectory is in much better agreement with the reference trajectory.

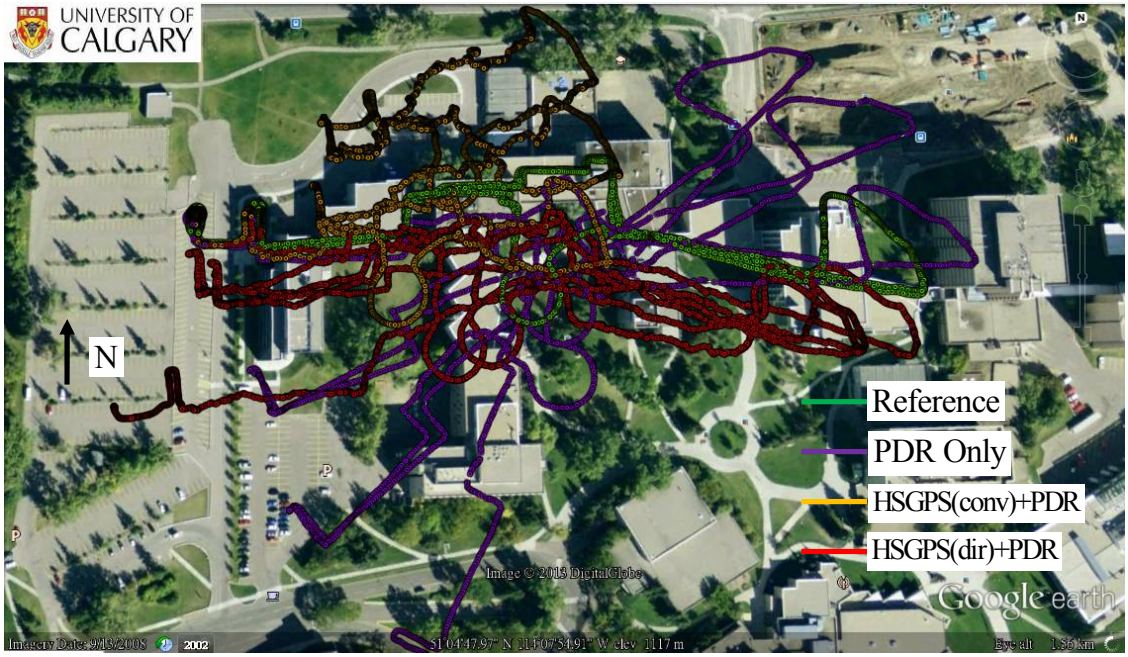

Figure 6.14: Trajectories of various navigation solutions – CCIT –ICT test

From these results, it can be concluded that the Doppler from the direct vector HSGPS can benefit the PDR as compared to the conventional HSGPS Doppler measurements that uses block processing techniques.

6.3 Summary

This chapter focused on evaluating the benefits of using Doppler measurements from a direct vector receiver to integrate with PDR for indoor navigation. Two indoor scenarios were tested, and results validated the effectiveness of such measurements over conventional high sensitivity GNSS receivers.

Chapter Seven: **CONCLUSIONS AND RECOMMENDATIONS**

This chapter first summarizes the main conclusions of the research work presented in this thesis and then lists several possible ways that would further improve, enhance and extend the work conducted herein.

The major goals of this research were three-fold. The first was to characterize the Doppler errors of high sensitivity receivers in indoor environments in order to derive a signal and multipath model that could be used for the assessment of navigation accuracy. The second was to develop a more robust and reliable Doppler and velocity estimation algorithm for indoor navigation applications as compared to that of conventional techniques. Third, was to evaluate the performance of tightly integrated high sensitivity GNSS/PDR solutions with real indoor data. A software program with a direct vector receiver architecture that has GLONASS capability was also developed as part of this work and was used to process and analyse the results shown in previous chapters.

7.1 Conclusions

The velocity estimated by using direct vector receiver architecture showed better results than the conventional high sensitivity receiver based on a block processing techniques. It was shown that the proposed method performs as well as or better than the conventional method in terms of Doppler and velocity estimation accuracy, which is consistent with the theoretical development presented in the thesis. The benefits depend on the user-satellite geometry and multipath effects on each satellite. Detailed conclusions that are drawn from the work presented in the thesis are as follows:

1) *Doppler Error Characterization Indoors*

i) In indoor multipath dense environments, the Doppler estimated by using block processing techniques can be biased due to the combined effects of multipath and user dynamics.

ii) This bias can be related to indoor multipath channel statistics, such as Ricean factors, averaged multipath azimuth, averaged multipath azimuth beamwidth, averaged multipath elevation angles, and corresponding beamwidths, as shown in Equation (4.17)

iii) Both Ricean and Rayleigh fading can be considered as special cases of the generalized directional multipath models proposed herein. For example, whenever the beamwidths of multipath signals are infinite, or equivalently stating that phase is uniformly distributed, the signal envelope obeys the Rayleigh or Ricean distribution.

iv) By processing real indoor data, the proposed model was found to be consistent with the observed results, even though some approximations were used.

2) *Improved Velocity/Doppler Estimation Indoors*

i) In indoor environments, the CRLB of Doppler is related not only to the signal to noise ratio, but also to multipath statistics, such as the multipath AOAs and Ricean factor.

ii) The proposed direct velocity estimation method indoors performs as good as or better than the conventional method (see Table 5.1, Table 5.2, Table 5.3 and Table 5.4). The benefit of the direct velocity estimation is composed of

two parts as shown in equation (5.23). The first part comes from satellite geometry, which is the ratio between two geometry dependent factors. The second part comes from the direct processing itself, which automatically weights each Doppler estimate according to its CRLB.

iii) The Doppler CRLB using the direct vector receiver is also derived and shown in equation (5.24). It was further shown that the proposed method actually has a weighted harmonic average process over Doppler measurements for all satellites as well as weightings that are based on user-satellite geometry.

iv) For the j^{th} satellite Doppler estimation, a loose bound has been shown in equation (5.27). When the j^{th} satellite's CRLB weight is smaller than the j^{th} satellite's geometry dependent factor weight, the Doppler estimated by using the proposed algorithm begins to outperform the Doppler estimated by block processing techniques. This indicates that the direct vector receiver will be beneficial when the LOS signals are partially visible for all satellites in view.

v) By jointly processing GPS and GLONASS data, more signal power is effectively used for velocity estimation and that power is more centralized around the true value as compared to the GPS-only case. In outdoor environments, the performance of the direct vector HSGNSS is about the same as that of conventional HSGNSS. When it comes to indoors, the improvements of direct velocity HSGNSS over the conventional HSGNSS velocity estimation accuracy are environment and case dependent. For the three data sets, six indoor scenarios (MacEwan, Engineering building, CCIT-

B, CCIT-C, CCIT-D, CCIT-E) considered here, the minimum velocity RMS error improvement is about 11%.

vi) In indoor environments, the performance of direct vector HSGNSS velocity estimation by using GPS plus GLONASS and GPS-only is about the same, but both cases outperform the conventional HSGNSS.

3) HSGNSS/PDR Integration for Consistent Navigation Indoors

i) Office Space Indoor Environments (engineering block): As shown in Table 6.1, when integrating PDR with Doppler estimated by the proposed method, there are apparent improvements over the solutions by integrating PDR with conventional high sensitivity GNSS Doppler measurements. For example, in the position domain, the proposed method improves the performance in east, north and up axes by 71%, 45% and 51%, respectively. In terms of the velocity RMS errors, there is no significant improvement in the east axis. However, the north velocity RMS error improves by 30%.

ii) Office Space Indoor Environments (engineering block): It was found that by integrating PDR with Doppler from conventional HSGNSS receiver, the final solution gets worse in all axes as compared with a PDR-only solution. This means that conventional Doppler measurements are not beneficial for heading estimates. This is due to the fact that multipath can dominate the signals and such Doppler measurements cannot provide any more useful information than the PDR.

iii) Office Space Outdoor Environments (engineering block): When comparing the PDR-only solution with the PDR integrated with the proposed direct vector GNSS receiver in this indoor environment, it was observed that the east positioning accuracy improves by 44%, and the north and vertical positioning accuracy degrade by 17% and 35%, respectively. In terms of overall velocity RMS errors, the proposed method improves the east, and north velocity axes by 18%, and 17%. However, the vertical direction has been degraded by 33%.

iv) Office Space Indoor Environments (engineering block): The benefits of using GLONASS along with GPS in this type of indoor environments were not apparent.

v) Large Space Indoor Environments (MacEwan): From Table 6.3, it can be seen that when integrating PDR with conventional Doppler measurements, the east, north and vertical positioning accuracies improve by 49%, 27% and 26%, respectively. If integrating PDR with Doppler measurements estimated by using direct vector receiver, the east, north and vertical positioning accuracy improve by 56%, 63%, and 46%, respectively. These results suggest that by integrating the Doppler measurements from the proposed direct vector receiver with PDR algorithm, the long term heading drifts are reduced more effectively than the conventional method.

vi) Complex indoors (CCIT-ICT): From this long data set (4300 s), it can be observed that if PDR is integrated with the proposed direct vector HSGPS, the overall east and north position estimation accuracy are improved by 24% and

60% compared to the PDR-only solution. The east velocity estimation accuracy of these two solutions is about the same, while the north velocity estimation gets better by 13% as compared to PDR-only solution. It can also be seen that east and north velocity estimation improves by about 16% and 9% when comparing the PDR integrated with the proposed direct vector HSGPS to the PDR integrated with the conventional HSGPS solutions.

4) Analysis of GNSS DOP Metrics

i) The term geometry dependent factor (λ) was defined and used to better characterize the user satellite geometry and assess the benefits of the proposed direct vector receiver. This factor proved to be useful. For example, it was conveniently used for the following assessments, to describe a few:

- GNSS DOP metrics could be analytically expressed as the ratio between the geometry dependent factor (λ) and the norm of the design matrix for this axis. For example, EDOP, NDOP, UDOP and TDOP have closed forms as shown in equations (A.40), (A.41), (A.42) and (A.43). By using these formulas, there is no need to compute the inverse of the gram matrix ($H^T H$) when computing DOP metrics.
- The DOP degradation between range and pseudorange measurements could also be clearly expressed as the ratio between two individual geometry dependent factors, as shown in equation (A.34).

ii) The DOP correlation coefficients (ρ) were derived and given in equations (A.45),(A.46), (A.47), (A.47), (A.48), (A.49) and (A.50). These terms

theoretically illustrate the correlation between DOP metrics. Real data clearly showed that $\rho_{UDOP\&TDOP}$ is very close to one, which indicates a strong correlation between errors in the vertical axis and time axis, while $\rho_{EDOP\&TDOP}$ and $\rho_{NDOP\&TDOP}$ may vary due to the satellite geometry. By carefully selecting satellites according to these coefficients, a controlled correlation of errors between east, north, vertical and time axes could be obtained.

7.2 Recommendations

The following recommendations are made for potential future investigations on high sensitivity GNSS Doppler and velocity estimation for indoor navigation purposes:

iii) Extend the direct vector receiver to estimate the position from code phase dimensions. In this thesis only the velocity and Doppler are estimated by using the direct vector receiver. Analogously, one could extend this to the position and code phase domains with multiple systems.

iv) Develop a more efficient way to obtain an estimate in the direct vector receiver. The direct estimation algorithm considered herein is actually a multiple dimension optimization problem. The search space is quite large when a good resolution is expected.

v) Further investigate the effects of low quality oscillators. The oscillator used in all the experiments was an OCXO, which is highly stable. It would be

interesting to evaluate the Doppler and velocity estimation by using the direct vector receiver architecture with a low quality oscillator such as TCXOs.

vi) Implement a GNSS software receiver with the navigation feedback. The current GSNRx^{TM} that has the block processing functionality only uses a reference trajectory to control the centre of the correlator outputs in code phase and Doppler domains. This gives the best achievable results one can obtain with real data. It would be more useful to control the centre of the correlators using the navigation feedback.

vii) A more thorough analysis of the direct velocity and/or position method as a detection problem is needed. The work shown in previous chapters tackled the problem in terms of estimation. It would be more beneficial if the threshold of a successful detection could be found.

viii) Further investigations on optimizing the high sensitivity GNSS receiver performance indoors are needed. The combined effects of the quality of oscillators, user dynamics and multipath distortions all affect the Doppler and velocity estimation.

REFERENCES

Abdi, A., and M. Kaveh (2002) "A Parametric Model for the Distribution of the Angle of Arrival and the Associated Correlation Function and Power Spectrum at the Mobile Station," *IEEE Transaction on Vehicular Technology*, *Vol. 51*(No. 3), pp.425-434.

Afzal, H., V. Renaudin and G. Lachapelle (2011) "Multi-magnetometer based perturbation mitigation for indoor orientation estimation," *NAVIGATION*, *Vol.58*, 4, pp.279-292

Aminian, B., V. Renaudin, D. Borio, and G. Lachapelle (2010) "Indoor Doppler Measurement and Velocity Characterization Using a Reference-Rover Receiver," in *Proceedings of ION GNSS 2010*, The Institute of Navigation, Portland, OR, September 21-23, pp. 3069-3079

Andersson, E. (2012) *Motion Classification and Step Length Estimation for GPS/INS Pedestrian Navigation*, Department of Electrical Engineering, MSc. thesis, , KTH. pp.1-60

Babu, R., and J. Wang (2006) "Ultra-Tight Integration of Pseudolites With INS," in *Proceedings of ION IEEE/ION PLANS 2006*, San Diego CA, pp.705-714

Beauregard, S., and H. Haas (2006) "Pedestrian Dead Reckoning: A Basis for Personal Positioning," in *Proceedings of the 3rd Workshop on Positioning, Navigation and Communication (WPNC'06)*, edited, pp. 27-35.

Ben-Israel, A. (1999) "The Change of Variables Formula using Matrix Volume," *SIAM J. Matrix Analysis*, *21*, 13. pp300-312

Bertz, J. W., and K. R. Kolodziejski (2009) "Generalized theory of code tracking with an early-late discriminator part1-lower bound and coherent processing," *IEEE Transactions on aerospace and Electronic Systems*, *Vol 45*(No. 4), pp1538-1550

Borio, D., N. Sokolova, and G. Lachepelle (2010) "Doppler Measurement Accuracy in Standard and High-Sensitivity GNSS Receivers," *IET Radar, Sonar & Navigation*, Vol 5, No. 6, pp.657-665

Brenner, J. (2011), *Wideband Frequency Discriminator And Radiolocalization Receiver*, US Patent US7966359 B2, 20 pages

Brown, A., and M. Sturza (1990) "The Effects of Geometry on Integrity Monitoring Performance," in *Proceeding of ION ITM 1990*, Atlantic City, NJ, pp.121-129

Bullock, J. B., M. Foss, G. J. Geier, and M. King (2006) "Integration of GPS with Other Sensors and Network Assistance," [Chapter 9] in *Understanding GPS: Principles and Applications*, E. Kaplan and C. J. Hegarty, Artech House, Inc., Norwood, MA, pp.459

Closas, P., C. Fernandez-Prades, and J. A. Fernandez-Rubio (2007) "Maximum Likelihood Estimation of Position in GNSS," *IEEE Signal Processing Letters*, *Vol 14*(No 5), pp.359-362.

Counselman, C. C. (1989) "Multipath-rejecting GPS Antennas," in *Proceedings of the IEEE*, *Vol. 87*(No. 1), pp.86-91.

Duda, K. (2010) "Accurate Guaranteed Stable Sliding DFT," in *IEEE Signal Processing Magazine*, pp. 124-127.

El-Sheimy, N. (2007) *Inertial Techniques and INS/DGPS Integration*, ENGO 623 Course Notes, Department of Geomatics Engineering, University of Calgary, Canada

Fontan, F. P., and P. M. Espineira (2008), *Modelling the Wireless Propagation Channel*, John Wiley&Sons Ltd.

Foxlin, E. (2005) "Inertial Head-tracker Sensor Fusion by a Complementary Separate-Bias Kalman Filter," *IEEE Computer Graphics and Applications*, *Vol. 25*(No. 6), pp.38-46.

Gaggero, P. (2008) *Effect of oscillator instability on GNSS signal integration time*. Masters Thesis, Institute of Microtechnology, University of Neuchtel, Switzerland, pp1-200

Gebre-Egziabher, D., A. Ravzi, P. Enge, J. Gautier, S. Pullen, B. Pervan, and D. Akos (2005) "Sensitivity and Performance Analysis of Doppler-Aided GPS Carrier-Tracking Loops," *Navigation*, *Vol. 52*(No. 2), pp.49-60.

Giremus, A., J.-Y. Tourneret, and V. Calmettes (2005) "Joint Detection/Estimation of Multipath Effects for the Global Positioning System," paper presented at ICASSP-05, Philadelphia, pp.17-20

Giremus, A., J.-Y. Tourneret, and V. Calmettes (2007) "A Particale Filtering Approach for Joint Detection/Estimation of Multipath Effects on GPS Measurements," *IEEE Transaction on Signal Processing*, *Vol.55*(No 4), pp. 1275-1285

Godha, S., G. Lachapelle, and C. M. E. (2006) "Integrated GPS/INS System for Pedestrian Navigation in a Signal Degraded Environment," in *Proceeding of ION GNSS 2006*, (Forth Worth, 26-29 Sep, Session A5), The Institute of Navigation, 14 pages.

Goldsmith, A. (2005) *Wireless Communicaiton*, Cambridge Univeristy Press.

Goyal, P., V. J. Ribeiro, H. Saran, and A. Kumar (2011) "Strap-Down Pedestrian Dead-Reckoning System," in *International Conference on Indoor Positioning and Indoor Navigation (IPIN) 2011*, Guimaraes, Portugal, pp1-7.

Gustafson, D., J. Dowdle, and K. Flueckiger (2000) "A Deeply Integrated Adaptive GPS-Based Navigator with Extended Range Code Tracking," in *Proceeding of IEEE/ION PLANS 2000*, pp.118-124

He, Z., M. Petovello, and G. Lachapelle (2012a) "Modeling HSGPS Doppler Errors in Indoor Environments for Pedestrian Dead-Reckoning," in Proceeding of ION ITM, ION, Newport Beach, CA, Jan30-Feb1.

He, Z., M. G. Petovello, and G. Lachapelle (2012b) "Improved Velocity Estimation with High-Sensitivity Receivers in Indoor Environments," paper presented at ION GNSS 2012, Nashville, TN.

ICD-GLONASS (2008) GLONASS Interface Control Document (Version 5.1), Engineering, R. I. o. S. D.

ICD-GPS-200D (2004) *Navstar GPS Space Segment/Navigation User Interfaces*, ARINC Engineering Services, El Segundo, CA

Jones, F. (2004) *Honors Calculus III/IV*, MATH 221/222 Lecture Notes

Jovancevic, A., A. Brown, S. Ganguly, J. Noronha and B. Sirpatil (2004) "Ultra Tight Coupling Implementation Using Real Time Software Receiver," in *Proceeding of ION GNSS 2004*, Institute of Navigation, Long Beach, CA, pp.1578-1586

Juang, J.-C., and Y.-H. Chen (2009) "Phase/Frequency Tracking in a GNSS Receiver," *IEEE Journal of Selected Topics in Signal Processing*, *Vol. 3*(No.4), pp10.

Kay, S. M. (1993a), *Fundamentals of Statistical Signal Processing:Estimation theory*, Prentice Hall.

Kay, S. M. (1993b), *Fundamentals of Statistical Signal Processing: Detection Theory*, Prentice Hall.

Kiesel, S., M. M. Held, and G. F. Trommer (2007) "Realization of a Deeply Coupled GPS/INS Navigation System Based on INS-VDLL Integration," in *Proceeding of ION NTM 2007*, Institute of Navigation, , San Diego CA, pp.522-531

Kim, H. S., S. C. Bu, G. I. Jee, and C. G. Park (2003) "An Ultra-Tightly Coupled GPS/INS Integration Using Federated Filtering," in *Proceeding of ION GNSS 2003*, Institute of Navigation, Portland, OR, pp. 2878-2885

Kjærgaard, M. B., H. Blunck, T. Godsk, T. Toftkjær, D. L. Christensen, and K. Grønbæk (2010) "Indoor Positioning Using GPS Revisited," paper presented at 8th international conference on Pervasive Computing.

Kubo, Y., T. Kindo, A. Ito, and S. Sugimoto (1999) "DGPS/INS/Wheel Sensor Integration for High Accuracy Land-Vehicle Positioning," in *Proceeding of ION GPS 1999*, Nashville, TN, pp.555-564

Lachapelle, G. (2009) *Advanced GNSS Theory And Applications*, ENGO 625 Course Notes, Department of Geomatics Engineering, University of Calgary, Canada

Lachapelle, G. (2007) "Pedestrian navigation with high sensitivity GPS receivers and MEMS," *Personal and Ubiquitous Computing*, *Volume 11*, pp.481-488.

Ladetto, Q. (2000) "On foot navigation : continuous step calibration using both complementary recursive prediction and adaptive Kalman filtering," in Proceedings of ION GPS 2000, Salt Lake City, UT, pp1735-1740

Ladetto, Q., and B. Merminod (2002) "Digital Magnetic Compass and Gyroscope Integration for Pedestrian Navigation," presented in *9th Saint Petersburg International Conference on Integrated Navigation Systems*, Saint Petersburg, Russia.

Ladetto , Q., V. Gabaglio, and B. Merminod (2001) "Two different approaches for augmented GPS pedestrian navigation," presented in *International Symposium on Location Based Services for Cellular Users*, Locellus.

Larson, K., D. Akos, and L. Marti (2008) "Characterizing Multipath from Satellite Navigation Measurements in Urban Environments," paper presented at IEEE Communication Society CCNC 2008.

Leppakoski, H., J. Kappi, J. Syrjarinne, and J. Takala (2002) "Error Analysis of Step Length Estimation in Pedestrian Dead Reckoning," in *Proceeding of ION GPS 2002*, , Portland, pp. 1136-1142

Li, T., M. Petovello, G. Lachapelle, and C. Basnayake (2010) "Ultra-tightly Coupled GPS/Vehicle Sensor Integration for Land Vehicle Navigation," *Navigation*, *Vol. 57*(No. 4), pp.263-274.

Lin, T., J. T. Curran, C. O'Driscoll, and G. Lachapelle (2011) "Implementation of a Navigation Domain GNSS Signal Tracking Loop," in Proceeding of ION GNSS 2011, Portland, OR, pp.3644-3651

Ma, M. S. H., C. O'Driscoll, and G. Lachapelle (2011) "Automatic Parameter Determination for Real-Time Acquisition using Frequency Domain Methods in a High Sensitivity Software Receiver," in *Proceeding of ION ITM2011*, San Diego, pp. 1257-1269

Mardia, K. V. (1975) "Statistics of Directional Data," *Journal of the Royal Statistical Society. Series B*, *Vol. 37*(No. 3), pp.349-393.

Mats, B. (1996) "Integrated GNS/Inertial Fault Detection Availability," *Navigation*, *Vol. 43*(No. 2), pp.339-358.

Mezentsev, O., J. Collin, and G. Lachapelle (2003) "Vehicular Navigation in Urban Canyons Using a High Sensitivity GPS Receiver Augmented with a Medium Grade IMU," paper presented at 10th Saint Petersburg International Conference on Integrated Navigation Systems, Russia.

Mezentsev, O., G. Lachapelle, and J. Collin (2005) "Pedestrian Dead Reckoning - A Solution to Navigation in GPS Signal Degraded Areas," *Geomatica*, *Vol. 59*(No.2), pp175-182.

Misra, P. N., R. I. Abbot, and E. M. Gaposchkin (1996) "Integrated Use of GPS and GLONASS: PZ-90– WGS84 Transformation," in *Proceeding of ION ITM 1996*, Institute of Navigation, Kansas City, Missouri, pp.307-314

Misra, P. and P. Enge (2001) *Global Positioning System - Signals, Measurements, and Performance*, Ganga-Jamuna Press.

Mitrikas, V. V., S. G. Revnivykh, and E. V. Bykhanov (1998) "WGS84/PZ90 Transformation Parameters Determination Based On Laser And Ephemeris Long-Term GLONASS Orbital Data Processing," in *Proceeding of ION ITM 1998*, Institute of Navigation, Nashville, TN, pp.1625-1635

Natali, F. D. (1984) "AFC Tracking Algorithms," *IEEE Transactions on Communications*, *Vol. 32*(No. 8), pp.13.

Novatel (2010), SPAN™ Brochure, Calgary, Canada

O'Driscoll, C., G. Lachapelle, and M. Tamazin (2011) "Dynamic Duo – Combined GPS/GLONASS Receivers in Urban Environments," in *GPS World*, pp. 51-58.

O'Driscoll, C., and D. Borio (2009) *GNSS Receiver Design*, ENGO638 Course Notes, Department of Geomatics Engineering, University of Calgary, Canada

O'Driscoll, C., M. G. Petovello, and G. Lachapelle (2008)"Impact of Extended Coherent Integration Times on Weak Signal RTK in an Ultra-Tight Receiver," paper presented at NAV08 Conference, Royal Institute of Navigation, London, 28-30 October.

O'Driscoll, C., M. Tamazin, D. Borio, and G. Lachapelle (2010) "Investigation of the Benefits of Combined GPS/GLONASS for High Sensitivity Receiver," in *Proceeding of ION GNSS 2010*, Institute of Navigation, Portland, OR, pp.2840-2851

O'Driscoll, C., D. Borio, M. G. Petovello, T. Williams, and G. Lachapelle (2009) "The Soft Approach: A Recipe for a Multi-System, Multi-Frequency GNSS Receiver," in *Inside GNSS Magazine*, edited, pp. 46-51.

Ohlmeyer, E. J. (2006) "Analysis of an Ultra-Tightly Coupled GPS/INS System in Jamming," in *Proceeding of IEEE/ION PLANS 2006*, pp44-53

Oppenheim, A. V., R. W. Schafer, and J. R. Buck (1998) *Discrete-time Signal Processing*, 2nd ed., Prentice Hall.

Pany, T. (2010) *Navigation Signal Processing for Gnss Software Receivers*, Artech House.

Pany, T., and B. Eissfeller (2006) "Use of a Vector Delay Lock Loop Receiver for GNSS Signal Power Analysis in Bad Signal Conditions," in *Proceeding of IEEE/ION PLANS 2006*, pp.893-903

Pany, T., H. Euler, and J. Winkel (2012) "Difference Correlators – Does Indoor Carrier Phase Tracking Allow Indoor RTK?," in *Inside GNSS*,May/June

Pany, T., et al. (2009) "Performance of a Partially Coherent Ultra-Tightly Coupled GNSS/INS Pedestrian Navigation System Enabling Coherent Integration Times of Several Seconds to Track GNSS Signals Down to 1.5 dBHz," in *Proceeding of ION GNSS 2009, Institute of Navigation*, Savannah Georgia, pp.919-934

Papoulis, A. (1965) *Probability, Random Variables and Stochastic Process*, McGraw-Hill Book Company.

Petovello, M. G., C. O'Driscoll, G. Lachapelle, and D. Borio (2008), Architecture and Benefits of an Advanced GNSS Software Receiver, *Journal of GPS2008*, *Vol. 7*(No. 2), 156-169.

Petovello, M.G., O. Mezentsev, G. Lachapelle and M.E. Cannon (2003) "High Sensitivity GPS Velocity Updates For Personal Indoor Navigation Using Inertial Navigation Systems," in Proceedings of GPS2003 (Session F6, Portland, OR, 9-12 September), The Institute of Navigation

Petovello, M. G. (2003) *Real-Time Integration of a Tactical-Grade IMU and GPS for High-Accuracy Positioning and Navigation*, PhD Thesis, published as UCGE Report No. 20173, Department of Geomatics Engineering, University of Calgary, Calgary, pp.64-79

Petovello, M. G., and G. Lachapelle (2006) "Comparison of Vector-Based Software Receiver Implementations with Application to Ultra-tight GPS/INS Integration," in Proceeding of ION GNSS 2006, Fort Worth TX, pp.1790-1799

Petovello, M. G., C. O'Driscoll, and G. Lachapelle (2008) "Weak Signal Carrier Tracking Using Extended Coherent Integration with an Ultra-Tight GNSS/IMU Receiver," paper presented at ENC2008, Toulouse, 23-25 April.

Polischuk, G. M., et al. (2002) "The Global Navigation System GLONASS: Development and Usage in the 21st Century," paper presented at 34th Annual Precise Time and Time Interval (PTTI) Meeting.

Proakis, J. (2001) *Digital Communications, 4th edition*, McGraw-Hill Companies, Inc.

Randell, C., C. Djiallis, and H. Muller (2003) "Personal position measurement using dead reckoning," paper presented at Proceedings of the Seventh International Symposium on Wearable Computers, October 2003.

Renaudin, V., M. Susi, and G. Lachapelle (2012) "Step Length Estimation using Handheld Inertial Sensors," *Sensors,* pp.8507-8525.

Renaudin, V., Z. He, and M. G. Petovello (2012) "Characterization of the Impact of Indoor Doppler Errors on Pedestrian Dead Reckoning," in Proceeding of ION/IEEE PLANS, Myrtle Beach, SC, pp.969-979

Revenivykh, S. (2012) "GLONASS Ground Control Segment: Orbit, Clock, Time Scale and Geodesy Definition," presented at ION GNSS 2012, Institute of Navigation, Nashville, TN.

Rife, D. C., and R. R. Boorstym (1974) "Signle-Tone Parameter Estimation from Discrete-Time Observations," *IEEE Transactions on Information Theory*, *Vol. IT-20*(No. 5), pp591-598.

Robach, U. (2000) *Positioning and Navigation Using the Russian Satellite System GLONASS*, Ph.D thesis, University FAF Munich, pp.1-167

Salychev, O. S., V. V. Voronov, M. E. Cannon, R. Nayak, and G. Lachapelle (2000) "Low Cost INS/GPS Integration: Concepts and Testing," in *Proceeding of ION NTM 200*0, Institute of Navigation, Alexandria, VA, pp.98-105

Schwarz, K. P., and M. Wei (1999) *INS/GPS Integration for Geodetic Applications*, ENGO623 Course Notes, Department of Geomatics Engineering, University of Calgary, Canada

Sennott, J., and D. Senffner (1997) "Robustness of Tightly Coupled Integrations for Real-Time Centimeter GPS Positioning," in *Proceeding of ION GPS 1997*, Institute of Navigation, Alexandria, VA.

Shin, S. H., and C. G. Park (2001) "Adaptive Step Length Estimation Algorithm Using Low-cost MEMS Inertial Sensors," paper presented at IEEE Sensors Applications Symposium, pp.1-5

Shin, S. H., M. S. Lee, and C. G. Park (2010) "Pedestrian Dead Reckoning System with Phone Location Awareness Algorithm," in Proceeding of ION/IEEE PLANS 2010, Institute of Navigation, pp.97-101.

Simon, M. K., S. M. Hinedi, and W. C. Lindsey (1995) *Digital Communication Techniques-Signal Design and Detection*, Prentice-Hall, NJ.

Soler, T., and L. D. Hothem (1988) "Coordinate System used in Geodesy: Basic Definitions and Concepts," *Journal of Surveying Engineering*, *114*, pp.84-97.

Soloviev, A., and J. Dickman (2011) "Extending GPS Carrier Phase Availability Indoors with a Deeply Integrated Receiver Architecture," *IEEE Wireless Communications*, Vol. 18, No.2, pp.36-44.

Soloviev, A., F. van Graas, and S. Gunawardena (2004) "Implementation of Deeply Integrated GPS/Low-Cost IMU for Reacquisition and Tracking of Low CNR GPS Signals," in *Proceeding of ION NTM 2004*, Institute of Navigation, pp.925-935

Soloviev, A., G. Gunawardena, and F. van Graas (2008) "Deeply Integrated GPS/Low-Cost IMU for Low CNR Signal Processing: Concept Description and In-Flight Demonstration," *Navigation*, *Vol. 55*(No. 1), pp.1-13.

Spangenberg, M., V. Calmettes, O. Julien, and J.-Y. Tourneret (2010) "Detection of Variance Changes and Mean Value Jumps in Measurement Noise for Multipath Mitigation in Urban Navigation," *Navigation*, *Vol. 51*(No. 1).

Spilker, J. J., Jr. (1996) "Fundamentals of Signal Tracking Theory," [Chapter 7] in *Global Positioning System: Theory And Applications*, Parkinson and J. J. J. Spilker, American Institute of Aeronautics and Astronautics, Inc.

Spilker, J. J., Jr. (1977) *Digital Communications by Satellite*, Prentice-Hall.

Stein, S., and J. J. Jones (1967) *Modern Communication Principles with application to digital signaling*, McGraw Hill Company.

Steingass, A., and A. Lehner (2004) "Measuring the Navigation Multipath Channel - A statistifcal analysis," paper presented at 2nd ESA Workshop on Satellite Navigation User Equipment Technologies.

Stephane Beauregard, H. H. (2006) "Pedestrian Dead Reckoning: A Basis for Personal Positioning," in *Proceedings of the 3rd Workshop on Positioning, Navigation and Communication (WPNC'06)*, edited, pp. 27-35.

Strang, G. (1988) *Linear Algebra and Its Applications*, Harcourt Brace Jovanovich.

Sun, D., M. G. Petovello, and M. E. Cannon (2008) "GPS/Reduced IMU with a Local Terrain Predictor in Land Vehicle Navigation," *International Journal of Navigation and Observation*.Vol 2008, 15pages, doi:10.1155/2008/813821

Tazartes, D. A., and J. G. Mark (1988) "Integration of GPS Receivers into Existing Inertial Navigation Systems," *Navigation*, *Vol. 35*(Vol. 1), pp.105-119.

Tepedelenlioglu, C., A. Abdi, G. B. Giannakis, and M. Kaveh (2001) "Estimation of Doppler spread and signal strength in mobile communications with applications to handoff and adaptive transmission," *Wireless Communications and Mobile Computing*, *1*, pp.221-242.

Titterton, D., and J. Weston (2004), *Strap-down Inertial Navigation Technology*, IET.

van Dierendonck, A. J. (1996) "GPS Receivers," [Chapter 8], in *Global Positioning System: Theory And Applications*, edited by B. Parkinson and J. J. J. Spilker, American Institute of Aeronautics and Astronautics, Inc.

van Dierendonck, A. J., P. Fenton, and T. Ford (1992) "Theory and Performance of Narrow Correlator Spacing in a GPS Receiver," *Navigation*, *Vol. 39*(No. 3), pp.265-283.

van Diggelen, F. (2009) *A-GPS Assisted GPS GNSS and SBAS*, ArtechHouse

van Graas, A. S. F., Maarten Uijt de Haag, Sandjeev Gunawardena, Michael Braasch (2005) "Comparison of Two Approaches for GNSS Receiver Algorithms: Batch

Processing and Sequential Processing Considerations," in *Proceeding of ION GNSS 2005*, Institute of Navigaiton, Long Beach, pp. 200-211

Vodhanel, M. T. (2012) *Problems in GPS Accuracy*, Ph.D thesis, Claremont Graduate University.

Ward, P. W., J.W. Betz and C.J. Hegarty (2006) "Satellite Signal Acquisition, Tracking, and Data Demodulation," [Chapter 5] in *Understanding GPS Principles and Applications*, E. D. Kaplan and C. J. Hegarty, Artech House.

Weil, L. R. (2010) "A High Performance Code and Carrier Tracking Architecture for Ground-Based Mobile GNSS Receivers," in Proceeding of ION ITM, Portland, OR, September 21-24, pp.3054-3068

APPENDIX A: GEOMETRIC ANALYSIS OF GNSS DOP METRIC

It is well known that RMS position or velocity errors depend largely on the geometry of the satellites. And the term DOP is often used to quantify such relationship. Given the measurement accuracy, one can directly determine the RMS errors of position and velocity. However, the DOP only provides a general characterization of the user-satellite geometry. In order to further assess the performance of the proposed direct vector receiver under bad signal conditions, algebraic and geometric interpretation of the DOP metrics are needed and thus introduced here. Most importantly, several novel terminologies are defined and used, in order to fully capture the user-satellite geometry, such as geometry dependent factor, joint DOPs, and DOP correlation coefficients. Closed form analytical expressions are also derived and given. With the theory developed in this appendix, the satellite geometry can be conveniently represented, compared and optimized for various navigation purposes. One major outcome is the use of the novel terminology to analytically characterize the benefits of a direct vector receiver, as proposed and discussed in the previous chapters.

A.1 Gram matrix, Volume, and DOP

In this section, an algebraic approach will first be briefly discussed to analyze the GNSS DOP metrics. Results developed in this section will be shown to be consistent with those obtained by geometric approach discussed in the succeeding sections.

In GNSS positioning and navigation, the rank of column and row space for the design matrix is four, which represent the east, north, up and clock dimensions. Let $\mathbf{H}$ denote the $M \times 4$ design matrix. In this case, M is the number of the available satellites as

$$\mathbf{H} = \begin{bmatrix} \mathbf{h}_E & \mathbf{h}_N & \mathbf{h}_U & \mathbf{h}_{Clk} \end{bmatrix}_{M \times 4} \tag{A.1}$$

where $\mathbf{h}_E$, $\mathbf{h}_N$ $\mathbf{h}_U$ and $\mathbf{h}_{Clk}$ are $M \times 1$ vectors, which can be determined by calculating the directional unit vector from the receiver to the satellite. Correspondingly, the DOP will then be obtained by computing $(\mathbf{H}^T\mathbf{H})^{-1}$ as

$$(\mathbf{H}^T\mathbf{H})^{-1} = \begin{bmatrix} EDOP^2 & * & * & * \\ * & NDOP^2 & * & * \\ * & * & UDOP^2 & * \\ * & * & * & TDOP^2 \end{bmatrix} \tag{A.2}$$

On the other hand, recall that the gram matrix is the matrix of all possible inner products of the vectors. The matrix $\mathbf{H}^T\mathbf{H}$ is by definition a gram matrix and has the following form:

$$\text{Gram}\left(\mathbf{h}_E, \mathbf{h}_N, \mathbf{h}_U, \mathbf{h}_{Clk}\right) = G = \mathbf{H}^T\mathbf{H} = \begin{bmatrix} \|\mathbf{h}_E\|^2 & \mathbf{h}_E^T\mathbf{h}_N & \mathbf{h}_E^T\mathbf{h}_U & \mathbf{h}_E^T\mathbf{h}_{Clk} \\ \mathbf{h}_N^T\mathbf{h}_E & \|\mathbf{h}_N\|^2 & \mathbf{h}_N^T\mathbf{h}_U & \mathbf{h}_N^T\mathbf{h}_{Clk} \\ \mathbf{h}_U^T\mathbf{h}_E & \mathbf{h}_U^T\mathbf{h}_N & \|\mathbf{h}_U\|^2 & \mathbf{h}_U^T\mathbf{h}_{Clk} \\ \mathbf{h}_{clk}^T\mathbf{h}_E & \mathbf{h}_{clk}^T\mathbf{h}_N & \mathbf{h}_{clk}^T\mathbf{h}_U & \|\mathbf{h}_{Clk}\|^2 \end{bmatrix} \tag{A.3}$$

where $\mathbf{h}_i = \begin{bmatrix} h_{i,1} \\ h_{i,2} \\ \vdots \\ h_{i,M} \end{bmatrix}$, $G_{ij} = \mathbf{h}_i^T\mathbf{h}_j$, $i, j \in \{E, N, U, Clk\}$

By comparing equations (A.2) and (A.3), one discovers that the square of the DOP values are the diagonal elements of the inverse of the gram matrix expressed as G^{-1}. Before computing the inverse of the gram matrix, the following properties are introduced to better understand the physical interpretation.

First, the term 'gram determinant', or called Gramian has the following relationship with the column vectors of the design matrix $\mathbf{h}_E, \mathbf{h}_N, \mathbf{h}_U, \mathbf{h}_{Clk}$ (Jones 2004):

$$\begin{aligned} \text{Gramian}\left(\mathbf{h}_E, \mathbf{h}_N, \mathbf{h}_N, \mathbf{h}_{Clk}\right) &= \left|\mathbf{H}^T\mathbf{H}\right| = \left\|\mathbf{h}_E \wedge \mathbf{h}_N \wedge \mathbf{h}_U \wedge \mathbf{h}_{Clk}\right\|^2 \\ \text{Gramian}\left(\mathbf{h}_E, \mathbf{h}_N, \mathbf{h}_U, \mathbf{h}_{Clk}\right) &= \left|\mathbf{H}^T\mathbf{H}\right| = \text{Volume}(\Xi\left(\mathbf{h}_E, \mathbf{h}_N, \mathbf{h}_U, \mathbf{h}_{Clk}\right))^2 \end{aligned} \tag{A.4}$$

In equation(A.4), $\wedge$ is the exterior product (Jones 2004), $\Xi(\bullet)$ denotes the parallelotope formed by the vectors inside the bracket. The upper equation shows that the Gramian is directly related to the exterior product of the vectors. The bottom equation shows that the Gramian of the design matrix is the square of the volume of the parallelotope formed by the vectors $\mathbf{h}_E, \mathbf{h}_N, \mathbf{h}_U, \mathbf{h}_{Clk}$. For example, the volume represents an area in a 2D case.

It is also known that the inverse of a square matrix is the adjoint of that matrix divided by its determinant (Strang 1988). In order to use the adjoint formula to compute the matrix inverse, the sub-matrix M_{ii} is defined as a matrix eliminating the i^{th} column and row from the Gram matrix (G). For example, $M_{11}, M_{22}, M_{33}, M_{44}$ are

$$
\begin{aligned}
M_{11} &= \begin{bmatrix} \circ & \circ & \circ & \circ \\ \circ & G_{22} & G_{23} & G_{24} \\ \circ & G_{32} & G_{33} & G_{34} \\ \circ & G_{42} & G_{43} & G_{44} \end{bmatrix}, |M_{11}| = \text{Gramian}\left(\mathbf{h}_N, \mathbf{h}_U, \mathbf{h}_{Clk}\right) \\
M_{22} &= \begin{bmatrix} G_{11} & \circ & G_{13} & G_{14} \\ \circ & \circ & \circ & \circ \\ G_{31} & \circ & G_{33} & G_{34} \\ G_{41} & \circ & G_{43} & G_{44} \end{bmatrix}, |M_{22}| = \text{Gramian}\left(\mathbf{h}_E, \mathbf{h}_U, \mathbf{h}_{Clk}\right) \\
M_{33} &= \begin{bmatrix} G_{11} & G_{12} & \circ & G_{14} \\ G_{21} & G_{22} & \circ & G_{24} \\ \circ & \circ & \circ & \circ \\ G_{41} & G_{42} & \circ & G_{44} \end{bmatrix}, |M_{33}| = \text{Gramian}\left(\mathbf{h}_E, \mathbf{h}_N, \mathbf{h}_{Clk}\right) \\
M_{44} &= \begin{bmatrix} G_{11} & G_{12} & G_{13} & \circ \\ G_{21} & G_{22} & G_{23} & \circ \\ G_{31} & G_{32} & G_{33} & \circ \\ \circ & \circ & \circ & \circ \end{bmatrix}, |M_{44}| = \text{Gramian}\left(\mathbf{h}_E, \mathbf{h}_N, \mathbf{h}_U\right)
\end{aligned}
\tag{A.5}
$$

It is obvious that the sub-matrix is itself a smaller gram matrix and the determinant of the sub-matrix $|M_{ii}|$ is the $i^{th} - i^{th}$ minor of the gram matrix G. By using the adjoint formula of matrix inverse, the diagonal elements of inverse of G can be represented as

$$
\begin{aligned}
\left(G^{-1}\right)_{ii} &= \frac{(-1)^{2i}\left|M_{ii}\right|}{\left|G\right|} = \frac{\left|M_{ii}\right|}{\left|G\right|} \\
\left(G^{-1}\right)_{11} &= EDOP^2 = \left(\frac{\text{Volume}(\Xi(\mathbf{h}_N,\mathbf{h}_U,\mathbf{h}_{Clk}))}{\text{Volume}(\Xi(\mathbf{h}_E,\mathbf{h}_N,\mathbf{h}_U,\mathbf{h}_{Clk}))}\right)^2 \\
\left(G^{-1}\right)_{22} &= NDOP^2 = \left(\frac{\text{Volume}(\Xi(\mathbf{h}_E,\mathbf{h}_U,\mathbf{h}_{Clk}))}{\text{Volume}(\Xi(\mathbf{h}_E,\mathbf{h}_N,\mathbf{h}_U,\mathbf{h}_{Clk}))}\right)^2 \\
\left(G^{-1}\right)_{33} &= UDOP^2 = \left(\frac{\text{Volume}(\Xi(\mathbf{h}_E,\mathbf{h}_N,\mathbf{h}_{Clk}))}{\text{Volume}(\Xi(\mathbf{h}_E,\mathbf{h}_N,\mathbf{h}_U,\mathbf{h}_{Clk}))}\right)^2 \\
\left(G^{-1}\right)_{44} &= TDOP^2 = \left(\frac{\text{Volume}(\Xi(\mathbf{h}_E,\mathbf{h}_N,\mathbf{h}_U))}{\text{Volume}(\Xi(\mathbf{h}_E,\mathbf{h}_N,\mathbf{h}_U,\mathbf{h}_{Clk}))}\right)^2
\end{aligned}
\tag{A.6}
$$

In equation (A.6), the EDOP, NDOP, UDOP and TDOP are mathematically related with the ratio between volumes composed of difference vectors. And in the next section, the DOP will be derived with some geometric interpretations.

In this section, an algebra approach to derive the GNSS DOP metrics is introduced. It has also been found that Vodhanel (2011) used novel parallelepiped theory to analyze GPS accuracy. But Vodhanel neglects the impact of clock bias term on ENU DOPs, which might weaken the conclusions he made. For example, when computing PDOP, the effect of clock axis should also be considered, otherwise it will lead to incorrect results.

The algebra approach showed in this section, along with the geometric method to be developed in the next section all rest on the real 4D coordinates (east, north, up, and time) for GNSS applications. Some DOP related terminologies will then be defined in order to better characterize the satellite-user geometry. The impacts of introducing a time axis on DOP are also analyzed and illustrated.

A.2 Geometric Analysis of DOP

In the following, a geometric approach will be developed in order to better interpret the user-satellite geometry. First, an illustrative 2D example (north and east) will be discussed. Then, the discussions will be extended to two different 3D coordinates: east, north and vertical dimensions and also east, north and time dimensions. Finally, the real situation that is composed of 4D (east, north, vertical, and time) will be considered and closed form analytical formulas will be derived.

A.2.1 DOPs of 2D coordinate-East, North

To begin, consider a simple 2D satellite geometry as shown Figure A.1. The user is in the origin of the coordinate system, as shown with $\circ$. Two satellites are orthogonally placed along the east and north axes. Satellite 1 is along the east direction and satellite 2 is in the north direction with respect to the receiver. The arrows represent the unit direction vector $(\mathbf{e}_1, \mathbf{e}_2)$ pointing from the receiver to the satellites.

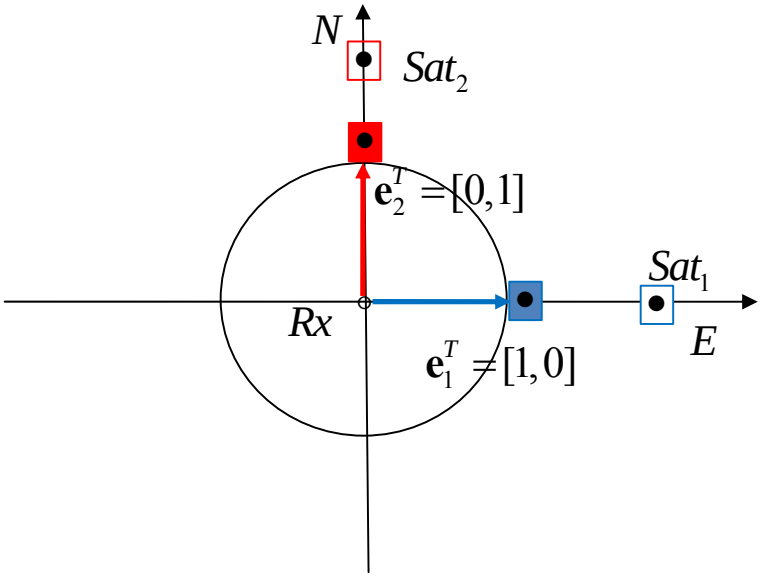

Figure A.1: 2D orthogonal satellite geometry

Assume that satellite 1 and satellite 2 are transmitting ranging signals. The satellite-user geometry is orthogonal between these two satellites. The receiver can use these ranging signals to compute its position in the east and north coordinates. The observations and estimation model in this scenario can be written as

$$\text{Observation: } \begin{bmatrix} \Delta\rho_1 \\ \Delta\rho_2 \end{bmatrix} = \begin{bmatrix} 1 & 0 \\ 0 & 1 \end{bmatrix} \begin{bmatrix} \Delta E \\ \Delta N \end{bmatrix}$$

$$\text{or } \Delta\boldsymbol{\rho} = H\Delta\mathbf{r} = \left[\mathbf{h}_E, \mathbf{h}_N\right]\Delta\mathbf{r}$$

$$\text{or } \Delta\boldsymbol{\rho} = \begin{bmatrix} \mathbf{e}_1^T \\ \mathbf{e}_2^T \end{bmatrix}\Delta\mathbf{r} \qquad \text{(A.7)}$$

$$\text{Estimation: } \Delta\hat{\mathbf{r}} = (H^T H)^{-1} H^T \Delta\boldsymbol{\rho}$$

Equation (A.7) illustrates the fact that a change of east position (ΔE) of the receiver will only cause a change of the satellite 1's range measurement ($\Delta\rho_1$)and ΔE will not affect the satellite 2's range measurement ($\Delta\rho_2$), and vice versa.

There are several coordinates or spaces/subspaces in these equations, which are important for the succeeding analysis. So they are listed and briefly discussed here. The first one is the E-N coordinate shown in this 2D case, which is Euclidean 2-space (R^2). All the navigation solutions are computed and discussed in this space, so this E-N coordinate is also called 'navigation coordinate'. For example, $\Delta\mathbf{r}$ and $\Delta\hat{\mathbf{r}}$ all lie in this coordinate space. This also applies for more general cases such as 3D and 4D coordinates/spaces where navigation coordinates are in R^3 or R^4.

The second one is the coordinate or subspace where the observations lie in. It can be called the 'observation coordinate'. For example the vector $\Delta\boldsymbol{\rho}$ is in this space. Given this, it is apparent that this observation coordinate is of dimension M, where M is the number of independent observations from all available satellites. And for the above case, where there are only two observations, M equals 2. Strictly speaking, this observation coordinate is Euclidean M-space (R^M).

The third one is the subspace spanned by the row vector of the design matrix, i.e., $\mathbf{e_1}$ and $\mathbf{e_2}$, or termed as $R(H^T)$. The relationship between the row space of design matrix and navigation coordinate (space) is that $R(H^T) \subseteq R^2$ for the 2D cases shown here. It means that the row space of the design matrix is embedded in the navigation coordinate. In real

scenarios, $R(H^T)$ has full rank, thus the navigation coordinate space can be considered the same as $R(H^T)$ for simplicity.

The forth subspace is the one perpendicular to the row space of the design matrix. It is the null space of design matrix or expressed as $N(H)$. Due to dimension theory in linear algebra, this subspace is of rank zero.

The fifth subspace is the column space of the design matrix $R(H)$. The shape of this subspace will affect the final estimation results. The dimension of $R(H)$ is the same as dimension of $R(H^T)$. The relationship between $R(H)$ and observation coordinate is that this column space is embedded in the observation coordinate or R^M.

The last subspace is the one that the residual vector lies in. It is perpendicular to the column space of the design matrix and is actually the left null space of the design matrix ($N(H^T)$).

The above relationships are plotted in a more general sense in Figure A.2. The navigation coordinate is composed of east, north, up and time axes and there are M observations available for estimation. $\oplus$ is the direct sum of two perpendicular subspaces. Dim denotes the dimension of the space.

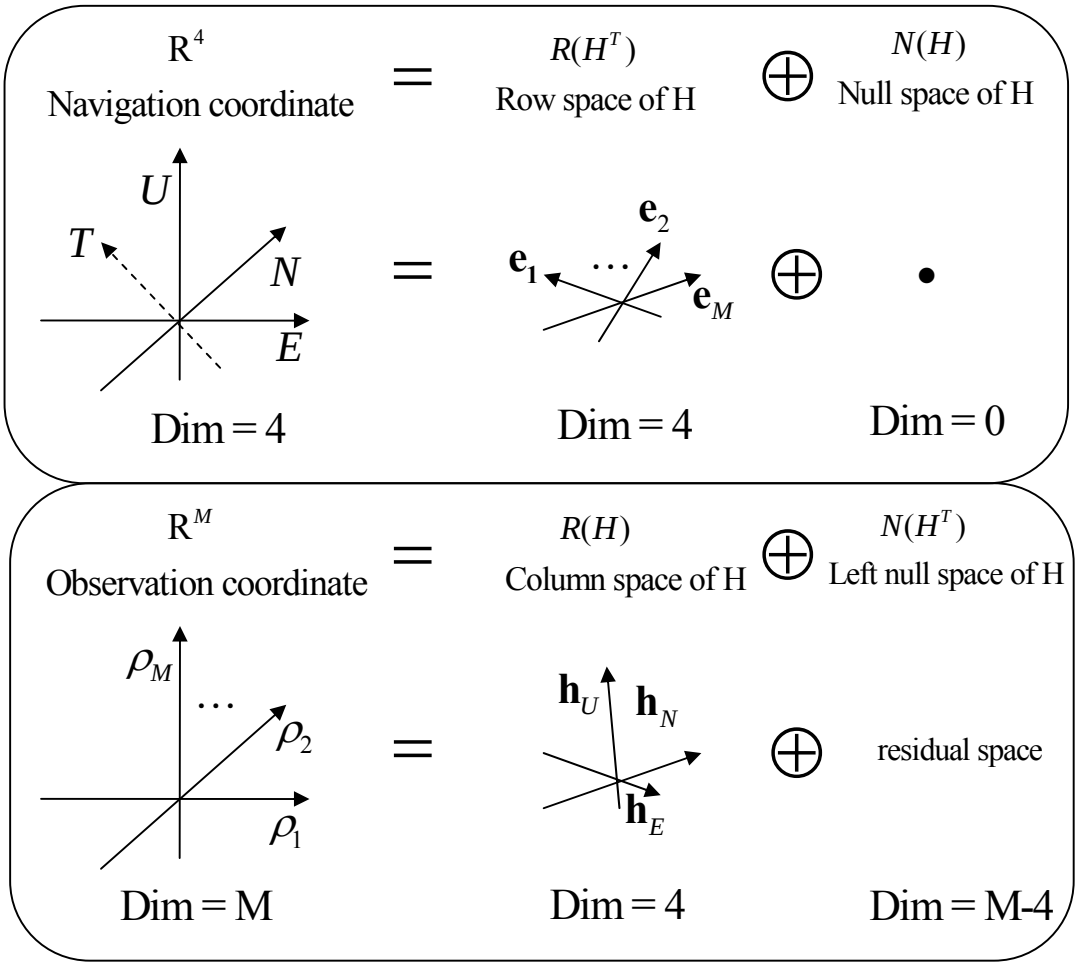

Figure A.2: Coordinates and spaces for estimation in navigation

In order to understand how the errors propagate in the estimation process, the term *error volume* is defined here. This term represents the total errors or uncertainty region contained in one coordinate or space. For example, assume that all observations have a unit variance and thus the error volume in the observation coordinate is 1. If the corresponding error volume in the navigation coordinate can be computed, it will then be convenient to characterize the errors in navigation coordinate with arbitrary observation accuracy. In the following it will be shown that the error volume in the navigation

coordinate depends on the shape of the design matrix. For example, in the 1D navigation coordinate, the error volume can be expressed as

$$\begin{aligned} \mathrm{Vol}_{1D,E} &= |\Delta E| \\ \mathrm{Vol}_{1D,N} &= |\Delta N| \end{aligned} \tag{A.8}$$

The 2D error volume is defined as the length of the tensor product of the base vector in this space as

$$\mathrm{Vol}_{2D,EN} = \|\Delta E \wedge \Delta N\| \tag{A.9}$$

In Figure A.3, the relationship between the error volumes of the navigation and observation coordinates are illustrated. In the E-N navigation coordinate, the overall uncertainty area can be divided into many small rectangular regions, such as rectangle $A'B'C'D'$ shown in the E-N coordinate. The sides of the rectangle are parallel to the E-axis and N-axis. Assume that the coordinate of point A' is (E_0, N_0), that of point B' is $(E_0 + \Delta E, N_0)$, C' is $(E_0 + \Delta E, N_0 + \Delta N)$, and D' is $(E_0, N_0 + \Delta N)$. In the observation coordinate (M=2 for simplicity), **i** is the unit base vector along ρ_1 axis while **j** is that along the ρ_2 axis.

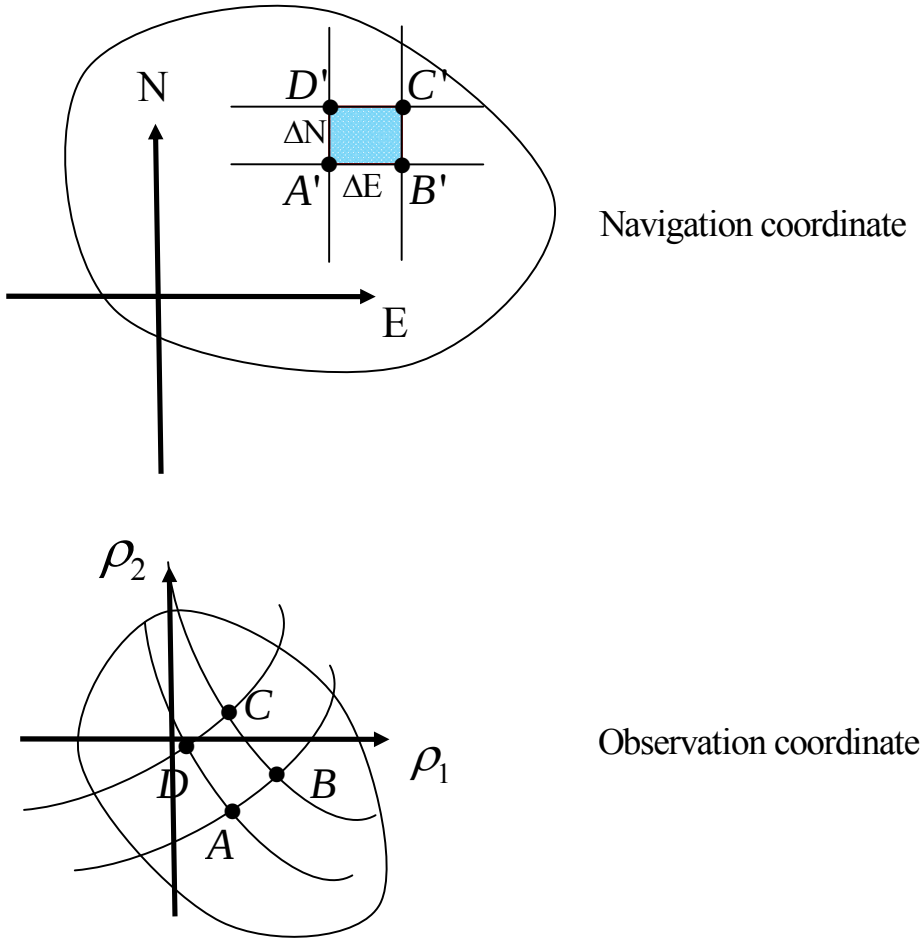

Figure A.3: 2D Error volumes in the navigation and observation coordinate

Generally speaking, whenever the unit direction vectors $\mathbf{e}_1, \mathbf{e}_2$ are not orthogonal, then the rectangular area ($A'B'C'D'$) under the linear transformation (observation model shown in equation(A.7)) will be a curved quadrangle ($ABCD$). If $\Delta E, \Delta N$ are very small, then the area of the curved quadrangle can be approximated as

$$Area = Vol_{2D,\rho_1,\rho_2} = \left\| \overrightarrow{AB} \wedge \overrightarrow{AD} \right\| \tag{A.10}$$

It is easy to prove that

$$\begin{aligned}\overrightarrow{AB} &= (\rho_1(E_0+\Delta E, N_0)-\rho_1(E_0,N_0))\mathbf{i}+(\rho_2(E_0+\Delta E, N_0)-\rho_2(E_0,N_0))\mathbf{j} \\ &\approx \frac{\partial \rho_1}{\partial E}\Delta E\mathbf{i}+\frac{\partial \rho_2}{\partial E}\Delta E\mathbf{j} \\ \overrightarrow{AD} &\approx \frac{\partial \rho_1}{\partial N}\Delta N\mathbf{i}+\frac{\partial \rho_2}{\partial N}\Delta N\mathbf{j}\end{aligned} \tag{A.11}$$

Before computing the area of the curved quadrangle, the vector component can be first calculated as

$$\begin{aligned}\overrightarrow{AB}\wedge\overrightarrow{AD} &\approx \begin{vmatrix}\frac{\partial \rho_1}{\partial E}\Delta E & \frac{\partial \rho_1}{\partial N}\Delta N \\ \frac{\partial \rho_2}{\partial E}\Delta E & \frac{\partial \rho_2}{\partial N}\Delta N\end{vmatrix}\mathbf{k} \\ &= \left(\frac{\partial \rho_1}{\partial E}\frac{\partial \rho_2}{\partial N}\Delta E\Delta N-\frac{\partial \rho_1}{\partial N}\frac{\partial \rho_2}{\partial E}\Delta E\Delta N\right)\mathbf{k} \\ &= \frac{\partial(\rho_1,\rho_2)}{\partial(E,N)}\Delta E\Delta N\mathbf{k}\end{aligned} \tag{A.12}$$

The area is just the value of the $\overrightarrow{AB}\wedge\overrightarrow{AD}$, so that the area of the curved quadrangle is

$$Vol_{\rho_1,\rho_2}=\left\|\overrightarrow{AB}\wedge\overrightarrow{AD}\right\|=\left|\frac{\partial(\rho_1,\rho_2)}{\partial(E,N)}\right|\Delta E\Delta N=\left\|\begin{bmatrix}h_{1E} & h_{1N}\\ h_{2E} & h_{2N}\end{bmatrix}\right\|\Delta E\Delta N=\left\|\begin{bmatrix}h_{1E} & h_{1N}\\ h_{2E} & h_{2N}\end{bmatrix}\right\|Vol_{E,N} \tag{A.13}$$

Since $\Delta E, \Delta N$ represent the unit errors in the east and north direction, the area of the rectangle ($A'B'C'D'$) represents the unit 2D error volume in the E-N navigation coordinates. In equation (A.13), Vol_{ρ_1,ρ_2} is the transformed error volume in the observation coordinate and it is related to the determinant of the design matrix ($\left\|\begin{bmatrix}h_{1E} & h_{1N}\\ h_{2E} & h_{2N}\end{bmatrix}\right\|$) and unit error volume in the E-N coordinates ($\Delta E\Delta N$ or $Vol_{E,N}$). The term $\left|\frac{\partial(\rho_1,\rho_2)}{\partial(E,N)}\right|$ or

$\left|\begin{bmatrix} h_{1E} & h_{1N} \\ h_{2E} & h_{2N} \end{bmatrix}\right|$ is also the determinant of the Jacobian matrix which projects from $\mathbb{R}^2$ to $\rightarrow \mathbb{R}^2$ (E-N navigation coordinates to the $\rho_1 - \rho_2$ observation coordinates). And in real scenarios, the measurement accuracy is known a priori, and the accuracies of the E-N coordinates are to be estimated. Then the whole process is inversed and the following relationship holds:

$$Vol_{E,N} = \left|\begin{bmatrix} h_{1E} & h_{1N} \\ h_{2E} & h_{2N} \end{bmatrix}\right|^{-1} \Delta\rho_1 \Delta\rho_2 = \left|\begin{bmatrix} h_{1E} & h_{1N} \\ h_{2E} & h_{2N} \end{bmatrix}\right|^{-1} Vol_{\rho_1,\rho_2} \tag{A.14}$$

For the 2D case considered here, the general relationship between the error volumes in navigation and observation coordinates can be expressed as

$$\begin{aligned} Vol_{Observation} &= \left|H_{2\times 2}\right| Vol_{Navigation} \\ Vol_{Navigation} &= \left|H_{2\times 2}\right|^{-1} Vol_{Observation} \end{aligned} \tag{A.15}$$

Due to the fact that the pseudorange errors in different satellites are assumed to be statistically independent, these errors are orthogonal. In equation (A.14), if each pseudorange has a unit error uncertainty, then it has unit error volumes in the observation coordinates.

The Jacobian matrix determinant only makes sense when the dimension of the row space equals the dimension of the range space. For example, in equation (A.13) or equation (A.14), the dimensions of the E-N navigation coordinate and $\rho_1 - \rho_2$ observation coordinate are both 2. Consequently, the Jacobian matrix is a square matrix and its determinant is easy to compute. In GNSS, the number of available satellites is required to be more than the dimension of the navigation coordinate (east, north, up and time) in

order to get redundancy. This is also the basic requirement for the least squares problem if the residuals are to be significant. In such cases, the conventional Jacobian determinant is not valid anymore. But one could use the concept of a generalized Jacobian determinant. Remember that the determinant of the matrix is equivalent to its volume and the 'Jacobian' determinant can then be generalized for non-square mapping matrices as the volume of the matrices. Some mathematical proof on this point can be found in Ben-Israel (1999) and will not be restated herein. Then, the following general conclusion holds:

$$\begin{aligned} Vol_{Observation} &= Vol_H Vol_{Navigation} \\ Vol_{Navigation} &= Vol_H^{-1} Vol_{Observation} \end{aligned} \tag{A.16}$$

In equation (A.16), $Vol_{Observation}$ is actually $Vol_{\rho_1,\rho_2,\cdots\rho_M}$, Vol_H is the volume of the design matrix or equivalently it is considered the volume of the parallelotope formed by its column vector. In the 2D case considered here this term can also be expressed as $Vol(\Xi(\mathbf{h}_E, \mathbf{h}_N))$ and similarly $Vol_{Navigation}$ can be $Vol_{E,N}$.

Similarly, in the 1D case, the navigation coordinate only has one axis, take east axis for example, then Vol_H will be $Vol(\Xi(\mathbf{h}_E))$, and $Vol_{Navigation}$ is expressed as Vol_E. These 1D error volumes are as follows:

$$\begin{aligned} Vol_E &= Vol(\Xi(\mathbf{h}_E))^{-1} Vol_{\rho_1,\rho_2,\cdots\rho_M} = \frac{1}{\|\mathbf{h}_E\|} Vol_{\rho_1,\rho_2,\cdots\rho_M} \\ Vol_N &= Vol(\Xi(\mathbf{h}_N))^{-1} Vol_{\rho_1,\rho_2,\cdots\rho_M} = \frac{1}{\|\mathbf{h}_N\|} Vol_{\rho_1,\rho_2,\cdots\rho_M} \end{aligned} \tag{A.17}$$

It is now useful to see how DOP values are related to error volumes discussed above. Recall that the DOP actually reflects navigation errors with unit observation variance. In such a case, the error volume in the observation coordinate is one and DOP values are only affected by the volume of the parallelotope formed by column vectors of design matrix. The relationship between DOP values and the volume of the design matrix column space is shown in Figure A.4.

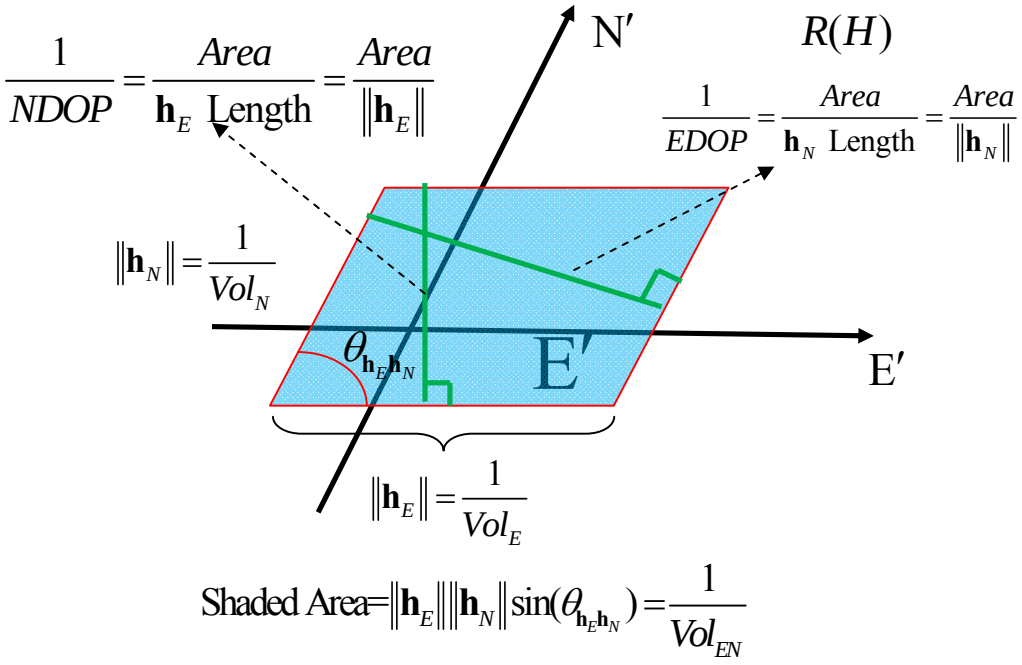

Figure A.4: Volume of design matrix in column space and its relationship with DOP – 2D case

As one can see, the column space of the design matrix in this scenario is spanned by $\mathbf{h}_E$ and $\mathbf{h}_N$. They will form a parallelotope with angle $\theta_{\mathbf{h}_E\mathbf{h}_N}$. The 2D error volume in this case is the reciprocal of the shaded area and can be computed as

$$\mathrm{Vol}(\Xi(\mathbf{h}_E,\mathbf{h}_N)) = \|\mathbf{h}_E \times \mathbf{h}_N\| = \|\mathbf{h}_E\|\|\mathbf{h}_N\|\sin(\theta_{\mathbf{h}_E\mathbf{h}_N}) = \|\mathbf{h}_E\|\|\mathbf{h}_N\|\sqrt{1-\rho^2_{\mathbf{h}_E\mathbf{h}_N}} \tag{A.18}$$

where $\theta_{\mathbf{h}_E\mathbf{h}_N} = \arccos\dfrac{\mathbf{h}_E^T\mathbf{h}_N}{\|\mathbf{h}_E\|\|\mathbf{h}_N\|}$. Alternatively, the correlation coefficients are related with this angle as $\rho_{\mathbf{h}_E\mathbf{h}_N} = \cos\theta_{\mathbf{h}_E\mathbf{h}_N}$, where $\rho_{\mathbf{h}_E\mathbf{h}_N} = \dfrac{\mathbf{h}_E^T\mathbf{h}_N}{\|\mathbf{h}_E\|\bullet\|\mathbf{h}_N\|}$.

The two side lengths of the parallelotope represent the reciprocal of 1D error volume corresponding to the axis in navigation coordinates. For example, $\|\mathbf{h}_E\|$ denotes the reciprocal of Vol_E. In this way, the reciprocal of NDOP is actually the shaded area divided by the east side length of the parallelotope in the design matrix column space. In a more simple form, NDOP is considered as Vol_{EN} divided by Vol_E.

In this way, the term *dilution of precision* could be thought of as the 'effective error height', which is the 'error volume' divided by 'error base'. For example, in the 2D case, east DOP (EDOP) is the 2D error volume (EN volume) divided by the 1D north error volume. And the north DOP (NDOP) is the 2D error volume (EN volume) divided by the 1D east error volume. These relationships can be written as

$$\begin{aligned} EDOP &= \frac{Vol_{E,N}}{Vol_N} = \frac{\|\mathbf{h}_N\|}{Vol(\Xi(\mathbf{h}_E,\mathbf{h}_N))} \\ NDOP &= \frac{Vol_{E,N}}{Vol_E} = \frac{\|\mathbf{h}_E\|}{Vol(\Xi(\mathbf{h}_E,\mathbf{h}_N))} \end{aligned} \tag{A.19}$$

Compared to equation (A.6), equation (A.19) only represents a special 2D case, which closely matches the algebraic results. The east and north DOP metrics can be written as

$$
\begin{aligned}
&\text{EDOP}=\frac{\|\mathbf{h}_N\|}{\text{Vol}(\Xi(\mathbf{h}_E,\mathbf{h}_N))}=\frac{\lambda_{E,1D}}{\|\mathbf{h}_E\|}\\
&\lambda_{E,1D}=1/\sqrt{1-\rho^2_{\mathbf{h}_E\mathbf{h}_N}}\\
&\text{NDOP}=\frac{\|\mathbf{h}_E\|}{\text{Vol}(\Xi(\mathbf{h}_E,\mathbf{h}_N))}=\frac{\lambda_{N,1D}}{\|\mathbf{h}_N\|}\\
&\lambda_{N,1D}=1/\sqrt{1-\rho^2_{\mathbf{h}_E\mathbf{h}_N}}
\end{aligned}
\qquad \text{(A.20)}
$$

In equation (A.20), $\lambda_{E,1D}$ and $\lambda_{N,1D}$ are called the east and north geometry dependent factors in the 2D case. The usefulness of these terms will be further investigated in the following sections. With equation (A.19) and (A.20), the EDOP and NDOP of Figure A.1 can be easily obtained as

$$
\begin{aligned}
&EDOP=\;=\frac{\|\mathbf{h}_N\|}{\text{Vol}(\mathbf{h}_E,\mathbf{h}_N)}=1\\
&NDOP=\frac{\|\mathbf{h}_E\|}{\text{Vol}(\mathbf{h}_E,\mathbf{h}_N)}=1
\end{aligned}
\qquad \text{(A.21)}
$$

These results match one's intuitive understanding of symmetric satellite geometry on positioning accuracy. With the orthogonal geometry discussed, it is more of interest to examine the different satellite geometry shown in Figure A.5.

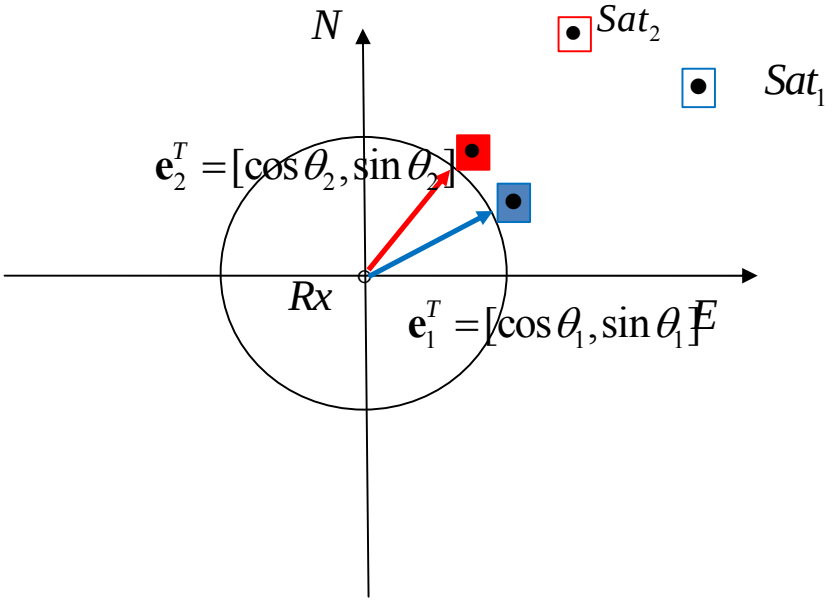

Figure A.5: 2-D correlated satellite geometry

The observation equation for Figure A.5 is

$$\begin{bmatrix}\Delta\rho_1\\ \Delta\rho_2\end{bmatrix}=\begin{bmatrix}\cos\theta_1 & \sin\theta_1\\ \cos\theta_2 & \sin\theta_2\end{bmatrix}\begin{bmatrix}\Delta E\\ \Delta N\end{bmatrix} \tag{A.22}$$

In this 'correlated' satellite geometry scenario, the corresponding EDOP and NDOP can be analogously calculated as

$$EDOP=\frac{\|\mathbf{h}_N\|}{Vol(\Xi(\mathbf{h}_E,\mathbf{h}_N))}=\frac{\left(\sin^2\theta_1+\sin^2\theta_2\right)^{\frac{1}{2}}}{\left|\sin(\theta_2-\theta_1)\right|}$$
$$NDOP=\frac{\|\mathbf{h}_E\|}{Vol(\Xi(\mathbf{h}_E,\mathbf{h}_N))}=\frac{\left(\cos^2\theta_1+\cos^2\theta_2\right)^{\frac{1}{2}}}{\left|\sin(\theta_2-\theta_1)\right|} \tag{A.23}$$

Using the concepts developed for the 2D case, it is convenient to extend the discussion of DOP metrics for the 3D case.

A.2.2 DOPs of 3D coordinate-East, North, Up

In the previous section, the 2D satellite user geometry was analyzed, while here a 3D navigation coordinate is considered, consisting of east, north and up axes. Analogously, the 3D DOP values can be expressed as

$$\begin{aligned} EDOP &= \frac{Vol_{E,N,U}}{Vol_{N,U}} = \frac{Vol(\Xi(\mathbf{h}_N, \mathbf{h}_U))}{Vol(\Xi(\mathbf{h}_E, \mathbf{h}_N, \mathbf{h}_U))} \\ NDOP &= \frac{Vol_{E,N,U}}{Vol_{E,U}} = \frac{Vol(\Xi(\mathbf{h}_E, \mathbf{h}_U))}{Vol(\Xi(\mathbf{h}_E, \mathbf{h}_N, \mathbf{h}_U))} \\ UDOP &= \frac{Vol_{E,N,U}}{Vol_{E,N}} = \frac{Vol(\Xi(\mathbf{h}_E, \mathbf{h}_N))}{Vol(\Xi(\mathbf{h}_E, \mathbf{h}_N, \mathbf{h}_U))} \end{aligned} \tag{A.24}$$

As an example, the satellite user geometry shown in Figure A.6 is considered herein.

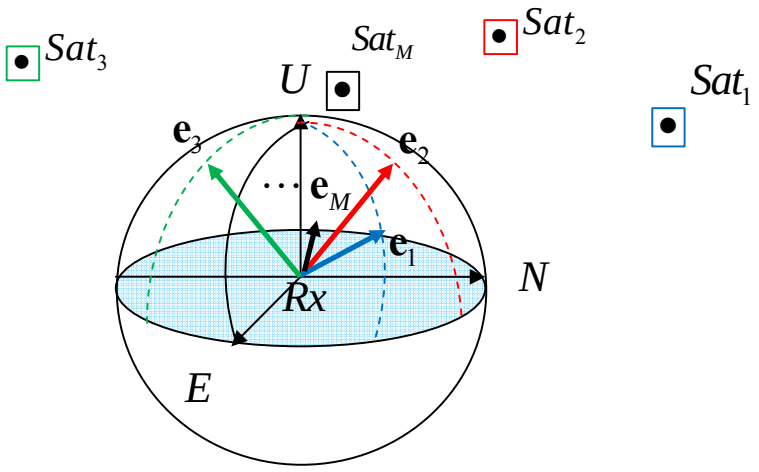

Figure A.6: 3D satellite geometry

In Figure A.6, there are M satellites in view and the observation equations are as follows:

$$\begin{bmatrix} \Delta\rho_1 \\ \Delta\rho_2 \\ \vdots \\ \Delta\rho_M \end{bmatrix} = \begin{bmatrix} \mathbf{e}_1^T \\ \mathbf{e}_2^T \\ \vdots \\ \mathbf{e}_M^T \end{bmatrix} \begin{bmatrix} \Delta E \\ \Delta N \\ \Delta U \end{bmatrix} \quad or \quad \Delta\boldsymbol{\rho} = \begin{bmatrix} \mathbf{h}_E & \mathbf{h}_N & \mathbf{h}_U \end{bmatrix} \begin{bmatrix} \Delta E \\ \Delta N \\ \Delta U \end{bmatrix} \tag{A.25}$$

In equation (A.25), there are M observations. In order to get the DOP values, the volume of the design matrix in its column space need be calculated. The relationship between the volume of design matrix and DOP values are shown in Figure A.7.

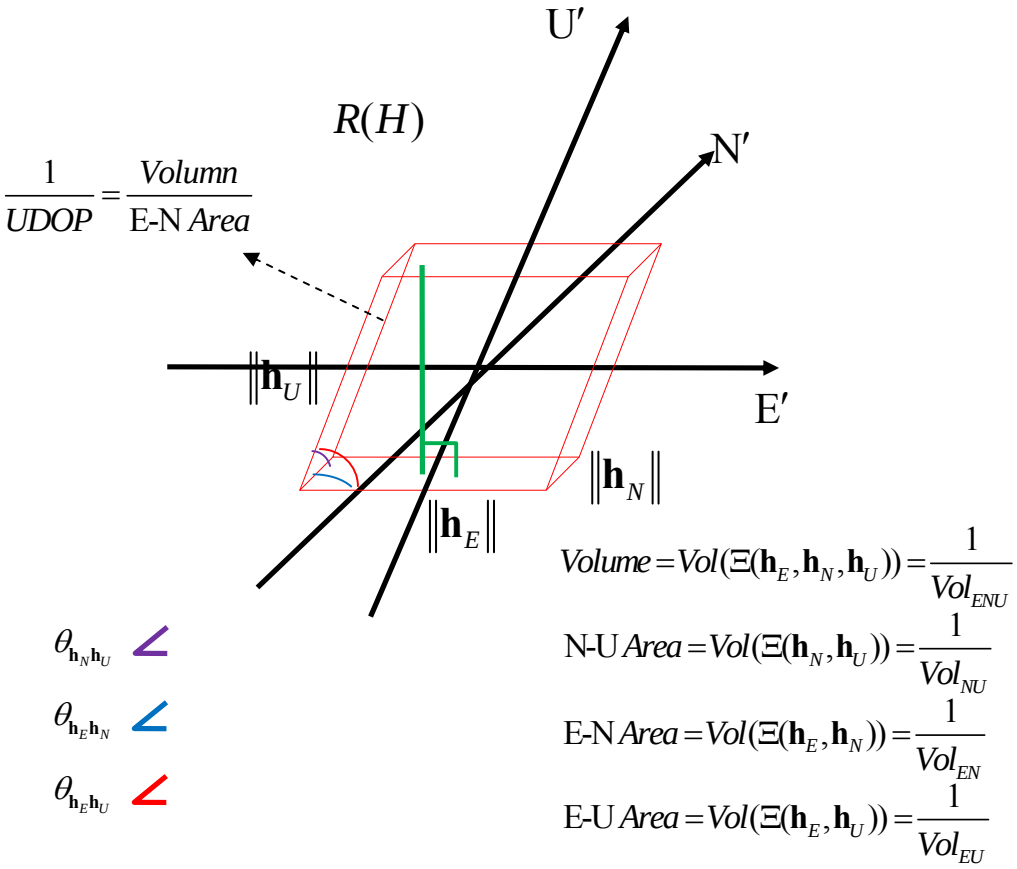

Figure A.7: Volume of design matrix in column space and its relationship with DOP – 3D case

In Figure A.7, the parallelepiped shown on the right has edges of $\|\mathbf{h}_E\|, \|\mathbf{h}_N\|, \|\mathbf{h}_U\|$. The angles between them are $\theta_{\mathbf{h}_E\mathbf{h}_N}, \theta_{\mathbf{h}_E\mathbf{h}_U}, \theta_{\mathbf{h}_N\mathbf{h}_U}$. The areas formed by adjacent edges are $Vol(\Xi(\mathbf{h}_E, \mathbf{h}_N))$, $Vol(\Xi(\mathbf{h}_E, \mathbf{h}_U))$, $Vol(\Xi(\mathbf{h}_N, \mathbf{h}_U))$. They are the reciprocal of the 2D error volume (E-N), the 2D error volume (E-U) and the 2D error volume (N-U) respectively. The total volume of this parallelepiped is $Vol(\Xi(\mathbf{h}_E, \mathbf{h}_N, \mathbf{h}_U))$ and it is the reciprocal of the total 3D error volume (E-N-U). According to equation (A.24), we only need to compute 2D and 3D volumes. The 3D volume of the design matrix can be obtained by using the following formula:

$$\mathrm{Vol}(\Xi(\mathbf{h}_E, \mathbf{h}_N, \mathbf{h}_U)) = \|\mathbf{h}_E\| \bullet \|\mathbf{h}_N\| \bullet \|\mathbf{h}_U\| \left\{1 + 2\rho_{\mathbf{h}_E\mathbf{h}_N}\rho_{\mathbf{h}_N\mathbf{h}_U}\rho_{\mathbf{h}_E\mathbf{h}_U} - \rho^2_{\mathbf{h}_E\mathbf{h}_N} - \rho^2_{\mathbf{h}_N\mathbf{h}_U} - \rho^2_{\mathbf{h}_E\mathbf{h}_U}\right\}^{1/2} \quad \text{(A.26)}$$

where $\rho_{\mathbf{h}_E\mathbf{h}_N}$ equals $= \dfrac{\mathbf{h}_E^T\mathbf{h}_N}{\|\mathbf{h}_E\| \bullet \|\mathbf{h}_N\|}$ and $\rho_{\mathbf{h}_E\mathbf{h}_U} = \dfrac{\mathbf{h}_E^T\mathbf{h}_U}{\|\mathbf{h}_E\| \bullet \|\mathbf{h}_U\|}$, $\rho_{\mathbf{h}_N\mathbf{h}_U} = \dfrac{\mathbf{h}_N^T\mathbf{h}_U}{\|\mathbf{h}_N\| \bullet \|\mathbf{h}_U\|}$. $\|\bullet\|$ represents the $l2$ norm. The relationships between the correlation coefficients and the angles between adjacent vectors are

$$\begin{aligned}
\theta_{\mathbf{h}_E\mathbf{h}_N} &= \arccos\frac{\mathbf{h}_E^T\mathbf{h}_N}{\|\mathbf{h}_E\|\|\mathbf{h}_N\|} \\
\theta_{\mathbf{h}_E\mathbf{h}_U} &= \arccos\frac{\mathbf{h}_E^T\mathbf{h}_U}{\|\mathbf{h}_E\|\|\mathbf{h}_U\|} \\
\theta_{\mathbf{h}_N\mathbf{h}_U} &= \arccos\frac{\mathbf{h}_N^T\mathbf{h}_U}{\|\mathbf{h}_N\|\|\mathbf{h}_U\|}
\end{aligned} \quad \text{(A.27)}$$

With the 2D and 3D volume formula shown in equation (A.18) and (A.26), the DOP values can be easily calculated as follows according to equation(A.24):

$$
\begin{aligned}
EDOP &= \frac{Vol_{E,N,U}}{Vol_{N,U}} = \frac{Vol(\Xi(\mathbf{h}_N, \mathbf{h}_U))}{Vol(\Xi(\mathbf{h}_E, \mathbf{h}_N, \mathbf{h}_U))} \\
&= \frac{\|\mathbf{h}_N\| \bullet \|\mathbf{h}_U\| \sqrt{1-\rho^2_{\mathbf{h}_N\mathbf{h}_U}}}{\|\mathbf{h}_E\| \bullet \|\mathbf{h}_N\| \bullet \|\mathbf{h}_U\| \left\{1+2\rho_{\mathbf{h}_E\mathbf{h}_N}\rho_{\mathbf{h}_N\mathbf{h}_U}\rho_{\mathbf{h}_E\mathbf{h}_U} - \rho^2_{\mathbf{h}_E\mathbf{h}_N} - \rho^2_{\mathbf{h}_N\mathbf{h}_U} - \rho^2_{\mathbf{h}_E\mathbf{h}_U}\right\}^{1/2}} \\
&= \frac{\lambda_{E,3D,ENU}}{\|\mathbf{h}_E\|} \\
\lambda_{E,3D,ENU} &= \left\{\frac{1-\rho^2_{\mathbf{h}_N\mathbf{h}_U}}{1+2\rho_{\mathbf{h}_E\mathbf{h}_N}\rho_{\mathbf{h}_N\mathbf{h}_U}\rho_{\mathbf{h}_E\mathbf{h}_U} - \rho^2_{\mathbf{h}_E\mathbf{h}_N} - \rho^2_{\mathbf{h}_N\mathbf{h}_U} - \rho^2_{\mathbf{h}_E\mathbf{h}_U}}\right\}^{1/2}
\end{aligned}
\tag{A.28}
$$

$$
\begin{aligned}
NDOP &= \frac{Vol_{E,N,U}}{Vol_{E,U}} = \frac{Vol(\Xi(\mathbf{h}_E, \mathbf{h}_U))}{Vol(\Xi(\mathbf{h}_E, \mathbf{h}_N, \mathbf{h}_U))} \\
&= \frac{\|\mathbf{h}_E\| \bullet \|\mathbf{h}_U\| \sqrt{1-\rho^2_{\mathbf{h}_E\mathbf{h}_U}}}{\|\mathbf{h}_E\| \bullet \|\mathbf{h}_N\| \bullet \|\mathbf{h}_U\| \left\{1+2\rho_{\mathbf{h}_E\mathbf{h}_N}\rho_{\mathbf{h}_N\mathbf{h}_U}\rho_{\mathbf{h}_E\mathbf{h}_U} - \rho^2_{\mathbf{h}_E\mathbf{h}_N} - \rho^2_{\mathbf{h}_N\mathbf{h}_U} - \rho^2_{\mathbf{h}_E\mathbf{h}_U}\right\}^{1/2}} \\
&= \frac{\lambda_{N,3D,ENU}}{\|\mathbf{h}_N\|} \\
\lambda_{N,3D,ENU} &= \left\{\frac{1-\rho^2_{\mathbf{h}_E\mathbf{h}_U}}{1+2\rho_{\mathbf{h}_E\mathbf{h}_N}\rho_{\mathbf{h}_N\mathbf{h}_U}\rho_{\mathbf{h}_E\mathbf{h}_U} - \rho^2_{\mathbf{h}_E\mathbf{h}_N} - \rho^2_{\mathbf{h}_N\mathbf{h}_U} - \rho^2_{\mathbf{h}_E\mathbf{h}_U}}\right\}^{1/2}
\end{aligned}
\tag{A.29}
$$

$$
\begin{aligned}
UDOP &= \frac{Vol_{E,N,U}}{Vol_{E,N}} = \frac{Vol(\Xi(\mathbf{h}_E, \mathbf{h}_N))}{Vol(\Xi(\mathbf{h}_E, \mathbf{h}_N, \mathbf{h}_U))} \\
&= \frac{\|\mathbf{h}_E\| \bullet \|\mathbf{h}_N\| \sqrt{1-\rho^2_{\mathbf{h}_E\mathbf{h}_N}}}{\|\mathbf{h}_E\| \bullet \|\mathbf{h}_N\| \bullet \|\mathbf{h}_U\| \left\{1+2\rho_{\mathbf{h}_E\mathbf{h}_N}\rho_{\mathbf{h}_N\mathbf{h}_U}\rho_{\mathbf{h}_E\mathbf{h}_U} - \rho^2_{\mathbf{h}_E\mathbf{h}_N} - \rho^2_{\mathbf{h}_N\mathbf{h}_U} - \rho^2_{\mathbf{h}_E\mathbf{h}_U}\right\}^{1/2}} \\
&= \frac{\lambda_{U,3D,ENU}}{\|\mathbf{h}_U\|} \\
\lambda_{U,3D,ENU} &= \left\{\frac{1-\rho^2_{\mathbf{h}_E\mathbf{h}_N}}{1+2\rho_{\mathbf{h}_E\mathbf{h}_N}\rho_{\mathbf{h}_N\mathbf{h}_U}\rho_{\mathbf{h}_E\mathbf{h}_U} - \rho^2_{\mathbf{h}_E\mathbf{h}_N} - \rho^2_{\mathbf{h}_N\mathbf{h}_U} - \rho^2_{\mathbf{h}_E\mathbf{h}_U}}\right\}^{1/2}
\end{aligned}
\tag{A.30}
$$

From the equations (A.28), (A.29) and(A.30), the EDOP, NDOP and UDOP are related to the norms of the $\mathbf{h}_E, \mathbf{h}_N, \mathbf{h}_U$ and have different scale factors of $\lambda_{E,3D}, \lambda_{N,3D}, \lambda_{U,3D}$, which are the geometry dependent factors for the 3D case.

A.2.3 DOPs of 3D Coordinate-East, North, Time

The 3D space coordinate discussion in the previous section is sufficient to characterize the DOP metrics for traditional range measurements. In the field of GNSS however, there is one additional unknown axis, namely time. This unknown state directly affects east, north and up DOPs. In this section, a 3D coordinate, which is composed of the east, north, and time axes are discussed. All the analysis of 3D east, north and up navigation coordinate applies for the new coordinate, except that the column vector for the up axis ($\mathbf{h}_U$) is replaced by the one denoting the time axis in design matrix ($\mathbf{h}_{Clk}$). The following formulas can be derived accordingly:

$$EDOP = \frac{Vol_{E,N,T}}{Vol_{N,T}} = \frac{Vol(\Xi(\mathbf{h}_N, \mathbf{h}_{Clk}))}{Vol(\Xi(\mathbf{h}_E, \mathbf{h}_N, \mathbf{h}_{Clk}))}$$
$$= \frac{\lambda_{E,3D,ENT}}{\|\mathbf{h}_E\|} \qquad \text{(A.31)}$$
$$\lambda_{E,3D,ENT} = \left\{ \frac{1-\rho^2_{\mathbf{h}_N\mathbf{h}_{Clk}}}{1+2\rho_{\mathbf{h}_E\mathbf{h}_N}\rho_{\mathbf{h}_N\mathbf{h}_{Clk}}\rho_{\mathbf{h}_E\mathbf{h}_U} - \rho^2_{\mathbf{h}_E\mathbf{h}_N} - \rho^2_{\mathbf{h}_N\mathbf{h}_{Clk}} - \rho^2_{\mathbf{h}_E\mathbf{h}_{Clk}}} \right\}^{1/2}$$

$$NDOP = \frac{Vol_{E,N,Clk}}{Vol_{E,Clk}} = \frac{Vol(\Xi(\mathbf{h}_E, \mathbf{h}_{Clk}))}{Vol(\Xi(\mathbf{h}_E, \mathbf{h}_N, \mathbf{h}_U))}$$
$$= \frac{\lambda_{N,3D,ENT}}{\|\mathbf{h}_N\|} \tag{A.32}$$
$$\lambda_{N,3D,ENT} = \left\{ \frac{1-\rho^2_{\mathbf{h}_E\mathbf{h}_{Clk}}}{1+2\rho_{\mathbf{h}_E\mathbf{h}_N}\rho_{\mathbf{h}_N\mathbf{h}_{Clk}}\rho_{\mathbf{h}_E\mathbf{h}_{Clk}} - \rho^2_{\mathbf{h}_E\mathbf{h}_N} - \rho^2_{\mathbf{h}_N\mathbf{h}_{Clk}} - \rho^2_{\mathbf{h}_E\mathbf{h}_{Clk}}} \right\}^{1/2}$$

$$TDOP = \frac{Vol_{E,N,Clk}}{Vol_{E,N}} = \frac{Vol(\Xi(\mathbf{h}_E, \mathbf{h}_N))}{Vol(\Xi(\mathbf{h}_E, \mathbf{h}_N, \mathbf{h}_{Clk}))}$$
$$= \frac{\lambda_{T,3D,ENT}}{\|\mathbf{h}_{Clk}\|} \tag{A.33}$$
$$\lambda_{T,3D,ENT} = \left\{ \frac{1-\rho^2_{\mathbf{h}_E\mathbf{h}_N}}{1+2\rho_{\mathbf{h}_E\mathbf{h}_N}\rho_{\mathbf{h}_N\mathbf{h}_{Clk}}\rho_{\mathbf{h}_E\mathbf{h}_{Clk}} - \rho^2_{\mathbf{h}_E\mathbf{h}_N} - \rho^2_{\mathbf{h}_N\mathbf{h}_{Clk}} - \rho^2_{\mathbf{h}_E\mathbf{h}_{Clk}}} \right\}^{1/2}$$

By comparing equation (A.31) and (A.32) with equation(A.20), one can easily justify the DOP differences between using range measurements and pseudorange measurements. The major difference between these two terminologies is whether the time axis is included. The following equations show the ratio of EDOP and NDOP between the E-N-T navigation coordinate and the E-N navigation coordinate.

$$\gamma_{EDOP,3/2D} = \frac{EDOP_{ENT}}{EDOP_{EN}} = \frac{\lambda_{E,3D-ENT}}{\lambda_{E,2D-EN}} = \frac{\left(1-\rho^2_{\mathbf{h}_N\mathbf{h}_{Clk}}\right)^{1/2}\left(1-\rho^2_{\mathbf{h}_E\mathbf{h}_N}\right)^{1/2}}{\left\{1+2\rho_{\mathbf{h}_E\mathbf{h}_N}\rho_{\mathbf{h}_N\mathbf{h}_{Clk}}\rho_{\mathbf{h}_E\mathbf{h}_{Clk}} - \rho^2_{\mathbf{h}_E\mathbf{h}_N} - \rho^2_{\mathbf{h}_N\mathbf{h}_{Clk}} - \rho^2_{\mathbf{h}_E\mathbf{h}_{Clk}}\right\}}$$
$$= \left\{ \frac{1-\rho^2_{\mathbf{h}_N\mathbf{h}_{Clk}} - \rho^2_{\mathbf{h}_E\mathbf{h}_N} + \rho^2_{\mathbf{h}_E\mathbf{h}_N}\rho^2_{\mathbf{h}_N\mathbf{h}_{Clk}}}{1-\rho^2_{\mathbf{h}_N\mathbf{h}_{Clk}} - (\rho_{\mathbf{h}_E\mathbf{h}_N} - \rho_{\mathbf{h}_E\mathbf{h}_{Clk}})^2 - 2(1-\rho_{\mathbf{h}_N\mathbf{h}_{Clk}})\rho_{\mathbf{h}_E\mathbf{h}_N}\rho_{\mathbf{h}_E\mathbf{h}_{Clk}}} \right\}^{1/2} \tag{A.34}$$

$$\gamma_{NDOP,3/2D} = \frac{NDOP_{ENT}}{NDOP_{EN}} = \frac{\lambda_{N,3D-ENT}}{\lambda_{N,2D-EN}} = \frac{\left(1-\rho^2_{\mathbf{h}_E\mathbf{h}_{Clk}}\right)^{1/2}\left(1-\rho^2_{\mathbf{h}_E\mathbf{h}_N}\right)^{1/2}}{\left\{1+2\rho_{\mathbf{h}_E\mathbf{h}_N}\rho_{\mathbf{h}_N\mathbf{h}_{Clk}}\rho_{\mathbf{h}_E\mathbf{h}_{Clk}} - \rho^2_{\mathbf{h}_E\mathbf{h}_N} - \rho^2_{\mathbf{h}_N\mathbf{h}_{Clk}} - \rho^2_{\mathbf{h}_E\mathbf{h}_{Clk}}\right.}$$
$$= \left\{\frac{1-\rho^2_{\mathbf{h}_E\mathbf{h}_{Clk}} - \rho^2_{\mathbf{h}_E\mathbf{h}_N} + \rho^2_{\mathbf{h}_E\mathbf{h}_N}\rho^2_{\mathbf{h}_E\mathbf{h}_{Clk}}}{1-\rho^2_{\mathbf{h}_N\mathbf{h}_{Clk}} - (\rho_{\mathbf{h}_E\mathbf{h}_N} - \rho_{\mathbf{h}_E\mathbf{h}_{Clk}})^2 - 2(1-\rho_{\mathbf{h}_N\mathbf{h}_{Clk}})\rho_{\mathbf{h}_E\mathbf{h}_N}\rho_{\mathbf{h}_E\mathbf{h}_{Clk}}}\right\}^{1/2} \quad \text{(A.35)}$$

where $\gamma_{EDOP,3/2D}, \gamma_{NDOP,3/2D}$ reflect the effect of adding the time dimension unknown. These terms also represent the degradation of the DOP when using pseudorange measurements instead of range measurements. It can be seen that these degradation terms can be simply computed as the ratio between the corresponding geometry dependent factors.

A.2.4 DOPs of 4D coordinate-East, North, Up and Time

With DOP metrics analyzed in 2D and 3D coordinates, it is convenient to extend these metrics to the real 4D coordinate that includes east, north, up and time axis. The 4D coordinate satellite geometry is shown in Figure A.8.

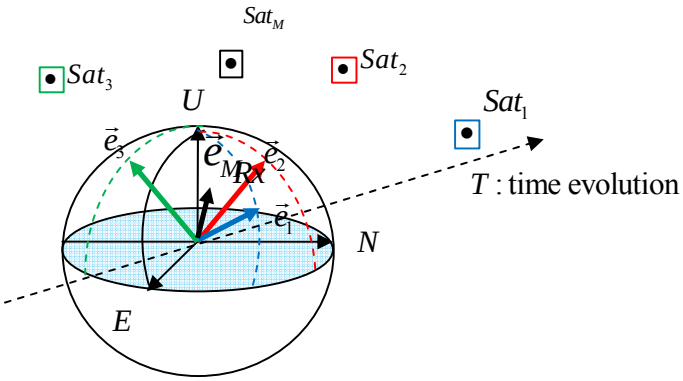

Figure A.8: 4D Satellite-user geometry

According to this 4D satellite-user geometry, the observation models are as follows:

$$\Delta\boldsymbol{\rho} = \begin{bmatrix} \mathbf{h}_E & \mathbf{h}_N & \mathbf{h}_U & \mathbf{h}_{Clk} \end{bmatrix} \begin{bmatrix} \Delta E \\ \Delta N \\ \Delta U \\ \Delta T \end{bmatrix} \tag{A.36}$$

Analogously, the DOP metrics can be derived as

$$\begin{aligned} EDOP &= \frac{\mathrm{Vol}(\Xi(\mathbf{h}_N, \mathbf{h}_U, \mathbf{h}_{Clk}))}{\mathrm{Vol}(\Xi(\mathbf{h}_E, \mathbf{h}_N, \mathbf{h}_U, \mathbf{h}_{Clk}))} \\ NDOP &= \frac{\mathrm{Vol}(\Xi(\mathbf{h}_E, \mathbf{h}_U, \mathbf{h}_{Clk}))}{\mathrm{Vol}(\Xi(\mathbf{h}_E, \mathbf{h}_N, \mathbf{h}_U, \mathbf{h}_{Clk}))} \\ UDOP &= \frac{\mathrm{Vol}(\Xi(\mathbf{h}_E, \mathbf{h}_N, \mathbf{h}_{Clk}))}{\mathrm{Vol}(\Xi(\mathbf{h}_E, \mathbf{h}_N, \mathbf{h}_U, \mathbf{h}_{Clk}))} \\ TDOP &= \frac{\mathrm{Vol}(\Xi(\mathbf{h}_E, \mathbf{h}_N, \mathbf{h}_U))}{\mathrm{Vol}(\Xi(\mathbf{h}_E, \mathbf{h}_N, \mathbf{h}_U, \mathbf{h}_{Clk}))} \end{aligned} \tag{A.37}$$

Before calculating the DOP metric by using geometric methods, the 4D volume of the design matrix is required and is given by

$$\begin{aligned}&\mathrm{Vol}(\Xi(\mathbf{h}_E,\mathbf{h}_N,\mathbf{h}_U,\mathbf{h}_{Clk}))=\|\mathbf{h}_E\|\|\mathbf{h}_N\|\|\mathbf{h}_U\|\|\mathbf{h}_{Clk}\|(1-\rho_{en}^2(1-\bar{h}_u^2)-\rho_{eu}^2(1-\bar{h}_n^2)-\rho_{nu}^2(1-\bar{h}_e^2)+2\bar{h}_n\bar{h}_u(\rho_{nu}-\rho_{en}\rho_{eu})...\\&+2\bar{h}_n\bar{h}_e(\rho_{en}-\rho_{eu}\rho_{nu})+2\bar{h}_u\bar{h}_e(\rho_{eu}-\rho_{en}\rho_{nu})+2\rho_{en}\rho_{nu}\rho_{eu}-\bar{h}_e^2-\bar{h}_n^2-\bar{h}_u^2)^{\frac{1}{2}}\end{aligned} \tag{A.38}$$

In equation (A.38), due to the fact that $\mathbf{h}_{Clk}=\mathbf{1}$, the correlation coefficients between time and east, north and up column vector actually denote the normalized average and are defined as

$$\begin{aligned}\bar{h}_e&=\rho_{eClk}=\frac{\mathbf{h}_E^T\mathbf{h}_{Clk}}{\|\mathbf{h}_E\|\|\mathbf{h}_{Clk}\|}=\frac{\mathbf{h}_E^T\mathbf{1}}{\|\mathbf{h}_E\|\|\mathbf{1}\|},\\\bar{h}_n&=\frac{\mathbf{h}_N^T\mathbf{h}_{Clk}}{\|\mathbf{h}_N\|\|\mathbf{h}_{Clk}\|},\\\bar{h}_u&=\frac{\mathbf{h}_U^T\mathbf{h}_{Clk}}{\|\mathbf{h}_U\|\|\mathbf{h}_{Clk}\|}\end{aligned} \tag{A.39}$$

With the above definitions, the analytical expressions for GNSS DOP metrics can be derived as shown in the following equations:

$$\begin{aligned}EDOP&=\frac{\mathrm{Vol}(\Xi(\mathbf{h}_N,\mathbf{h}_U,\mathbf{h}_{Clk}))}{\mathrm{Vol}(\Xi(\mathbf{h}_E,\mathbf{h}_N,\mathbf{h}_U,\mathbf{h}_{Clk}))}\\&=\frac{\|\mathbf{h}_N\|\|\mathbf{h}_U\|\|\mathbf{h}_{Clk}\|(1+2\rho_{nu}\rho_{ut}\rho_{tn}-\rho_{nu}^2-\rho_{ut}^2-\rho_{tn}^2)^{\frac{1}{2}}}{\left\{\begin{array}{l}\|\mathbf{h}_E\|\|\mathbf{h}_N\|\|\mathbf{h}_U\|\|\mathbf{h}_{Clk}\|(1-\rho_{en}^2(1-\bar{h}_u^2)-\rho_{eu}^2(1-\bar{h}_n^2)-\rho_{nu}^2(1-\bar{h}_e^2)+2\bar{h}_n\bar{h}_u(\rho_{nu}-\rho_{en}\rho_{eu})...\\+2\bar{h}_n\bar{h}_e(\rho_{en}-\rho_{eu}\rho_{nu})+2\bar{h}_u\bar{h}_e(\rho_{eu}-\rho_{en}\rho_{nu})+2\rho_{en}\rho_{nu}\rho_{eu}-\bar{h}_e^2-\bar{h}_n^2-\bar{h}_u^2)^{\frac{1}{2}}\end{array}\right\}}\\&=\frac{\lambda_{EDOP}}{\|\mathbf{h}_E\|}\end{aligned} \tag{A.40}$$

$$\lambda_{EDOP}=\left\{\frac{\begin{array}{l}1-\rho_{en}^2(1-\bar{h}_u^2)-\rho_{eu}^2(1-\bar{h}_n^2)-\rho_{nu}^2(1-\bar{h}_e^2)+2\bar{h}_n\bar{h}_u(\rho_{nu}-\rho_{en}\rho_{eu})...\\+2\bar{h}_n\bar{h}_e(\rho_{en}-\rho_{eu}\rho_{nu})+2\bar{h}_u\bar{h}_e(\rho_{eu}-\rho_{en}\rho_{nu})+2\rho_{en}\rho_{nu}\rho_{eu}-\bar{h}_e^2-\bar{h}_n^2-\bar{h}_u^2\end{array}}{1+2\rho_{nu}\rho_{ut}\rho_{tn}-\rho_{nu}^2-\rho_{ut}^2-\rho_{tn}^2}\right\}^{-\frac{1}{2}}\geq 1$$

$$NDOP = \frac{\mathrm{Vol}(\Xi(\mathbf{h}_E, \mathbf{h}_U, \mathbf{h}_{Clk}))}{\mathrm{Vol}(\Xi(\mathbf{h}_E, \mathbf{h}_N, \mathbf{h}_U, \mathbf{h}_{Clk}))}$$

$$= \frac{\|\mathbf{h}_E\|\|\mathbf{h}_U\|\|\mathbf{h}_{Clk}\|(1+2\rho_{eu}\rho_{ut}\rho_{te}-\rho_{eu}^2-\rho_{ut}^2-\rho_{te}^2)^{\frac{1}{2}}}{\left\{\begin{array}{l}\|\mathbf{h}_E\|\|\mathbf{h}_N\|\|\mathbf{h}_U\|\|\mathbf{h}_{Clk}\|(1-\rho_{en}^2(1-\bar{h}_u^2)-\rho_{eu}^2(1-\bar{h}_n^2)-\rho_{nu}^2(1-\bar{h}_e^2)+2\bar{h}_n\bar{h}_u(\rho_{nu}-\rho_{en}\rho_{eu})... \\ +2\bar{h}_n\bar{h}_e(\rho_{en}-\rho_{eu}\rho_{nu})+2\bar{h}_u\bar{h}_e(\rho_{eu}-\rho_{en}\rho_{nu})+2\rho_{en}\rho_{nu}\rho_{eu}-\bar{h}_e^2-\bar{h}_n^2-\bar{h}_u^2)^{\frac{1}{2}}\end{array}\right\}}$$

$$= \frac{\lambda_{NDOP}}{\|\mathbf{h}_N\|} \tag{A.41}$$

$$\lambda_{NDOP} = \left\{\begin{array}{l}(1-\rho_{en}^2(1-\bar{h}_u^2)-\rho_{eu}^2(1-\bar{h}_n^2)-\rho_{nu}^2(1-\bar{h}_e^2)+2\bar{h}_n\bar{h}_u(\rho_{nu}-\rho_{en}\rho_{eu})... \\ \frac{+2\bar{h}_n\bar{h}_e(\rho_{en}-\rho_{eu}\rho_{nu})+2\bar{h}_u\bar{h}_e(\rho_{eu}-\rho_{en}\rho_{nu})+2\rho_{en}\rho_{nu}\rho_{eu}-\bar{h}_e^2-\bar{h}_n^2-\bar{h}_u^2}{1+2\rho_{eu}\rho_{ut}\rho_{te}-\rho_{eu}^2-\rho_{ut}^2-\rho_{te}^2}\end{array}\right\}^{-\frac{1}{2}} \geq 1$$

$$UDOP = \frac{\mathrm{Vol}(\Xi(\mathbf{h}_E, \mathbf{h}_N, \mathbf{h}_{Clk}))}{\mathrm{Vol}(\Xi(\mathbf{h}_E, \mathbf{h}_N, \mathbf{h}_U, \mathbf{h}_{Clk}))}$$

$$= \frac{\|\mathbf{h}_E\|\|\mathbf{h}_N\|\|\mathbf{h}_{Clk}\|(1+2\rho_{en}\rho_{nt}\rho_{te}-\rho_{en}^2-\rho_{nt}^2-\rho_{te}^2)^{\frac{1}{2}}}{\left\{\begin{array}{l}\|\mathbf{h}_E\|\|\mathbf{h}_N\|\|\mathbf{h}_U\|\|\mathbf{h}_{Clk}\|(1-\rho_{en}^2(1-\bar{h}_u^2)-\rho_{eu}^2(1-\bar{h}_n^2)-\rho_{nu}^2(1-\bar{h}_e^2)+2\bar{h}_n\bar{h}_u(\rho_{nu}-\rho_{en}\rho_{eu})... \\ +2\bar{h}_n\bar{h}_e(\rho_{en}-\rho_{eu}\rho_{nu})+2\bar{h}_u\bar{h}_e(\rho_{eu}-\rho_{en}\rho_{nu})+2\rho_{en}\rho_{nu}\rho_{eu}-\bar{h}_e^2-\bar{h}_n^2-\bar{h}_u^2)^{\frac{1}{2}}\end{array}\right\}}$$

$$= \frac{\lambda_{UDOP}}{\|\mathbf{h}_U\|} \tag{A.42}$$

$$\lambda_{UDOP} = \left\{\begin{array}{l}(1-\rho_{en}^2(1-\bar{h}_u^2)-\rho_{eu}^2(1-\bar{h}_n^2)-\rho_{nu}^2(1-\bar{h}_e^2)+2\bar{h}_n\bar{h}_u(\rho_{nu}-\rho_{en}\rho_{eu})... \\ \frac{+2\bar{h}_n\bar{h}_e(\rho_{en}-\rho_{eu}\rho_{nu})+2\bar{h}_u\bar{h}_e(\rho_{eu}-\rho_{en}\rho_{nu})+2\rho_{en}\rho_{nu}\rho_{eu}-\bar{h}_e^2-\bar{h}_n^2-\bar{h}_u^2}{1+2\rho_{en}\rho_{nt}\rho_{te}-\rho_{en}^2-\rho_{nt}^2-\rho_{te}^2}\end{array}\right\}^{-\frac{1}{2}} \geq 1$$

$$
\begin{aligned}
TDOP &= \frac{\mathrm{Vol}(\Xi(\mathbf{h}_E, \mathbf{h}_N, \mathbf{h}_U))}{\mathrm{Vol}(\Xi(\mathbf{h}_E, \mathbf{h}_N, \mathbf{h}_U, \mathbf{h}_{Clk}))} \\
&= \frac{\|\mathbf{h}_E\|\|\mathbf{h}_N\|\|\mathbf{h}_U\|(1+2\rho_{en}\rho_{nu}\rho_{ue}-\rho_{en}^2-\rho_{nu}^2-\rho_{ue}^2)^{\frac{1}{2}}}{\left\{\begin{array}{l}\|\mathbf{h}_E\|\|\mathbf{h}_N\|\|\mathbf{h}_U\|\|\mathbf{h}_{Clk}\|(1-\rho_{en}^2(1-\bar{h}_u^2)-\rho_{eu}^2(1-\bar{h}_n^2)-\rho_{nu}^2(1-\bar{h}_e^2)+2\bar{h}_n\bar{h}_u(\rho_{nu}-\rho_{en}\rho_{eu})... \\ +2\bar{h}_n\bar{h}_e(\rho_{en}-\rho_{eu}\rho_{nu})+2\bar{h}_u\bar{h}_e(\rho_{eu}-\rho_{en}\rho_{nu})+2\rho_{en}\rho_{nu}\rho_{eu}-\bar{h}_e^2-\bar{h}_n^2-\bar{h}_u^2)^{\frac{1}{2}}\end{array}\right\}} \\
&= \frac{\lambda_{TDOP}}{\|\mathbf{h}_{Clk}\|}
\end{aligned}
\tag{A.43}
$$

$$
\lambda_{TDOP} = \left\{\begin{array}{l}(1-\rho_{en}^2(1-\bar{h}_u^2)-\rho_{eu}^2(1-\bar{h}_n^2)-\rho_{nu}^2(1-\bar{h}_e^2)+2\bar{h}_n\bar{h}_u(\rho_{nu}-\rho_{en}\rho_{eu})... \\ \dfrac{+2\bar{h}_n\bar{h}_e(\rho_{en}-\rho_{eu}\rho_{nu})+2\bar{h}_u\bar{h}_e(\rho_{eu}-\rho_{en}\rho_{nu})+2\rho_{en}\rho_{nu}\rho_{eu}-\bar{h}_e^2-\bar{h}_n^2-\bar{h}_u^2}{1+2\rho_{en}\rho_{nu}\rho_{ue}-\rho_{en}^2-\rho_{nu}^2-\rho_{ue}^2}\end{array}\right\}^{-\frac{1}{2}} \geq 1
$$

In these equations, λ denotes the geometry dependent factor in 4D cases. Its subscripts, such as EDOP, NDOP, UDOP, and TDOP denote the corresponding axis. When comparing these pseudorange DOP terms with the range measurement DOP shown in equation (A.28), (A.29), and (A.30), the degradation ratios $\gamma_{E,4/3D}, \gamma_{N,4/3D}, \gamma_{U,4/3D}$ can also be easily computed by comparing equation (A.28) with equation (A.40), equation (A.29) with equation (A.42), and equation (A.30) with equation (A.43).

A.3 Satellite Geometry Characterization

In the previous sections, a geometric analysis on GNSS DOP was introduced and some fundamental formulas were derived. There are several benefits in using this geometric analysis method. First, it provides a more insightful way to interpret DOP metrics. Second, this geometric method provides some analytical closed form expressions, which are useful for further theoretical analysis on related topics. Third, the method can also be

conveniently used to extend some useful concepts related with DOP metrics, such as *joint DOP*, and *DOP correlation coefficients*.

A.3.1 Joint DOP & DOP Correlation coefficients

By using the geometric method, it is convenient to derive the joint DOP values, such as ENDOP, EUDOP, NUDOP, ETDOP, NTDOP and UTDOP. These terms are defined as the total error volume divided by the appropriate `error base`.

$$\begin{aligned} &ENDOP = \frac{Vol_{ENUClk}}{Vol_{UClk}}, EUDOP = \frac{Vol_{ENUClk}}{Vol_{NClk}}, NUDOP = \frac{Vol_{ENUClk}}{Vol_{EClk}} \\ &ETDOP = \frac{Vol_{ENUClk}}{Vol_{NU}}, NTDOP = \frac{Vol_{ENUClk}}{Vol_{EU}}, UTDOP = \frac{Vol_{ENUClk}}{Vol_{EN}} \end{aligned} \tag{A.44}$$

Then the correlation coefficients between east, north, vertical and time axis can be derived as

$$\begin{aligned} \rho_{EDOP,NDOP} &= \sqrt{1-\left(\frac{ENDOP}{EDOP \bullet NDOP}\right)^2} = \sqrt{1-\left\{\frac{Vol_{ENUClk}}{Vol_{UClk}} / \left(\frac{Vol_{ENUClk}}{Vol_{NUClk}} \frac{Vol_{ENUClk}}{Vol_{EUClk}}\right)\right\}^2} \\ &= \sqrt{1-\left(\frac{Vol_{NUClk} \bullet Vol_{EUClk}}{Vol_{ENUClk} \bullet Vol_{UClk}}\right)^2} \\ &= \sqrt{1-\frac{\left\{\begin{array}{l}(1-\overline{h}_u^2)(1-\rho_{en}^2(1-\overline{h}_u^2)-\rho_{eu}^2(1-\overline{h}_n^2)-\rho_{nu}^2(1-\overline{h}_e^2)+2\overline{h}_n\overline{h}_u(\rho_{nu}-\rho_{en}\rho_{eu})\ldots \\ +2\overline{h}_n\overline{h}_e(\rho_{en}-\rho_{eu}\rho_{nu})+2\overline{h}_u\overline{h}_e(\rho_{eu}-\rho_{en}\rho_{nu})+2\rho_{en}\rho_{nu}\rho_{eu}-\overline{h}_e^2-\overline{h}_n^2-\overline{h}_u^2)\end{array}\right\}}{\left\{(1+2\rho_{\mathbf{h}_N\mathbf{h}_U}\overline{h}_u\overline{h}_n-\rho_{\mathbf{h}_N\mathbf{h}_U}^2-\overline{h}_u^2-\overline{h}_n^2)(1+2\rho_{\mathbf{h}_E\mathbf{h}_U}\overline{h}_u\overline{h}_e-\rho_{\mathbf{h}_E\mathbf{h}_U}^2-\overline{h}_u^2-\overline{h}_e^2)\right\}}} \end{aligned} \tag{A.45}$$

$$\rho_{EDOP,UDOP} = \sqrt{1-\left(\frac{EUDOP}{EDOP \bullet UDOP}\right)^2} = \sqrt{1-\left\{\frac{Vol_{ENUClk}}{Vol_{NClk}} / \left(\frac{Vol_{ENUClk}}{Vol_{NUClk}} \frac{Vol_{ENUClk}}{Vol_{ENClk}}\right)\right\}^2}$$

$$= \sqrt{1-\left\{\frac{Vol_{NUClk} \bullet Vol_{ENClk}}{Vol_{ENUClk} \bullet Vol_{NClk}}\right\}^2} \tag{A.46}$$

$$= \sqrt{1-\frac{\left\{\begin{array}{l}(1-\bar{h}_n^2)(1-\rho_{en}^2(1-\bar{h}_u^2)-\rho_{eu}^2(1-\bar{h}_n^2)-\rho_{nu}^2(1-\bar{h}_e^2)+2\bar{h}_n\bar{h}_u(\rho_{nu}-\rho_{en}\rho_{eu})\ldots \\ +2\bar{h}_n\bar{h}_e(\rho_{en}-\rho_{eu}\rho_{nu})+2\bar{h}_u\bar{h}_e(\rho_{eu}-\rho_{en}\rho_{nu})+2\rho_{en}\rho_{nu}\rho_{eu}-\bar{h}_e^2-\bar{h}_n^2-\bar{h}_u^2)\end{array}\right\}}{(1+2\rho_{\mathbf{h}_N\mathbf{h}_U}\bar{h}_u\bar{h}_n-\rho_{\mathbf{h}_N\mathbf{h}_U}^2-\bar{h}_u^2-\bar{h}_n^2)(1+2\rho_{\mathbf{h}_E\mathbf{h}_N}\bar{h}_n\bar{h}_e-\rho_{\mathbf{h}_E\mathbf{h}_N}^2-\bar{h}_n^2-\bar{h}_e^2)}}$$

$$\rho_{NDOP,UDOP} = \sqrt{1-\left(\frac{NUDOP}{NDOP \bullet UDOP}\right)^2} = \sqrt{1-\left\{\frac{Vol_{ENUClk}}{Vol_{EClk}} / \left(\frac{Vol_{ENUClk}}{Vol_{EUClk}} \frac{Vol_{ENUClk}}{Vol_{ENClk}}\right)\right\}^2}$$

$$= \sqrt{1-\left(\frac{Vol_{EUClk} \bullet Vol_{ENClk}}{Vol_{ENUClk} \bullet Vol_{EClk}}\right)^2} \tag{A.47}$$

$$= \sqrt{1-\frac{\left\{\begin{array}{l}(1-\bar{h}_e^2)(1-\rho_{en}^2(1-\bar{h}_u^2)-\rho_{eu}^2(1-\bar{h}_n^2)-\rho_{nu}^2(1-\bar{h}_e^2)+2\bar{h}_n\bar{h}_u(\rho_{nu}-\rho_{en}\rho_{eu})\ldots \\ +2\bar{h}_n\bar{h}_e(\rho_{en}-\rho_{eu}\rho_{nu})+2\bar{h}_u\bar{h}_e(\rho_{eu}-\rho_{en}\rho_{nu})+2\rho_{en}\rho_{nu}\rho_{eu}-\bar{h}_e^2-\bar{h}_n^2-\bar{h}_u^2)\end{array}\right\}}{(1+2\rho_{\mathbf{h}_E\mathbf{h}_U}\bar{h}_u\bar{h}_e-\rho_{\mathbf{h}_E\mathbf{h}_U}^2-\bar{h}_u^2-\bar{h}_e^2)(1+2\rho_{\mathbf{h}_E\mathbf{h}_N}\bar{h}_n\bar{h}_e-\rho_{\mathbf{h}_E\mathbf{h}_N}^2-\bar{h}_n^2-\bar{h}_e^2)}}$$

$$\rho_{EDOP,TDOP} = \sqrt{1-\left(\frac{ETDOP}{EDOP \bullet TDOP}\right)^2} = \sqrt{1-\left\{\frac{Vol_{ENUClk}}{Vol_{NU}} / \left(\frac{Vol_{ENUClk}}{Vol_{NUClk}} \frac{Vol_{ENUClk}}{Vol_{ENU}}\right)\right\}^2}$$

$$= \sqrt{1-\left(\frac{Vol_{NUClk} \bullet Vol_{ENU}}{Vol_{ENUClk} \bullet Vol_{NU}}\right)^2} \tag{A.48}$$

$$= \sqrt{1-\frac{\left\{\begin{array}{l}(1-\rho_{\mathbf{h}_N\mathbf{h}_U}^2)(1-\rho_{en}^2(1-\bar{h}_u^2)-\rho_{eu}^2(1-\bar{h}_n^2)-\rho_{nu}^2(1-\bar{h}_e^2)+2\bar{h}_n\bar{h}_u(\rho_{nu}-\rho_{en}\rho_{eu})\ldots \\ +2\bar{h}_n\bar{h}_e(\rho_{en}-\rho_{eu}\rho_{nu})+2\bar{h}_u\bar{h}_e(\rho_{eu}-\rho_{en}\rho_{nu})+2\rho_{en}\rho_{nu}\rho_{eu}-\bar{h}_e^2-\bar{h}_n^2-\bar{h}_u^2)\end{array}\right\}}{(1+2\rho_{\mathbf{h}_N\mathbf{h}_U}\bar{h}_u\bar{h}_n-\rho_{\mathbf{h}_N\mathbf{h}_U}^2-\bar{h}_u^2-\bar{h}_n^2)(1+2\rho_{\mathbf{h}_E\mathbf{h}_N}\rho_{\mathbf{h}_N\mathbf{h}_U}\rho_{\mathbf{h}_E\mathbf{h}_U}-\rho_{\mathbf{h}_E\mathbf{h}_N}^2-\rho_{\mathbf{h}_N\mathbf{h}_U}^2-\rho_{\mathbf{h}_E\mathbf{h}_U}^2}}$$

$$\rho_{NDOP,TDOP} = \sqrt{1-\left(\frac{NTDOP}{NDOP \bullet TDOP}\right)^2} = \sqrt{1-\left\{\frac{Vol_{ENUClk}}{Vol_{EU}} \Big/ \left(\frac{Vol_{ENUClk}}{Vol_{EUClk}} \frac{Vol_{ENUClk}}{Vol_{ENU}}\right)\right\}^2}$$

$$= \sqrt{1-\left(\frac{Vol_{EUClk} \bullet Vol_{ENU}}{Vol_{ENUClk} \bullet Vol_{EU}}\right)^2}$$

$$= \sqrt{1-\frac{\left\{\begin{array}{l}(1-\rho^2_{\mathbf{h}_E\mathbf{h}_U})(1-\rho^2_{en}(1-\overline{h}_u^2)-\rho^2_{eu}(1-\overline{h}_n^2)-\rho^2_{nu}(1-\overline{h}_e^2)+2\overline{h}_n\overline{h}_u(\rho_{nu}-\rho_{en}\rho_{eu})\ldots \\ +2\overline{h}_n\overline{h}_e(\rho_{en}-\rho_{eu}\rho_{nu})+2\overline{h}_u\overline{h}_e(\rho_{eu}-\rho_{en}\rho_{nu})+2\rho_{en}\rho_{nu}\rho_{eu}-\overline{h}_e^2-\overline{h}_n^2-\overline{h}_u^2)\end{array}\right\}}{(1+2\rho_{\mathbf{h}_E\mathbf{h}_U}\overline{h}_u\overline{h}_e-\rho^2_{\mathbf{h}_E\mathbf{h}_U}-\overline{h}_u^2-\overline{h}_e^2)(1+2\rho_{\mathbf{h}_E\mathbf{h}_N}\rho_{\mathbf{h}_N\mathbf{h}_U}\rho_{\mathbf{h}_E\mathbf{h}_U}-\rho^2_{\mathbf{h}_E\mathbf{h}_N}-\rho^2_{\mathbf{h}_N\mathbf{h}_U}-\rho^2_{\mathbf{h}_E\mathbf{h}_U})}} \quad \text{(A.49)}$$

$$\rho_{UDOP,TDOP} = \sqrt{1-\left(\frac{UTDOP}{UDOP \bullet TDOP}\right)^2} = \sqrt{1-\left\{\frac{Vol_{ENUClk}}{Vol_{EN}} \Big/ \left(\frac{Vol_{ENUClk}}{Vol_{ENClk}} \frac{Vol_{ENUClk}}{Vol_{ENU}}\right)\right\}^2}$$

$$= \sqrt{1-\left(\frac{Vol_{ENClk} \bullet Vol_{ENU}}{Vol_{ENUClk} \bullet Vol_{EN}}\right)^2}$$

$$= \sqrt{1-\frac{\left\{\begin{array}{l}(1-\rho^2_{\mathbf{h}_E\mathbf{h}_N})(1-\rho^2_{en}(1-\overline{h}_u^2)-\rho^2_{eu}(1-\overline{h}_n^2)-\rho^2_{nu}(1-\overline{h}_e^2)+2\overline{h}_n\overline{h}_u(\rho_{nu}-\rho_{en}\rho_{eu})\ldots \\ +2\overline{h}_n\overline{h}_e(\rho_{en}-\rho_{eu}\rho_{nu})+2\overline{h}_u\overline{h}_e(\rho_{eu}-\rho_{en}\rho_{nu})+2\rho_{en}\rho_{nu}\rho_{eu}-\overline{h}_e^2-\overline{h}_n^2-\overline{h}_u^2)\end{array}\right\}}{(1+2\rho_{\mathbf{h}_E\mathbf{h}_N}\overline{h}_n\overline{h}_e-\rho^2_{\mathbf{h}_E\mathbf{h}_N}-\overline{h}_n^2-\overline{h}_e^2)(1+2\rho_{\mathbf{h}_E\mathbf{h}_N}\rho_{\mathbf{h}_N\mathbf{h}_U}\rho_{\mathbf{h}_E\mathbf{h}_U}-\rho^2_{\mathbf{h}_E\mathbf{h}_N}-\rho^2_{\mathbf{h}_N\mathbf{h}_U}-\rho^2_{\mathbf{h}_E\mathbf{h}_U})}} \quad \text{(A.50)}$$

It is well known that the vertical axis is affected most significantly by clock errors. Simply put, the vertical errors have the strongest correlation with the clock errors, while the east and north axes have less correlation. However, to the best of the author's knowledge, there is little literature that quantifies this correlation. Zhang (1997) has empirically computed the correlation between the vertical and time axis. The correlation coefficient concepts developed herein fill in this gap and provide analytical expressions to quantify such values.

It is known that by using more satellites, the DOP values decrease. In real situations, chances are that the error in one axis is usually more significant than in the others. By

using the DOP correlation coefficients, one can choose the geometry with controlled correlation between different axes.

A.3.2 Experimental Data Illustration

The previous sections analyze the GNSS DOP metrics theoretically while this section provides an example to show how the concepts developed in this chapter can be used to characterize the satellite-user geometry.

Some open sky data was collected on the campus of University of Calgary. The GPS and GLONASS ephemeris and observations were logged using a Novatel receiver. A reference antenna mounted on the roof of the CCIT building was used. The satellite sky-plot is shown in Figure A.9. There are five GPS satellites (PRN 9, PRN15, PRN17, PRN27, PRN28) and there are three GLONASS satellites (GLO15, GLO17, and GLO18).

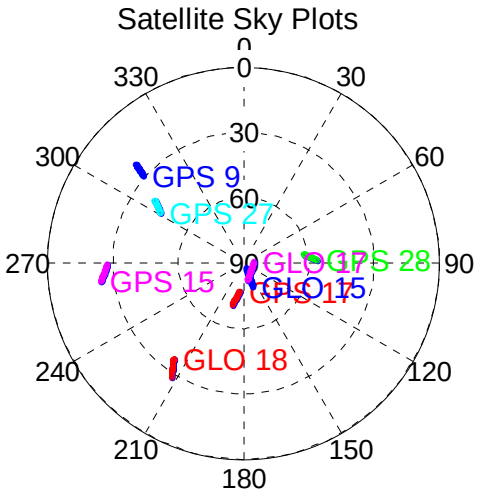

Figure A.9: Experimental data sky plot

With the satellite geometry shown in Figure A.9, the DOP metrics using GPS only and GPS plus GLONASS are plotted in Figure A.10 where it can be seen that there is a significant improvement in NDOP and UDOP by adding GLONASS. However, there is only a slight improvement for EDOP. In order to further explore the benefits brought by GLONASS, the DOP correlation coefficients defined in equations (A.45) to (A.50) are used.

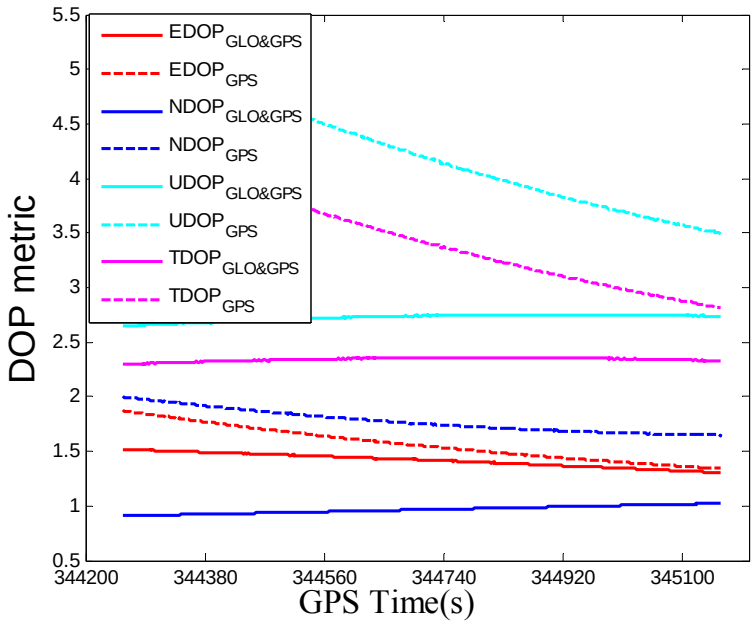

Figure A.10: GPS+GLONASS & GPS only DOPs

The correlation coefficients between E-N, E-U and N-U are plotted in Figure A.11 and the following can be observed: First, the correlation between EDOP and UDOP ($\rho_{EDOP\&UDOP}$) is the largest according to this satellite geometry. Before adding GLONASS signals, $\rho_{NDOP\&UDOP-GPS}$ is larger than $\rho_{EDOP\&NDOP-GPS}$. But after adding GLONASS, the

correlation coefficient $\rho_{NDOP\&UDOP-GPS+GLO}$ is smaller than $\rho_{EDOP\&NDOP-GPS+GLO}$. Another interesting finding is that, with GPS plus GLONASS, the correlation between EDOP and UDOP is greater than that in the GPS only case for certain epochs.

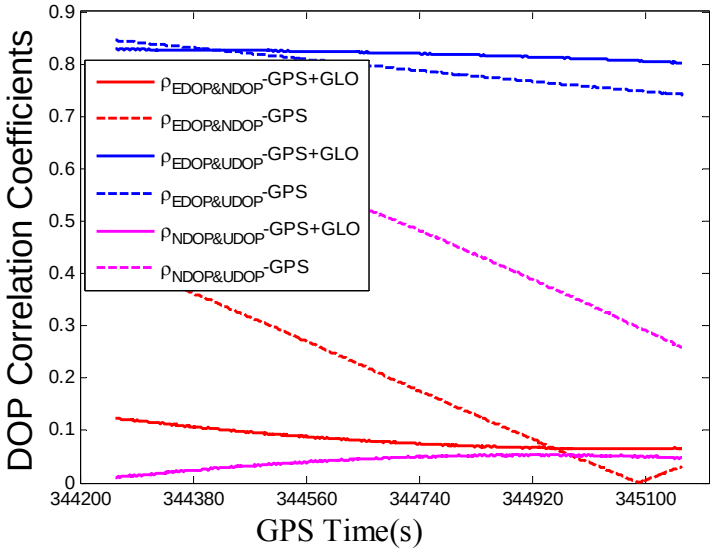

Figure A.11: GNSS DOP correlation coefficients of E-N, E-U, and N-U

Similarly, the correlation coefficients between E-T, N-T and U-T can also be computed and are shown in Figure A.12. From Figure A.12, it is apparent that UDOP is nearly in perfect correlation with TDOP, which matches intuition. And furthermore, it is observed that the correlation between EDOP and TDOP is much greater than the correlation between NDOP and TDOP. By adding GLONASS measurements, $\rho_{NDOP\&TDOP}$ is significantly de-correlated.

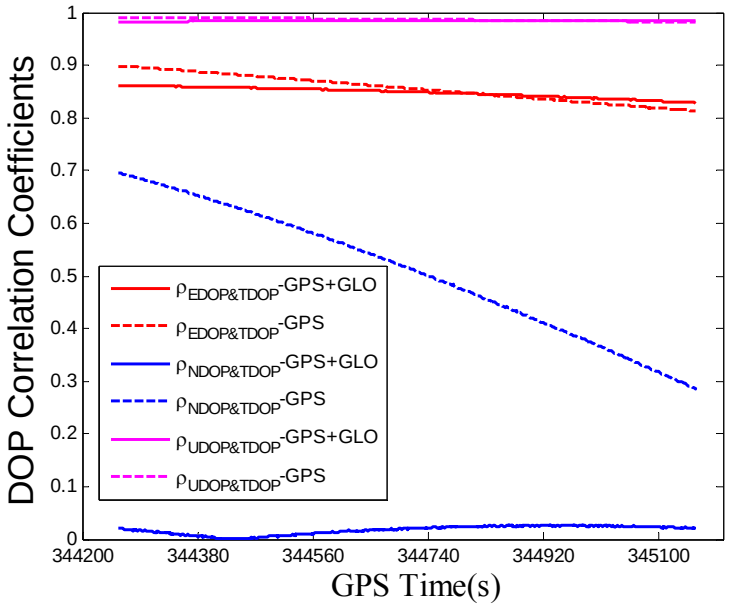

Figure A.12: GNSS DOP correlation coefficients of E-T, N-T, and U-T

In this appendix, some geometric analyses of GNSS DOPs have been completed with some important terms being defined and derived. In particular, the geometry dependent factor in 4D navigation coordinate has been obtained (equation (A.40) to equation (A.43)), with the aim to further assess the benefits of a direct vector receiver to be discussed in previous chapters.